



The  
University  
Of  
Sheffield.

# Personalisation of musculoskeletal models using Magnetic Resonance Imaging

Erica Montefiori

A thesis submitted in partial fulfilment of the requirements for the degree of  
Doctor of Philosophy

INSIGNEO Institute for in silico Medicine  
Department of Mechanical Engineering  
Faculty of Engineering  
The University of Sheffield

July 2019



# Summary

Musculoskeletal (MSK) disorders affecting locomotion represent one of the leading causes for disability in the developed countries, impacting on the patients' lifestyle and social inclusion, as well as the national healthcare resources.

Due to the different aetiologies and progression of such diseases, and to the individual needs of patients, personalised assessment is currently promoted as the gold standard for the diagnosis and treatment of MSK disorders. The introduction of MSK models has recently integrated more traditional measurements of gait-related parameters, enabling the simulation of clinical scenarios and rehabilitation plans within a computational environment, therefore limiting the invasiveness of the experiments. However, the lack of standardised and validated procedures currently limits the adoption of these techniques in the clinical practice and restricts their shareability across the research community.

The aim of this PhD thesis was to develop an innovative, robust, and repeatable procedure for the definition of MRI-based subject-specific MSKMs of the lower limb. A fully documented procedure (and associated methodologies) for producing such models was proposed. The final scope of this project is to promote the adoption of personalised modelling in the clinical assessment of lower-limb MSK disorders.

The versatility of the proposed modelling approach was successfully tested by applying it in cohorts featured by different age (juvenile and elderly), genders and health conditions (juvenile idiopathic arthritis and osteopenia). In particular the model was tested for its ability to: discriminate joint kinematics and joint loadings that are typical of different populations; identify informative biomechanical parameters to characterise disease and disease progression in juvenile idiopathic arthritis; quantify the effect of different physiological muscle features, such as volumes and geometry, on the estimate of joint loading.

As a result of the work carried out as part of the above studies, a significant advance in the standardisation and automation of the procedures needed for building fully personalised MRI-based models of the MSK system has been achieved. The model outputs were proved to have good repeatability and reproducibility and to be informative in all above applications. The proposed approach also showed a clear potential toward complementing traditional

clinical gait analysis approaches by providing information on the muscle and joint internal forces, otherwise not easily accessible *in-vivo*.

Future work will aim at reducing the cost, operator time, and errors associated to MRI-based MSK modelling by further improving and automating the image processing techniques and even replacing the MRI with affordable and portable technologies, such as ultrasound-based systems.

# Acknowledgements

I would like to acknowledge my supervisor Prof Claudia Mazzà for the professional and personal support throughout the whole PhD journey. I also wish to thank the colleagues in the MSK group at INSIGNEO, especially Luca Modenese, Barbara Kalkman, Freddie Greatrex, Bart van Veen, Lorenza Angelini and Giuliano Lamberto.

I would have never been able to proceed in my studies and achieve this milestone without the constant guidance and unconditional appreciation from my mum and dad. I would have never found the motivation to pursue my objectives without the encouragement and the exhortation from Ivan.

This would have never happened this quickly without You pushing and kicking from inside.

# Publications

## Refereed Journals

### In Print

1. **E. Montefiori**, L. Modenese, R. Di Marco, S. Magni-Manzoni, C. Malattia, M. Petrarca, A. Ronchetti, L. Tanturri de Horatio, P. van Dijkhuizen, A. Wang, S. Wesarg, M. Viceconti, C. Mazzà; MD-PAEDIGREE Consortium, “Linking Joint Impairment and Gait Biomechanics in Patients with Juvenile Idiopathic Arthritis”, *Ann Biomed Eng* (2019) doi: 10.1007/s10439-019-02287-0.
2. **E. Montefiori**, L. Modenese, R. Di Marco, S. Magni-Manzoni, C. Malattia, M. Petrarca, A. Ronchetti, L. Tanturri de Horatio, P. van Dijkhuizen, A. Wang, S. Wesarg, M. Viceconti, C. Mazzà; MD-PAEDIGREE Consortium, “A patient-specific kinematic model of the ankle and subtalar joints to assess the disease activity in children with Juvenile Idiopathic Arthritis”, *J Biomech* (2019) 85:27-36.
3. L. Modenese, **E. Montefiori**, A. Wang, S. Wesarg, M. Viceconti, C. Mazzà, “Investigation of the dependence of joint contact forces on musculotendon parameters using a codified workflow for image-based modelling”. *J Biomech* (2018) 73:108–118.
4. I. Hannah, **E. Montefiori**, L. Modenese, J. Prinold, M. Viceconti, C. Mazzà, "Sensitivity of a juvenile subject-specific musculoskeletal model of the ankle joint to the variability of operator dependent input", *Proc Inst Mech Eng H* (2017) 231(5):415–422.
5. F. Greatrex, **E. Montefiori**, D. McCririck, T. Grupp, J. Kozak, C. Mazzà, “Reliability of an Integrated Ultrasound and Stereophotogrammetric System for Lower Limb Anatomical Characterisation”, *Appl Bionics Biomech* (2017) 2017:4370649-1–8.

### Under review

1. B. van Veen, **E. Montefiori**, L. Modenese, C. Mazzà, M. Viceconti. “Muscle recruitment strategies can reduce joint loading during level walking”, submitted to *Journal of Biomechanics* in Mar 2019.
2. I. Benemerito, L. Modenese, **E. Montefiori**, C. Mazzà, M. Viceconti, D. Lacroix, L. Guo. “Extended discrete element method can evaluate the effect of time dependency and translation of the talus on the estimation of cartilage pressure at the ankle joint”, submitted to *Proc Inst Mech Eng H* in Jul 2019.

### In preparation

1. **E. Montefiori**, B. Kalkman, A. Clarke, M. Paggiosi, E. McCloskey, C. Mazzà. “7. The effect of muscle personalisation in the estimate of muscle forces and joint contact forces in post-menopausal women”, *IEEE Transaction on Biomedical Engineering*.

## Conference abstracts

### Oral presentations

1. **E. Montefiori**, B. Kalkman, B. van Veen, A. Clarke, M. Paggiosi, E. McCloskey, C. Mazzà. "Muscle variability effect on joint contact forces prediction in post-menopausal women". CMAS2019, Sheffield
2. M. Conconi, **E. Montefiori**, N. Sancisi, C. Mazzà. "From scaling to MRI defined subject-specific ankle joint models: a comparison of three approaches with increasing level of anatomical consistency". CMBBE2019, New York
3. **E. Montefiori**, B. Kalkman, A. Clarke, M. Paggiosi, E. McCloskey, C. Mazzà. "Muscle anatomical variability and joint contact forces prediction in post-menopausal women". ISB2019, Calgary
4. M. Conconi, **E. Montefiori**, N. Sancisi, C. Mazzà. "Evaluation of anatomical consistency of three subject-specific ankle joint modelling approaches". ISB2019, Calgary
5. **E. Montefiori**, B. Kalkman, A. Clarke, M. Paggiosi, E. McCloskey, C. Mazzà. "A subject-specific musculoskeletal model to estimate joint loading at different walking speeds". SIAMOC 2018, (Gait&Pos, Oct;66 Suppl 1:s28)
6. **E. Montefiori**, L. Modenese, R. Di Marco, S. Magni-Manzoni, C. Malattia, M. Petrarca, A. Ronchetti, P. van Dijkhuizen, M. Viceconti, C. Mazzà; "MRI-based musculoskeletal models for the quantification of gait in children with Juvenile Idiopathic Arthritis". ESMAC 2018, Prague (Gait&Pos, Sep;65 Suppl 1:216-218)
7. **E. Montefiori**, L. Modenese, M. Viceconti, C. Mazzà, "Patient-specific musculoskeletal models to characterise the response to disease activity in patients with Juvenile Idiopathic Arthritis". VPH Conference 2018, Zaragoza, Spain
8. **E. Montefiori**, L. Modenese, M. Viceconti, C. Mazzà, "An MRI-based model for the estimate of patient-specific joint kinematics". 3D-AHM 2018, Salford, UK.
9. Benemerito, L. Modenese, **E. Montefiori**, C. Mazzà, M. Viceconti, D. Lacroix, L. Guo; "Evaluation of joint contact pressure in four subject specific discrete element-based models of the ankle joint" WCB 2018, Dublin, Ireland.
10. **E. Montefiori**, L. Modenese, M. Viceconti, C. Mazzà, "A subject-specific foot model for the estimation of subtalar joint kinematics". ISB 2017, Brisbane, Australia
11. L. Modenese, R. Di Marco, S. Magni-Manzoni, C. Malattia, C. Mazzà, **E. Montefiori**, M. Petrarca, A. Ronchetti, L. Tantarri de Horatio, P. van Dijkhuizen, M. Viceconti, A. Wang, S. Wesarg; MD-PAEDIGREE Consortium, "Subject-specific modelling unveils ankle joint protective mechanism in the gait of patients with Juvenile Idiopathic Arthritis". ISB 2017, Brisbane, Australia
12. Benemerito, L. Modenese, **E. Montefiori**, C. Mazzà, M. Viceconti, D. Lacroix, L. Guo; "Computation of joint contact pressure in a patient specific ankle model". ISB 2017, Brisbane, Australia
13. F. Greatrex, **E. Montefiori**, D. McCririck, T. Grupp, J. Kozak, C. Mazzà; "Validation of an Integrated Ultrasound and Stereophotogrammetric System for Lower Limb Anatomical Characterisation". ISB 2017, Brisbane, Australia
14. Hannah, **E. Montefiori**, L. Modenese, M. Viceconti, C. Mazzà; "Repeatability of operator dependent input in a patient-specific musculoskeletal model of the ankle". ESB 2016, Lyon, France

#### Poster presentations

1. L. Angelini, B. Kalkman, **E. Montefiori**, H. Horsewill, T. Jenkins, C. Mazzà; "MRI-based patient specific modelling of gait in Motor Neuron Disease". WCB 2018, Dublin, Ireland.

2. B. Kalkman, M. Woodward, **E. Montefiori**, C. Mazzà;” Volume-based calculation of maximal isometric muscle forces for the estimation of joint reaction forces in postmenopausal woman”. WCB 2018, Dublin, Ireland.
3. F. Greatrex, **E. Montefiori**, B. Kalkman, C. Mazzà. “3D ultrasound methods for image-based personalisation of musculoskeletal models”. CMBBE2019, New York
4. **E. Montefiori**, L. Modenese, M. Viceconti, C. Mazzà, “A patient-specific model of the subtalar and tibiotalar joints to assess gait in children with Juvenile Idiopathic Arthritis”. WCB 2018, Dublin, Ireland.

#### Workshops

- OpenSim Workshop, November 2018, Leuven, Belgium (attendee presentation)
- CMAS 2019, Sheffield, UK (organiser and presenter)

# Table of contents

Summary .....	3
Acknowledgements.....	5
Publications.....	6
Table of contents .....	9
Nomenclature .....	12
List of Figures .....	13
Declaration.....	17
1. Overview .....	18
1.1. Introduction.....	19
1.2. Thesis outline .....	21
1.3. References.....	24
2. Background information .....	27
2.1. Basic concepts .....	28
2.1.1. Anatomical and rotation planes .....	28
2.1.2. The lower-limb musculoskeletal system.....	29
2.2. Input data for musculoskeletal modelling .....	33
2.2.1. Magnetic resonance imaging.....	33
2.2.2. Marker-based gait analysis .....	35
2.3. Musculoskeletal models and simulations .....	38
2.3.1. Skeletal models .....	38
2.3.2. Muscular models.....	41
2.3.3. Scaled-generic and subject-specific musculoskeletal models .....	44
2.3.4. Musculoskeletal simulations.....	47

2.3.5.	Limitations of subject-specific musculoskeletal modelling .....	50
2.4.	Aim and objectives .....	53
2.5.	References.....	55
3.	An image-based kinematic model of the tibiotalar and subtalar joints and its application to gait analysis in children with Juvenile Idiopathic Arthritis .....	60
4.	Sensitivity of a juvenile subject-specific musculoskeletal model of the ankle joint to the variability of operator dependent input .....	72
5.	Methods for MRI-based anatomical modelling of the lower limb .....	82
5.1.	Optimised input data for musculoskeletal modelling.....	83
5.1.1.	Experimental protocols.....	83
5.2.	Anatomical model .....	84
5.2.1.	Creation of the joints .....	85
5.2.2.	Location of muscle attachment points .....	87
5.2.3.	Inertial properties .....	91
5.3.	References.....	92
6.	Linking joint impairments and gait biomechanics in patients with Juvenile Idiopathic Arthritis .....	94
7.	The effect of muscle personalisation in the estimate of muscle forces and joint contact forces in post-menopausal women .....	109
7.1.	Abstract .....	112
7.2.	Introduction.....	113
7.3.	Methods .....	115
7.3.1.	Participants and data acquisition .....	115
7.3.2.	Musculoskeletal models .....	117
7.3.3.	Data analysis .....	121
7.4.	Results .....	122
7.4.1.	Anatomical variability .....	122

7.4.2.	Musculotendon parameters .....	126
7.4.3.	Muscle activations .....	127
7.4.4.	Joint contact forces.....	129
7.5.	Discussion.....	132
7.6.	Conflict of interest.....	136
7.7.	Acknowledgments.....	136
7.8.	References.....	137
8.	General discussion and conclusions .....	141
8.1.	Limitations.....	142
8.2.	Critical appraisal of published work.....	143
8.3.	Impact.....	145
8.4.	Future work.....	147
8.5.	References.....	149
Appendix I	.....	I
Appendix II	.....	XXVII

# Nomenclature

BW	Body weight
CE	Contractile element
CGA	Clinical gait analysis
CoV	Coefficient of variation
CT	Computed tomography
DE	Dumping element
DoF	Degree of freedom
FLV	Force-length-velocity
GRF	Ground reaction force
ICP	Iterative closest point
ID	Inverse Dynamics
IK	Inverse Kinematics
JIA	Juvenile idiopathic arthritis
JCF	Joint contact force
MRI	Magnetic resonance image
MSK	Musculoskeletal
MSKM	Musculoskeletal model
PCSA	Physiological cross-sectional area
RF	Radio frequency
SE	Serial element
US	Ultrasound

# List of Figures

Figure 1-1 – Schematic of the outline of the thesis .....	23
Figure 2-1 – Anatomical planes and terminology .....	29
Figure 2-2 - The main bones of the lower limb.....	30
Figure 2-3 – Schematic representation of ball-and socket (left), ellipsoid (middle), and hinge (right) ideal joints (adapted from Maik et al. (2010)). .....	32
Figure 2-4 – Relaxation curves: T1 relaxation (left) is the process by which the longitudinal magnetization ( $M_z$ ) returns to its initial maximum value ( $M_0$ ); T2 relaxaiton (right) is the process by which the transverse magnetization ( $M_{xy}$ ) decays. ....	34
Figure 2-5 – Example of segmentation of the muscles of the lower limb form different views: transverse (top left), sagittal (top right), frontal (bottom right), and 3D perspective (bottom left).....	35
Figure 2-6 - Gait analysis laboratory ( <a href="http://www.qualisys.com">http://www.qualisys.com</a> ) .....	36
Figure 2-7 – Example of full-body marker placement (Plug-in Gait) and corresponding skeletal model with highlighted body segments and joints. Adapted from Plug-in Gait Reference Guide (Vicon Motion System, Oxford, UK).....	37
Figure 2-8 – Example of data collected during a gait analysis session. (top) Perspective of the walking showing the markers on the various segments of the lower limbs, with highlighted trajectories of the pelvis markers (red), and ground reaction force (GRF, yellow vector) measured by the force plates. (middle) Analog graphs showing the magnitude of the three components of the GRF. (bottom) Signals recorded by the electromyography sensors. ....	38
Figure 2-9 – Definition of the tibiotalar joint according to anatomical landmarks (i.e. the lateral and medial malleoli, LM and MM, respectively, red) and manual fitting of a cylinder to the talar dome (blue) and comparison of the two methods. ....	41

Figure 2-10 – Representation of the Gluteus maximum large muscle belly and attachment region by means of three bundles connecting three origin points to three insertion points and passing through one via point each.....42

Figure 2-11 – (top) Hill-type representation of the musculotendon unit adapted from Thelen (2003) including the active contractile element (CE) and the two passive elastic elements, DE and SE. (a) Description of the active (and passive) force-length relationship of muscles; (b) Force-velocity relationship curve presented as a function of the muscle activation; (c) Passive tendon force increasing with strain.....43

Figure 2-12 - OpenSim environment and generic model “gait2392” (<https://simtk-confluence.stanford.edu>). .....45

Figure 5-1 – Definition of the joint axes through morphological fitting of analytical shapes to the articular surface of the bones. Example for hip, knee and ankle fitted to sphere, cylinder, and cylinder, respectively. ....86

Figure 5-2 – Example of definition of the gluteus maximus path (red lines) according to the three-bundle schematisation proposed by Delp et al. (1990) and identification of the moment arm (*ma*) of the first bundle. ....88

Figure 5-3 – Identification of the via points of the muscles crossing the ankle on the transverse plane of the MRI. ....89

Figure 5-4 – Schematics of the ICP-based mapping of the muscle points. ....91

Figure 7-1 - Marker placement as used during gait analysis and MRI scanning. Sixteen markers were placed during both gait analysis and MRI (filled red circles), nine extra markers were only used during gait analysis (open red circles). EMG of five muscles (blue closed circles) was collected during gait analysis.....117

Figure 7-2 – A) Gen model, with scaled joint axes and muscle geometry (OpenSim Scaling Tool); B) joint axes identification through morphologic fitting in Hyb and SSp; C) identification of the muscle attachments and via points from manual palpation of the MRI in the Hyb model; D) identification of the muscle attachments and via points from the centre line of the

segmentations in the SSp model; E), F), G) calculation of the muscle parameters for Gen, Hyb and SSp, respectively. ....120

Figure 7-3 – Mean±SD muscle volume calculated as a fraction of total limb muscle volume for the right and left limb of the eleven subjects in the present study and for the cohort of young adults enrolled by Handsfield et al. (2014). ....123

Figure 7-4 - Mean±SD of muscle volumes (significant difference between left and right: \* p<0.05, \*\*p<0.01) and maximum SD from the repeatability analysis. Individual percentage difference between the legs is reported as a bar plot where each bar represents a participant: blue positive (red negative) values show that the right leg is bigger (smaller). DFs and PFs stand for dorsi and plantar flexors, respectively. ....124

Figure 7-5 - Mean±SD of musculotendon length (significant difference between left and right: \* p<0.05, \*\*p<0.01). Individual percentage difference between the legs is reported as a bar plot where each bar represents a participant: blue positive (red negative) values show that the right leg is bigger (smaller). DFs and PFs stand for dorsi and plantar flexors, respectively. ....125

Figure 7-6 – Mean±SD physiological cross-sectional area (PCSA) of the main muscles of the right and left lower limb estimated from muscle volumes of the eleven subjects in the present study and compared to those measured from cadavers by Ward et al. (2009). ....126

Figure 7-7 Mean±SD of the maximal isometric force for the right and left muscles personalised in the SSp model and percentage difference between Hyb and SSp (\* p<0.05, \*\*p<0.01). Individual percentage difference is reported as a bar plot where each bar represents a participant: green positive (orange negative) values show that the optimal fibre length in the Hyb model is bigger (smaller). DFs and PFs stand for dorsi and plantar flexors, respectively. ....128

Figure 7-8 - Comparison of muscle activation patterns between the different models. Average difference over all subjects for SSp vs Gen model (top), SSp vs Hyb model (middle) and Hyb vs Gen model (bottom). Each row corresponds to an individual muscle according to the list

specified in the table. Vertical dashed line indicates the time instant when toe off occurred.  
DFs and PFs stand for dorsi and plantar flexors, respectively.....130

Figure 7-9 - Example of EMG signal (bottom box) and muscle activation (top box) estimated with SSp , Hyb and Gen for five muscles of one subject. ....131

Figure 7-10 - Mean±1SD JCFs (bold lines) for the SSp and Gen (top), Gen and Hyb (middle), and SSp and Hyb (bottom) and SSp-Gen (top), Gen-Hyb (middle), and SSp-Hyb (bottom) differences for individual limbs (thin lines). Black bars indicate significant differences (post hoc test,  $p=0.017$ ). ....131

Figure 7-11 - Statistical distribution of the peak JCF for hip, knee, and ankle with the Hyb, by Hyb<sub>SSpPath</sub>, Hyb<sub>SSpFmax</sub>, and SSp models. \* = significant difference ( $p<0.001$ ).....132

# Declaration

I declare that this PhD thesis has been produced as the results of my own course of study and research whilst employed and enrolled as a PhD staff candidate at The University of Sheffield between May 2016 and July 2019. The thesis has been submitted as "alternative format thesis", in accordance to the University guidelines, after approval from the Department of Mechanical Engineering.

The work was conducted as part of two large collaborative national and international research projects, involving various clinical centres and technical partners, which are all gratefully acknowledged. Specific contribution and sources are mentioned in the individual chapters. These projects were financially supported by the European Commission (MD-PAEDIGREE project, FP7-ICT Programme, Project ID: 600932) and by the UK EPSRC (Multisim project, Grant number: EP/K03877X/1).

# 1. Overview

## 1.1. Introduction

Musculoskeletal disorders are recognised as one of the first causes for disability in the western countries, typically leading to significant pain and joint destruction, and premature mortality (Kvien, 2004). For example, worldwide, 10% to 15% of all adults over 60 years of age are affected by osteoarthritis, with higher prevalence in women, and The United Nations estimate that by 2050 this number will reach the value of 20% due to a growth in population and increase in aging (Brennan-Olsen et al., 2017). Other forms of arthritis, such as rheumatoid arthritis, are estimated to affect between 0.5 and 1.0% of the adult population worldwide. It can develop at any age and therefore most patients require long-life treatment to control the progression, or even surgery (Kvien, 2004). Affecting the mobility and locomotion, often causing the inability to work, the social impact of musculoskeletal diseases is not negligible and the burden on the healthcare systems is significant (Kvien, 2004).

The increasing prevalence of these diseases, also associated to longer life expectancy and ageing, has raised the interest in individual and specific therapies to help patients with customised rehabilitation plans tailored to their lifestyle and activity level (Hedgecoe, 2004, Isaacs and Ferraccioli, 2011, Viceconti et al., 2015). Such approaches, of course, require the development of more advanced quantitative tools allowing to assess individual cases without multiplying the costs in terms of effort and time. *In-silico* techniques and computational methods have therefore been proposed as non-invasive alternatives aiming at reproducing virtual patients, or populations of patients, and simulate the effect of different intervention plans. The increasing availability of medical data and patients' information from routine examinations is promoting the implementation of these *in-silico* techniques also in the clinical practice other than in the research (Viceconti et al., 2008, Viceconti et al., 2016).

Locomotion, despite involving extremely complex synchronisation between the neural system and the musculoskeletal system and perfect muscles coordination, represents a natural and easy task common to animals and humans. Due to the fundamental role of walking in everyday life, the biomechanics of human motion has been object of study since many years and has become more and more systematic and advanced to enable the quantitative understanding of musculoskeletal kinematics and kinetics (Baker, 2007, Whittle, 1996).

Experimental measurements can provide crucial information about the fundamentals of human locomotion. For example, gait analysis entails the systematic observation of human movement with the support of specific instrumentation, i.e. cameras and sensors, in order to measure the mechanics of the body, including kinematics (describing bodies' motion) and kinetics (relating motion to its causes, i.e. forces and torques) (Baker, 2006, Oatis and Craik, 1994). The external observation of the human motion is then associated to the movement of the skeleton thanks to models assuming a rigid relationship between the surface of the body and the bones (Lu and O'connor, 1999). This technique finds application in a number of clinical settings to support the diagnosis of musculoskeletal alterations, better treatment planning and rehabilitation programmes (Gage, 1991, Gage, 1993, Hartmann et al., 2010, Merker et al., 2015, Sutherland and Davids, 1993). However, the specific role of the muscle system is only partially accounted for in gait analysis, therefore the application is limited to the investigation of the joint angles and torques. A further step is needed if interested in understanding the individual contribution of muscles to the generation of these torques and the resulting movement. This gap is filled through computational techniques, such as the use of musculoskeletal models (MSKMs) who can provide information about those quantities that are otherwise not easily accessible experimentally or available in a non-invasive manner (i.e. individual muscle forces and forces internal to the joints) (Anderson and Pandy, 1999, Arnold et al., 2005, Arnold et al., 2010, Delp et al., 1990).

The presence of a pathological condition, rising from either skeletal or neurological problems, is often the cause for anatomical alterations, such as bone deformities, variations in the musculotendon path, or functional impairments, like limited or abnormal joint mobility and changes in muscular activity. Especially in these cases, musculoskeletal analysis and modelling should aim at developing specific personalised tools for the investigation of the cause-effect mechanisms behind these pathologies and the prevention of their progression through the planning of individual intervention and rehabilitation programmes (Carbone et al., 2015, Hannah et al., 2017, Marra et al., 2015, Montefiori et al., 2019, Prinold et al., 2016).

Over the past two decades computational modelling techniques have been developed aiming at providing the tools and methods for increasing the anatomical resemblance and the model personalisation to account for individual characteristics and address specific research/clinical questions (Arnold and Delp, 2005, Arnold et al., 2010, Delp et al., 1990). These techniques

were found promising in several applications as they have the potential to provide patient-specific quantifications and predictions to be used in a number of different critical clinical scenarios, ranging from orthopaedics (i.e. joint replacement and simulations of intervention scenarios) (Delp et al., 1990, Fregly et al., 2012, Steele et al., 2012), to inflammatory (i.e. arthritis) (Hannah et al., 2017, Montefiori et al., 2019, Prinold et al., 2016), to neuromotor conditions (i.e. cerebral palsy, motor neuron disease, etc. ) (Arnold and Delp, 2005, Thompson et al., 1998). However, they are not yet adopted as part of the conventional clinical practice, mainly due to the lack of standardised and validated protocols (Hicks et al., 2015) and to the costs associated with the procedures. Indeed, the economic factor must be taken into account when evaluating the suitability of such a methodology and its application has to be limited to those cases that can benefit from the collection of additional anatomical information and motion data, i.e. musculoskeletal diseases with associated bone deformities and joint misalignments, joint degeneration pathologies, joint replacements.

Driven by the motivations summarised in the preamble, the overall aim of this PhD thesis was that of developing and assessing an innovative, robust, and reliable methodology for the definition of MRI-based subject-specific MSKMs of the lower limb in order to foster their wider usability and clinical application. Additionally, the personalisation of the MSKMs through extracting skeletal and muscular anatomical information from MRI was explored.

## **1.2. Thesis outline**

The thesis is divided in eight chapters (Figure 1-1). Chapter 1 presents an overview on the topic, setting the framework and the motivation for the study. Chapter 2 defines the background, including an introduction to the lower limb anatomy, the basics of musculoskeletal modelling and its application, with details on different modelling approaches. Chapters 3 to 7 are dedicated to the development and clinical application of MRI-based personalised MSKMs of the lower limb. More detailly, chapter 3 includes the published paper “An image-based kinematic model of the tibiotalar and subtalar joints and its application to gait analysis in children with Juvenile Idiopathic Arthritis”, presenting a morphology-based semi-automated methodology for producing kinematic MSKMs of the ankle and its employment in a clinical scenario, namely Juvenile Idiopathic Arthritis (JIA).

Chapter 4 is based on the published paper “Sensitivity of a juvenile subject-specific musculoskeletal model of the ankle joint to the variability of operator dependent input”, where the repeatability of manually producing patient-specific MSKMs of the ankle is assessed. My contribution consisted in the design of the study, implementation of the MSKMs, quantification the intra- and inter-operator variability in the input parameters used to build the same models, and finally identification of the modelling steps being more sensitive to operator error. Chapter 5 describes in brief an optimised and robust pipeline for collecting input data and repeatably producing MSKMs presented as additional material to the journal publication “Investigation of the dependence of joint contact forces on musculotendon parameters using a codified workflow for image-based modelling”. The aim of this paper was twofold, with my contribution mainly relating to the second part, i.e. to the development of the codified workflow described in the document “Pipeline for building a subject-specific MSK model from MRI and motion capture data” (Appendix I of this thesis). Chapter 6 is based on the journal publication “Linking joint impairments and gait biomechanics in patients with Juvenile Idiopathic Arthritis” where I implemented a lower-limb MSKM to investigate alteration of gait biomechanics associated to musculoskeletal impairment in a JIA population. Chapter 7 presents a further development of the modelling pipeline introducing the MRI-based personalisation of muscle parameters and geometry in the context of ageing and elderly population. This chapter is structured in a publication-like fashion as its content is planned to be submitted for publication to the journal IEEE Transactions on Biomedical Engineering by October 2019. The last chapter, chapter 8, summarises the main findings and contributions to the state of the art gained from the current research to draw an overall conclusion of the thesis work and to present a plan for future developments.

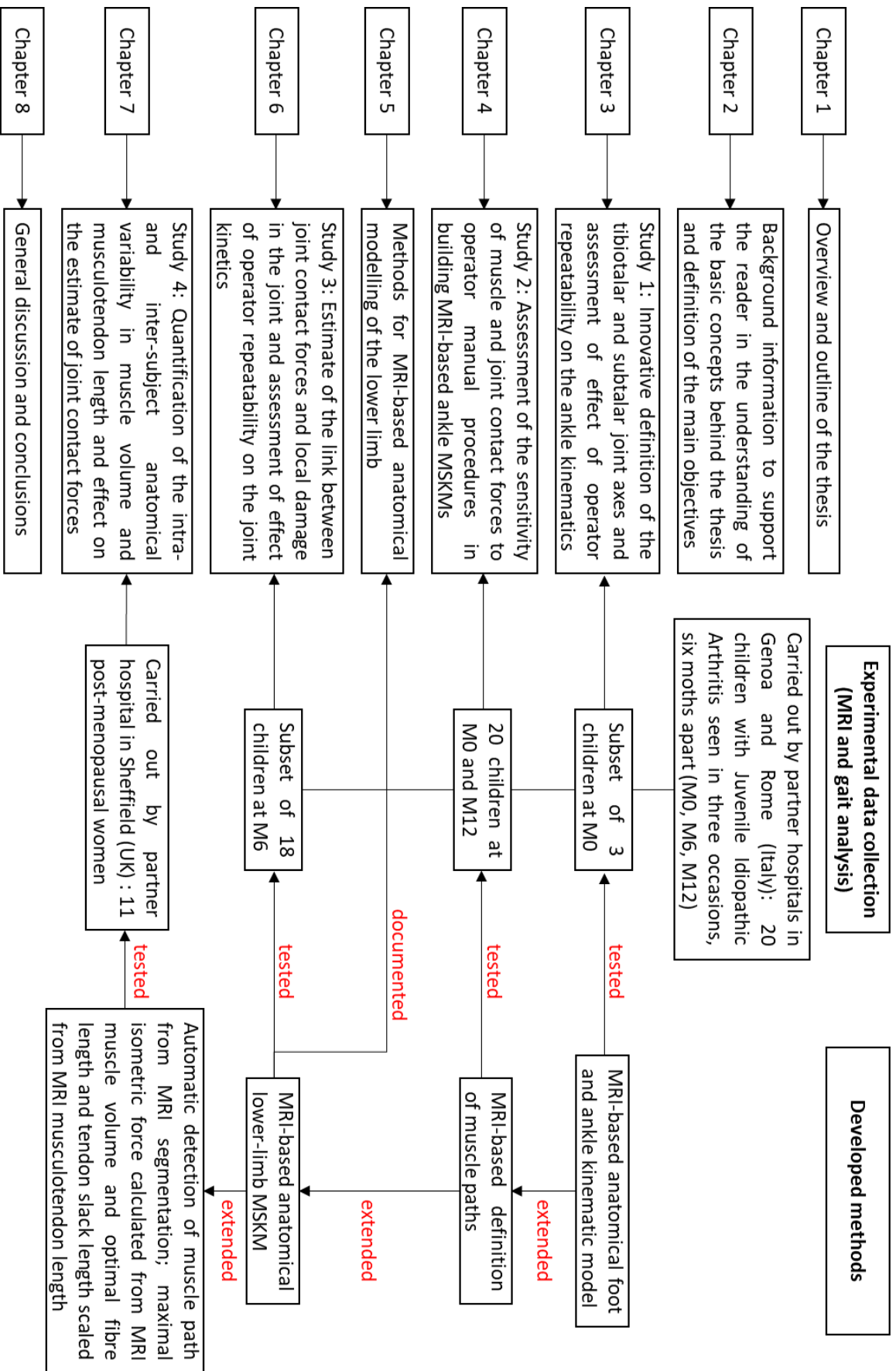


Figure 1-1 – Schematic of the outline of the thesis

## 1.3. References

- Anderson, F. C. & Pandy, M. G. 1999. A dynamic optimization solution for vertical jumping in three dimensions. *Computer methods in biomechanics biomedical engineering*, 2, 201-231.
- Arnold, A. & Delp, S. 2005. Computer modeling of gait abnormalities in cerebral palsy: application to treatment planning. *Theoretical Issues in Ergonomics Science*, 6, 305-312.
- Arnold, A. S., Anderson, F. C., Pandy, M. G. & Delp, S. L. 2005. Muscular contributions to hip and knee extension during the single limb stance phase of normal gait: a framework for investigating the causes of crouch gait. *Journal of Biomechanics*, 38, 2181-2189.
- Arnold, E. M., Ward, S. R., Lieber, R. L. & Delp, S. L. 2010. A model of the lower limb for analysis of human movement. *Annals of biomedical engineering*, 38, 269-279.
- Baker, R. 2006. Gait analysis methods in rehabilitation. *Journal of neuroengineering and rehabilitation*, 3, 4.
- Baker, R. 2007. The history of gait analysis before the advent of modern computers. *Gait & posture*, 26, 331-342.
- Brennan-Olsen, S. L., Cook, S., Leech, M., Bowe, S. J., Kowal, P., Naidoo, N., Ackerman, I., Page, R., Hosking, S. & Pasco, J. 2017. Prevalence of arthritis according to age, sex and socioeconomic status in six low and middle income countries: analysis of data from the World Health Organization study on global AGEing and adult health (SAGE) Wave 1. *BMC musculoskeletal disorders*, 18, 271.
- Carbone, V., Fluit, R., Pellikaan, P., Van Der Krogt, M., Janssen, D., Damsgaard, M., Vigneron, L., Feilkas, T., Koopman, H. F. & Verdonshot, N. 2015. TLEM 2.0—A comprehensive musculoskeletal geometry dataset for subject-specific modeling of lower extremity. *Journal of Biomechanics*, 48, 734-741.
- Delp, S. L., Loan, J. P., Hoy, M. G., Zajac, F. E., Topp, E. L. & Rosen, J. M. 1990. An interactive graphics-based model of the lower extremity to study orthopaedic surgical procedures. *IEEE Transactions on Biomedical engineering*, 37, 757-767.
- Fregly, B. J., Besier, T. F., Lloyd, D. G., Delp, S. L., Banks, S. A., Pandy, M. G. & D'lima, D. D. 2012. Grand challenge competition to predict in vivo knee loads. *Journal of Orthopaedic Research*, 30, 503-513.
- Gage, J. R. 1991. *Gait analysis in cerebral palsy*, Mac Keith Press London.
- Gage, J. R. 1993. Gait analysis. An essential tool in the treatment of cerebral palsy. *Clinical orthopaedics*, 126-134.
- Hannah, I., Montefiori, E., Modenese, L., Prinold, J., Viceconti, M. & Mazza, C. 2017. Sensitivity of a juvenile subject-specific musculoskeletal model of the ankle joint to the variability of operator-dependent input. *Proceedings of the Institution of Mechanical Engineers, Part H: Journal of Engineering in Medicine*, 231, 415-422.

- Hartmann, M., Kreuzpointner, F., Haefner, R., Michels, H., Schwirtz, A. & Haas, J. 2010. Effects of juvenile idiopathic arthritis on kinematics and kinetics of the lower extremities call for consequences in physical activities recommendations. *International journal of pediatrics*, 2010.
- Hedgecoe, A. 2004. *The politics of personalised medicine: Pharmacogenetics in the clinic*, Cambridge University Press.
- Hicks, J. L., Uchida, T. K., Seth, A., Rajagopal, A. & Delp, S. L. 2015. Is my model good enough? Best practices for verification and validation of musculoskeletal models and simulations of movement. *Journal of biomechanical engineering*, 137, 020905.
- Isaacs, J. D. & Ferraccioli, G. 2011. The need for personalised medicine for rheumatoid arthritis. *Annals of the rheumatic diseases*, 70, 4-7.
- Kvien, T. K. 2004. Epidemiology and burden of illness of rheumatoid arthritis. *Pharmacoeconomics*, 22, 1-12.
- Lu, T.-W. & O'Connor, J. 1999. Bone position estimation from skin marker co-ordinates using global optimisation with joint constraints. *Journal of Biomechanics*, 32, 129-134.
- Marra, M. A., Vanheule, V., Fluit, R., Koopman, B. H., Rasmussen, J., Verdonchot, N. & Andersen, M. S. 2015. A subject-specific musculoskeletal modeling framework to predict in vivo mechanics of total knee arthroplasty. *Journal of biomechanical engineering*, 137, 020904.
- Merker, J., Hartmann, M., Kreuzpointner, F., Schwirtz, A. & Haas, J.-P. 2015. Pathophysiology of juvenile idiopathic arthritis induced pes planovalgus in static and walking condition—A functional view using 3d gait analysis. *Pediatric Rheumatology*, 13, 21.
- Montefiori, E., Modenese, L., Di Marco, R., Magni-Manzoni, S., Malattia, C., Petrarca, M., Ronchetti, A., De Horatio, L. T., Van Dijkhuizen, P., Wang, A., Wesarg, S., Viceconti, M. & Mazzà, C. 2019. An image-based kinematic model of the tibiotalar and subtalar joints and its application to gait analysis in children with Juvenile Idiopathic Arthritis. *Journal of Biomechanics*, 85, 27-36.
- Oatis, C. A. & Craik, R. 1994. *Gait analysis: theory and application*, Mosby.
- Prinold, J. A., Mazzà, C., Di Marco, R., Hannah, I., Malattia, C., Magni-Manzoni, S., Petrarca, M., Ronchetti, A. B., De Horatio, L. T. & Van Dijkhuizen, E. P. 2016. A patient-specific foot model for the estimate of ankle joint forces in patients with juvenile idiopathic arthritis. *Annals of biomedical engineering*, 44, 247-257.
- Steele, K. M., Demers, M. S., Schwartz, M. H. & Delp, S. L. 2012. Compressive tibiofemoral force during crouch gait. *Gait & posture*, 35, 556-560.
- Sutherland, D. H. & Davids, J. R. 1993. Common gait abnormalities of the knee in cerebral palsy. *Clinical orthopaedics related research*, 139-147.
- Thompson, N., Baker, R., Cosgrove, A., Corry, I. & Graham, H. 1998. Musculoskeletal modelling in determining the effect of botulinum toxin on the hamstrings of patients with crouch gait. *Developmental Medicine Child Neurology*, 40, 622-625.

Viceconti, M., Clapworthy, G. & Jan, S. V. S. 2008. The Virtual Physiological Human—A European Initiative for In Silico Human Modelling—. *The journal of physiological sciences*, 0810200082-0810200082.

Viceconti, M., Henney, A. & Morley-Fletcher, E. 2016. In silico clinical trials: how computer simulation will transform the biomedical industry. *International Journal of Clinical Trials*, 3, 37-46.

Viceconti, M., Hunter, P. & Hose, R. 2015. Big data, big knowledge: big data for personalized healthcare. *IEEE journal of biomedical and health informatics*, 19, 1209-1215.

Whittle, M. W. 1996. Clinical gait analysis: A review. *Human Movement Science*, 15, 369-387.

## **2. Background information**

## **2.1. Basic concepts**

### **2.1.1. Anatomical and rotation planes**

The unambiguous definition of movement is crucial to the general understanding and discussion of complex motion patterns happening between body parts during human locomotion. As the body movements occur in different planes and around different axes, the use of a standard terminology avoids confusion.

Anatomical planes are imaginary planes crossing the body at different levels (Figure 2-1):

- The sagittal plane runs vertically dividing the body into left and right sides. Flexion and extension movement are referred to this plane.
- The frontal plane divides the body into the front and the back; therefore, abduction and adduction movements belong to this plane.
- The transverse plane cuts the body horizontally into the upper and lower half. Rotation movements occur in this plane.

Additionally, the use of the centre of the body as a reference to identify other anatomical parts is commonly used to avoid confusion (Figure 2-1). In fact, we refer to medial (or lateral) as we move close (or away) to the centre of the body, we refer to superior (or inferior) if we move towards the head (or the feet), we refer to anterior (or posterior) if we move towards the front (or the back) of the body. Finally, we define as proximal (or distal) the extremity of a body part (i.e. long bones) that is towards (or away) from the centre of body.

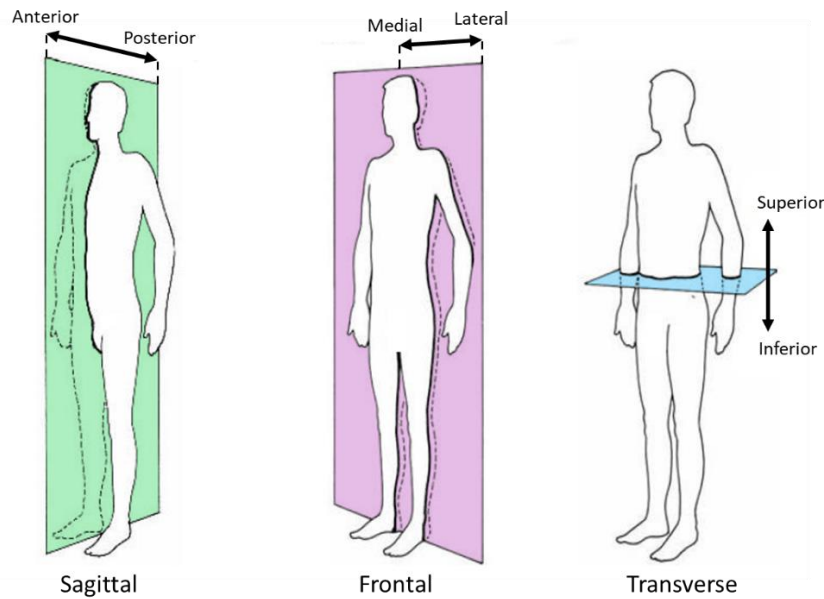


**Figure 2-1 – Anatomical planes and terminology**

### **2.1.2. The lower-limb musculoskeletal system**

In this context, I will refer to the musculoskeletal system as the complex including both the skeleton and skeletal muscles. The former, comprehending the bones and the cartilage covering the articulating portions of the bone extremity, gives support to the body and creates a protective structure for the underlying organs; the latter represents the actuator of the body movements.

#### *The bones of the lower limb*

The main bones of the lower limb are pelvis, including the ilium and sacrum, femur in the upper leg, and patella, tibia and fibula in the lower leg (Figure 2-2). The bones forming the foot are talus, calcaneus, cuneiforms, cuboid, navicular, metatarsals and phalanges (Gray, 1918).

The femur is a long bone, the longest of the body, whose proximal extremity is characterized by a spherical head, which articulates with the acetabulum of the pelvis, forming the hip joint. The femur head is connected to an upper lateral tuberosity, called great trochanter, by means of the femur neck. On the posterior-medial aspect of the bone shaft, a smaller tuberosity is projected medially, namely the lesser trochanter. These tuberosities, as most of the tuberosities in the lower-limb bones, represents the areas where muscles attach. The distal

portion of the femur presents two condyles, the medial and the lateral, forming the knee joint together with the tibia and the patella.

The tibia has a proximal flat surface, known as the tibial plateau, and extends distally to its end where an expansion, the tibial dome, takes part into the ankle joint. Parallel to the tibia, the fibula is a much thinner long bone that presents two heads, one at each extremity, where ligaments and tendons attach to give stability to both the knee and ankle joints. In their distal portion both tibia and fibula present a bony tuberosity projected inferiorly on the medial and lateral side, respectively, called malleoli.

The bones composing the foot are usually twenty-six, although anatomical variants exist. The tarsal bones are seven irregularly shaped bones located proximally and mostly involved in the ankle motion. The talus is primarily involved in the articulation with tibia and fibula; the calcaneus, below the talus, presents a posterior aspect where the calf muscles attach. The metatarsals, which are five long bones and connect the tarsals to the phalanges, namely the bones of the toes. Connected in a complex pattern of articulating surfaces, the foot bones give stability to the segment supporting the body weight and their flexible structure absorbs the impact when hitting the ground during walking.

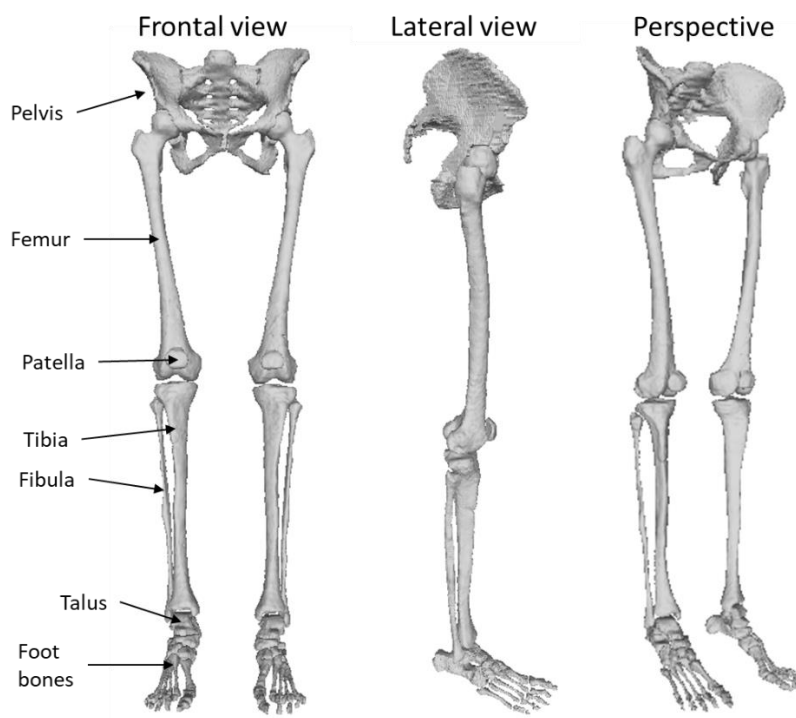


**Figure 2-2 - The main bones of the lower limb**

### *The joints of the lower limb*

The joints are the links between bony segments of our body. In the lower limb, several joints exist, with the most important being the hip, the knee and the ankle. These joints enable the movement, allowing rotations and/or translations in those directions representing their degrees of freedom (DoFs) (Gray, 1918). Together with the ligaments, they represent a constraint to the free movement of the lower-limb segments and are classified as hinge, ellipsoid, or ball-and-socket, allowing for uniaxial, bi-axial, or three-axial rotations, respectively (Figure 2-3).

The hip is a ball-and-socket joint where pelvis and femur articulate thanks to the contacting surfaces of the pelvis acetabulum (a cup-like hollow on the inferolateral aspect of the pelvis) and femur head, which fits completely into the cavity of the acetabulum. The hip serves primarily as a weight-bearing joint and allows flexion/extension, abduction/adduction, and internal/external rotations.

The knee joint is a bicondylar joint consisting of two articulations, the tibiofemoral (where the medial and lateral condyles articulate with the tibia), and the patellofemoral (where the femur articulates with the patella). The tibiofemoral joint is responsible for weight-bearing and its motion is particularly complex. In fact, despite a main flexion/extension component, it also allows for small abduction/adduction, internal/external rotations, and translations along the three anatomical axes.

The ankle joint, also known as tibiotalar joint, articulates between tibia and fibula and the talus. It mainly allows for plantar/dorsiflexion of the foot. A further important joint articulates between the talus and the calcaneus, the subtalar joint, being involved in the inversion/eversion of the foot. A series of other joints between the small bones of the foot allows smooth movements and stability within the hind-, mid-, and forefoot.

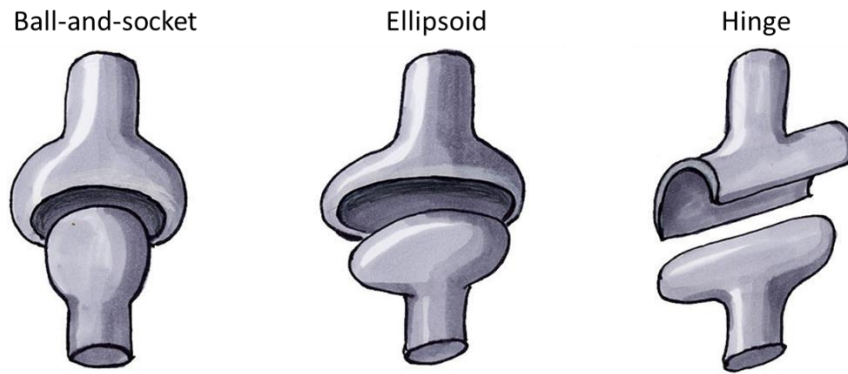


**Figure 2-3 – Schematic representation of ball-and socket (left), ellipsoid (middle), and hinge (right) ideal joints (adapted from Maik et al. (2010)).**

### *The muscles of the lower limb*

The skeletal muscles are responsible for the movement of the body by acting on the bone through their tendinous connections. When contracting, the muscles shorten the length of their fibres and pull adjacent body segment close to each other or release them when the fibres relax (Huxley, 1974).

The muscles of the lower limb can be divided into clusters or groups. From proximal to distal, the first muscle group is the glutei, localised posterior to the pelvis. Their origin is in the ilium, the uppermost and largest part of the pelvis, and their insertion is on the femur. They give stability to the hip joint and are involved in the actuation of the hip movements: abduction, extension, and rotation. The glutei muscles are composed of three subgroups, namely the gluteus maximum, medius, and minimus. Other small muscles contribute to the hip movement, i.e. the piriformis, the gemellus, and the quadratus femoris, all located deeper in the lower region of the ilium. Moving distally, in the anterior compartment, the main muscles of the thigh are the pectineus, the sartorius and the quadriceps femoris, who constitute one of the most powerful group in the body. The pectineus contributes to the adduction and flexion of the hip; the sartorius to the abduction, extension, and rotation of the hip, and to the flexion of the knee; the quadriceps femoris to the extension of the knee and the stabilization of the patella. In the medial compartment of the thigh, the gracilis, obturator externus, adductor brevis, adductor longus and adductor magnus together contribute to the hip adduction. The posterior compartment includes the biceps femoris, the semitendinosus and the semimembranosus, also known as hamstrings, acting to extend the hip and to flex the knee.

The lower leg has its main bulk in the posterior compartment, where the gastrocnemius, soleus, and posterior tibialis compose the calf complex, responsible for the plantarflexion of the ankle. The anterior part has the tibialis anterior, extensor digitorum longus, extensor hallucis longus and peroneus muscles, acting to dorsiflex the foot. The lower leg muscles have also a role in the inversion/eversion of the foot.

In the foot, a group of extensors, which contribute to raise the toes in the first phase of the step forward, and a group of flexors, which help stabilize the toes when contacting the ground, play a major role.

## **2.2. Input data for musculoskeletal modelling**

To be able to produce a musculoskeletal model (MSKM), input data must be collected, i.e. information about the anatomy of the subject and her/his locomotion pattern. The acquisition of the former is achieved in a variety of manners, ranging from very basic (i.e. pictures, height, mass, body segment lengths) to more advanced levels of detail (i.e. medical imaging); the latter can be done through instrumented gait analysis.

### **2.2.1. Magnetic resonance imaging**

Magnetic resonance imaging (MRI) is an imaging technique that uses strong magnetic fields and radio frequency (RF) waves to scan the human body and image the different internal tissues. A patient is placed on the MRI bed and surrounded by a uniform magnetic field. A source signal generated from the RF coil is transmitted through the patient's body to excite the protons contained in the water molecules of the body. These hydrogen atoms respond to the excitation emitting a RF signal received at the level of the receiving coil.

Different tissues require different time to return to their original state after excitation. This is called relaxation time and its measure allows to discriminate between the tissues of the body (Bloch, 1946). If we are interested in the time that protons' spins need to realign with the main magnetic field ( $B_0$ ) after put into the transverse plane (longitudinal relaxation), we will be acquiring a T1-weighted MRI, otherwise, if interested in the time for the hydrogen dipoles to progressively diphas (spin-spin relaxation), we will be collecting T2-weighted MRI (Figure

2-4). The former shows bright fat tissue (low relaxation time) and dark bone tissue, water, and air (high relaxation time); the latter, associated to the percentage content of water in the tissue, exhibits brighter colours when the tissue contains more water (namely when the relaxation time is high).

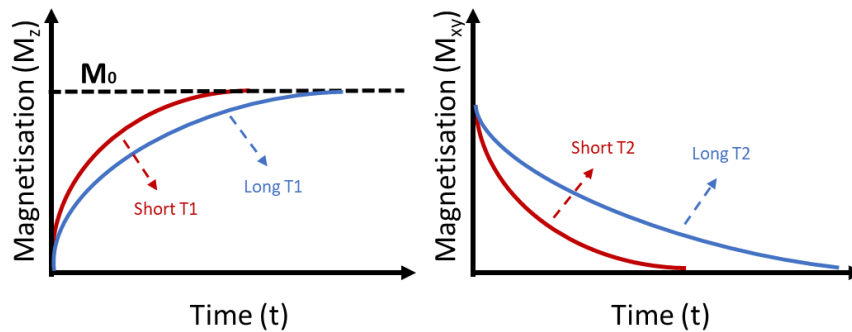


**Figure 2-4 – Relaxation curves: T1 relaxation (left) is the process by which the longitudinal magnetization ( $M_z$ ) returns to its initial maximum value ( $M_0$ ); T2 relaxation (right) is the process by which the transverse magnetization ( $M_{xy}$ ) decays.**

Besides its utility in diagnostic and treatment planning, MRI is used in musculoskeletal modelling with the purpose of gaining information about the subject's anatomy. Musculoskeletal imaging focuses on the visualisation of bone and muscle tissue, and less frequently of tendons, ligaments and cartilage. It is particularly useful in imaging the soft tissue but has been adopted for visualising bones as well, as an alternative to the more invasive, due to ionising radiation, Computed tomography (CT) technique. The flexibility of the MRI, with its T1- and T2-weighting options allows to optimise the image contrast/grey scale to the specific tissue of interest, or to find the best compromise for imaging more tissues at the same time. In particular, the 3D geometry of the different tissues can be extracted via image segmentation techniques.

### *Image segmentation*

Image segmentation is a technique used to process medical images in order to extract the 3D shape of the various anatomical structures forming the body, i.e. bones, muscles, ligaments, etc..., (Figure 2-5). It can be either manual, semi-automatic, or automatic. The former entails manually drawing the contour of the region/tissue/organ of interest on a 2D cross-section of the object visible on a single image slice. This procedure is obviously dependent on the ability and expertise of the operator performing the manual drawing, and potentially affected by the poor image quality. However, it is considered the gold standard when pathology-related

abnormal anatomical structures impede the use of automatic algorithm to identify the different structures.

A 3D object is then reconstructed interpolating the 2D segmentations on the different image slices. Mesh-processing algorithms, such as smoothing and repairing filters, can be used to improve the visual quality of the object.

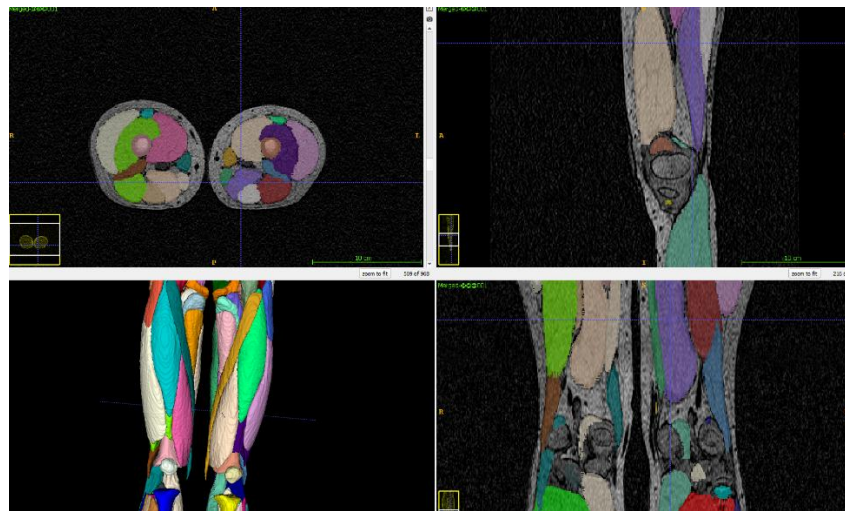


**Figure 2-5 – Example of segmentation of the muscles of the lower limb from different views: transverse (top left), sagittal (top right), frontal (bottom right), and 3D perspective (bottom left).**

### **2.2.2. Marker-based gait analysis**

Gait analysis provides a quantitative investigation of several aspects of human locomotion, from spatio-temporal parameters, such as step length, width, speed, to kinematic information, i.e. joint angles, to kinetic quantities, like the force exchanged with the ground (ground reaction force, GRF) and the moments generated at the joints (Oatis and Craik, 1994, Whittle, 1996).

The analysis of healthy gait has improved understanding of the biomechanical and physiological mechanisms behind locomotion and set the basis for the application of gait analysis in pathological scenarios. In this context it supports the identification of movement-related problems, such as alterations in the biomechanics of walking, or impairments being cause or effect of musculoskeletal diseases. Clinical gait analysis allows diagnoses and is used in clinical practice to assess, plan, and treat individuals with conditions affecting their ability to walk (Baker, 2006).

A typical gait analysis laboratory (Figure 2-6) has several cameras (video and/or infrared) placed around a walkway and connected to an acquisition system. The minimum number of cameras for acquiring 3D information from the lab is three, however a higher number is recommended to increase the resolution of the data. The lab floor is usually equipped with force platforms, synchronised with the motion capture system and embedded in the ground, used to measure the GRF. In order to acquire walking trials from a subject, reflective markers are placed on the subject's body segments, according to the marker placement protocol chosen for the specific application (Figure 2-7).

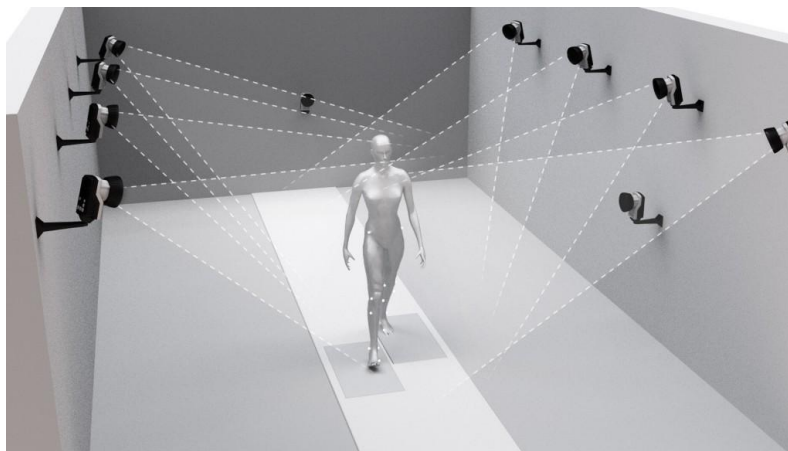


**Figure 2-6 - Gait analysis laboratory (<http://www.qualisys.com>)**

The marker placement is a very delicate task, requiring the lab technician to accurately palpate points on the skin in correspondence to meaningful anatomical bony landmarks. The operator-dependency implies that the procedure is likely to introduce errors and uncertainties, therefore the operator ability and experience is crucial to the success of the marker placement (Baker, 2006, Whittle, 1996). Additionally, the markers' position is susceptible to soft tissue artefact due to the presence of a layer of skin which impedes to rigidly fixing the markers to the underlying bone and introduces a relative movement between the two (Baker, 2006).

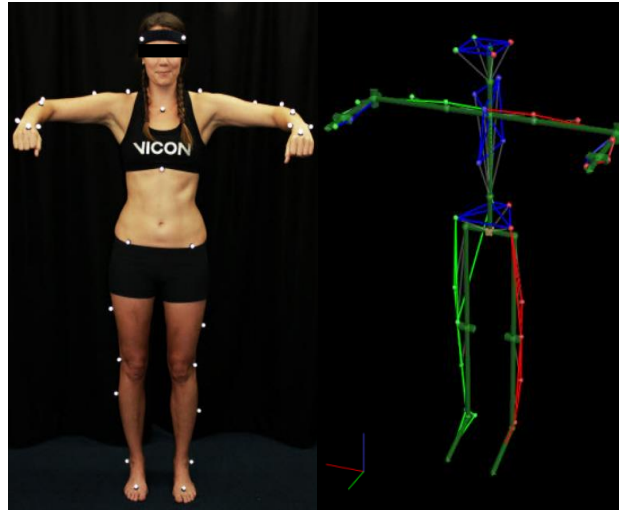


**Figure 2-7 – Example of full-body marker placement (Plug-in Gait) and corresponding skeletal model with highlighted body segments and joints. Adapted from Plug-in Gait Reference Guide (Vicon Motion System, Oxford, UK)**

During the acquisition of a trial, the subject walks back and forth along a straight walkway in the centre of the lab, where the cameras can track the location of each marker (see colourful dots in Figure 2-8, top). Additional dedicated tasks can be acquired, i.e. joint flexion/extension movements aiming at more accurately identify the relative orientation of the various body segments and the functional centre of the joints (Besier et al., 2003, Donnelly et al., 2012). If the lab is equipped with force plates, the external forces (i.e. GRF) are simultaneously collected (Figure 2-8, middle) during the trials and used for a complete dynamic description of the system. Electromyography (EMG) signals (Figure 2-8, bottom) can also be acquired thanks to the placement of EMG transducers on the surface of the skin, in correspondence to the belly of certain superficial muscles (Whittle, 1996).

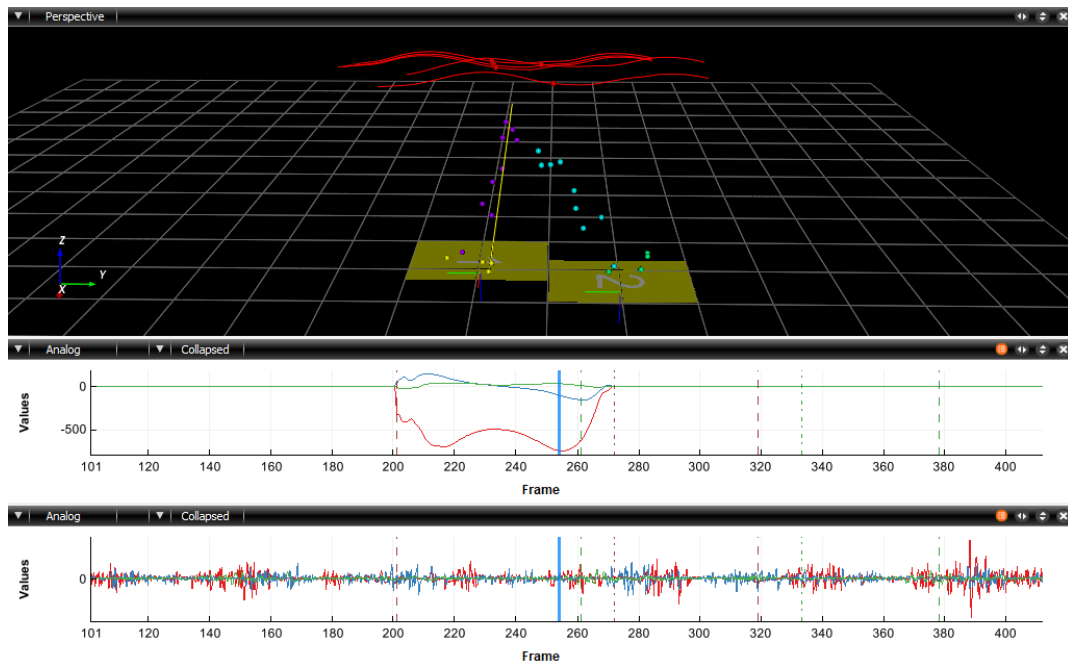


**Figure 2-8 – Example of data collected during a gait analysis session. (top) Perspective of the walking showing the markers on the various segments of the lower limbs, with highlighted trajectories of the pelvis markers (red), and ground reaction force (GRF, yellow vector) measured by the force plates. (middle) Analog graphs showing the magnitude of the three components of the GRF. (bottom) Signals recorded by the electromyography sensors.**

## 2.3. Musculoskeletal models and simulations

Among all the possible parallels between the human body and a mechanical system, the perspective of human movement analysis is that of comparing the musculoskeletal complex to a multibody structure, including segments linked through joints, and moving one relative to the others. The framework in which multibody MSKMs are adopted denotes the complexity of their representation.

### 2.3.1. Skeletal models

Simple 2D inverted pendulum, either single and double, can be implemented for understanding the dynamic equations of walking (Pandy, 2003). Other planar systems with limited DoFs can be implemented to explore the rational mechanics behind the locomotion and interaction of the model with the environment (Kuo, 2007). For these applications, a non-muscular model is preferred, as it simplifies the understanding of the relationship between cause and effect of motion (Pandy, 2003). If the purpose of the investigation is to fully

characterise the motion of the different parts of the lower-limb multibody system, joint angles and segmental orientations are to be estimated by solving the motion of a skeletal model through the solution of Direct Kinematics (DK) or Inverse Kinematics (IK) problems. Lu and O’connor (1999) highlight how the former treats each body segment independently without imposing constraints to the joints, whereas the latter describes the various joints connecting the links as ideal joints, whose degree of complexity and resemblance is dictated by the level of detail of the analysis. In simple 2D models of the lower limb, pin joints are used to describe planar rotations of the segments with respect to each other, whereas in 3D representation ideal hinges, ball-and-socket, ellipsoid, or more elaborate joints might be implemented.

The definition of joint’s axes of rotation in MSKMs generally follows the recommendation proposed by the International Society of Biomechanics (ISB) standards (Wu et al., 2002), or other alternative proposals, and is typically based on one of the following approaches:

- Manual/virtual palpation (Figure 2-9): the identification of meaningful anatomical landmarks on the skin (or on the bone surface, if medical imaging is available) of the subject in proximity of the joint (Van Alsenoy et al., 2014, van Sint Jan, 2007).
- Functional method: identifies the joint centre as the centre of rotation of the distal segment relative to the proximal segment while performing a prescribed movement recorded by motion capture cameras (Camomilla et al., 2006). The axes of rotation of a joint can be identified through dynamic optimisation algorithms based on the minimisation of the squared differences between the model estimated motion and the measured motion (Leitch et al., 2010, van den Bogert et al., 1994)
- Morphologic fitting (Figure 2-9): the alignment of analytical shapes, representing the ideal joint to model (i.e. cylinder for hinges or sphere for ball-and-sockets), to the articular region of interest, with the intent of fitting the shape’s surface to the bony surface (Ding et al., 2019, Prinold et al., 2016).

With respect to this, a debate is still open in the literature concerning the best approach to model the axes of the ankle. This is explained by the fact that the ankle presents multiple anatomical structures and bones articulating between each other. The main joints of the ankle

are the tibiotalar and the subtalar, constraining the movement between tibia and talus (the former) and talus and calcaneus (the latter) (Isman et al., 1969). The complexity of the structure, and associated movements, challenges the research to understand which modelling approach can better perform in investigating the biomechanics of the ankle. Besides this, an accurate measure of the *in-vivo* kinematics and kinetics of the tibiotalar and subtalar joints is limited by inadequate instrumentations (Di Marco et al., 2016, Nichols et al., 2017, Westblad et al., 2002) and costly or invasive experimental protocols (i.e. fluoroscopy or intracortical bone pins). This considered, a simple approach to the ankle modelling, where tibiotalar and subtalar joints are schematised as idealised hinges, is often preferred and widely adopted in modelling (Arnold et al., 2010, Delp et al., 1990, Dul and Johnson, 1985, Modenese et al., 2018, Montefiori et al., 2019, Siegler et al., 1988). The tibiotalar axis of rotation is commonly associated to the axis connecting the lateral and medial malleoli (Wu et al., 2002), often relaying on the position of gait markers in order to locate these anatomical points. In this proposal, the tibiotalar joint origins in the inter-malleolar point (midway between the tips of the lateral and medial malleoli, LM and MM, respectively) and the rotational axis is that connecting LM and MM (Figure 2-9).

Alternatively, the tibiotalar axis can be derived from fitting of the talar dome with a cylindrical shape (Hannah et al., 2017, Prinold et al., 2016) aiming at identifying the axis and centre of rotation of the joint as that of the cylinder (Figure 2-9). This procedure is performed manually and, although accounting for the individual morphology of the talus, is still unreliable as dependent on the judgement and ability of the operator. The subtalar joint is often neglected, or scaled from generic models (Arnold et al., 2010, Delp et al., 1990) where this axis has been identified on an average geometry, derived from cadaveric data, on the basis of functional anatomy indications (Isman et al., 1969). In other cases the flexion/extension and inversion/eversion components of the ankle are coupled together in a ball-and-socket joint, centred in the correspondence to the inter-malleolar point (Ding et al., 2019).

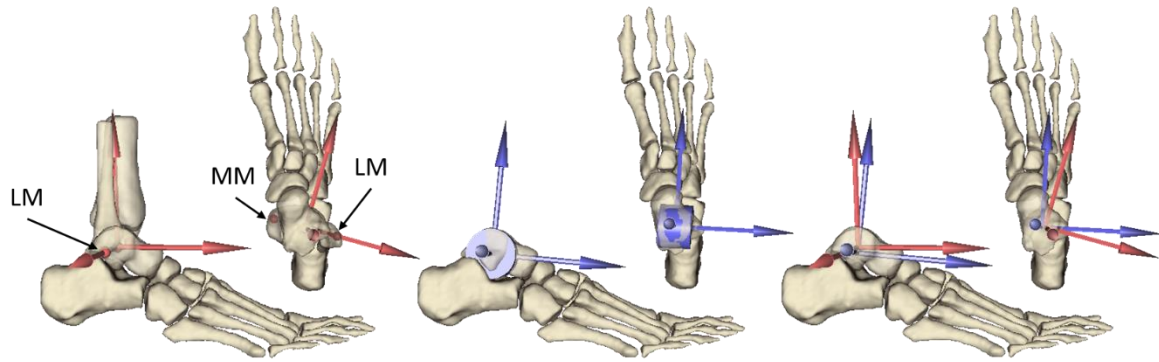


**Figure 2-9 – Definition of the tibiotalar joint according to anatomical landmarks (i.e. the lateral and medial malleoli, LM and MM, respectively, red) and manual fitting of a cylinder to the talar dome (blue) and comparison of the two methods.**

### **2.3.2. Muscular models**

When exploring the forces within the bodies of the lower-limb chain, or when interested in the contribution of individual muscles to actuate the locomotion, the model needs to carry information on the inertial properties of the segments and a geometrical and architectural description of the musculotendon unit, namely a representation of the muscle structure at the fibre/molecule level.

#### *Musculotendon unit*

Musculotendon units represent the skeletal muscles and their function of actuating the movement producing force. In MSKMs, they are schematised as straight lines, connecting two attachment points, the origin and the insertion, or turning around the joints by means of via points. This schematisation is considered acceptable for fusiform muscles, however, larger muscles with wide attachment area may be split into multiple bundles with different origins or insertions Figure 2-10. These bundles can contribute to different movement directions. Assuming that this representation of the muscles provides a good approximation of their geometry, the description of their behaviour requires the introduction of a number of parameters, i.e. mechanical elements, that mimic the force-generating capacity of the system (Yamaguchi, 2005).

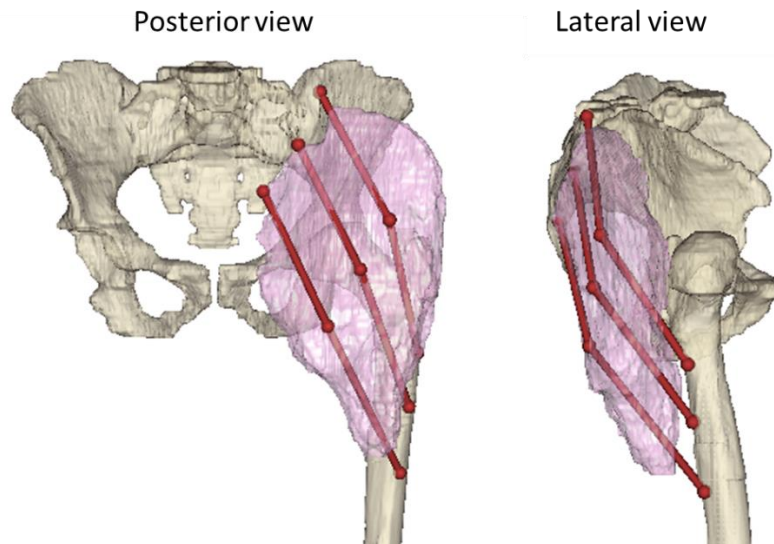


**Figure 2-10 – Representation of the Gluteus maximum large muscle belly and attachment region by means of three bundles connecting three origin points to three insertion points and passing through one via point each.**

Muscles are composed by many muscle tissues organised in fibres. The elemental part of these fibres is the sarcomere, where *myosin* and *actin* proteins bridge together during the muscle contraction and causing the shortening of the fibres. This process is regulated by electric and chemical stimuli from the central neural control involving the brain and the motor neuron. Given its complexity, a realistic representation of these complex mechanisms is still far-off being available for integration in MSKMs. However, in the 20<sup>th</sup> century researchers began to produce simplified muscle models, including a representation of the different molecular structures composing the sarcomeres, under the hypothesis of isolated fibres under prolonged maximal stimulation (tetanic contraction). The most commonly adopted model is that proposed by Hill (Hill, 1938) where the muscle sarcomere is schematised as series between a passive elastic serial element (SE), representing the tendon, and a parallel between an active contractile element (CE) and a passive damping element (DE), representing the viscoelasticity of the structure (Figure 2-11).

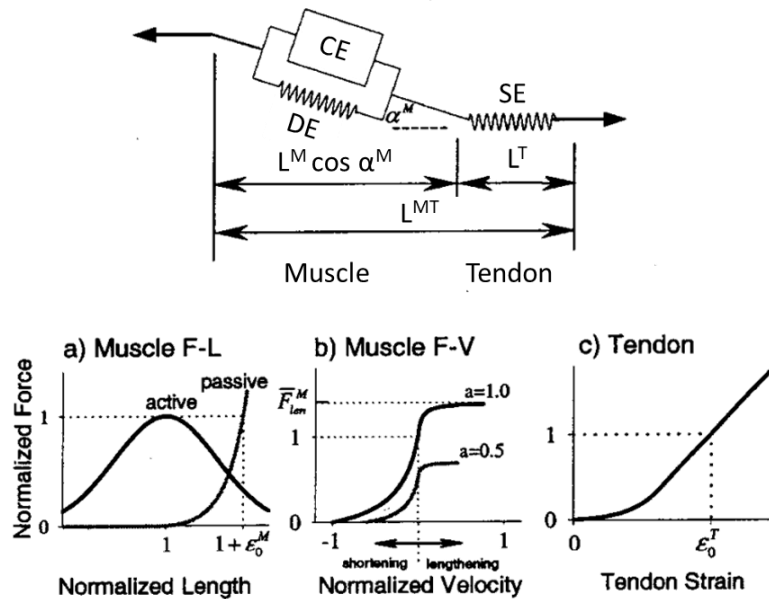


**Figure 2-11 – (top) Hill-type representation of the musculotendon unit adapted from Thelen (2003) including the active contractile element (CE) and the two passive elastic elements, DE and SE. (a) Description of the active (and passive) force-length relationship of muscles; (b) Force-velocity relationship curve presented as a function of the muscle activation; (c) Passive tendon force increasing with strain.**

The overall description of the muscle force relies on the definition of three curves (Arnold et al., 2013): the active and passive normalised force-length relationship of the muscle fibre, suggesting that there is an optimal fibre length at which the muscle can produce maximal isometric force; the normalised force-velocity relationship, adding a dynamic connotation to the system and showing that when the muscle reaches its maximum shortening velocity, the capacity of generating force is minimal, and progressively increased up to a maximum when maximally elongated (Zajac, 1989); the normalised force-length relationship of the tendon.

To integrate this system in MSKMs, the following essential parameters need to be defined (Zajac, 1989):

- maximal isometric force of a muscle;
- optimal fibre length;
- the tendon slack length;
- pennation angle;
- contraction velocity.

The concept of maximal isometric force is linked to the geometry of the muscle, in fact it is proportional to the physiological cross-sectional area, (namely the cross-section of the muscle perpendicular to the fibres) and represents the maximal force that a muscle can generate in isometric conditions (namely without changing its length during contraction) (Sacks and Roy, 1982). The optimal fibre length is the length at which fibres can exert the maximal force in isometric conditions. The tendon slack length is the resting length of the tendon; the pennation angle is the angle between the tendon and the muscle fibres at optimal fibre length; the maximum contraction velocity is the maximum velocity at which fibres can contract.

### **2.3.3. Scaled-generic and subject-specific musculoskeletal models**

In this thesis MSKMs are intended as computational tools adopted for the simulation of locomotion. Several MSKMs are available in the literature, from full-body to lower-limb to shoulder models (Arnold et al., 2010, Damsgaard et al., 2006, Delp et al., 1990, Holzbaur et al., 2005). The majority of these models, so called “generic”, are the result of averaged anatomical and anthropometric measurements on cadavers or *ex-vivo* samples.

The development of musculoskeletal modelling benefited from the advances in the fields of biomechanics, physiology, anatomy, but also from the progress in computer science promoting the advent of several commercial and open-source software packages, like Anybody (Damsgaard et al., 2006) and OpenSim (Figure 2-12) (Delp et al., 2007), employed for solving the complex equations of motion of the multibody systems.

OpenSim is widely adopted among the researchers in the field of musculoskeletal modelling and computational biomechanics as it is open-source and represents a state-of-the art tool in multibody dynamics and simulations, as described in Section 2.3.4. Additionally it comes with a detailed documentation and examples/tutorials are available through the platform SimTK (<https://simtk-confluence.stanford.edu>), together with a database of generic MSKMs being published in the past thirty years. This data repository and exchange made available to science and industry promotes circulation of the models and tools and their adoption into clinical practice.

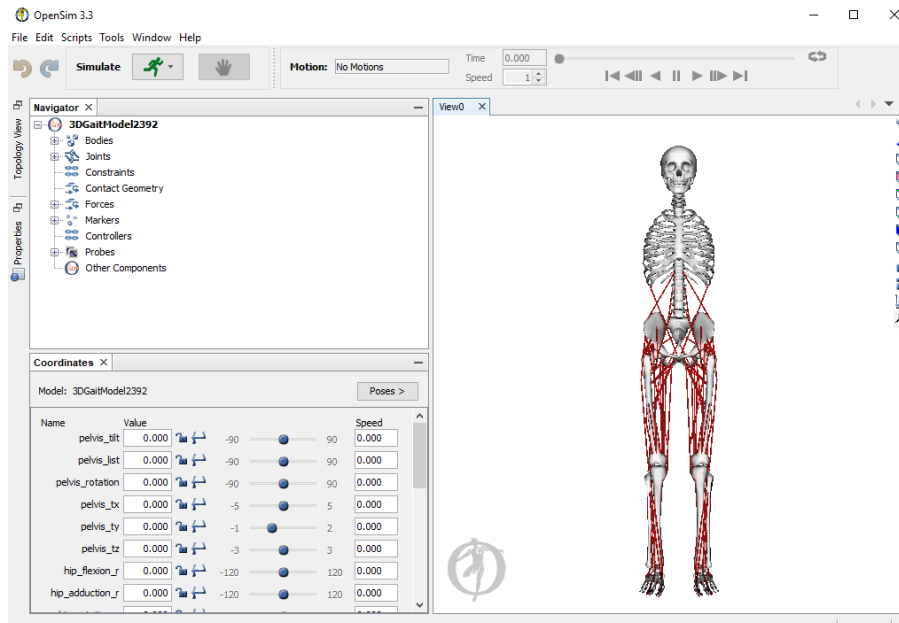


**Figure 2-12 - OpenSim environment and generic model “gait2392” (<https://simtk-confluence.stanford.edu>).**

Scaled models are generic MSKMs whose segments’ dimension (such as bones and muscles lengths) has been scaled to match the real anthropometry of the subject to be modelled. The procedure to scale a model requires the use of so-called “scaling factors” which represent the ratio between measurements in the models and in the body of the subject. In fact, to get the scaled size ( $S_{SM}^i$ ) of a segment  $i$  of the model, its dimension before scaling ( $S_M^i$ ) is to be multiplied by the ratio between a certain measure ( $M_S^i$ ), taken on the subject, and representative of the segment, and a measure ( $M_M^i$ ), taken on the original model before scaling, representative of the same segment, according to the following equation:

$$S_{SM}^i = S_M^i * \frac{M_S^i}{M_M^i}$$

The measures ( $M_S^i$  and  $M_M^i$ ) can be estimated in various fashions, i.e. using anthropometric measurements, referred to easily identifiable bony landmarks in the body, or using the distance between couples of gait markers placed both on the subject (during the experimental acquisition) and on the model (virtually palpated in the locations corresponding to the experimental markers). These operations are usually carried out using data from a static collection where the subject is asked to stand still in neutral position. The result of the scaling is a model, so called “scaled-generic” whose size matches the size of the subject for whom experimental data were collected. The scaled-generic model is therefore a copy of the

original model with increased or reduced (depending on the scaling factors) segments' size and updated muscle geometry and length-dependent musculotendon parameters (i.e. optimal fibre length and tendon slack length), according to the new dimension. Additionally, a list of “residual errors”, for each couple of markers included in the scaling, gives a quantification of the success of the procedure. The lower the residual error, the better the registration of the virtual markers onto the experimental markers in the standing position.

The OpenSim scaling tool also allows the scaling of the masses and inertial parameters. The scaled mass ( $m_{SM}^i$ ) of each segment  $i$  is obtained by multiplying the mass of each segment ( $m_M^i$ ) of the model by the ratio between the mass of the subject ( $m_S$ ) and the mass of the model ( $m_M$ ):

$$m_{SM}^i = m_M^i * \frac{m_S}{m_M}$$

Muscle maximal isometric force is not scaled within the tool; therefore, a further step of scaling should be performed outside OpenSim, i.e. in MATLAB (The MathWorks, Inc., USA). Various scaling approaches have been proposed in the literature for this parameter, either based on the ratio between subject and model mass (Modenese et al., 2018) or its powers (van der Krogt et al., 2016), or introducing more complicated scaling factors including subject height (Steele et al., 2012b) or individual musculotendon lengths (Correa and Pandy, 2011).

The accuracy of scaled-generic models is being increasingly questioned, since it unavoidably introduces errors and uncertainties due to the assumptions made on the geometry and morphology of the bony structures. In fact, scaled models neglect any natural variability or pathology-related alterations in the anatomy of the subject. Scaling can therefore affect the kinematic and kinetic output of the model simulations, as the definition of the joint axes depends on this step. Furthermore, even small uncertainties in the description of the musculotendon geometry can have a substantial impact on the estimate of muscle forces and joint internal forces calculated between adjacent body segments (Ackland et al., 2012, Bahl et al., 2019, Scheys et al., 2011, Scheys et al., 2008).

Aiming at improving the accuracy and reliability of the models, an alternative to scaled-generic models is subject-specific models, where medical data from a specific individual are used to gain a better representation of the anatomy and anthropometry. In this context

medical images, such as MRI and CT, are collected and registered to motion capture data thanks to the use of visible markers present in both data acquisitions. However, considering the burden of medical imaging on the health service and on the patients, their application is often limited to those cases where a higher level of anatomical accuracy is beneficial, i.e. pathological scenarios or musculoskeletal alterations. On the contrary, when interested in the locomotion of healthy, able subjects, then scaled-generic models may suffice.

In fact, whereas healthy subjects often share common anatomical features (except for differences due to sex, age and ethnicity), pathologic subjects can exhibit bone deformities and joint misalignments, affecting the movement and the flexibility, and causing altered locomotion. Personalisation of the models from medical imaging allows to account for these alterations. In particular, although CT scans represent the gold standard for imaging the bones, MRI ensures a good visualisation of both bone and soft tissue (i.e. muscles and tendons, ligaments, cartilage) with a lower level of invasiveness for the subject.

#### **2.3.4. Musculoskeletal simulations**

##### *Inverse kinematics*

Kinematics is the branch of mechanics related to the study of movement in terms of trajectories, angles and velocities of bodies or segments of a multibody system. In human motion analysis, segmental kinematics aims at reconstructing the movement of single bodies within the musculoskeletal chain during the execution of a motor task, which can be walking, running, jumping, etc...

When the geometry of the system is known, the position and orientation of the various segments can be identified by tracking the trajectories of the skin markers located onto the different body segments at each time frame. The relative movement (i.e. rotations and translations) between two adjacent segments of the chain is estimated through inverse kinematics, under the assumption that the bodies are rigid, therefore neglecting any deformation. Inverse kinematics is based on the concept of global optimisation, first proposed by Lu & O'connor in 1999, that minimises the difference between the location of the virtual (on the model) and experimental (on the subject) markers. This approach allows to minimise the global error reducing the sensitivity of the system to experimental errors due to skin

movement artefact (Lu and O’connor, 1999), improving the model estimates with respect to the direct kinematic method. The optimisation algorithm allows to identify the generalised coordinates describing the position and orientation of the segments of the musculoskeletal chain, under the assumption that the joints are mechanically constrained by idealised joints. In fact, an accurate definition of the joints is required, to limit their DoFs to a subset of rotations and translations, avoiding displacements and co-penetrations between segments (Lu and O’connor, 1999).

### *Inverse dynamics*

Dynamics is the branch of mechanics interested in investigating what causes the movement, namely forces. Therefore, the inertial properties of the multibody system, neglected during the inverse kinematics, should be accounted in this step. The output of the inverse kinematics step, namely the generalised coordinates of the joints in time, are here integrated to extract the generalised velocities and accelerations. These quantities, together with the external forces acting on the system (the GRF collected by the force platforms in the case of gait analysis), are the input to estimate the net torques about the joints for each instant of time.

The Newton-Euler equation (Eq. 2.3.4.1) of motion is recursively solved for each body segment, from distal to proximal, to compute the joint torques (i.e. the net forces and net moments):

$$M(\vec{q})\ddot{\vec{q}} + \vec{C}(\vec{q}, \dot{\vec{q}}) + \vec{G}(\vec{q}) + \vec{E}(\vec{q}, \dot{\vec{q}}) = \vec{\tau} \quad (2.3.4.2)$$

where  $\vec{q}(t)$ ,  $\dot{\vec{q}}(t)$ , and  $\ddot{\vec{q}}(t)$  are the generalised angular positions, velocities, and accelerations of the joints;  $M(\vec{q})$  is the matrix of the masses in the system,  $\vec{C}(\vec{q}, \dot{\vec{q}})$  represents the centrifugal and Coriolis forces and torques,  $\vec{G}(\vec{q})$  is the gravitational component,  $\vec{E}(\vec{q}, \dot{\vec{q}})$  contains the external forces, and  $\vec{\tau}$  is the unknown vector of forces and moments acting at the generalized coordinates. These forces and moments include the residuals acting on the most proximal segment of the musculoskeletal chain to compensate for the inconsistency between the acceleration computed at the various joints and the external forces measured by the force plates, and also for the forces and moments due to the body segments ignored in the system (i.e. the upper body when studying the lower limb).

### *Static optimisation*

As muscles are the actuators responsible for generating the torques at the joints, static optimisation is used to further extend the inverse dynamic approach to the calculation of the individual muscle forces contributing to the total joint moments. The estimate of the muscle forces represents one of the biggest challenges of musculoskeletal modelling, due to the complexity of the system constituted by a redundant number of actuators synergically contributing to the movement. This implies that for each estimated joint torque, there are multiple combinations of muscle activations and forces representing a possible solution of the equations. To solve the problem, the musculotendon properties (chapter 2.3.2) must be considered, as well as the activation-contraction dynamics of the unit, describing the dependency between the force generated within the muscle fibre and its length and contracting velocity.

Static optimisation relies on the formulation of cost functions to minimise certain performance criterion, i.e. the muscle force, activation, energy, metabolic consumption (Anderson and Pandy, 2001, Crowninshield, 1978, Crowninshield and Brand, 1981, Rasmussen et al., 2001), in order to solve the redundancy problem and provide a unique solution that satisfies both the cost function minimisation and the relations:

$$\begin{aligned} \vec{\tau} &= R(\vec{q})\vec{F} \\ \vec{0} &\leq \vec{F} \leq \vec{F}_{max} \end{aligned} \tag{2.3.4.3}$$

where  $R(\vec{q})$  is the matrix of the moment arms (i.e. the perpendicular distances from the line of action of a muscle to the center of rotation of the joints the muscle is crossing),  $\vec{F}$  is the vector of muscle forces, and  $\vec{F}_{max}$  is the vector of maximal muscle forces according to the musculotendon dynamics relationship. A common choice for the cost function, also implemented in OpenSim, is the minimisation of the sum of the muscle activations squared:

$$J(\vec{F}) = \sum_{i=1}^n \left( \frac{\vec{F}_i}{\vec{F}_{max,i}} \right)^2 \tag{2.3.4.4}$$

where  $n$  is the number of muscles in the system.

Static optimisation solves the equations using a quasi-static approach, therefore there is no integration between subsequent instance in time, allowing for the solver to quickly reach a solution.

#### *Joint reaction analysis*

When interested in understanding and quantifying the forces acting on the articular surface of the bones, the Joint Reaction Analysis Tool, first proposed by Steele et al. (2012a), can be of help. This tool allows to estimate the so-called joint contact forces (JCFs), assumed acting at the joint centre, and calculated solving each segment free body diagram, from distal to proximal, including the external forces (i.e. GRF) acting on the system, the inertial forces, and the muscle forces. On the adjacent proximal segment, the distal contact force is equal and opposite to the one previously calculated on the distal segment. In such a way, all the reaction forces can be calculated iteratively, up to the most proximal segment of the chain.

### **2.3.5. Limitations of subject-specific musculoskeletal modelling**

The lack of standardised methods and validated procedures still represents a limitation in the adoption of MRI-based MSKMs in the clinical practice. In fact, the implementation of such models is still highly dependent on the quality of the data collections: experimental procedures can represent a significant source of errors and incomplete data (due to either availability of the patients, technical limitations, or human errors) often impede the full exploitation of the modelling potential.

As a rule, modellers should be aware of the uncertainty related to input data and ensure to limit the sensitivity of the model's output to such error. In this sense, further errors associated to the model definition (including model simplification and assumption) or operator-dependent procedures should be quantified and minimised, when possible. In order to achieve this, models should be tested for repeatability and reproducibility. This would provide robust protocols and promote the adoption of unified techniques, facilitating inter-laboratory comparisons of the results. When input errors exist, an acceptable model repeatability/reproducibility should be set in order to guarantee that the input accuracy is preserved, without adding further uncertainty. On the other hand, improving the model precision, beyond the resolution of the experimental data would be unnecessary.

As the generation of MSKMs implies the tuning of many input parameters, numerous sensitivity studies have recently aimed at testing the robustness of the models to several input, i.e. the location of virtual markers, the idealisation of the joints, and the identification of their axes, the definition of the musculotendon geometry (Bahl et al., 2019, Carbone et al., 2012, Martelli et al., 2015, Navacchia et al., 2016, Wesseling et al., 2016). These studies highlighted the criticalities of musculoskeletal modelling through probabilistic approaches, but none of them tested the actual variability associated to one (or more) operator manually producing the models.

In this respect, some researchers have questioned on the feasibility of adopting subject-specific models as part of the clinical practice, especially due to the cost and time, and to the required expertise, mostly associated to the imaging acquisition and processing. In fact, the cost for one MRI is about £500 in the UK, and the time for extracting anatomical information from the images can reach 40 hours of work, depending on the experience of the operator and the level of detail required by the study. The use of generic-scaled models is proposed as a cheaper alternative, however, this approach proved to be highly inaccurate in the case of patients with anatomical or morphological variations (Bahl et al., 2019), or in children (Kainz et al., 2017). Indeed, scaling an adult-derived anatomical dataset onto a child is not feasible and proved to introduce non-negligible errors in the models' output (Kainz et al., 2017). A generic paediatric model built from children data would be needed to overcome this limitation and provide a better template, compared to existing generic models, for adopting a scaling approach when medical images are not available, i.e. in retrospective studies or in studies where modelling time and costs represent a limitation.

Otherwise, costs associated to subject-specific modelling could be reduced by introducing alternative and cheaper imaging techniques, such as Ultrasound, and improving the image processing phase by developing automated procedure to both limit modelling time and manual intervention.

Furthermore, the adoption of MSKMs in the clinical routine is limited by the lack of strong evidence supporting their validity. Many studies apply MSKMs to investigate the biomechanical features of a disease based on small cohorts due to difficulties in enrolling participants or in obtaining ethical permission for conducting certain invasive tests. Limited numbers of participants often reduce the statistical strength of the results, i.e. impeding to

generalise on the outcome of a study. In fact, large datasets should be analysed in order to produce solid conclusions. On the other hand, in comparative studies, the ultimate aim is that of discriminating between groups of subjects, i.e. pathological versus healthy controls. In this thesis, the validity of the adopted modelling technique, with respect to the specific application/research question, was assessed by ensuring that the discriminating power of the analysed parameter was above its uncertainty.

Moreover, some areas are still highly debated among the MSK modelling community, i.e. the modelling of the ankle joint. Experimental evidence proved that this is a very complex structure, including the tibiotalar and subtalar joints, whose movements are only partially described when assuming a hinge-like behaviour. Despite this, the hinge representation is commonly adopted in musculoskeletal modelling, especially due to limitations in tracking the real movement of these joints *in-vivo*. In fact, a more complex modelling could not be supported by equally accurate input data when simulating walking activities. Additionally, current approaches to the identification of the ankle axes resulted very sensitive to experimental variability and human error. For example, the ISB (International Society of Biomechanics) standards fully rely on the palpation of anatomical points to identify the joint axes, being unavoidably affected by landmark placement errors. An alternative method is based on the manual location of a cylinder in the correspondence of the talar dome (Prinold et al., 2016), however this approach is highly dependent on the operator capabilities. Moreover, these two methods provided inconsistent results when compared: Prinold et al. (2016) reported up to 83% of difference in the ankle peak JCF when using a landmark-based or fitting-based approach. Therefore, the inaccuracy and ambiguity of ankle models (Hannah et al., 2017, Leitch et al., 2010, Prinold et al., 2016) restrict their applicability to healthy populations where anatomical variability is less remarkable.

Many authors reported on the anatomical variability between subjects and they assessed the sensitivity of the models to variations in the parameters constituting the musculotendon unit (Ackland et al., 2012, Carbone et al., 2016, De Groote et al., 2010, Modenese et al., 2018, Navacchia et al., 2016, Valente et al., 2014) mostly based on probabilistic analysis varying the input parameters within ranges provided by *in-vivo* or *ex-vivo* anatomical studies (Handsfield et al., 2014, Horsman et al., 2007, Ward et al., 2009). Despite the large amount of literature on this topic, no study, to the best of our knowledge, has quantified the model output when

personalising the musculotendon parameters accounting for the actual anatomical variability within a certain cohort.

## 2.4. Aim and objectives

This PhD thesis aimed to develop and assess an innovative, robust, and reliable procedure for the definition of MRI-based subject-specific MSKMs of the lower limb in order to foster their wider usability and clinical application. To achieve all this, several objectives were fulfilled.

**Objective 1:** quantify the intra- and inter-operator repeatability of manual steps required for the personalisation of MRI-based MSKMs of the foot and ankle complex. The work reported in chapters 3 and 4 was intended to investigate this aspect.

**Objective 2:** define and validate an innovative approach to personalised modelling of the tibiotalar and subtalar joints, compatible with currently available lower limb MSKMs. This led to the development of the kinematic model (presented in chapter 3) whose anatomical fidelity was verified against *ex-vivo* literature.

**Objective 3:** define the minimum input requirements and set of procedures to implement an MRI-based semi-automated lower-limb musculoskeletal modelling pipeline in order to obtain an output accuracy in line with equivalent manual modelling approaches in the literature (i.e. MRI- or CT-based MSKMs). Such a pipeline, intended as the ensemble of the steps needed to produce MSKMs and simulate human gait in a patient-specific manner, would standardise models' output, promoting a wider adoption of the technique. In this sense, part of chapter 5 aims at providing suggestions for standardising input data and briefly reports general guidelines for producing an MSKM (full details are included in Appendix I).

**Objective 4:** test the robustness of the lower-limb musculoskeletal modelling pipeline to operator-related errors and uncertainties and identify the critical steps aiming at further improve the subject-specific estimates. Chapter 6 aimed at achieving this objective.

**Objective 5:** account for intra- and inter-subject muscle anatomical variability in MSKMs and quantify the effect of muscle personalisation on the estimate of muscle and joint contact forces. To fill this gap in the literature, chapter 7 analyses the anatomical variability in a group of older women and adjust musculotendon parameters to match the actual values for these

subjects. A comparison to less personalised techniques, based on generic-scaled models is also pursued.

## 2.5. References

- Ackland, D. C., Lin, Y.-C. & Pandy, M. G. 2012. Sensitivity of model predictions of muscle function to changes in moment arms and muscle–tendon properties: a Monte-Carlo analysis. *Journal of Biomechanics*, 45, 1463-1471.
- Anderson, F. C. & Pandy, M. G. 2001. Static and dynamic optimization solutions for gait are practically equivalent. *Journal of Biomechanics*, 34, 153-161.
- Arnold, E. M., Hamner, S. R., Seth, A., Millard, M. & Delp, S. L. 2013. How muscle fiber lengths and velocities affect muscle force generation as humans walk and run at different speeds. *Journal of Experimental Biology*, 216, 2150-2160.
- Arnold, E. M., Ward, S. R., Lieber, R. L. & Delp, S. L. 2010. A model of the lower limb for analysis of human movement. *Annals of biomedical engineering*, 38, 269-279.
- Bahl, J. S., Zhang, J., Killen, B. A., Taylor, M., Solomon, L. B., Arnold, J. B., Lloyd, D. G., Besier, T. F. & Thewlis, D. 2019. Statistical shape modelling versus linear scaling: effects on predictions of hip joint centre location and muscle moment arms in people with hip osteoarthritis. *Journal of Biomechanics*.
- Baker, R. 2006. Gait analysis methods in rehabilitation. *Journal of neuroengineering and rehabilitation*, 3, 4.
- Besier, T. F., Sturnieks, D. L., Alderson, J. A. & Lloyd, D. G. 2003. Repeatability of gait data using a functional hip joint centre and a mean helical knee axis. *Journal of Biomechanics*, 36, 1159-1168.
- Bloch, F. 1946. Nuclear induction. *Physical review*, 70, 460.
- Camomilla, V., Cereatti, A., Vannozzi, G. & Cappozzo, A. 2006. An optimized protocol for hip joint centre determination using the functional method. *Journal of biomechanics*, 39, 1096-1106.
- Carbone, V., Van Der Krogt, M., Koopman, H. F. & Verdonschot, N. 2016. Sensitivity of subject-specific models to Hill muscle–tendon model parameters in simulations of gait. *Journal of Biomechanics*, 49, 1953-1960.
- Carbone, V., Van Der Krogt, M. M., Koopman, H. F. & Verdonschot, N. 2012. Sensitivity of subject-specific models to errors in musculo-skeletal geometry. *Journal of Biomechanics*, 45, 2476-2480.
- Correa, T. A. & Pandy, M. G. 2011. A mass–length scaling law for modeling muscle strength in the lower limb. *Journal of Biomechanics*, 44, 2782-2789.
- Crowninshield, R. D. 1978. Use of optimization techniques to predict muscle forces. *Journal of biomechanical engineering*, 100, 88-92.
- Crowninshield, R. D. & Brand, R. A. 1981. A physiologically based criterion of muscle force prediction in locomotion. *Journal of Biomechanics*, 14, 793-801.

- Damsgaard, M., Rasmussen, J., Christensen, S. T., Surma, E. & De Zee, M. 2006. Analysis of musculoskeletal systems in the AnyBody Modeling System. *Simulation Modelling Practice and Theory*, 14, 1100-1111.
- De Groote, F., Van Campen, A., Jonkers, I. & De Schutter, J. 2010. Sensitivity of dynamic simulations of gait and dynamometer experiments to hill muscle model parameters of knee flexors and extensors. *Journal of Biomechanics*, 43, 1876-1883.
- Delp, S. L., Anderson, F. C., Arnold, A. S., Loan, P., Habib, A., John, C. T., Guendelman, E. & Thelen, D. G. 2007. OpenSim: open-source software to create and analyze dynamic simulations of movement. *IEEE transactions on biomedical engineering*, 54, 1940-1950.
- Delp, S. L., Loan, J. P., Hoy, M. G., Zajac, F. E., Topp, E. L. & Rosen, J. M. 1990. An interactive graphics-based model of the lower extremity to study orthopaedic surgical procedures. *IEEE Transactions on Biomedical engineering*, 37, 757-767.
- Di Marco, R., Rossi, S., Racic, V., Cappa, P. & Mazzà, C. 2016. Concurrent repeatability and reproducibility analyses of four marker placement protocols for the foot-ankle complex. *Journal of Biomechanics*, 49, 3168-3176.
- Ding, Z., Tsang, C. K., Nolte, D., Kedgley, A. E. & Bull, A. M. 2019. Improving musculoskeletal model scaling using an anatomical atlas: the importance of gender and anthropometric similarity to quantify joint reaction forces. *IEEE Transactions on Biomedical Engineering*.
- Donnelly, C. J., Lloyd, D. G., Elliott, B. C. & Reinbolt, J. A. 2012. Optimizing whole-body kinematics to minimize valgus knee loading during sidestepping: implications for ACL injury risk. *Journal of Biomechanics*, 45, 1491-1497.
- Dul, J. & Johnson, G. 1985. A kinematic model of the ankle joint. *Biomedical Engineering*, 7, 137-143.
- Gray, H. 1918. *Anatomy of the human body*, 20th edn Philadelphia: Lea & Febiger.
- Handsfield, G. G., Meyer, C. H., Hart, J. M., Abel, M. F. & Blemker, S. S. 2014. Relationships of 35 lower limb muscles to height and body mass quantified using MRI. *Journal of biomechanical engineering*, 47, 631-638.
- Hannah, I., Montefiori, E., Modenese, L., Prinold, J., Viceconti, M. & Mazza, C. 2017. Sensitivity of a juvenile subject-specific musculoskeletal model of the ankle joint to the variability of operator-dependent input. *Proceedings of the Institution of Mechanical Engineers, Part H: Journal of Engineering in Medicine*, 231, 415-422.
- Hill, A. V. 1938. The heat of shortening and the dynamic constants of muscle. *Proceedings of the Royal Society of London. Series B-Biological Sciences*, 126, 136-195.
- Holzbaur, K. R., Murray, W. M. & Delp, S. L. 2005. A model of the upper extremity for simulating musculoskeletal surgery and analyzing neuromuscular control. *Annals of biomedical engineering*, 33, 829-840.
- Horsman, M. K., Koopman, H. F., Van Der Helm, F. C., Prosé, L. P. & Veeger, H. 2007. Morphological muscle and joint parameters for musculoskeletal modelling of the lower extremity. *Clinical biomechanics*, 22, 239-247.
- Huxley, A. 1974. Muscular contraction. *The Journal of physiology*, 243, 1-43.

- Isman, R. E., Inman, V. T. & Poor, P. 1969. Anthropometric studies of the human foot and ankle. *Bull Prosthet Res*, 11, 129.
- Kainz, H., Carty, C. P., Maine, S., Walsh, H. P., Lloyd, D. G. & Modenese, L. 2017. Effects of hip joint centre mislocation on gait kinematics of children with cerebral palsy calculated using patient-specific direct and inverse kinematic models. *Gait & posture*, 57, 154-160.
- Kuo, A. D. 2007. The six determinants of gait and the inverted pendulum analogy: A dynamic walking perspective. *Human movement science*, 26, 617-656.
- Leitch, J., Stebbins, J. & Zavatsky, A. B. 2010. Subject-specific axes of the ankle joint complex. *Journal of biomechanics*, 43, 2923-2928.
- Lu, T.-W. & O'Connor, J. 1999. Bone position estimation from skin marker co-ordinates using global optimisation with joint constraints. *Journal of Biomechanics*, 32, 129-134.
- Maik, V., Paik, D., Lim, J., Park, K. & Paik, J. 2010. Hierarchical pose classification based on human physiology for behaviour analysis. *IET computer vision*, 4, 12-24.
- Martelli, S., Valente, G., Viceconti, M. & Taddei, F. 2015. Sensitivity of a subject-specific musculoskeletal model to the uncertainties on the joint axes location. *Computer methods in biomechanics biomedical engineering*, 18, 1555-1563.
- Modenese, L., Montefiori, E., Wang, A., Wesarg, S., Viceconti, M. & Mazzà, C. 2018. Investigation of the dependence of joint contact forces on musculotendon parameters using a codified workflow for image-based modelling. *Journal of Biomechanics*, 73, 108-118.
- Montefiori, E., Modenese, L., Di Marco, R., Magni-Manzoni, S., Malattia, C., Petrarca, M., Ronchetti, A., De Horatio, L. T., Van Dijkhuizen, P., Wang, A., Wesarg, S., Viceconti, M. & Mazzà, C. 2019. Linking Joint Impairment and Gait Biomechanics in Patients with Juvenile Idiopathic Arthritis. *Annals of biomedical engineering*, 1-13.
- Navacchia, A., Myers, C. A., Rullkoetter, P. J. & Shelburne, K. B. 2016. Prediction of in vivo knee joint loads using a global probabilistic analysis. *Journal of biomechanical engineering*, 138, 031002.
- Nichols, J. A., Roach, K. E., Fiorentino, N. M. & Anderson, A. E. 2017. Subject-Specific Axes of Rotation Based on Talar Morphology Do Not Improve Predictions of Tibiotalar and Subtalar Joint Kinematics. *Annals of biomedical engineering*, 45, 2109-2121.
- Oatis, C. A. & Craik, R. 1994. *Gait analysis: theory and application*, Mosby.
- Pandy, M. G. 2003. Simple and complex models for studying muscle function in walking. *Philosophical Transactions of the Royal Society of London. Series B: Biological Sciences*, 358, 1501-1509.
- Prinold, J. A., Mazzà, C., Di Marco, R., Hannah, I., Malattia, C., Magni-Manzoni, S., Petrarca, M., Ronchetti, A. B., De Horatio, L. T. & Van Dijkhuizen, E. P. 2016. A patient-specific foot model for the estimate of ankle joint forces in patients with juvenile idiopathic arthritis. *Annals of biomedical engineering*, 44, 247-257.
- Rasmussen, J., Damsgaard, M. & Voigt, M. 2001. Muscle recruitment by the min/max criterion—a comparative numerical study. *Journal of Biomechanics*, 34, 409-415.

- Sacks, R. D. & Roy, R. R. 1982. Architecture of the hind limb muscles of cats: functional significance. *Journal of Morphology*, 173, 185-195.
- Scheys, L., Desloovere, K., Suetens, P. & Jonkers, I. 2011. Level of subject-specific detail in musculoskeletal models affects hip moment arm length calculation during gait in pediatric subjects with increased femoral anteversion. *Journal of Biomechanics*, 44, 1346-1353.
- Scheys, L., Van Campenhout, A., Spaepen, A., Suetens, P. & Jonkers, I. 2008. Personalized MR-based musculoskeletal models compared to rescaled generic models in the presence of increased femoral anteversion: effect on hip moment arm lengths. *Gait & posture*, 28, 358-365.
- Siegler, S., Chen, J. & Schneck, C. 1988. The three-dimensional kinematics and flexibility characteristics of the human ankle and subtalar joints—Part I: Kinematics. *Journal of biomechanical engineering*, 110, 364-373.
- Steele, K. M., Demers, M. S., Schwartz, M. H. & Delp, S. L. 2012a. Compressive tibiofemoral force during crouch gait. *Gait & posture*, 35, 556-560.
- Steele, K. M., Van Der Krogt, M. M., Schwartz, M. H. & Delp, S. L. 2012b. How much muscle strength is required to walk in a crouch gait? *Journal of Biomechanics*, 45, 2564-2569.
- Valente, G., Pitto, L., Testi, D., Seth, A., Delp, S. L., Stagni, R., Viceconti, M. & Taddei, F. 2014. Are subject-specific musculoskeletal models robust to the uncertainties in parameter identification? *PLoS One*, 9, e112625.
- Van Alsenoy, K. K., De Schepper, J., Santos, D., Vereecke, E. E. & D'août, K. 2014. The Subtalar Joint Axis Palpation Technique—Part 1: Validating a Clinical Mechanical Model. *Journal of the American Podiatric Medical Association*, 104, 238-246.
- Van Den Bogert, A. J., Smith, G. D. & Nigg, B. M. 1994. In vivo determination of the anatomical axes of the ankle joint complex: an optimization approach. *Journal of biomechanics*, 27, 1477-1488.
- Van Der Krogt, M. M., Bar-On, L., Kindt, T., Desloovere, K. & Harlaar, J. 2016. Neuro-musculoskeletal simulation of instrumented contracture and spasticity assessment in children with cerebral palsy. *Journal of neuroengineering and rehabilitation*, 13, 64.
- Van Sint Jan, S. 2007. *Color Atlas of Skeletal Landmark Definitions E-Book: Guidelines for Reproducible Manual and Virtual Palpations*, Elsevier Health Sciences.
- Ward, S. R., Eng, C. M., Smallwood, L. H. & Lieber, R. L. 2009. Are current measurements of lower extremity muscle architecture accurate? *Clinical orthopaedics related research*, 467, 1074-1082.
- Wesseling, M., De Groote, F., Bosmans, L., Bartels, W., Meyer, C., Desloovere, K. & Jonkers, I. 2016. Subject-specific geometrical detail rather than cost function formulation affects hip loading calculation. *Computer methods in biomechanics biomedical engineering*, 19, 1475-1488.
- Westblad, P., Hashimoto, T., Winson, I., Lundberg, A. & Arndt, A. 2002. Differences in ankle-joint complex motion during the stance phase of walking as measured by superficial and bone-anchored markers. *Foot & ankle international*, 23, 856-863.
- Whittle, M. W. 1996. Clinical gait analysis: A review. *Human Movement Science*, 15, 369-387.

- Wu, G., Siegler, S., Allard, P., Kirtley, C., Leardini, A., Rosenbaum, D., Whittle, M., D D'lima, D., Cristofolini, L. & Witte, H. 2002. ISB recommendation on definitions of joint coordinate system of various joints for the reporting of human joint motion—part I: ankle, hip, and spine. *Journal of Biomechanics*, 35, 543-548.
- Yamaguchi, G. T. 2005. *Dynamic modeling of musculoskeletal motion: a vectorized approach for biomechanical analysis in three dimensions*, Springer Science & Business Media.
- Zajac, F. E. 1989. Muscle and tendon: properties, models, scaling, and application to biomechanics and motor control. *Critical reviews in biomedical engineering*, 17, 359-411.

**3. An image-based kinematic model of the  
tibiotalar and subtalar joints and its  
application to gait analysis in children with  
Juvenile Idiopathic Arthritis**

### *Acknowledgement of co-authorship*

This chapter includes the published paper “An image-based kinematic model of the tibiotalar and subtalar joints and its application to gait analysis in children with Juvenile Idiopathic Arthritis” produced as the results of the research carried out in collaboration with the co-authors listed in the paper.

My personal contribution was in the design of the study, implementation of the proposed methodology in the models, quantification of the intra- and inter-operator repeatability of the models’ output, verification of the validity of the methodology with respect to available literature, application of the models to answer the specific clinical question, interpretation of the results with respect to the clinical context. Additionally, I was responsible for writing the paper, producing figures and tables and leading the submission and review process.

Student:

Erica Montefiori		Date	25/07/2019
------------------	---	------	------------

The main co-authors:

Claudia Mazza'		Date	25/07/2019
----------------	---	------	------------

Luca Modenese		Date	24/07/2019
---------------	---	------	------------



Contents lists available at ScienceDirect

## Journal of Biomechanics

journal homepage: [www.elsevier.com/locate/jbiomech](http://www.elsevier.com/locate/jbiomech)  
[www.JBiomech.com](http://www.JBiomech.com)

# An image-based kinematic model of the tibiotalar and subtalar joints and its application to gait analysis in children with Juvenile Idiopathic Arthritis



Erica Montefiori<sup>a,\*</sup>, Luca Modenese<sup>a</sup>, Roberto Di Marco<sup>b</sup>, Silvia Magni-Manzoni<sup>c</sup>, Clara Malattia<sup>d</sup>, Maurizio Petrarca<sup>e</sup>, Anna Ronchetti<sup>f</sup>, Laura Tanturri de Horatio<sup>g</sup>, Pieter van Dijkhuizen<sup>h</sup>, Anqi Wang<sup>i</sup>, Stefan Wesarg<sup>i</sup>, Marco Viceconti<sup>a</sup>, Claudia Mazzà<sup>a</sup>, for the MD-PAEDIGREE Consortium

<sup>a</sup> Department of Mechanical Engineering and INSIGNEO Institute for in silico Medicine, University of Sheffield, Sheffield, United Kingdom

<sup>b</sup> Department of Mechanical and Aerospace Engineering, "Sapienza" University of Rome, Rome, Italy

<sup>c</sup> Pediatric Rheumatology Unit, IRCCS "Bambino Gesù" Children's Hospital, Passoscuro, Rome, Italy

<sup>d</sup> Pediatria II – Reumatologia, Istituto Giannina Gaslini, Genoa, Italy

<sup>e</sup> Movement Analysis and Robotics Laboratory (MARLab), Neurorehabilitation Units, IRCCS "Bambino Gesù" Children's Hospital, Passoscuro, Rome, Italy

<sup>f</sup> UOC Medicina Fisica e Riabilitazione, IRCCS Istituto Giannina Gaslini, Genoa, Italy

<sup>g</sup> Department of Imaging, IRCCS "Bambino Gesù" Children's Hospital, Passoscuro, Rome, Italy

<sup>h</sup> Paediatric Immunology, University Medical Centre Utrecht, Wilhelmina Children's Hospital, Utrecht, the Netherlands

<sup>i</sup> Visual Healthcare Technologies, Fraunhofer IGD, Darmstadt, Germany

## ARTICLE INFO

## Article history:

Accepted 28 December 2018

## Keywords:

Biomechanics

Ankle joint axis

Musculoskeletal modelling

Gait analysis

Patient-specific modelling

## ABSTRACT

*In vivo* estimates of tibiotalar and the subtalar joint kinematics can unveil unique information about gait biomechanics, especially in the presence of musculoskeletal disorders affecting the foot and ankle complex. Previous literature investigated the ankle kinematics on *ex vivo* data sets, but little has been reported for natural walking, and even less for pathological and juvenile populations. This paper proposes an MRI-based morphological fitting methodology for the personalised definition of the tibiotalar and the subtalar joint axes during gait, and investigated its application to characterise the ankle kinematics in twenty patients affected by Juvenile Idiopathic Arthritis (JIA). The estimated joint axes were in line with *in vivo* and *ex vivo* literature data and joint kinematics variation subsequent to inter-operator variability was in the order of 1°. The model allowed to investigate, for the first time in patients with JIA, the functional response to joint impairment. The joint kinematics highlighted changes over time that were consistent with changes in the patient's clinical pattern and notably varied from patient to patient. The heterogeneous and patient-specific nature of the effects of JIA was confirmed by the absence of a correlation between a semi-quantitative MRI-based impairment score and a variety of investigated joint kinematics indexes. In conclusion, this study showed the feasibility of using MRI and morphological fitting to identify the tibiotalar and subtalar joint axes in a non-invasive patient-specific manner. The proposed methodology represents an innovative and reliable approach to the analysis of the ankle joint kinematics in pathological juvenile populations.

© 2019 Elsevier Ltd. All rights reserved.

## 1. Introduction

Functional anatomy literature describes the ankle joint as a very complex structure allowing for multiple movements due to the combination of various mechanically coupled joints, including

the tibiotalar (i.e. between tibia and talus) and subtalar (i.e. between talus and calcaneus) joints (Hicks et al., 1953; Siegler et al., 1988; Dettwyler et al., 2004). The biomechanical behaviour of the ankle during locomotion and its relationship with the anatomy have been investigated since the beginning of the last century (Fick, 1911; Manter, 1941; Barnett and Napier, 1952; Isman and Inman, 1969; Inman, 1976) and many authors have also estimated the kinematics of the tibiotalar and subtalar joints *ex vivo* (Hicks et al., 1953; Rasmussen and Tovborg-Jensen, 1982; van Langelaan, 1983; Siegler et al., 1988). The possibility of estimating

\* Corresponding author at: Room C+13 – INSIGNEO Institute for in silico Medicine, The University of Sheffield, The Pam Liversidge Building, Mappin Street, Sheffield, United Kingdom.

E-mail address: [e.montefiori@sheffield.ac.uk](mailto:e.montefiori@sheffield.ac.uk) (E. Montefiori).

the kinematics of the ankle's intrinsic joints from *in vivo* data is of interest when investigating musculoskeletal diseases. Nonetheless, a comprehensive understanding of the joint's intrinsic movement during walking is still lacking. This is because measuring the motion associated to foot inversion/eversion is not trivial and most literature has focused on the quantification of articular range of motion (ROM) for the various joint's degrees of freedom (DOFs) under controlled conditions (Lundberg et al., 1989; Mattingly et al., 2006; Lewis et al., 2009).

*In vivo* tracking of the relative movement of the talus relative to the calcaneus using skin markers and a standard gait analysis technique is complicated by the small size of these bones and the absence of visible superficial landmarks (Scott et al., 1991; Di Marco et al., 2016). Few studies have investigated the kinematics of the intrinsic joints of the ankle during walking and running (Arndt et al., 2004, 2006) using intracortical bone pins, and compared the results to those from using superficial markers (Westblad et al., 2002). These studies clearly showed a description of plantar/dorsiflexion is possible with traditional gait analysis methods, however, estimates of inversion/eversion movement are still far from being accurate. Intracortical pin-based studies partially overcome this lack of accuracy but, due to the invasiveness of the technique, the number of participants is usually limited to few healthy volunteers, whose natural gait pattern can be altered by the possible pain and discomfort related to the implant. Both *in vivo* and *ex vivo* studies reported high intra-subject and inter-subject variability in the subtalar joint kinematics with ROM up to 60° (Roas and Anderson, 1982; Sepic et al., 1986; Lundberg, 1989).

The functional complexity of the subtalar joint led to a number of different modelling approaches, from the attempt to capture its mobility through multi-segmental foot models where the subtalar articulation was interpreted as a motion between hind-foot and fore-foot (Prinold et al., 2016; Saraswat et al., 2010), to a more anatomical representation as a universal or hinge joint (Delp et al., 1990; Malaquias et al., 2017). The hinge-like schematisation also applies to the tibiotalar joint and this approach is currently used within widely adopted musculoskeletal models (Delp et al., 1990). When simultaneously modelling both joints as hinges (Dul and Johnson, 1985), a reasonable simplification is made with respect to their real functional role (Siegler et al., 1988), according to which the tibiotalar and subtalar joints describe the plantar/dorsiflexion and inversion/eversion motions, respectively. This latter motion, despite its simplified appearance, is justified because the predominant motion occurs about a single axis of rotation (Scott and Winter, 1991). However, this DOF has been reported to be less accurately described with current musculoskeletal modelling approaches, mainly due to the difficulties in identifying the joint functional axis *in vivo* (Van den Bogert et al., 1994; Dettwyler et al., 2004; Parr et al., 2012). A high variability within- and between-subjects has been observed in the modelled joint axes, which is also related to the specific locomotion task (Leitch et al., 2010). In the presence of musculoskeletal disorders, the adoption of image-based patient-specific modelling approaches has been previously proposed (Prinold et al., 2016; Hannah et al., 2017) and proved to increase anatomical modelling accuracy (Correa and Pandey 2011; Durkin et al., 2006; Scheys et al., 2009). The use of this technique accounts for patients' anatomical features and peculiarities, crucial when impairments and gait limitations affect the subjects. In this study, we propose an image-based modelling procedure to define the tibiotalar and subtalar joints axes, avoiding operator-dependent steps and related variability issues (Prinold et al., 2016; Hannah et al., 2017). Once compared against literature, the procedure will be used as part of a patient-specific musculoskeletal modelling approach to investigate the gait ankle kinematics in children with Juvenile Idiopathic Arthritis (JIA), a

paediatric group of diseases of unknown aetiology characterised by joint inflammation potentially leading to cartilage damage. Altered gait patterns and physical disabilities (Ravelli and Martini, 2007) are possible outcomes in JIA. This longitudinal study will prove whether our modelling approach is capable of detecting clinical changes observed in the tibiotalar and the subtalar joint functions and quantify for the first time the relationship between these changes and the underlying joint impairments.

## 2. Methods

### 2.1. Subjects and data acquisition

Twenty participants (5 males, 15 females, age:  $11.6 \pm 3.1$  years, mass:  $47.6 \pm 18.2$  kg, height:  $148 \pm 17$  cm, 11 new onsets) affected by Juvenile Idiopathic Arthritis (JIA) of various sub-types (oligoarticular onset JIA, polyarticular JIA, psoriatic arthritis, and undifferentiated arthritis) (Ravelli and Martini, 2007) were recruited among those referred to two different children's hospitals (Istituto Giannina Gaslini, Genoa (Lab 1), and "Bambino Gesù" Children's Hospital, Rome (Lab 2)). The study was conducted following Helsinki's declaration on human rights and was approved by the ethical committee of both hospitals. Written informed consent was obtained by patients' parents.

Medical resonance images (MRI) and gait analysis data were collected at three time-points (6 months apart) to follow the disease progression. The imaging performed at month 0 (M0) and month 12 (M12) included a foot and ankle regional MRI (multi-slice multi-echo 3D Gradient Echo (mFFE) with water-only selection (WATS) with 0.5 mm in-plane resolution and 1 mm slice thickness). The month 6 (M6) imaging included a full lower limb MRI (3D T1-weighted fat-suppression sequence (e-THRIVE) with 1 mm in-plane resolution and 1 mm slice thickness). The core set of basic sequences and definitions suggested by the Outcome Measure in Rheumatology (OMERACT) MRI Working Group (Ostergaard et al., 2003; Nusman et al., 2016) was used to provide an MRI-based evaluation of the joints (Table 1). A weighted, average index ( $I_{MRI}$ ) was used to quantify the overall level of impairment of the foot and ankle region.

Gait analysis was based on stereophotogrammetry and data were collected using a 6-camera system (BTS, Smart DX, 100 Hz) with two force plates (Kistler, 1 kHz) in Lab 1, and an 8-camera system (Vicon, MX, 200 Hz) and two force plates (AMTI, OR6, 1 kHz) in Lab 2. Five walking trials at self-selected speed were performed and a minimum of three trials were used for the analysis. The marker set included forty-four markers from the Vicon Plug in gait protocol (Vicon Motion System) and the modified Oxford Foot Model (mOFM) protocol (Stebbins et al., 2006). A subset of MRI-visible markers (twenty-eight in the lower limb MRI and six in the regional MRI scans) was retained during the imaging acquisition for data registration. Despite being collected in different centres and with different equipment, the raw-data underwent the same pre-processing in terms of labelling, gap-filling (spline algorithm built in Vicon Nexus 1.8.5 (Woltring et al., 1986)), and smoothing (4th-order Butterworth filter, 6 Hz cut-off (Barlett et al., 2007)).

### 2.2. Anatomical model

A statistical shape modelling approach (Steger et al., 2012) was used to segment the lower limb bones from the MRI and subject-specific anatomical models were produced using specialised software (NMSBuilder, Valente et al., 2017). For each patient, two bilateral three-segment anatomical models were built using the M0 and M12 datasets, resulting in 80 foot models. Twelve of these were excluded due to incompleteness of the experimental dataset,

**Table 1**  
MRI scoring.

Index	MRI sequence	Scale	Sites
Bone erosion	T1-weighted fat-saturated	Range 0–10 % of eroded articular surface (Ostergaard et al., 2003) 0 = no erosion; 1 = 1–10%; 2 = 11–20%; 3 = 21–30%; 4 = 31–40%; 5 = 41–50%; 6 = 51–60%; 7 = 61–70%; 8 = 61–80%; 9 = 81–90%; 10 = 91–100%	Distal tibial epiphysis Distal fibula epiphysis Tarsal bones Metatarsal bases
Cartilage damage	WATS	Range 0–3 % of damaged cartilage surface 0 = no damage; 1 = 1–33%; 2 = 34–66%; 3 = 67–100%; 4 = extensive damage causing ankyloses	Tibiotalar Between distal talus and calcaneus, Talonavicular Calcaneocuboid Cuneonavicular Between cuneiforms and I, II and III metatarsal bones Between cuboid and IV and V metatarsal bones
Synovitis	T1-weighted fat-saturated	Range 0–3 Degree of synovial enhancement and synovial thickness (Ostergaard et al., 2003; Malattia et al., 2011) 0 = normal; 1 = mild; 2 = moderate; 3 = severe	Tibio-peroneo-talar Subtalar Talonavicular Calcaneocuboid I-V tarsometatarsal Cuneonavicular
Tenosynovitis	T1-weighted fat-saturated with enhancement	Range 0–3 Degree of peritendinous effusion or synovial proliferation 0 = normal; 1 = mild (less than 2 mm); 2 = moderate (2–5 mm); 3 = severe (>5 mm)	Anterior tibial Extensor digitorum longus Extensor hallucis longus Posterior tibial Flexor digitorum longus Flexor hallucis longus Peroneal tendons

resulting in a final dataset of 68 feet. The joints' reference frames, namely tibiotalar joint (between tibia and talus) and subtalar (between talus and foot) were defined according to the ISB conventions (Baker et al., 2003) and the joint axes were identified through morphological fitting of articular surfaces (Fig. 1A–C). The subtalar joint axis (*SubAxis*) was defined as the axis connecting the centres of the spheres fitted to the anterior (Talonavicular sphere) and to the posterior-inferior (*Talocalcaneal sphere*) facets of the talus respectively (Fig. 1B). This was similar to that proposed by Parr et al., 2012, who, however, used the anterior-inferior portion of the talus surface to define the Talonavicular sphere. To define the tibiotalar joint axis (*TibAxis*), a cylinder was fitted to the entire trochlea (*Talartrochlea cylinder*) as a simplification of the approach proposed by Siegler et al., 2014 (Modenese et al., 2018). The fitting was implemented in Meshlab (Cignoni et al., 2008) by identifying the articular surfaces from the segmented geometries and minimising the least squares distance between the identified surface and the corresponding best fitting analytical shape (Least Squares

Geometric Elements library, Matlab). The distal tibia (segmented from the M0/12 MRI) was afterwards registered to the entire tibia (M6 dataset) using the Iterative Closest Point algorithm in Meshlab to obtain a full lower limb model. A comprehensive description of the modelling procedure is available as supplementary material in Modenese et al. (2018). The data and models presented in this paper are available on Figshare (doi: <https://doi.org/10.15131/shef.data.5863443.v1>).

### 2.3. Joint kinematics

The OpenSim's (Delp et al., 2007) Inverse Kinematics (IK) tool was run to estimate the tibiotalar and subtalar joint angles starting from a set of sixteen skin markers (five on the tibia, eleven on the foot, Fig. 2), eight were also virtually palpated on the medical images. The difference between the virtual and experimental markers estimated by the IK tool was less than 1 cm on average over all the time-steps, as suggested in the OpenSim best practice recommendations (Hicks et al., 2015).

### 2.4. Model evaluation

#### 2.4.1. Sensitivity to operator-dependent input

The bone segmentations from three randomly chosen patients were used to investigate the effect of operator-dependent variability in the definition of *TibAxis* and *SubAxis*. Three operators repeated the morphological fitting three times and the coordinates of the *Talartrochlea cylinder*, *Talocalcaneal sphere* and *Talonavicular sphere* centres were used for the comparison. A 3D quantification of their variability ( $SD_{3d}$ ) was calculated from the standard deviation of the point coordinates ( $sd_x, sd_y, sd_z$ ) as:

$$SD_{3d} = \sqrt{sd_x^2 + sd_y^2 + sd_z^2}$$

For the foot that led to the worst-case scenario (higher inter-operator  $SD_{3d}$ ), a second level of analysis was conducted to quantify the propagation of this error on the joint kinematics. The nine models built by the three operators were then used to estimate the tibiotalar and subtalar joint kinematics using data from one randomly selected gait trial from the same patient. The maximum value of the mean and standard deviation calculated over the nine repetitions for each point of the gait cycle was then used to quantify the maximum expected error.

#### 2.4.2. Consistency with literature data

Among the 68 available models, 38 were selected (19 per side, preferentially from M12) to conduct the following analysis. A standing trial collected during the gait analysis session was used to identify the pose of each subject and the resulting neutral position of the foot. The transverse, sagittal, and coronal anatomical planes, the midline of the foot (*FootAxis*) and the long axis of tibia (*TibiaAxis*) were identified using the standing trial markers (Fig. 3A–B). These allowed quantifying the tibiotalar inclination ( $Tib_{Incl}$ ) and deviation ( $Tib_{Dev}$ ), and the subtalar inclination ( $Sub_{Incl}$ ) and deviation ( $Sub_{Dev}$ ) as shown by the angles in Fig. 3C.  $Tib_{Incl}$ ,  $Tib_{Dev}$ ,  $Sub_{Incl}$  and  $Sub_{Dev}$  were compared to literature data from *ex vivo* cadaveric specimens (Isman and Inman, 1969; Inman, 1976) and from healthy adults (Van den Bogert et al., 1994). The estimations of *TibAxis* and *SubAxis* at M0 and M12 were also compared. All 26 models for which the 3D anatomy was available at both time-points (52 models) were used for a between-session comparison. For this analysis, the angle between the two joint axes (*InterAxis*) was preferred over the measures of  $Tib_{Incl}$ ,  $Tib_{Dev}$ ,  $Sub_{Incl}$ , and  $Sub_{Dev}$  to avoid the effect of experimental markers repositioning (between the two sessions) on these angles. Mean and maximum between-session variations were quantified, and a paired-two-sided

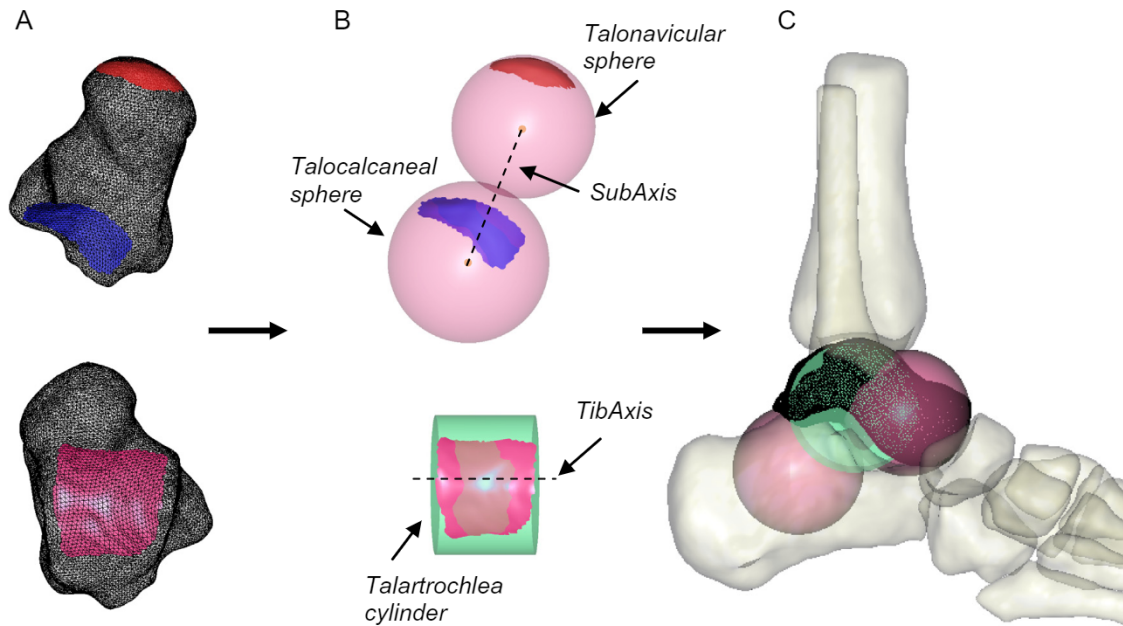


**Fig. 1.** (A) Plantar (top) and dorsal (bottom) views of the right talus (black wireframe) with highlighted articular regions: anterior facet (red), posterior-inferior facet (blue), trochlea (fuchsia). (B) Fitting of analytical shapes to the selected articular regions: two spheres (light pink) identify the axis of the subtalar joint (SubAxis) as the axis connecting the centres of the spheres and a cylinder (light green) identifies the axis of the tibiotalar joint (TibAxis) as the cylinder axis. (C) Example of the fitted geometries integrated within the ankle anatomical model. (For interpretation of the references to colour in this figure legend, the reader is referred to the web version of this article.)

Label	Description	Markers	
		MRI	Stereo
HFB	Head of the fibula	Yes	Yes
SHN	Anterior aspect of shin	Yes	Yes
TUB	Tibial tuberosity	-	Yes
MMA	Medial malleolus	Yes	Yes
ANK	Lateral malleolus	Yes	Yes
PCA	Posterior medial aspect of heel	-	Yes
STL	Sustentaculum tali	-	Yes
LCA	Lateral calcaneus	-	Yes
CPG	Wand marker on posterior calcaneus aligned with transverse orientation	-	Yes
HEE	Posterior distal aspect of heel	-	Yes
P1M	Lateral aspect of 1 <sup>st</sup> metatarsal base	-	Yes
P5M	Lateral aspect of 5 <sup>th</sup> metatarsal base	-	Yes
TOE	Between 2 <sup>nd</sup> and 3 <sup>rd</sup> metatarsal heads	Yes	Yes
D1M	Lateral aspect of 1 <sup>st</sup> metatarsal head	Yes	Yes
D5M	Lateral aspect of 5 <sup>th</sup> metatarsal head	Yes	Yes
HLX	Medial side of the proximal hallux	Yes	Yes

**Fig. 2.** Experimental markers used in the imaging (MRI) and stereo-photogrammetric (Stereo) measurements.

Wilcoxon signed-rank test ( $\alpha = 0.05$ ) was performed under the null hypothesis showed that no statistical difference existed between the two repeated measures. This was intended as a repeatability assessment of the proposed method, assuming in the investigated age range, and within 12 months, neither disease progression (Ravelli and Martini, 2007) nor growth (Evans, 2010) would cause changes in the joint morphology.

#### 2.4.3. Effect of clinical impairment on joint kinematics

The models from 13 subjects (3 males, 10 females, age:  $11.0 \pm 3.1$  years, mass:  $44.5 \pm 16.9$  kg, height:  $143 \pm 13$  cm, 8 new onsets), for whom both clinical and biomechanical information was available, were used to test the link between changes in the kinematics and impairment of the ankle as measured from the MRI. The  $I_{MRI}$  scores were used to classify the disability level of each

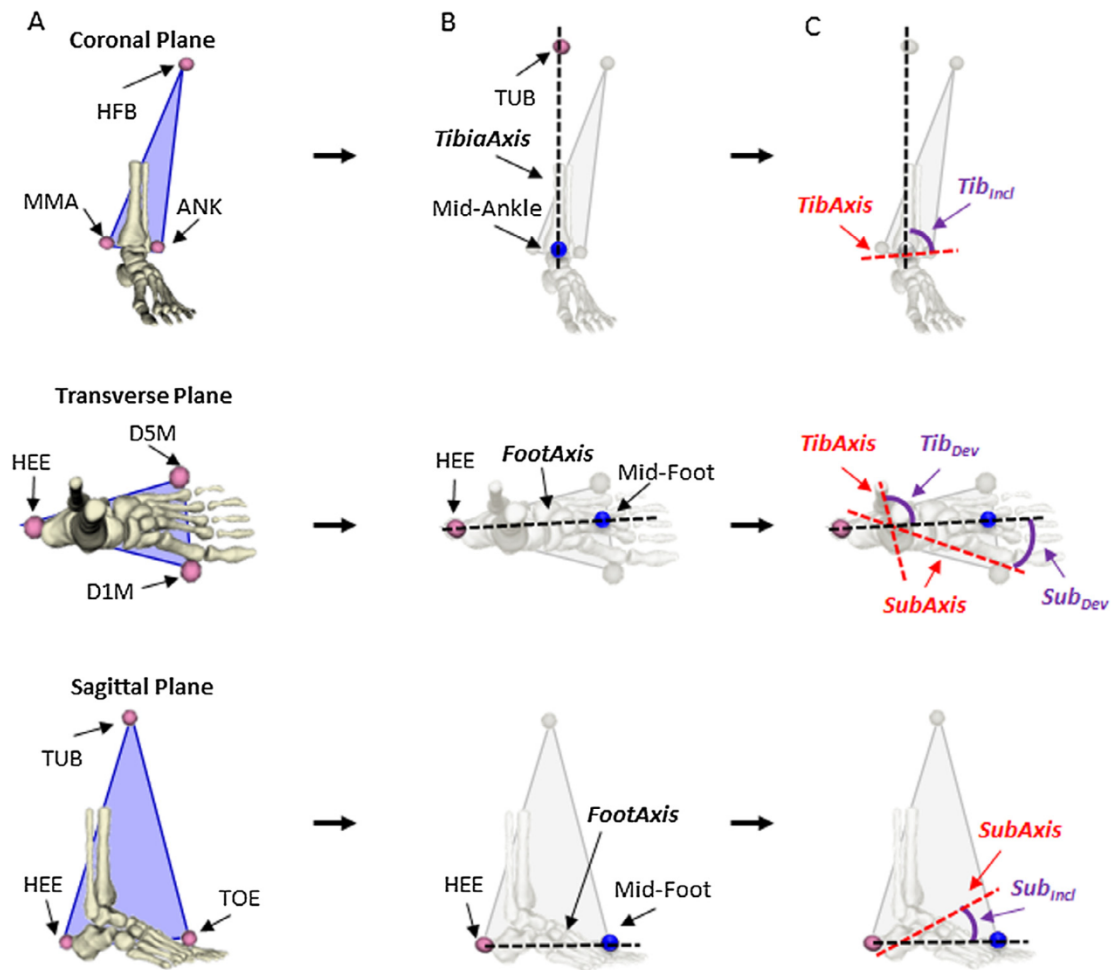


**Fig. 3.** (A) Identification of anatomical planes (blue triangles) as defined using the virtual markers (pink) corresponding to the experimental markers listed in Fig. 2. (B) Definition of the anatomical axes (midline of the foot = *FootAxis*, long axis of the tibia = *TibiaAxis*, black dashed lines) by calculating average points (blue markers) between virtual marker pairs (Mid-Foot = midpoint between D1M and D5M; Mid-Ankle = midpoint between ANK and MMA). (C) Quantification of the inclination ( $Tib_{Incl}$ ) and deviation ( $Tib_{Dev}$ ) of tibiotalar joint and inclination ( $Sub_{Incl}$ ) and deviation ( $Sub_{Dev}$ ) of subtalar joint as the angles (purple arches) between the anatomical axes and the joint axes (red dashed lines) as defined through morphological fitting (Fig. 1). (For interpretation of the references to colour in this figure legend, the reader is referred to the web version of this article.)

ankle and identify better and worse time-points. They were then placed into “low-involvement” and “high-involvement” groups accordingly. The joint kinematics of the two groups were then compared using a non-parametric 1D two-tailed paired *t*-test ( $\alpha = 0.05$ ) (Nichols and Holmes, 2002) based on Statistical Parametric Mapping (SPM) in MATLAB (v9.1, R2016b, Mathworks, USA), using the SPM1D package (Pataky et al., 2012). This was chosen since the data were not normally distributed. The following kinematic parameters were also calculated to investigate the correlation with the  $I_{MRI}$ : area under the curves of the tibiotalar and subtalar joint angles, maximum plantarflexion (PF) and dorsiflexion (DF) angles, maximum inversion (Inv) and eversion (Ev) angles, and joint ROM. Furthermore, the asymmetry between the left and right foot kinematics was quantified using the Root Mean Square Deviation (RMSD) and Mean Absolute Variability (MAV) (Di Marco et al., 2018), as well as the between-side difference of ROM and standard deviations (SD). RMSD, MAV, ROM and SD were measured at the two time-points and compared using a two-sided Wilcoxon signed-rank test ( $\alpha = 0.05$ ). The absolute difference ( $\Delta I_{MRI}$ ) between left and right  $I_{MRI}$  was also calculated and a correlation analysis was used to assess whether an asymmetry in the clinical score, namely higher  $\Delta I_{MRI}$ , corresponded to higher values of the kinematic parameters.

### 3. Results

#### 3.1. Sensitivity to operator-dependent input

$SD_{3d}$  of *Talonavicular sphere* and *Talocalcaneal sphere*'s centres are reported in Table 2, as well as the resulting maximum angular variability of the *TibiaAxis* and *SubAxis*, whose maximum value ( $9.6^\circ$ ) was found for the inclination of *SubAxis* in patient P3. For this patient, the propagation of inter-operator variability on the articular kinematics introduced a maximum standard deviation of  $0.6^\circ$  and  $1.3^\circ$  for the tibiotalar and subtalar joints respectively, both occurring at 63% of the gait cycle.

#### 3.2. Consistency with literature data

The residual error of the fitting algorithm (average ( $\pm$ SD) across the 52 models) was equal to  $0.16 (\pm 0.05)$  mm,  $0.48 (\pm 0.21)$  mm, and  $0.28 (\pm 0.11)$  mm for the *Talonavicular*, *Talocalcaneal*, and *Talar-trochlea* surfaces, respectively. The average ( $\pm$ SD) values of the measured foot angles ( $Tib_{Incl}$ ,  $Tib_{Dev}$ ,  $Sub_{Incl}$ , and  $Sub_{Dev}$ ) (Table 3) were found to be in line with the corresponding *ex vivo* (Isman and Inman, 1969; Inman, 1976) and *in vivo* (Van den Bogert

**Table 2**  
Inter-operator standard deviation (SD) of fitted surfaces centres and axes.

Patients	Talartrochlea center $SD_{3d}$ [mm]	Talonavicular center $SD_{3d}$ [mm]	Talocalcaneal center $SD_{3d}$ [mm]	TibAxis SD [°]	SubAxis SD [°]
P1	0.4	0.4	1.4	0.6	1.7
P2	0.5	0.8	1.5	0.8	1.3
P3	0.8	2.1	5.1	2.0	5.6

et al., 1994) measurements available in the literature. The average absolute difference between the M0 and M12 measures of *Inter-Axes* was  $2.2^\circ \pm 2.1^\circ$ , which was not statistically significant (Wilcoxon test  $p = 0.648$ ).

### 3.3. Effect of clinical impairment on joint kinematics

Fig. 4 shows the estimated kinematics of two subjects with different clinical scoring: patient 1 was similarly affected by the pathology at the two observations, whereas at M12 patient 2 was in total remission, as defined by Ravelli and Martini (2007). This example highlights how the models clearly capture different kinematic patterns associated with different paths of disease progression. The observation of the joint angles also clearly indicates the ability of the model to describe changes in the gait patterns happening between the two time-points, which were also confirmed by consistent changes in the walking speed ( $1.51 \pm 0.05$  m/s at M0 and  $1.22 \pm 0.05$  m/s at M12 for subject 1;  $0.83 \pm 0.03$  m/s at M0 and  $1.20 \pm 0.04$  m/s at M12 for subject 2). For the whole cohort, walking speed varied from  $1.01 \pm 0.24$  m/s at M0 to  $1.12 \pm 0.13$  m/s at M12, and was  $1.14 \pm 0.17$  m/s and  $0.93 \pm 0.33$  m/s at the “low-involvement” and “high-involvement” time-points respectively, with no significant difference. Walking speed values did not correlate with the joint impairment level, as measured with the  $I_{MRI}$  ( $R = -0.21$  and  $R = 0.16$  at M0 and M12, respectively). Similarly, no correlation was observed between  $I_{MRI}$  and the kinematic parameters (Fig. 5). This was confirmed by the absence of a group-wise statistically significant difference between the joint kinematics of the ankles at the “low-involvement” and “high-involvement” time-points throughout the gait cycle (Fig. 6). Fig. 7 clearly shows the absence of a significant correspondence between the asymmetry of impairment ( $\Delta I_{MRI}$ ) and the RMSD, MAV,  $\Delta ROM$  and  $\Delta SD$  observed at M0 and M12. However, a smaller  $\Delta I_{MRI}$  at M12 was generally associated to a smaller value of the kinematics indices at that time-point, except for the  $\Delta SD$  of the tibiotalar joint and the  $\Delta ROM$  of the subtalar joint.

## 4. Discussion

The aim of the study was to propose a kinematic model of the tibiotalar and subtalar joints, and to use this model to investigate the ankle joint kinematics in a group of children with JIA. The anatomical model was based on a morphological fitting approach and underwent repeatability analysis.

The procedure proved to be robust to the operator-dependent input. Even in the worst-case scenario, where the definition of the subtalar axis was associated with high inter-operator error ( $9.6^\circ$ ), the joint kinematics varied less than  $1.3^\circ$ . The inter-operator variability was mainly associated with the quality of the segmented images, i.e. low resolution, bias field or noise in the MRI, and to the complexity of segmenting bone tissue in young subjects, where cortical bone is not completely ossified (Evans, 2010). Nonetheless, this error was still acceptable when compared to other possible sources of variability coming from the experimental errors, such as instrumental error and marker placement error (up to  $6^\circ \pm 2^\circ$  at the toe off (Di Marco et al., 2016)), or soft tissue artefact (up to 20% of variability in the ankle kinematics (Lamberto et al., 2017)), confirming the chosen morphological fitting approach is suitable in the presence of low quality images and/or poor bone reconstructions.

An *in vivo* validation of the proposed technique was not possible within the framework of this project due to ethics constraint in the use of approaches like dual-fluoroscopy in a paediatric population. However, the comparison with *ex vivo* (Isman and Inman, 1969; Inman, 1976), and *in vivo* (Van den Bogert et al., 1994) data certainly support the validity of the technique. Previous studies (Leitch et al., 2010; Van den Bogert et al., 1994) reported the highest between-subject variabilities in the deviation angle (up to  $15^\circ$ ); conversely, we found the biggest differences in the inclination of the subtalar axis ( $14^\circ$ ). This could be ascribed to the subtalar axis' definition relying on the identification of the anterior facet of the talus. In the youngest children, in fact, this surface can present a layer of unossified cartilage (Evans et al., 2010), which can complicate the identification of the bone contour in the MRI, consequently affecting the results of segmentation and morphological fitting.

The second goal of the study involved the application of the modelling approach as part of the clinical gait assessment of patients with JIA. The between-session repeatability showed no statistically significant difference between the measures of *Inter-Axis* at M0 and M12, confirming our hypothesis.

The observed joint kinematics reflected the heterogeneous and patient-specific nature of the pathology, which presents several sub-types, each with a specific progression (Ravelli and Martini, 2007). In fact, the individual differences (Fig. 4) were not representative of a group behaviour (Fig. 6) as a consequence of different possible evolutions of the disease. The absence of a recognisable group pattern was demonstrated by the lack of a direct relationship between a joint's clinical impairment and its kinematics.

**Table 3**  
Inclination and deviation of tibiotalar and subtalar joint axes and comparison with published literature datasets (n = number of subjects).

Angle	Isman and Inman (1969) (n = 46) mean ( $\pm SD$ ) [°]	Inman (1976) (n = 104) mean ( $\pm SD$ ) [°]	Van den Bogert et al. (1994) (n = 14) mean ( $\pm SD$ ) [°]	This study (n = 38) mean ( $\pm SD$ ) [°]
Gender	NA	NA	males	30 females/8 males
Age	Adults (age not specified)	Adults (age not specified)	Adults (age not specified)	$11.2 \pm 3.1$ years
TibIncl	$80(\pm 4)$	$82.7(\pm 3.7)$ (n = 107)	$85.4(\pm 7.4)$	$90.7(\pm 4.1)$
TibDev	$84(\pm 7)$	–	$89.0(\pm 15.1)$	$82.7(\pm 7.4)$
SubIncl	$41(\pm 9)$	$42(\pm 9)$	$35.3(\pm 4.8)$	$41.1(\pm 14.1)$
SubDev	$23(\pm 11)$	$23(\pm 11)$	$18.0(\pm 16.2)$	$27.0(\pm 9.0)$

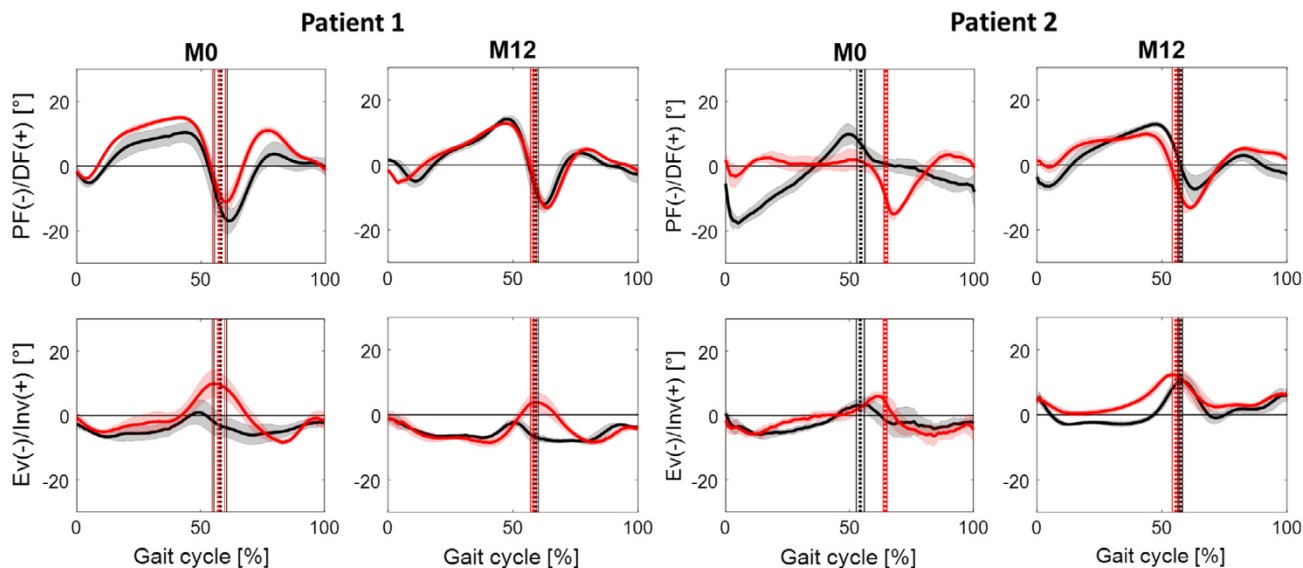


**Fig. 4.** Tibiotalar (PF/DF) and subtalar (Ev/Inv) joints kinematics for two JIA patients at M0 and M12. Average right (left) kinematics is shown with black (red) solid line with shadow representing  $\pm 1$  standard deviation. Toe off is shown with dotted vertical lines  $\pm 1$  standard deviation (solid vertical lines). Walking speed changed from  $1.51 \pm 0.05$  m/s at M0 to  $1.22 \pm 0.05$  m/s at M12 for patient 1 and from  $0.83 \pm 0.03$  m/s at M0 and  $1.20 \pm 0.04$  m/s at M12 for patient 2. (For interpretation of the references to colour in this figure legend, the reader is referred to the web version of this article.)

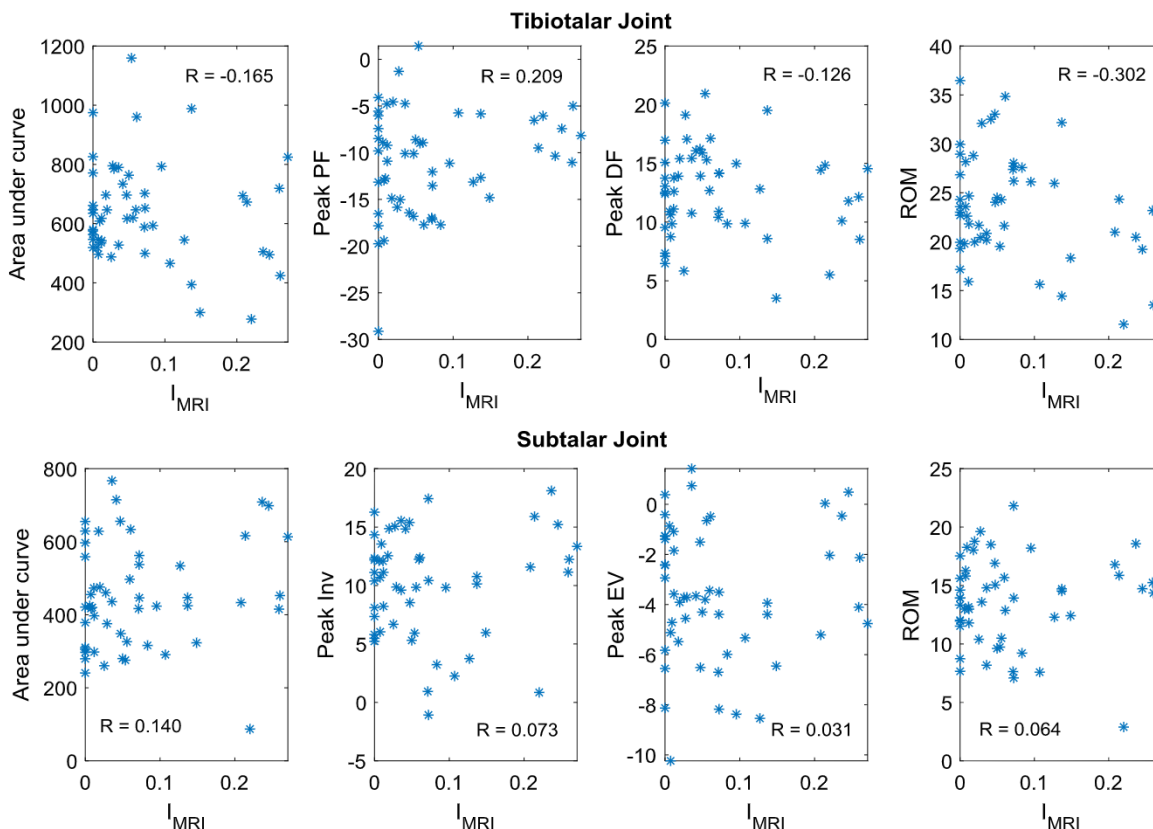


**Fig. 5.** Correlation between joint impairment level ( $I_{MRI}$ ) and joint kinematics parameters (area under the curve, peak of plantarflexion (Peak PF) and dorsiflexion (Peak DF), peak of Inversion (Peak Inv) and eversion (Peak Ev), ROM) for all feet and observations.

The inter-subject variability was probably exacerbated by the heterogeneity of the cohort in terms of age, anthropometry, disease subtype and activity level. This explains the lack of correlation between joint kinematics (and their changes between time points) and the patient's  $I_{MRI}$  scores. This also held true for the walking speed, which was not correlated with the MRI scores, but was found in line with the  $1.17 \pm 0.02$  m/s reported by [Esbjörnsson](#)

[et al. \(2015\)](#) for a group of JIA children with similar ankle involvement. If group stratification needs to be pursued, then further investigation should aim at involving larger subgroups for every sub-type of JIA and matching them by age and size.

The analysis of the between-limb asymmetry at the two time-points showed similar trends in the distribution of  $\Delta I_{MRI}$  and in the observed kinematics indices, despite none of the latter was

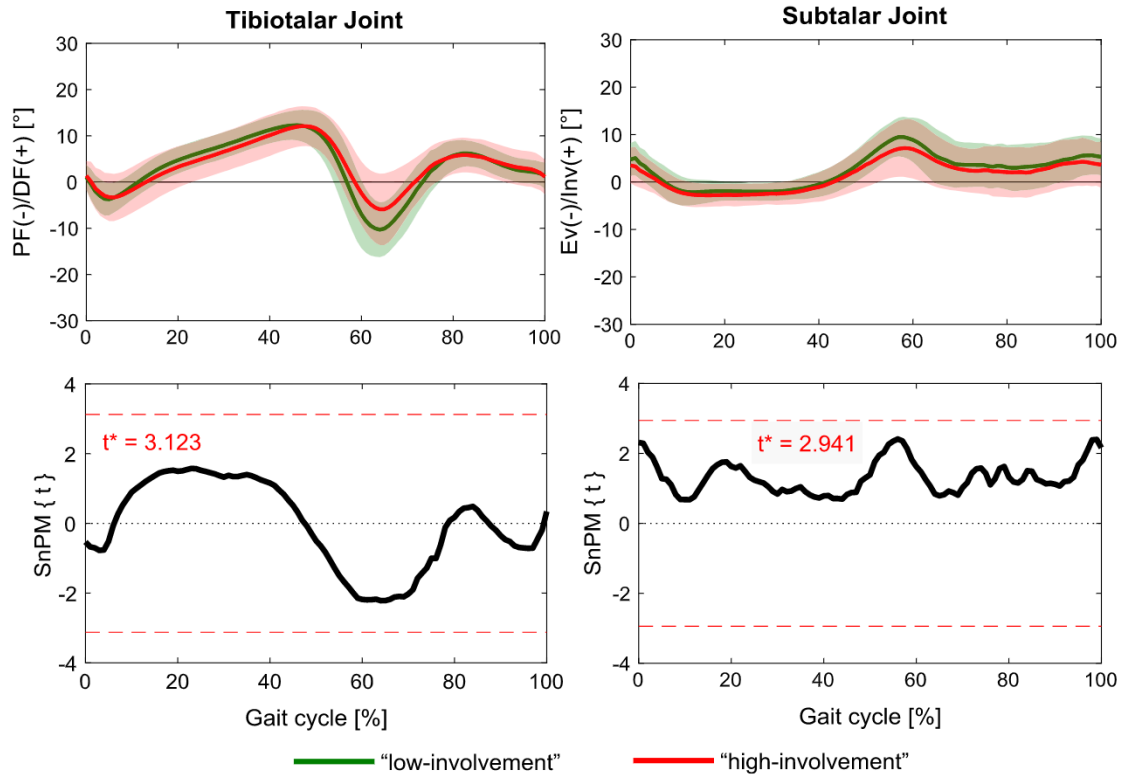


**Fig. 6.** Tibiotalar (PF/DF) and subtalar (Ev/Inv) joint kinematics of the 13 subjects as calculated at the “low-involvement” (green) and “high-involvement” (red) time-point. Solid lines in the left graphs represent mean values and bands represent  $\pm 1$  standard deviation. The right figures show the corresponding distribution of  $t$ -values (SnPM{ $t$ }) throughout the gait cycle as obtained from the non-parametric 1D paired  $t$ -test (Nichols and Holmes, 2002), calculated using the SPM1D package (Pataky et al., 2012). Each group includes 24 mono-lateral models (2 models were excluded from the analysis). (For interpretation of the references to colour in this figure legend, the reader is referred to the web version of this article.)

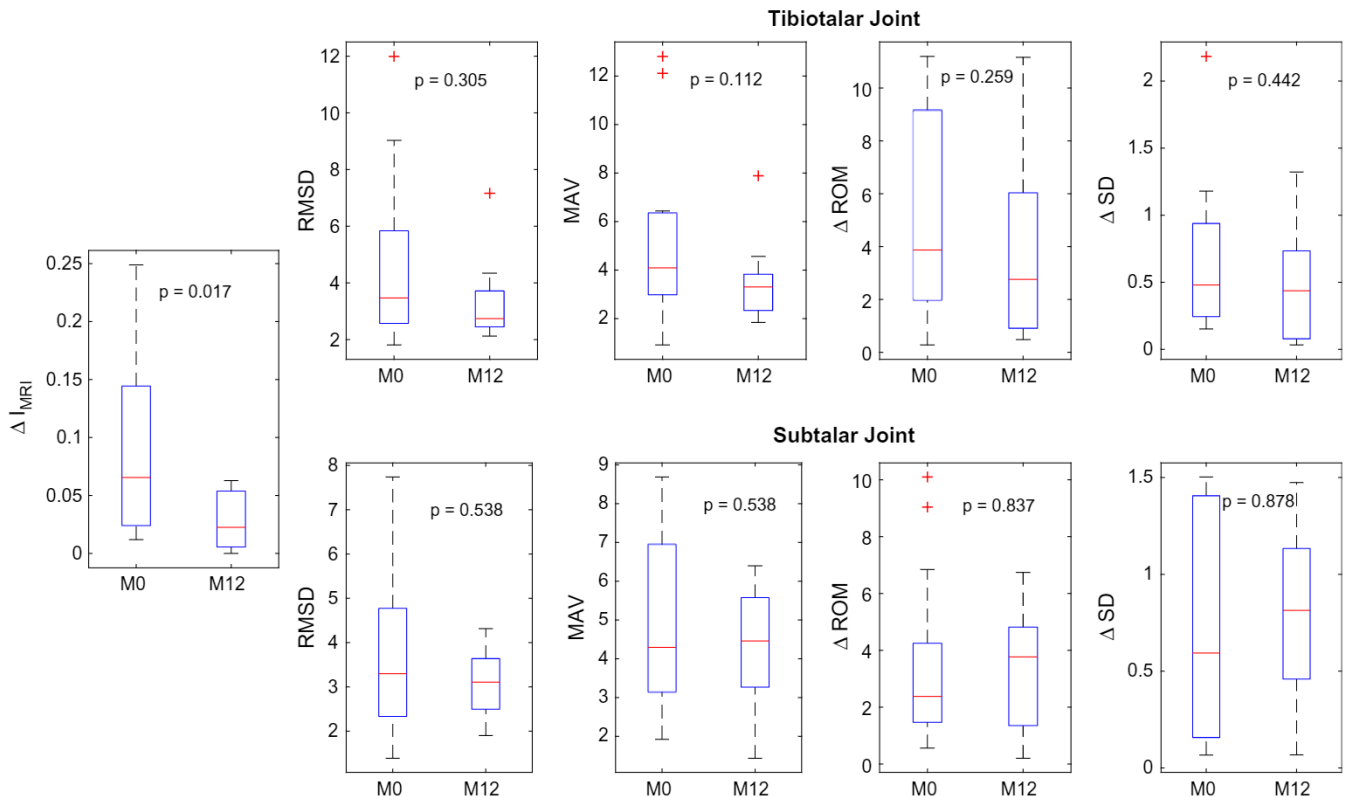


**Fig. 7.** Boxplot distribution of  $\Delta I_{MRI}$  and kinematics indices (RMSD, MAV,  $\Delta ROM$  and  $\Delta SD$ ) for both tibiotalar and subtalar joints ( $n = 13$ ) at M0 and M12.  $p$ -values from two-sided Wilcoxon signed-rank test are reported in each plot. Data outliers are marked with +.

significantly different between the two time-points. In the tibiotalar articulation, lower  $\Delta I_{MRI}$  at M12 corresponded to smaller RMSD and MAV, confirming the asymmetry in the clinical involvement of the ankles is reflected by an asymmetry in the biomechanics of gait. The subtalar kinematics was in general less informative and this is probably associated to a smaller ROM of this joint when compared to the tibiotalar joint, potentially resulting in smaller sensitivity to kinematics changes. Furthermore, disease-related alterations in the movement are likely to be compensated by the tibiotalar joint being dominant in the ankle kinematics (Lundberg et al., 1989) and therefore limiting the role of the subtalar joint. The lack of an independent clinical assessment of the two joints must be considered as a limitation in the study. In fact, the present work is based on the assumption that the  $I_{MRI}$  score, evaluating the overall condition of the ankle joint, is representative of both tibiotalar and subtalar impairment level. Nonetheless, a different level of involvement of the two joints could justify their different biomechanical response. Lastly, the assumption made in schematising the joints as hinge-like mechanisms represents a substantial simplification of the true articulating surfaces, potentially limiting the representation of their true 3D motion. However, the tibiotalar kinematics was only marginally affected by this modelling choice, as this movement mainly occurs in the sagittal plane (Roach et al., 2016). On the contrary, the subtalar joint might benefit from a more detailed representation and further studies are needed to investigate this aspect.

In conclusion, this study showed the feasibility of using morphological fitting of MRI-based bone segmentation to identify the tibiotalar and subtalar joint axes in a non-invasive patient-specific manner. Including these joints in a musculoskeletal model of the lower limb, coupled with an appropriate marker set, can give a better understanding of their individual contribution to the ankle biomechanics. This supports the adoption of the proposed modelling procedure into the practice of lower limb musculoskeletal modelling for the quantification of ankle biomechanics. The application to a pathological population, children with JIA, unveiled for the first time the absence of correlation between ankle impairment and biomechanical function, confirming the heterogeneous and systemic nature of this disease.

### Conflict of interest

The authors declare they do not have any financial or personal relationships with other people or organizations that could have inappropriately influenced this study.

### Acknowledgments

The authors want to acknowledge Dr. Norman Powell for the writing assistance. This research was supported by the European Commission (MD-PAEDIGREE project, FP7-ICT Programme, Project ID: 600932), by the UK EPSRC (Multisim project, Grant number: EP/K03877X/1) and by the NIHR Sheffield Biomedical Research Centre (BRC). The views expressed are those of the author(s) and not necessarily those of the NHS, the NIHR or the Department of Health and Social Care (DHSC).

### References

Arndt, A., Westblad, P., Winson, I., Hashimoto, T., Lundberg, A., 2004. Ankle and subtalar kinematics measured with intracortical pins during the stance phase of walking. *Foot Ankle Int.* 25, 357–364.

Arndt, A., Wolf, P., Nester, C., Liu, A., Jones, R., Howard, D., Stacoff, A., Lundgren, P., Lundberg, A., 2006. Intrinsic foot motion measured in vivo during barefoot running. *J. Biomech.* 39, S182.

Baker, R., 2003. Letter to the editor: ISB recommendation on definition of joint coordinate systems for the reporting of human joint motion—part I: ankle, hip and spine. *J. Biomech.* 36 (2), 300–302.

Bartlett, R., 2007. Introduction to sports biomechanics: analysing human movement patterns. Routledge, Abingdon, England.

Barnett, G.H., Napier, J.R., 1952. The axis of rotation at the ankle joint in man. Its influence upon the form of the talus and the mobility of the fibula. *J. Anat. Lond.* 86, 1–9.

Cignoni, P., Callieri, M., Corsini, M., Dellepiane, M., Ganovelli, F., Ranzuglia, G., 2008. Meshlab: an open-source mesh processing tool. Eurographics Italian Chapter Conference.

Correa, T.A., Pandy, M.G., 2011. A mass-length scaling law for modelling muscle strength in the lower limb. *J. Biomech.* 44 (16), 2782–2789.

Delp, S.L., Loan, J.P., Hoy, M.G., Zajac, F.E., Topp, E.L., Rosen, J.M., 1990. An interactive graphics-based model of the lower extremity to study orthopaedic surgical procedures. *IEEE Trans. Biomed. Eng.* 37, 757–767.

Delp, S.L., Anderson, F.C., Arnold, A.S., Loan, P., Habib, A., John, C.T., Guendelman, E., Thelen, D.G., 2007. OpenSim: open-source software to create and analyze dynamic simulations of movement. *IEEE Trans. Biomed. Eng.* 54, 1940–1950.

Dettwyler, M., Stacoff, A., Kramers-de Quervain, I.A., Stüssia, E., 2004. Modelling of the ankle joint complex. Reflections with regards to ankle prostheses. *Foot Ankle Surg.* 10, 109–119.

Di Marco, R., Rossi, S., Racic, V., Cappa, P., Mazzà, C., 2016. Concurrent repeatability and reproducibility analyses of four marker placement protocols for the foot-ankle complex. *J. Biomech.* 49, 3168–3176.

Di Marco, R., Scalona, E., Pacilli, A., Cappa, P., Mazzà, C., Rossi, S., 2018. How to choose and interpret similarity indices to quantify the variability in gait joint kinematics. *Int. Biomech.* 5 (1), 1–8.

Dul, J., Johnson, G.E., 1985. A kinematic model of the ankle joint. *J. Biomed. Eng.* 7, 137–143.

Durkin, J.L., Dowling, J.J., 2006. Body segment parameter estimation of the human lower leg using an elliptical model with validation from DEXA. *Ann. Biomed. Eng.* 34, 1483–1493.

Evans, A., 2010. Paediatrics. The Pocket Podiatry Guide. Churchill Livingstone Elsevier.

Esbjörnsson, A.C., Iversen, M.D., André, M., Hageberg, S., Schwartz, M.H., Broström, E.W., 2015. Effect of intraarticular corticosteroid foot injections on walking function in children with juvenile idiopathic arthritis. *Arthritis Care Res.* 67 (12), 1693–1701.

Fick, R., 1911. Handbuch der Anatomie und Mechanik der Gelenke: III, Spezielle Gelenk- und Muskelmechanik. Gustav Fischer Verlag, Jena.

Hannah, I., Montefiori, E., Modenese, L., Prinold, J., Viceconti, M., Mazzà, C., 2017. Sensitivity of a juvenile subject-specific musculoskeletal model of the ankle joint to the variability of operator-dependent input. *Proc. Inst. Mech. Eng. [H]* 231, 415–422.

Hicks, J.H., 1953. The mechanics of the foot: the joints. *J. Anat.* 87, 345–357.

Hicks, J., Uchida, T., Seth, A., Rajagopal, A., Delp, S.L., 2015. Is my model good enough? Best practices for verification and validation of musculoskeletal models and simulations of human movement. *J. Biomech. Eng.* 137 (2), 020905.

Inman, V.T., 1976. The Joints of the Ankle. Williams and Wilkins, Baltimore.

Isman, R.E., Inman, V.T., 1969. Anthropometric studies of the human foot and ankle. *Bullet. Prosthet. Res.* 10 (11), 97–129.

Lamberto, G., Martelli, S., Cappozzo, A., Mazzà, C., 2017. To what extent is joint and muscle mechanics predicted by musculoskeletal models sensitive to soft tissue artefacts. *J. Biomech.* 62, 68–76.

Leitch, J., Stebbins, J., Zavatsky, A.B., 2010. Subject-specific axes of the ankle joint complex. *J. Biomech.* 43, 2923–2928.

Lewis, G.S., Cohen, T.L., Seisler, A.R., Kirby, K.A., Sheehan, F.T., Piazza, S.J., 2009. In vivo tests of an improved method for functional location of the subtalar joint axis. *J. Biomech.* 42, 146–151.

Lundberg, A., 1989. Kinematics of the ankle and foot: in vivo roentgen stereophotogrammetry. Ph.D. Thesis, Department of Orthopaedics, Karolinska Hospital, Stockholm, Sweden. *Acta Orthopaedica Scandinavica* 60 (Suppl), 233.

Manter, J.T., 1941. Movements of the subtalar and transverse tarsal joints. *Anatomic. Record* 80, 397.

Malaquias, T.M., Silveira, C., Aerts, W., De Groot, F., Dereymaeker, G., Vander Sloten, J., Jonkers, I., 2017. Extended foot-ankle musculoskeletal models for application in movement analysis. *Comput. Methods Biomed. Biomed. Eng.* 20 (2), 153–159.

Malattia, C., Damasio, M.B., Pistorio, A., Ioseliani, M., Vilca, I., Valle, M., Ruperto, N., Viola, S., Buoncompagni, A., Magnano, G.M., Ravelli, A., Tomà, P., Martini, A., 2011. Development and preliminary validation of a paediatric-targeted MRI scoring system for the assessment of disease activity and damage in juvenile idiopathic arthritis. *Ann. Rheum. Dis.* 70, 440–446.

Mattingly, B., Talwalkar, V., Tylkowski, C., Stevens, D.B., Hardy, P.A., Pienkowski, D., 2006. Three-dimensional in vivo motion of adult hind foot bones. *J. Biomech.* 39 (4), 726–733.

Modenese, L., Montefiori, E., Wang, A., Wesarg, S., Viceconti, M., Mazzà, C., 2018. Investigation of the dependence of joint contact forces on musculotendon parameters using a codified workflow for image-based modelling. *J. Biomech.* 73, 108–118.

Nichols, T.E., Holmes, A.P., 2002. Nonparametric permutation tests for functional neuroimaging: a primer with examples. *Hum. Brain Mapp.* 15 (1), 1–25.

Nusman, C.M., Ording Muller, L.S., Hemke, R., Doria, A.S., Avenarius, D., Tzaribachev, N., et al., 2016. Current status of efforts on standardizing magnetic resonance imaging of Juvenile idiopathic arthritis: Report from the OMERACT MRI in JIA Working Group and Health-e-Child. *J. Rheumatol.* 43, 239–244.

Ostergaard, M., Peterfy, C., Conaghan, P., McQueen, F., Bird, P., Ejbjerg, B., et al., 2003. OMERACT rheumatoid arthritis magnetic resonance imaging studies. Core set of

- MRI acquisitions, joint pathology definitions, and the OMERACT RA-MRI scoring system. *J. Rheumatol.* 30, 1385–1386.
- Parr, W.C.H., Chatterjee, H.J., Soligo, C., 2012. Calculating the axes of rotation for the subtalar and talocrural joint using 3D bone reconstructions. *J. Biomech.* 45, 1103–1107.
- Pataky, T.C., 2012. One-dimensional statistical parametric mapping in Python. *Comput. Methods Biomech. Biomed. Eng.* 15, 295–301.
- Prinold, J.L., Mazzà, C., Di Marco, R., Hannah, I., Malattia, C., Magni-Manzoni, S., Petrarca, M., Ronchetti, A., Tanturri de Horatio, L., van Dijkhuizen, E.H.P., Wesarg, S., Viceconti, M., 2016. A patient-specific foot model for the estimate of ankle joint forces in patients with juvenile idiopathic arthritis. *Ann. Biomed. Eng.* 44, 247–257.
- Rasmussen, O., Tovborg-Jensen, I., 1982. Mobility of the ankle joint: recording of rotator movements in the talocrural joint in vitro with and without the lateral collateral ligaments of the ankle. *Acta Orthop. Scand.* 53, 155–160.
- Ravelli, A., Martini, A., 2007. Juvenile idiopathic arthritis. *Lancet* 369 (9563), 767–778.
- Roas, A., Anderson, G.B., 1982. Normal range of motion of the hip, knee and ankle joints in male subjects, 30–40 years of age. *Acta Orthop. Scand.* 53 (2), 205–208.
- Roach, K.E., Wang, B., Kapron, A.L., Fiorentino, N.M., Saltzman, C.L., Foreman, K.B., Anderson, A.E. In, 2016. Vivo kinematics of the tibiotalar and subtalar joints in asymptomatic subjects: a high-speed dual fluoroscopy study. *ASME J. Biomech. Eng.* 138 (9), pp. 091006–091006-9.
- Saraswat, P., Andersen, M.S., MacWilliams, B.A., 2010. A musculoskeletal foot model for clinical gait analysis. *J. Biomech.* 43 (9), 1645–1652.
- Scheys, L., Loeckx, D., Spaepen, A., Suetens, P., Jonkers, I., 2009. Atlas-based non-rigid image registration to automatically define line-of-action muscle models: a validation study. *J. Biomech.* 42, 565–572.
- Scott, S.H., Winter, D.A., 1991. Talocrural and talocalcaneal joint kinematics and kinetics during the stance phase of walking. *J. Biomech.* 24, 743–752.
- Sepic, S.B., Murray, M.P., Mollinger, L.A., Spurr, G.B., Gardner, G.M., 1986. Strength and range of motion in the ankle in two age groups of men and women. *Am. J. Phys. Med.* 65, 75–84.
- Siegler, S., Chen, J., Schneck, C.D., 1988. The three-dimensional kinematics and flexibility characteristics of the human ankle and subtalar joints. Part 1: kinematics. *J. Biomech. Eng.* 110, 364–373.
- Siegler, S., Toy, J., Seale, D., Pedowitz, D., 2014. The clinical biomechanics award 2013 – presented by the international society of biomechanics: new observations on the morphology of the talar dome and its relationship to ankle kinematics. *Clin. Biomech.* 29 (1), 1–6.
- Stebbins, J., Harrington, M., Thompson, N., Zavatsky, A., Theologis, T., 2006. Repeatability of a model for measuring multi-segment foot kinematics in children. *Gait & Posture* 23, 401–410.
- Steger, S., Kirschner, M., Wesarg, S., 2012. Articulated atlas for segmentation of the skeleton from head & neck CT datasets. In: 9th IEEE International Symposium on Biomedical Imaging (ISBI), Barcelona, Spain.
- Valente, G., Crimi, G., Vanella, N., Schileo, E., Taddei, F., 2017. nmsBuilder: Freeware to create subject-specific musculoskeletal models for OpenSim. *Comput. Methods Programs Biomed.* 152, 85–92.
- van den Bogert, A.J., Smith, G.D., Nigg, B.M., 1994. In vivo determination of the anatomical axes of the ankle joint complex: an optimization approach. *J. Biomech.* 27, 1477–1488.
- van Langelaan, E.J., 1983. A kinematical analysis of the tarsal joints. An X-ray photogram-metric study. Ph.D. Thesis. *Acta Orthopaedica Scandinavia* 54 (Suppl), 204.
- Vicon Motion Systems, L., 2012. Biomechanical Research, 2012. [http://www.irc-web.co.jp/vicon\\_web/news\\_bn/PIGManualver1.pdf](http://www.irc-web.co.jp/vicon_web/news_bn/PIGManualver1.pdf).
- Westblad, P., Hashimoto, T., Winson, I., Lundberg, A., Arndt, A., 2002. Differences in ankle-joint complex motion during the stance phase of walking as measured by superficial and bone-anchored markers. *Foot Ankle Int.* 23 (9), 856–863.
- Woltring, H.J., 1986. A FORTAN package for generalized cross-validated spline smoothing and differentiation. *Adv. Eng. Softw.* 8 (2), 104–113.

**4. Sensitivity of a juvenile subject-specific musculoskeletal model of the ankle joint to the variability of operator dependent input**

### *Acknowledgement of co-authorship*

This chapter includes the published paper “Sensitivity of a juvenile subject-specific musculoskeletal model of the ankle joint to the variability of operator dependent input” produced as the results of the research carried out in collaboration with the co-authors listed in the paper.

My personal contribution was in designing the study, implementing the models, quantifying the intra- and inter-operator variability in the input parameters used to build the same models, and finally identifying the modelling steps being more sensitive to operator error.

Student:

Erica Montefiori		Date	26/07/2019
------------------	---	------	------------

The main co-authors:

Iain Hannah		Date	25/07/2019
-------------	---	------	------------

Claudia Mazza'		Date	26/07/2019
----------------	---	------	------------

Luca Modenese		Date	27/07/2019
---------------	---	------	------------

# Sensitivity of a juvenile subject-specific musculoskeletal model of the ankle joint to the variability of operator-dependent input

Iain Hannah<sup>1,2</sup>, Erica Montefiori<sup>1,2</sup>, Luca Modenese<sup>1,2</sup>, Joe Prinold<sup>1,2</sup>, Marco Viceconti<sup>1,2</sup> and Claudia Mazzà<sup>1,2</sup>

Proc IMechE Part H:  
J Engineering in Medicine  
2017, Vol. 231(5) 415–422  
© IMechE 2017



Reprints and permissions:

sagepub.co.uk/journalsPermissions.nav

DOI: 10.1177/0954411917701167

journals.sagepub.com/home/pih



## Abstract

Subject-specific musculoskeletal modelling is especially useful in the study of juvenile and pathological subjects. However, such methodologies typically require a human operator to identify key landmarks from medical imaging data and are thus affected by unavoidable variability in the parameters defined and subsequent model predictions. The aim of this study was to thus quantify the inter- and intra-operator repeatability of a subject-specific modelling methodology developed for the analysis of subjects with juvenile idiopathic arthritis. Three operators each created subject-specific musculoskeletal foot and ankle models via palpation of bony landmarks, adjustment of geometrical muscle points and definition of joint coordinate systems. These models were then fused to a generic Arnold lower limb model for each of three modelled patients. The repeatability of each modelling operation was found to be comparable to those previously reported for the modelling of healthy, adult subjects. However, the inter-operator repeatability of muscle point definition was significantly greater than intra-operator repeatability ( $p < 0.05$ ) and predicted ankle joint contact forces ranged by up to 24% and 10% of the peak force for the inter- and intra-operator analyses, respectively. Similarly, the maximum inter- and intra-operator variations in muscle force output were 64% and 23% of peak force, respectively. Our results suggest that subject-specific modelling is operator dependent at the foot and ankle, with the definition of muscle geometry the most significant source of output uncertainty. The development of automated procedures to prevent the misplacement of crucial muscle points should therefore be considered a particular priority for those developing subject-specific models.

## Keywords

Repeatability, gait, biomechanics, juvenile idiopathic arthritis, foot, OpenSim, NMSBuilder, magnetic resonance imaging

Date received: 3 June 2016; accepted: 21 February 2017

## Introduction

The use of musculoskeletal models to determine the muscle and joint contact forces (JCFs) during gait has long been reported.<sup>1</sup> The sensitivity of model outputs to experimental errors such as misplacement of stereophotogrammetric markers and soft tissue artefact has been explored through probabilistic analysis.<sup>2–4</sup> Similarly, there is a significant body of evidence demonstrating model sensitivity to the defined musculoskeletal anatomy with the joint coordinate systems, inertial parameters, muscle properties and muscle path geometries all investigated.<sup>5–8</sup> However, the error involved in accurately identifying these anatomical properties from experimental data is less well understood. Due to variability in patient anatomy, concerns have been raised

about the accuracy of outputs obtained with scaled, generic models.<sup>9</sup> This is particularly the case when applying such methods to juvenile or pathological subjects, whose anatomy may differ significantly from the cadavers upon which the generic models are based.<sup>10,11</sup>

Driven by the need for more accurate model predictions and facilitated by advances in medical imaging

<sup>1</sup>INSIGNEO Institute for *in silico* Medicine, University of Sheffield, Sheffield, UK

<sup>2</sup>Department of Mechanical Engineering, University of Sheffield, Sheffield, UK

### Corresponding author:

Claudia Mazzà, INSIGNEO Institute for *in silico* Medicine, University of Sheffield, Western Bank, Sheffield S10 2TN, South Yorkshire, UK.

Email: c.mazza@sheffield.ac.uk

technology, subject-specific modelling techniques are becoming more widely developed and adopted.<sup>12–19</sup> One such methodology<sup>20</sup> was developed for the study of subjects with juvenile idiopathic arthritis (JIA), an autoimmune disease which can cause physical function disabilities as a result of chronic inflammation of the synovial joint membrane. The aetiology of the disease remains unknown but it has been speculated that altered knee and ankle joint loading<sup>21</sup> may influence disease progression<sup>22</sup> and is thus a pathology that particularly warrants investigation with subject-specific musculoskeletal models.

As part of such methodologies, analysis of clinical imaging data allows, among other things, subject-specific muscle paths and joint coordinate systems to be identified and defined.<sup>4</sup> Despite efforts to automate these procedures,<sup>23,24</sup> this is typically conducted by a human operator and is thus liable to unavoidable inter- and intra-operator variability in the parameters defined.

To justify the time required for an operator to analyse subject medical images and manually modify a model parameter, two criteria should be met: first, that the model outputs are sensitive to its value, and second, that it can be repeatably and reliably identified. As such, several studies have aimed to quantify the variability and sensitivity of the parameters typically defined as part of a subject-specific modelling approach.<sup>25–27</sup>

Martelli et al.<sup>28</sup> reported the variation in predicted JCFs and muscle forces after altering lower limb joint coordinate systems in line with the inter- and intra-operator distributions. These distributions were determined from those recorded by five operators, each analysing computed tomography (CT) images of a subject. They found the largest impact of operator input on JCFs to be at the ankle, with a maximum change of 0.33 times bodyweight (BW) reported. However, muscle forces were found to vary more significantly, by up to 114% of their median value. Valente et al.<sup>4</sup> perturbed bony landmark locations, muscle path points and maximum muscle tensions via a Monte Carlo analysis and found them to have a greater impact on the ankle JCFs, with relevant values ranging by up to 1.58 BW, and on muscle forces, which varied by up to 1.58 BW. Such studies are extremely useful, allowing those developing musculoskeletal modelling approaches to identify the subset of critical parameters that are worth varying on a subject-specific basis.

However, the subject-specific models created as part of both of these studies were of healthy adult subjects. Conversely, little research has been done into the repeatability and sensitivity of such modelling methodologies when applied to juvenile or pathological subjects. As such, the aim of the following study was to investigate the inter- and intra-operator repeatability of a subject-specific modelling methodology developed for children with JIA. The sensitivity of the estimated ankle JCFs and muscle forces to the operator-dependent

variation in defined muscle geometries and joint coordinate systems was also investigated.

## Methods

### Subjects and data acquisition

The data collection was carried out by specialised clinical centres as part of the MD-Paedigree project (EC 7th FP, ICT Program, CN: 600932). Three female subjects with JIA were selected to take part in the study with written informed consent obtained from all subjects and/or their parents. Subject data, including the number of affected joints, a Child Health Assessment Questionnaire score (CHAQ)<sup>29</sup> and a composite disease activity score (JADAS-71),<sup>30</sup> are shown in Table 1. Gait analysis was based on the PlugIn Gait<sup>31</sup> and modified Oxford Foot Model (mOFM)<sup>32</sup> marker protocols (for detailed procedures, see Prinold et al.<sup>20</sup>) with three gait trials performed by each subject randomly selected for inclusion in this study.

Two sequences of magnetic resonance imaging (MRI) scans of the foot and distal tibia were obtained for each subject. The first sequence was a multi-slice, multi-echo 3D Gradient Echo (mFFE) scan in the sagittal plane with a 1 mm slice thickness and 0.5 mm in-plane resolution. The second sequence was a 3D short T1 inversion time inversion recovery fast field echo scan, again in the sagittal plane. The slice thickness was 2 mm with a 0.6 mm in-plane resolution. Subject bony geometries were segmented from the first MRI sequence by a single operator while the data from the second sequence was used to define subject-specific muscle paths.

### Musculoskeletal modelling approach

A generic unilateral lower limb model of each subject was created by scaling the geometry of the Arnold model<sup>33</sup> with the tools available in OpenSim.<sup>34</sup> The generic foot was subsequently replaced with a subject-specific, two-segment equivalent, fused to the generic model at the ankle joint. The process to create the

**Table 1.** Subject data.

	Subject A	Subject B	Subject C
Age (years)	9.5	12.9	15.9
Height (m)	1.37	1.53	1.45
Mass (kg)	40.6	64.2	50.0
BMI (kg/m <sup>2</sup> )	21.5	27.2	23.8
Affected joints	6	5	3
CHAQ	0	0.5	1.75
JADAS-71	13.8	–	16.4

BMI: body mass index.

CHAQ<sup>29</sup> is a measure of limitation to activities of daily living (range: 0–3; '3' being most severe). JADAS-71<sup>30</sup> is a composite disease activity score (range: 0–101; '101' being most severe).

subject-specific foot was reported in detail by Prinold et al.,<sup>20</sup> but is presented in brief here.

Once bony geometries of the foot and distal tibia have been segmented from the imaging data, the process of creating a subject-specific foot model can be broken down into four distinct phases, all of which were performed in NMSBuilder:<sup>4,35</sup>

1. *Virtual palpation of anatomical landmarks.* Key landmarks on the segmented bony geometries were identified by the operator according to Van Sint Jan.<sup>36</sup> These landmarks were divided into segment landmark clouds with the tibia, hindfoot, talus, metatarsal and forefoot segments requiring 3, 4, 4, 6 and 5 landmarks to be palpated, respectively. The 22 markers virtually palpated in this study are a subset of those reported in Prinold et al.<sup>20</sup> A full list of the markers used is available as a supplementary file accompanying this article.
2. *Registration of generic muscle atlas.* The location of the virtually palpated landmarks was subsequently used to register a generic atlas of muscle points<sup>33</sup> on to the subject-specific geometry. These served as first estimate of the subject-specific muscle paths. This process is not operator dependent.
3. *Manual adjustment of muscle paths.* All foot muscle origin, insertion and via points were adjusted by the operator to be consistent with the subject MRI data. Points captured by the MRI scan in the distal tibia were also altered resulting in a total of 74 muscle path points that had to be manually modified.
4. *Definition of joint coordinate systems.* Proximal and distal anatomical coordinate frames were defined for the ankle (tibia–hindfoot) and metatarsophalangeal (MTP) joint (hindfoot–forefoot) via palpation of bony landmarks as in Stebbins et al.<sup>32</sup> One exception was the ankle joint centre which was determined by fitting a cylinder to the talar dome with its mediolateral axis serving as the plantar/dorsi-flexion axis.<sup>20</sup>

The combined generic lower limb and subject-specific foot model had a total of five segments (pelvis, femur, tibia, hindfoot, forefoot) and 13 degrees of freedom: six at the pelvis, three at the hip, one at the knee (flexion/extension), two at the talocrural ankle joint (inversion/eversion and plantar/dorsi-flexion) and one at the hindfoot–forefoot (plantar/dorsi-flexion). A total of 54 muscle paths were defined in each model, of which 16 span the ankle joint.

### Simulation of gait trials

Muscle forces and JCFs were determined in OpenSim using a standard approach of inverse kinematics, followed by static optimisation and joint reaction analysis.<sup>34</sup> Model outputs were compared against joint angles, joint moments and muscle activation patterns

reported in the literature for level walking.<sup>37–40</sup> However, no attempts were made to validate the muscle forces obtained with the static optimisation tool against experimentally obtained electromyography measures as this was beyond the scope of the study.

Coordinate actuators were defined at the pelvis while residual actuators were employed at the hip joint only. As a two-segment foot was defined, the single ground reaction force (GRF) as recorded by the force platform had to be divided between the hindfoot and forefoot segments. This was achieved by applying the entire measured load to the hindfoot until the centre of pressure (COP) crossed the metatarsophalangeal joint, at which point the load was applied exclusively to the forefoot segment.<sup>20</sup>

### Operators

Following the methodology described above, a musculoskeletal model of each subject was created by each of three expert operators. One operator completed the full subject-specific modelling approach three times for a single subject (Subject C) such that intra-operator analyses could be performed. A minimum of 48 h was allowed to pass between each intra-operator modelling procedure.

### Statistical analysis

All operator-dependent inputs and model predictions were recorded to allow the robustness of the modelling approach to be investigated. Appropriate statistical tests were selected according to the purpose of the investigation and are detailed hereafter. The level of significance ( $p$ ) was set to be 0.05 in all analyses.

The repeatability of two modelling steps, i.e. the palpation of each virtual landmark and the definition of each muscle point location, was evaluated by calculating the standard deviation (SD) of the spatial coordinates defined for each point. For the analysis of virtually palpated landmarks, each segment landmark cloud was considered to be an independent variable. The repeatability of the definition of the joint coordinate systems was assessed by determining the variability (SD) in the Cardan rotation required to superimpose the proximal frame upon the distal frame for each joint in the model.

A one-way analysis of variance was run between the results obtained for each of the three subjects to test whether the anatomy of the patient was a significant factor in the repeatability of the methodology. This was performed at each stage of the modelling process considered (virtual palpation of anatomical landmarks, manual adjustment of muscle paths, definition of joint coordinate systems). Where no statistically significant inter-subject differences were observed, a comparison of inter- and intra-operator repeatability was also performed for one subject (Subject C) using a two-tailed, paired Student's  $t$ -test (Figure 1).

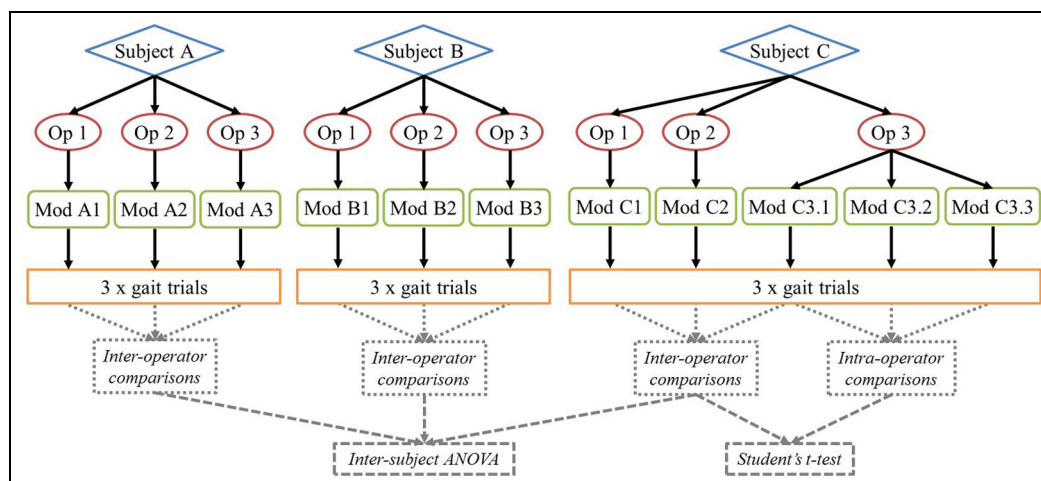


**Figure 1.** Flow chart illustrating inter- and intra-operator analysis and statistical tests employed. Subjects, operators (Op), models (Mod) and gait trials are shown. Inter- and intra-operator comparisons were performed on both model inputs and outputs.

The sensitivity of the ankle JCFs to inter- and intra-operator modelling was assessed via calculation of the variation in the mean vertical ankle JCF predicted for each subject in the ground reference frame across the three simulated gait trials. Similarly, the sensitivity of model estimated muscle forces was investigated by determining the mean of the maximum change in muscle force output at any point during each gait trial. This value was determined for each of six key muscles that cross the ankle joint: soleus, gastrocnemius medialis, gastrocnemius lateralis, tibialis posterior, tibialis anterior and peroneus longus, each of which to whom ankle JCF was shown to be most sensitive in a previous study.<sup>20</sup> Furthermore, they are also muscles spanning the ankle joint that have the largest physiological cross-sectional area. All JCFs and muscle loads were normalised to subject BW.

## Results

### Variability of model input

The maximum inter-operator SD in defined landmark location were 2.9, 2.9 and 2.7 mm for Subjects A, B and C, respectively, with mean inter-operator repeatability of all virtually palpated landmarks of  $0.90 \pm 0.60$  mm. In comparison, the maximum intra-operator SD was 2.3 mm with a mean across all landmarks of  $0.66 \pm 0.63$  mm. All statistical tests upheld the null hypothesis indicating virtual palpation is both operator and subject independent.

The inter-operator repeatability of the defined muscle point location ( $3.0 \pm 2.5$  mm) was found to be significantly lower ( $p < 0.05$ ) than intra-operator repeatability ( $1.7 \pm 1.9$  mm) for Subject C. The maximum variation in the spatial dimensions of any single muscle point was 14.3 mm (extensor hallucis brevis – via point) and 9.6 mm (flexor hallucis brevis – origin) for the inter- and intra-operator analyses, respectively.

Mean inter-subject SDs were found to be  $3.0 \pm 2.9$  mm for Subject A,  $2.7 \pm 2.3$  mm for Subject B and  $3.0 \pm 2.5$  mm for Subject C with the maximum SD of a single point being 17.0 mm (flexor hallucis brevis – origin), 12.3 mm (extensor digitorum longus – via point) and 14.3 mm (extensor hallucis brevis – via point), respectively. No significant inter-subject differences were observed. Further analysis of individual muscle points indicated that the forefoot muscle insertion points (flexors and extensors digitorum and hallucis) were the most repeatably identified while operators disagreed more about the location of via points relative to muscle origin and insertion points.

When considering the joint coordinate systems defined in the models (Figure 2), inter-operator SDs were found to range from  $1.36^\circ$  to  $3.02^\circ$  for the ankle inversion/eversion axis and from  $0.26^\circ$  to  $1.72^\circ$  for the plantar/dorsi-flexion axis. Variability at the metatarsophalangeal plantar/dorsi-flexion axis was greater,  $2.40^\circ$ – $7.04^\circ$ . The variance in the intra-operator joint coordinate systems was  $0.50^\circ$ ,  $1.15^\circ$  and  $0.88^\circ$  for the three axes, respectively. Inter- and intra-operator repeatability was not found to differ by a statistically significant margin and no inter-subject effects were observed (Table 2).

### Variability of model predictions

Figure 3 shows the inter-operator variation in the vertical mean ankle JCF calculated for each subject across the three modelled gait trials. The maximum ranges observed were 1.50 BW, 0.75 BW and 0.73 BW for Subjects A, B and C, respectively. The maximum intra-operator range was found to be smaller again, 0.28 BW for Subject C.

The average of the maximum inter-operator changes in vertical ankle JCF observed at any point during a gait trial was  $1.55 \pm 0.36$  BW for Subject A (20% of peak JCF),  $0.77 \pm 0.31$  BW for Subject B (16% of peak

**Table 2.** Inter- and intra-operator SD (°) in joint angle definitions.

Joint	Inter-operator						Intra-operator	
	Subject A		Subject B		Subject C		Subject C	
	Inv/Ev	PF/DF	Inv/Ev	PF/DF	Inv/Ev	PF/DF	Inv/Ev	PF/DF
	SD (°)	SD (°)	SD (°)	SD (°)	SD (°)	SD (°)	SD (°)	SD (°)
Ankle	1.36	1.64	3.02	1.72	1.36	0.26	0.50	1.15
MTP	–	2.40	–	7.04	–	3.37	–	0.88

SD: standard deviation; MTP: metatarsophalangeal. Inversion/eversion (Inv/Ev) and plantar/dorsi-flexion (PF/DF) axes are shown.

**Table 3.** Maximum difference (Max diff) in estimated muscle force.

Muscle	Inter-operator			Intra-operator
	Subject A	Subject B	Subject C	Subject C
	Max diff (BW)	Max diff (BW)	Max diff (BW)	Max diff (BW)
Soleus	1.25 ± 0.09	0.38 ± 0.23	0.85 ± 0.10	0.41 ± 0.02
Gastrocnemius medialis	1.03 ± 0.34	0.47 ± 0.35	0.76 ± 0.06	0.30 ± 0.02
Gastrocnemius lateralis	0.90 ± 0.51	0.31 ± 0.14	0.06 ± 0.00	0.01 ± 0.01
Tibialis posterior	0.98 ± 0.41	0.26 ± 0.08	0.54 ± 0.04	0.01 ± 0.03
Tibialis anterior	1.46 ± 0.29	0.25 ± 0.08	0.19 ± 0.02	0.17 ± 0.02
Peroneus longus	1.03 ± 0.34	0.40 ± 0.25	0.22 ± 0.01	0.08 ± 0.03

BW: bodyweight; SD: standard deviation. Mean ± SD across three gait trials is shown.

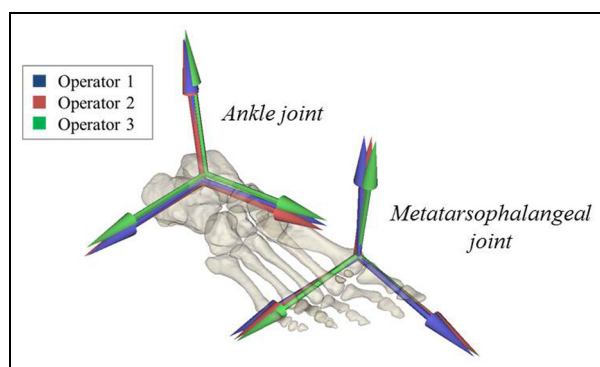
JCF) and  $0.75 \pm 0.02$  BW for Subject C (12% of peak JCF) with the maximum recorded in any individual trial of 1.86 BW (Subject A – 24% of peak JCF). The equivalent intra-operator value was smaller,  $0.33 \pm 0.15$  BW (6% of peak JCF), with a single trial maximum of 0.55 BW (10% of peak JCF).

Table 3 shows the average of the maximum difference in estimated muscle force output for six key muscles at any frame in the gait cycle. The muscles with the greatest inter- and intra-operator variation were the soleus, gastrocnemius medialis and tibialis anterior with the differences observed in Subject A consistently larger than with the other two models. The maximum inter-operator difference observed in any one trial was 1.94 BW for Subject A (tibialis anterior – 64% of peak

force), 0.96 BW for Subject B (gastrocnemius medialis – 73% of peak force) and 0.94 BW for Subject C (soleus – 40% of peak force). The maximum change output for a muscle force in the intra-operator analysis was 0.44 BW in the soleus (23% of peak force).

**Discussion**

In this study, subject-specific models of three pathological subjects were created such that the inter- and intra-operator uncertainty in model parameter definition could be estimated and the sensitivity of the ankle JCFs and muscle forces output with the models evaluated.



**Figure 2.** Distal segment anatomical coordinate frames defined by each operator. Ankle and metatarsophalangeal joints (Subject C).

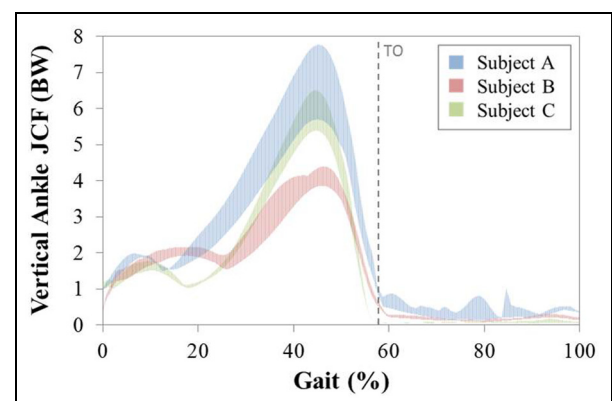


**Figure 3.** Range of inter-operator mean vertical ankle joint contact forces (BW) obtained across three gait trials in the ground reference frame. Dotted line represents average occurrence of toe-off (TO).

The virtual palpation of bony landmarks was found to be a repeatable operation, both intra- and inter-operator with the mean inter- and intra-operator variation in the defined spatial dimensions of 0.90 and 0.62 mm, respectively. This compares favourably with the value of 1.11 mm reported in a previous experimental study in which five individual operators each palpated subject MRI imagery three times.<sup>4</sup> However, separate inter- and intra-operator repeatability data were not reported, as here.

The definition of subject-specific muscle paths was found to be subject independent but not operator independent. This is crucial as errors in locating muscular attachments are the largest source of inconsistency in musculoskeletal output.<sup>4,20,23</sup> The mean variation in muscle point location was  $3.0 \pm 2.5$  mm, lower than the 5.0 mm uncertainty reported by Pal et al.,<sup>41</sup> when deriving muscle attachment points from the measurement of surface landmarks at the knee, and used as the level of uncertainty in Valente et al.'s<sup>4</sup> probabilistic analysis. As would be expected, this suggests that the repeatability of identifying muscle paths is improved when an operator has access to medical images of the subject.

Variability in the definition of model joint coordinate systems has been shown to have a minor influence on output JCFs but a considerable impact on the predicted muscle forces.<sup>28</sup> The mean inter-operator variation in the ankle coordinate systems was  $1.2^\circ$  for the plantar/dorsi-flexion axis and  $1.9^\circ$  for the inversion/eversion axis. These values are comparable to those reported by Martelli et al.,<sup>28</sup>  $0.4^\circ$  and  $2.0^\circ$ , respectively. Mean variability was higher at the metatarsophalangeal joint,  $4.3^\circ$ , indicating that the bony landmarks used to identify this joint<sup>32</sup> could be less repeatably identified.

When considering model outputs, the unavoidable variability in operator-defined subject-specific parameter definition had a clear effect on vertical ankle JCFs, with a maximum inter-operator variability of 1.86 BW observed, a value equal to 24% of the peak JCF. This is comparable with a similar study by Valente et al.,<sup>4</sup> who reported a slightly lower variation of 1.58 BW. However, while both studies varied the location of muscle path points, their study altered the location of bony landmarks and maximum muscle tensions, as opposed to the joint coordinate systems as reported here. Intra-operator variability in ankle JCF was found to be much smaller, only 0.33 BW, indicating that subject-specific model predictions obtained by a single operator are directly comparable. However, these findings can only be said to be valid for vertical ankle JCFs as shear forces have not been considered.

Consistent with previously reported studies,<sup>25,27</sup> perturbations of model input parameters had a considerable impact on the predicted muscle forces. When varying the defined joint coordinate systems, Martelli et al.<sup>28</sup> found muscle forces to vary by up to 114% compared to their median value, while Valente et al.<sup>4</sup> reported a maximum variation of 1.54 BW. These

values again compare favourably with the maximum variation in muscle force observed in this study, 1.94 BW. Furthermore, the muscles most affected in Valente et al.<sup>4</sup> at the ankle (soleus, gastrocnemius medialis, tibialis anterior) are the same as reported here. This indicates that it is the muscles with the larger physiological cross-sectional areas and moment arms that are most affected by uncertainty in their definition, and that their misplacement has the greatest impact on predicted muscle forces and JCFs.<sup>11,20</sup> Therefore, particular care should be taken when locating their bone insertion and via points.

The estimated inter-operator JCFs and muscle loads were considerably more varied for one subject than the other two. Although no statistically significant inter-subject differences in the model inputs were observed, this subject had the highest levels of variability in the definition of the muscle paths but interestingly, not in the definition of the joint coordinate systems. This is further evidence that it is the spatial location of muscle points which are the greatest source of variability in the outputs obtained with musculoskeletal models.<sup>4,20,23</sup> As such, the development of appropriate techniques for their reliable identification would be particularly advantageous and enable appropriate muscle moment arms, muscle lines of action and muscle-tendon lengths to be defined.

A number of limitations exist in the reported methodology that should be considered when reviewing the presented results. First, all operators based their models on the same segmented bony geometries, a procedure which, while sometime automated,<sup>42-44</sup> would also typically entail a further degree of inter-operator variation. The entire modelling methodology was also only completed multiple times by a single operator and for a single subject. While no statistically significant inter-subject differences were observed, the intra-operator analyses presented should therefore be interpreted with an understanding that the inclusion of further subjects and operators in the study could result in differing levels of uncertainty. Furthermore, only the reported subject-specific modelling methodology has been investigated, and adopting an alternative modelling approach may result in differing levels of repeatability and sensitivity.

A further limitation of the study is the use of a static optimisation technique to estimate muscle-tendon forces. Static optimisation assumes that muscle recruitment is such that the metabolic energy expenditure required to facilitate a movement is minimised<sup>45,46</sup> and this is implemented through the minimisation of an objective function (the sum of muscle activations squared in the case of this study). However, the gait of pathological individuals is likely to be suboptimal with regard to energetic efficiency, instead prioritising the reduction of articular loading at painful joints, for example. Caution should therefore be employed when evaluating the outputs of the model as optimal neuro-motor control has been assumed when simulating the motion of pathological subjects.

Alternative methodological approaches to overcome this limitation, such as personalizing the muscle recruitment strategy using electromyographically driven modelling techniques, are available in the literature.<sup>47</sup> However, this was not possible as EMG signals for all muscles crossing the ankle joint would be required and these were not collected in this study. Identification of a ‘disease-specific’ objective function would also be a challenging task requiring careful validation and is outside the scope of this investigation.

A final limitation of the reported study is the definition of generic muscle parameters in an otherwise subject-specific foot model, and their subsequent effect on model predictions via the force-length-velocity relationship.<sup>48</sup> It was considered reasonable to scale optimal fibre lengths and tendon slack lengths such that their relative ratio was maintained with respect to the total muscle-tendon length at rest. However, future studies could determine subject-specific muscle parameters by employing more complex anthropometric scaling tools.<sup>49</sup> Despite these limitations, it is clear that the reported methodology allowed the stated aim of the study to be achieved, to quantify the sensitivity of a juvenile subject-specific musculoskeletal foot and ankle model to the variation in operator-dependent input.

## Conclusion

This study investigated the inter- and intra-operator repeatability and sensitivity of a subject-specific modelling methodology developed for the analysis of juvenile, pathological subjects. The findings of the study indicate that the reported methodology exhibits comparable levels of repeatability and sensitivity to those reported for modelling healthy adults.<sup>4,28</sup> Inter-operator variation in the definition of muscle geometries remains significant and has the greatest impact on model outputs. As such, automated routines should be developed to reduce the significance of the operator’s role and prevent the misplacement of crucial muscle points. This will be of particular interest to those developing musculoskeletal models of juvenile or pathological subjects, for whom subject-specific modelling is of the greatest importance.<sup>10,11</sup>

## Declaration of conflicting interests

The author(s) declared no potential conflicts of interest with respect to the research, authorship and/or publication of this article.

## Funding

The author(s) disclosed receipt of the following financial support for the research, authorship, and/or publication of this article: This study has been supported by the European Commission (7th FP, ICT integrated project MD-Paedegree, Contract Number 600932) and by the EPSRC (Frontier Engineering

Awards, EP/K03877X/1). Data pertaining to model predictions and the virtual palpation of subject MRI are available through FigShare (DOI: 10.15131/shef.data.4286519).

## References

1. Fernandez JW and Pandy MG. Integrating modelling and experiments to assess dynamic musculoskeletal function in humans. *Exp Physiol* 2006; 91: 371–382.
2. Myers CA, Laz PJ, Shelburne KB, et al. A probabilistic approach to quantify the impact of uncertainty propagation in musculoskeletal simulations. *Ann Biomed Eng* 2015; 43: 1098–1111.
3. El Habachi A, Moissenet F, Duprey S, et al. Global sensitivity analysis of the joint kinematics during gait to the parameters of a lower limb multi-body model. *Med Biol Eng Comput* 2015; 53: 655–667.
4. Valente G, Pitto L, Testi D, et al. Are subject-specific musculoskeletal models robust to the uncertainties in parameter identification? *PLoS ONE* 2014; 9: e112625.
5. Ackland DC, Lin Y-C and Pandy MG. Sensitivity of model predictions of muscle function to changes in moment arms and muscle-tendon properties: a Monte-Carlo analysis. *J Biomech* 2012; 45: 1463–1471.
6. Jonkers I, Sauwen N, Lenaerts G, et al. Relation between subject-specific hip joint loading, stress distribution in the proximal femur and bone mineral density changes after total hip replacement. *J Biomech* 2008; 41: 3405–3413.
7. Valente G, Pitto L, Stagni R, et al. Effect of lower-limb joint models on subject-specific musculoskeletal models and simulations of daily motor activities. *J Biomech* 2015; 48: 4198–4205.
8. Bosmans L, Valente G, Wesseling M, et al. Sensitivity of predicted muscle forces during gait to anatomical variability in musculotendon geometry. *J Biomech* 2015; 48: 2116–2123.
9. Scheys L, Spaepen A, Suetens P, et al. Calculated moment-arm and muscle-tendon lengths during gait differ substantially using MR based versus rescaled generic lower-limb musculoskeletal models. *Gait Posture* 2008; 28: 640–648.
10. Correa TA, Baker R, Graham HK, et al. Accuracy of generic musculoskeletal models in predicting the functional roles of muscles in human gait. *J Biomech* 2011; 44: 2096–2105.
11. Carbone V, van der Krogt MM, Koopman HF, et al. Sensitivity of subject-specific models to errors in musculo-skeletal geometry. *J Biomech* 2012; 45: 2476–2480.
12. Ascani D, Mazzà C, De Lollis A, et al. A procedure to estimate the origins and the insertions of the knee ligaments from computed tomography images. *J Biomech* 2015; 48: 233–237.
13. Lenaerts G, De Groote F, Demeulenaere B, et al. Subject-specific hip geometry affects predicted hip joint contact forces during gait. *J Biomech* 2008; 41: 1243–1252.
14. Scheys L, Van Campenhout A, Spaepen A, et al. Personalized MR-based musculoskeletal models compared to rescaled generic models in the presence of increased femoral anteversion: effect on hip moment arm lengths. *Gait Posture* 2008; 28: 358–365.

15. Valente G, Taddei F and Jonkers I. Influence of weak hip abductor muscles on joint contact forces during normal walking: probabilistic modeling analysis. *J Biomech* 2013; 46: 2186–2193.
16. Cleather DJ, Goodwin JE and Bull AMJ. An optimization approach to inverse dynamics provides insight as to the function of the biarticular muscles during vertical jumping. *Ann Biomed Eng* 2011; 39: 147–160.
17. Delp SL, Loan JP, Hoy MG, et al. An interactive graphics-based model of the lower extremity to study orthopaedic surgical procedures. *IEEE Trans Biomed Eng* 1990; 37: 757–767.
18. Heller M, Bergmann G, Deuretzbacher G, et al. Musculo-skeletal loading conditions at the hip during walking and stair climbing. *J Biomech* 2001; 34: 883–893.
19. Modenese L, Phillips AT and Bull AM. An open source lower limb model: hip joint validation. *J Biomech* 2011; 44: 2185–2193.
20. Prinold JAI, Mazzà C, Di Marco R, et al. A patient-specific foot model for the estimate of ankle joint forces in patients with juvenile idiopathic arthritis. *Ann Biomed Eng* 2016; 44: 247–257.
21. Ravelli A and Martini A. Juvenile idiopathic arthritis. *Lancet* 2007; 369: 767–778.
22. Long AR and Rouster-Stevens KA. The role of exercise therapy in the management of juvenile idiopathic arthritis. *Curr Opin Rheumatol* 2010; 22: 213–217.
23. Scheys L, Loeckx D, Spaepen A, et al. Atlas-based non-rigid image registration to automatically define line-of-action muscle models: a validation study. *J Biomech* 2009; 42: 565–572.
24. Durkin JL and Dowling JJ. Body segment parameter estimation of the human lower leg using an elliptical model with validation from DEXA. *Ann Biomed Eng* 2006; 34: 1483–1493.
25. Herzog W. Sensitivity of muscle force estimations to changes in muscle input parameters using nonlinear optimization approaches. *J Biomech Eng* 1992; 114: 267.
26. Xiao M and Higginson J. Sensitivity of estimated muscle force in forward simulation of normal walking. *J Appl Biomech* 2010; 26: 142–149.
27. Brand RA, Pedersen DR and Friederich JA. The sensitivity of muscle force predictions to changes in physiologic cross-sectional area. *J Biomech* 1986; 19: 589–596.
28. Martelli S, Valente G, Viceconti M, et al. Sensitivity of a subject-specific musculoskeletal model to the uncertainties on the joint axes location. *Comput Methods Biomech Biomed Engin* 2015; 18: 1555–1563.
29. Klepper S. Measures of pediatric function: the Child Health Assessment Questionnaire (CHAQ), Juvenile Arthritis Functional Assessment Report (JAFAR), Juvenile Arthritis Functional Assessment Scale (JAFAS), Juvenile Arthritis Functional Status Index (JASI), and Pediatric Orthopedic Surgeons of North America (POSNA) Pediatric Musculoskeletal Functional Health Questionnaire. *Arthritis Rheum* 2003; 49: S5–S14.
30. Consolaro A, Ruperto N, Bazzo A, et al. Development and validation of a composite disease activity score for juvenile idiopathic arthritis. *Arthritis Rheum* 2009; 61: 658–666.
31. Vicon Motion Systems (Organisation). *Plug-In Gait manual*. 2012, [http://www.irc-web.co.jp/vicon\\_web/news\\_bn/PIGManualver1.pdf](http://www.irc-web.co.jp/vicon_web/news_bn/PIGManualver1.pdf)
32. Stebbins J, Harrington M, Thompson N, et al. Repeatability of a model for measuring multi-segment foot kinematics in children. *Gait Posture* 2006; 23: 401–410.
33. Arnold EM, Ward SR, Lieber RL, et al. A model of the lower limb for analysis of human movement. *Ann Biomed Eng* 2010; 38: 269–279.
34. Delp SL, Anderson FC, Arnold AS, et al. OpenSim: open-source software to create and analyze dynamic simulations of movement. *IEEE Trans Biomed Eng* 2007; 54: 1940–1950.
35. Taddei F, Ansaloni M, Testi D, et al. Virtual palpation of skeletal landmarks with multimodal display interfaces. *Med Inform Internet Med* 2007; 32: 191–198.
36. Van Sint Jan S. *Color atlas of skeletal landmark definitions: guidelines for reproducible manual and virtual palpations*. London: Elsevier Health Sciences, 2007, <https://www.elsevier.com/books/color-atlas-of-skeletal-landmark-definitions/van-sint-jan/978-0-443-10315-5>
37. Kadaba MP, Ramakrishnan HK, Wootten ME, et al. Repeatability of kinematic, kinetic, and electromyographic data in normal adult gait. *J Orthop Res* 1989; 7: 849–860.
38. Kadaba MP, Ramakrishnan HK and Wootten ME. Measurement of lower extremity kinematics during level walking. *J Orthop Res* 1990; 8: 383–392.
39. Schwartz MH, Rozumalski A and Trost JP. The effect of walking speed on the gait of typically developing children. *J Biomech* 2008; 41: 1639–1650.
40. Hicks JL, Uchida TK, Seth A, et al. Is my model good enough? Best practices for verification and validation of musculoskeletal models and simulations of human movement. *J Biomech Eng* 2014; 137: 020905.
41. Pal S, Langenderfer JE, Stowe JQ, et al. Probabilistic modeling of knee muscle moment arms: effects of methods, origin-insertion, and kinematic variability. *Ann Biomed Eng* 2007; 35: 1632–1642.
42. Schmid J and Magnenat-Thalmann N. MRI bone segmentation using deformable models and shape priors. *Med Image Comput Comput Assist Interv* 2008; 11: 119–126.
43. Seim H, Kainmueller D, Lamecker H, et al. Model-based auto-segmentation of knee bones and cartilage in MRI data. *Proc MICCAI Work Med Image Anal Clin* 2010; 215–223, <http://www.ski10.org/data/2010-11-09-1131.pdf>
44. Dodin P, Martel-Pelletier J, Pelletier J-P, et al. A fully automated human knee 3D MRI bone segmentation using the ray casting technique. *Med Biol Eng Comput* 2011; 49: 1413–1424.
45. Ackermann M and van den Bogert AJ. Optimality principles for model-based prediction of human gait. *J Biomech* 2010; 43: 1055–1060.
46. Anderson FC, Pandy MG, An KN, et al. Static and dynamic optimization solutions for gait are practically equivalent. *J Biomech* 2001; 34: 153–161.
47. Lloyd DG and Besier TF. An EMG-driven musculoskeletal model to estimate muscle forces and knee joint moments in vivo. *J Biomech* 2003; 36: 765–776.
48. Thelen DG. Adjustment of muscle mechanics model parameters to simulate dynamic contractions in older adults. *J Biomech Eng* 2003; 125: 70.
49. Modenese L, Ceseracciu E, Reggiani M, et al. Estimation of musculotendon parameters for scaled and subject specific musculoskeletal models using an optimization technique. *J Biomech* 2016; 49: 141–148.

## **5. Methods for MRI-based anatomical modelling of the lower limb**

This chapter collects the methods and results relative to the development of a detailed pipeline for image-based lower-limb musculoskeletal modelling: “Pipeline for building a subject-specific MSK model from MRI and motion capture data”, included in the Appendix I of this thesis. The pipeline was published as additional material to the paper “Investigation of the dependence of joint contact forces on musculotendon parameters using a codified workflow for image-based modelling” (Modenese et al., 2018), that I co-authored. This was produced with the aim of ensuring a robust and reliable pipeline for processing imaging and motion capture dataset and documenting automated or semi-automated procedures to be shared with the biomechanics community to produce musculoskeletal models (MSKMs). The purpose of this chapter is also to clarify and integrate the methods described in brief in the publications included in the chapters 4 -7.

## **5.1. Optimised input data for musculoskeletal modelling**

Subject-specific musculoskeletal modelling requires several input parameters. In order to reduce modelling errors and uncertainties, the accuracy of the input data (and relative experimental procedures) needs to be maximised. Aiming at fostering the adoption of a standardised and robust pipeline for musculoskeletal modelling, it is hence crucial to optimise the way in which parameters are measured and collected. Therefore, the first part of the PhD focused on the identification of the most critical aspects of data collections (including imaging and motion capture) toward the improvement of the input dataset. This was achieved pursuing a critical review of the limitations within previously collected datasets.

### **5.1.1. Experimental protocols**

An optimal dataset for subject-specific musculoskeletal modelling, including gait analysis and MRI data, must reflect the clinical needs, addressing correctly the purpose of the investigation, i.e. a specific clinical question for a particular population. In addition, it must compromise between the quality of the data and the available facilities, prioritizing the comfort of patients and subjects involved in the study. Within this framework, a protocol was designed to be used for musculoskeletal modelling for the analysis of muscle forces and joint

loading, which aimed at being used in an adult population, including both older and young adults.

*Data collection: gait analysis and medical imaging*

Being the marker placement one of the most time-consuming part of the gait analysis data collection, often uncomfortable for the subject who is asked to stand for a considerable period, it is recommendable to reduce the marker-set to a minimum number. This number should represent the optimal compromise between placement time and invasiveness of the procedure, and accuracy of the acquisition. In a similar manner, the number of liquid-filled MRI-visible markers to be retained during the medical imaging should be the minimum to guarantee an accurate registration of the data. In specific applications or for specific research purposes, where a higher level of accuracy and detail is required, this number can be increased and redundant makers can be added, being aware that toilsome procedures might not be easy to translate in the clinical practice.

A protocol for lower-limb MRI was developed as part of this PhD in collaboration with expert radiologists and clinicians with the purpose of improving two main aspects: the segmentation of bone geometries for the dentification of joint axes and the segmentation of muscle tissue to improve the discrimination between adjacent muscle and correctly identify their attachments and path. To achieve this, a 3D gradient echo in-and out of phase T1-weighted radial-volumetric interpolated breath-hold examination MRI sequence was selected, to be performed in 5 stacks from the feet up to the pelvis. A variable slice thickness was chosen: 3 mm in the articular region, when maximal accuracy is required, and 5 mm along the femur and tibia shaft, where less detail is acceptable; whereas the in-plane voxel size was set to 1.1x1.1 mm.

Additionally, it emerged that a critical aspect for the identification of the joint axes from the bone segmentation is the correct alignment of the body segment when the subject is lying on the MRI bed. The use of a foot positioner enabled to ensure a 90-degree ankle angle and with the foot facing forward, also limiting the internal/external rotation of the hip.

## **5.2. Anatomical model**

The lower limb anatomical model was developed within the application NMSBuilder (Valente et al., 2017), which is a freely-available software allowing to process biomedical data (medical images and segmentations) to be used for musculoskeletal modelling. The first step of the pipeline entailed importing the segmented geometries in NMSBuilder and organizing them in 11 segments composing the lower limbs, namely pelvis and bilateral femur, tibia, talus, midfoot, and phalanges. Each segment includes both bone and soft tissue (i.e. the outside contour of the skin) geometries.

### **5.2.1. Creation of the joints**

In order to describe the motion with respect to the environment, the initial configuration of the segmental chain needs to be known. In this sense, segmental frames define the pose of each body with respect to the ground. Movement is then represented by the rotation (or translation) of the distal reference system with respect to the proximal reference system. The pelvis, being the first segment of the chain, is referred to the ground by means of a free joint with 6 DoFs. Each distal body is referred to the proximal most adjacent one by means of rotational transformation. Ten joints were included in the model; two hips, schematized as ideal ball and socket with 3 DoFs, two knee joints, two tibiotalar joints, two subtalar joints, two metatarsophalangeal (MTP) joints, all schematized as ideal hinges with 1 DoF.

The description of the joints articulating between the body segments depends on the definition of two reference systems, one on the proximal and one on the distal segment, and on the relationship between the two. These anatomical frames are defined in NMSBuilder by means of three points, one representing the origin of the system, one setting the direction of the x axis, and one identifying the x-y plane. The z axis is derived as a consequence of the right-hand rule. To identify these points two methods can be implemented:

- Virtual palpation: referring to the identification of anatomical points, usually bony landmarks, on a 2D or 3D graphic representation of the human body, i.e. medical images or a model obtained from the segmentation of medical images (van Sint Jan, 2007).

- Morphological fitting: referring to the operation of fitting analytical shapes to bone geometries using a least squared error procedure for the identification of the optimal fitting (Modenese et al., 2018, Montefiori et al., 2019a, Montefiori et al., 2019b, Parr et al., 2012, Siegler et al., 2014). The procedure was implemented in a MATLAB (R2016b, The MathWorks, Inc., USA) script taking as an input the shape of the contacting articular region and giving as an output the centres and radii of the fitted geometries (Figure 5-1).

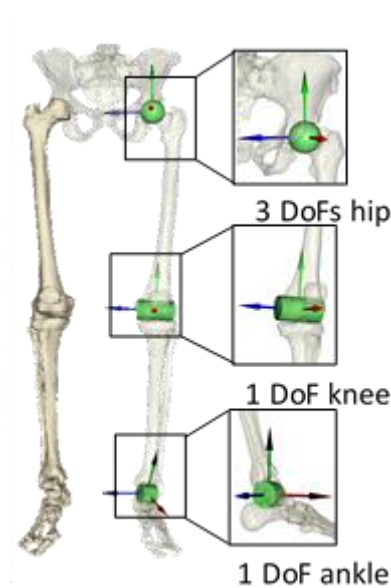


**Figure 5-1 – Definition of the joint axes through morphological fitting of analytical shapes to the articular surface of the bones. Example for hip, knee and ankle fitted to sphere, cylinder, and cylinder, respectively.**

Errors in the identification of these points introduce offsets in the relative position of the segments, ultimately leading to wrong estimates of the segmental kinematics. For this reason, morphologic fitting is preferred as less sensitive to operator-error. In fact, while the virtual palpation is a completely manual procedure, where the operator expertise is crucial to the successful location of the points, the fitting procedure is performed automatically through the algorithm, and the only manual operation is the selection of the articular surface to be fitted. The method has proved to be robust to differences in the selection of such area; full assessment of the repeatability and reproducibility of the methodology is reported in chapter

5 for the foot and ankle reference systems and in chapter 6 for the lower limb reference systems.

In brief, the identification of the axes of rotation of the different joints was achieved as follows (detailed procedure described in Appendix I):

- Pelvis joint (6 DoFs): through virtual palpation of the midpoint between the most anterior points on the superior iliac spines of the pelvis to identify the origin of the joint
- Hip joint (3 DoFs): through morphologic fitting of the femur head to a sphere, whose centre represented the origin of the joint;
- Knee joint (1 DoF): through morphologic fitting of the femur condyles to a cylinder, whose centre and axis represented the origin and axis of the joint, respectively;
- Ankle joint (1 DoF): through morphologic fitting of the talar dome to a cylinder, whose centre and axis represented the origin and axis of the joint, respectively;
- Subtalar joint (1 DoF): through morphologic fitting of the posterior-inferior talocalcaneal interface to a sphere, whose centre represented the origin of the joint and through morphologic fitting of the anterior talonavicular interface to a sphere, whose centres (connected to the origin of the joint) defined the axis of the joint
- Metatarsals joint (1 DoF): through virtual palpation of the most inferior point on the distal head of the first and fifth metatarsals to identify the origin (on the first metatarsals) and the axis of the joint (connecting the two points).

### **5.2.2. Location of muscle attachment points**

A description of the muscle geometry respectful of the real muscle anatomy represents one of the most critical steps in the construction of a personalised MSKM. In fact, many authors investigated the sensitivity of models to muscle geometry, especially muscle moment arm

(*ma*), namely the perpendicular distance between the muscle line of action and the centre of the joint the muscle is crossing (Figure 5-2) (Ackland et al., 2012, Bahl et al., 2019, Navacchia et al., 2016, Prinold et al., 2016, Sचेys et al., 2011, Sचेys et al., 2008a, Sचेys et al., 2008b, Valente et al., 2014).

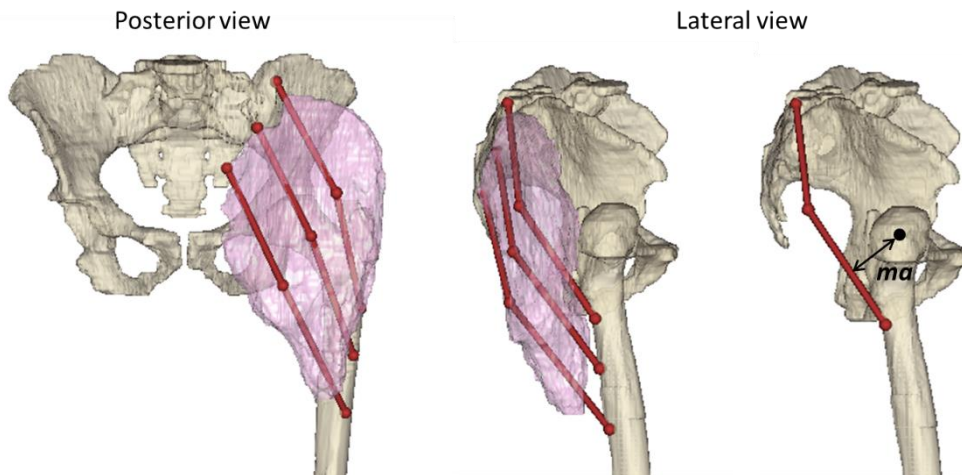


**Figure 5-2 – Example of definition of the gluteus maximus path (red lines) according to the three-bundle schematisation proposed by Delp et al. (1990) and identification of the moment arm (*ma*) of the first bundle.**

#### *Virtual palpation on MRI*

Muscle attachment points can be directly visible on the MRI, especially when they attach to bony tuberosity or prominences that enable to clearly identify the region on the bone where the muscle originates or inserts (Ascani et al., 2015). Via points and muscle paths can be easily located if the MRI contrast ensure the visibility of the different muscles and tendons. A clear example is shown in Figure 5-3 where ankle extensors and flexors via points can be selected on different MRI slices by means of virtual palpation of points on the images.

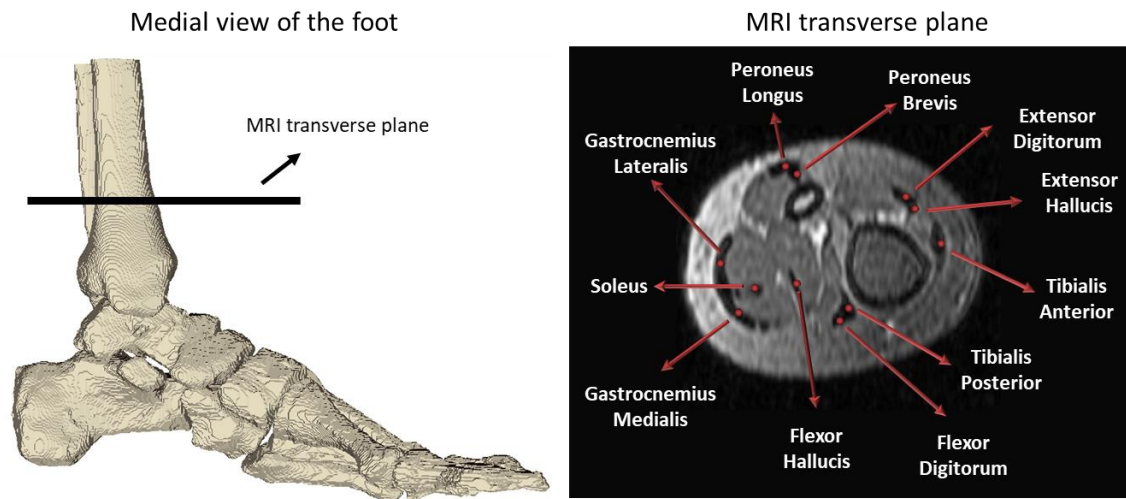


**Figure 5-3 – Identification of the via points of the muscles crossing the ankle on the transverse plane of the MRI.**

### *Supervised atlas registration*

This method is based on the use of an atlas of muscle points, taken from a literature generic model (Delp et al., 1990). In order to register these points on their corresponding location on a subject-specific model, a list of bony landmarks need to be added to the atlas. These bony landmarks must be placed in easily identifiable and meaningful position, to ensure the repeatability and reproducibility of their location. The same landmarks are then palpated on the subject-specific model and the bony landmark in the atlas are matched to their corresponding palpated markers through an affine transformation. This is made possible by using the same labelling for the markers in the atlas and in the subject-specific model. The resulting transformation, obtained from minimising the residual error of each transformation between couples of markers, is applied to the coordinates of the muscle points in the generic atlas, which are mapped onto the subject-specific model.

A MATLAB function (Modenese et al., 2018) is then used to snap the registered muscle points in order to adjust their location: origin and insertions are moved onto the nodes of the bone geometry they belong to, whereas via points are not moved, but eventually manually adjusted, if required (Modenese et al., 2018).

The repeatability of the whole procedure was assessed in the papers “Sensitivity of a juvenile subject-specific musculoskeletal model of the ankle joint to the variability of operator dependent input” and “Linking joint impairments and gait biomechanics in patients with

Juvenile Idiopathic Arthritis”, included in chapter 4 and 6, respectively, by measuring the intra- and inter-operator repeatability of both landmark palpation and muscle points identification.

#### *Iterative Closest Point approach*

This method relies on the existence of a musculoskeletal database including data from eleven older women, produced as part of the project Multisim, who partially funded this PhD. The database, to be released with the paper “The effect of muscle personalisation in the estimate of muscle forces and joint contact forces in post-menopausal women”, currently in preparation, contains bone and muscle geometries segmented from MRI in the format of stereolithographic files, a list of individual lower-limb muscle volumes and muscle points, as comma-separated vector of coordinates in the format of text files. Given the database ( $D$ ), containing eleven datasets ( $D_1, \dots, D_{11}$ ) an automatic identification of muscle points is possible through Iterative Closest Point (ICP) (Kjer and Wilm, 2010) algorithm registration in MATLAB (Figure 5-4). When a new model ( $M_{new}$ ) must be produced, a best matching dataset ( $D_{best}$ ) can be found among those available in  $D$ , based on a preliminary registration of the bone geometries in  $D_1, \dots, D_{11}$  onto  $M_{new}$ .  $D_{best}$  is identified as the dataset whose registration gives the lower residual error and is registered again to  $M_{new}$  through ICP mapping. Twenty iterations are implemented as resulted in the best compromise between computational time and residual error, which was found to decrease below 5% after the 18<sup>th</sup> iteration. The output of the registration is a transformation matrix that is afterwards applied to the cloud of muscle points associated to  $D_{best}$  in order to map them onto the  $M_{new}$  bone geometries. The previously described snapping algorithm is used here as well in order to adjust the final location of the muscle attachments and ensure their coordinates belong to the bone surface.

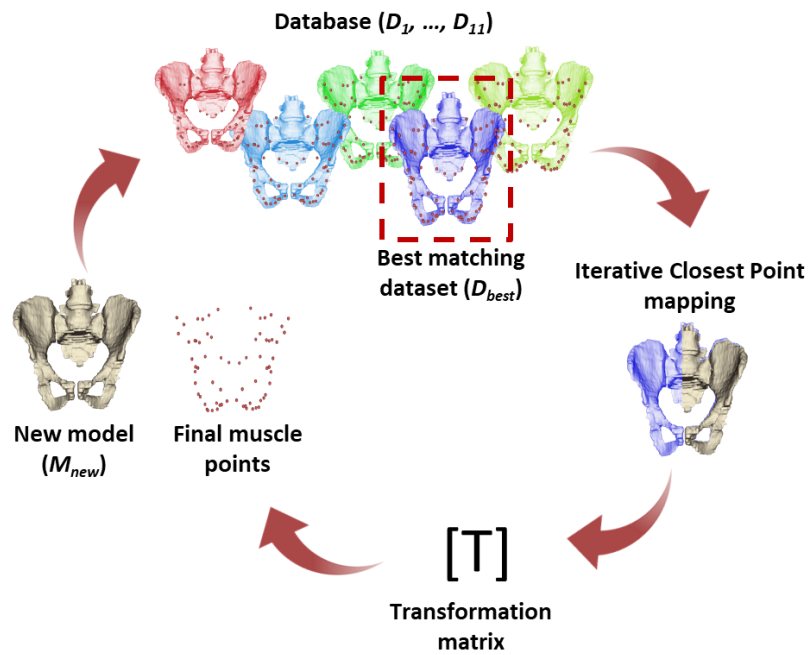


Figure 5-4 – Schematics of the ICP-based mapping of the muscle points.

### 5.2.3. Inertial properties

The estimate of the kinetics of the various joints requires the definition of the inertial parameters of each segment, i.e. their volume and density, as the mass cannot be measured. The volume is extracted from the volume of the segmented geometry, whereas the density is assigned from literature values:  $1.46 \text{ kg/cm}^3$  for the bones and  $1.02 \text{ kg/cm}^3$  (or  $1.03 \text{ kg/cm}^3$ ) for the soft tissue of females (or males) as estimate by White et al. (1987) accounting for both muscle, fat and other soft tissues in the body.

### 5.3. References

- Ackland, D. C., Lin, Y.-C. & Pandy, M. G. 2012. Sensitivity of model predictions of muscle function to changes in moment arms and muscle–tendon properties: a Monte-Carlo analysis. *Journal of Biomechanics*, 45, 1463-1471.
- Ascani, D., Mazzà, C., De Lollis, A., Bernardoni, M. & Viceconti, M. 2015. A procedure to estimate the origins and the insertions of the knee ligaments from computed tomography images. *Journal of Biomechanics*, 48, 233-237.
- Bahl, J. S., Zhang, J., Killen, B. A., Taylor, M., Solomon, L. B., Arnold, J. B., Lloyd, D. G., Besier, T. F. & Thewlis, D. 2019. Statistical shape modelling versus linear scaling: effects on predictions of hip joint centre location and muscle moment arms in people with hip osteoarthritis. *Journal of Biomechanics*.
- Delp, S. L., Loan, J. P., Hoy, M. G., Zajac, F. E., Topp, E. L. & Rosen, J. M. 1990. An interactive graphics-based model of the lower extremity to study orthopaedic surgical procedures. *IEEE Transactions on Biomedical engineering*, 37, 757-767.
- Kjer, H. M. & Wilm, J. 2010. *Evaluation of surface registration algorithms for PET motion correction*. Technical University of Denmark, DTU, DK-2800 Kgs. Lyngby, Denmark.
- Modenese, L., Montefiori, E., Wang, A., Wesarg, S., Viceconti, M. & Mazzà, C. 2018. Investigation of the dependence of joint contact forces on musculotendon parameters using a codified workflow for image-based modelling. *Journal of Biomechanics*, 73, 108-118.
- Montefiori, E., Modenese, L., Di Marco, R., Magni-Manzoni, S., Malattia, C., Petrarca, M., Ronchetti, A., De Horatio, L. T., Van Dijkhuizen, P., Wang, A., Wesarg, S., Viceconti, M. & Mazzà, C. 2019a. An image-based kinematic model of the tibiotalar and subtalar joints and its application to gait analysis in children with Juvenile Idiopathic Arthritis. *Journal of Biomechanics*, 85, 27-36.
- Montefiori, E., Modenese, L., Di Marco, R., Magni-Manzoni, S., Malattia, C., Petrarca, M., Ronchetti, A., De Horatio, L. T., Van Dijkhuizen, P., Wang, A., Wesarg, S., Viceconti, M. & Mazzà, C. 2019b. Linking Joint Impairment and Gait Biomechanics in Patients with Juvenile Idiopathic Arthritis. *Annals of biomedical engineering*, 1-13.
- Navacchia, A., Myers, C. A., Rullkoetter, P. J. & Shelburne, K. B. 2016. Prediction of in vivo knee joint loads using a global probabilistic analysis. *Journal of biomechanical engineering*, 138, 031002.
- Parr, W., Chatterjee, H. & Soligo, C. 2012. Calculating the axes of rotation for the subtalar and talocrural joints using 3D bone reconstructions. *Journal of Biomechanics*, 45, 1103-1107.
- Prinold, J. A., Mazzà, C., Di Marco, R., Hannah, I., Malattia, C., Magni-Manzoni, S., Petrarca, M., Ronchetti, A. B., De Horatio, L. T. & Van Dijkhuizen, E. P. 2016. A patient-specific foot model for the estimate of ankle joint forces in patients with juvenile idiopathic arthritis. *Annals of biomedical engineering*, 44, 247-257.
- Scheys, L., Desloovere, K., Suetens, P. & Jonkers, I. 2011. Level of subject-specific detail in musculoskeletal models affects hip moment arm length calculation during gait in pediatric subjects with increased femoral anteversion. *Journal of Biomechanics*, 44, 1346-1353.

- Scheys, L., Spaepen, A., Suetens, P. & Jonkers, I. 2008a. Calculated moment-arm and muscle-tendon lengths during gait differ substantially using MR based versus rescaled generic lower-limb musculoskeletal models. *Gait & posture*, 28, 640-648.
- Scheys, L., Van Campenhout, A., Spaepen, A., Suetens, P. & Jonkers, I. 2008b. Personalized MR-based musculoskeletal models compared to rescaled generic models in the presence of increased femoral anteversion: effect on hip moment arm lengths. *Gait & posture*, 28, 358-365.
- Siegler, S., Toy, J., Seale, D. & Pedowitz, D. 2014. The Clinical Biomechanics Award 2013--presented by the International Society of Biomechanics: new observations on the morphology of the talar dome and its relationship to ankle kinematics. *Clinical Biomechanics*, 29, 1-6.
- Valente, G., Crimi, G., Vanella, N., Schileo, E. & Taddei, F. 2017. nmsBuilder: Freeware to create subject-specific musculoskeletal models for OpenSim. *Computer methods programs in biomedicine*, 152, 85-92.
- Valente, G., Pitto, L., Testi, D., Seth, A., Delp, S. L., Stagni, R., Viceconti, M. & Taddei, F. 2014. Are subject-specific musculoskeletal models robust to the uncertainties in parameter identification? *PLoS One*, 9, e112625.
- Van Sint Jan, S. 2007. *Color Atlas of Skeletal Landmark Definitions E-Book: Guidelines for Reproducible Manual and Virtual Palpations*, Elsevier Health Sciences.
- White, D., Woodard, H. & Hammond, S. 1987. Average soft-tissue and bone models for use in radiation dosimetry. *The British journal of radiology*, 60, 907-913.

**6. Linking joint impairments and gait  
biomechanics in patients with Juvenile  
Idiopathic Arthritis**

### *Acknowledgement of co-authorship*

This chapter includes the published paper “Linking joint impairments and gait biomechanics in patients with Juvenile Idiopathic Arthritis” produced as the results of the research carried out in collaboration with the co-authors listed in the paper.

My personal contribution was in the design of the study, implementation of the modelling procedure, quantification of the intra- and inter-operator repeatability of the models’ output, application of the models to answer the specific clinical question, design of statistical analysis, interpretation of the results, and discussion with respect to the clinical context. Additionally, I was responsible for writing the paper, producing figures and tables and leading the submission and review process.

Student:

Erica Montefiori		Date	25/07/2019
------------------	---	------	------------

The main co-authors:

Claudia Mazza'		Date	25/07/2019
----------------	---	------	------------

Luca Modenese		Date	24/07/2019
---------------	---	------	------------



# Linking Joint Impairment and Gait Biomechanics in Patients with Juvenile Idiopathic Arthritis

ERICA MONTEFIORI <sup>1,2</sup> LUCA MODENESE <sup>2,3</sup> ROBERTO DI MARCO,<sup>2,4</sup> SILVIA MAGNI-MANZONI,<sup>5</sup> CLARA MALATTIA,<sup>6</sup> MAURIZIO PETRARCA,<sup>7</sup> ANNA RONCHETTI,<sup>8</sup> LAURA TANTURRI DE HORATIO,<sup>9</sup> PIETER VAN DIJKHUIZEN,<sup>10</sup> ANQI WANG,<sup>11</sup> STEFAN WESARG,<sup>11</sup> MARCO VICECONTI,<sup>12,13</sup> CLAUDIA MAZZÀ,<sup>1,2</sup> and FOR THE MD-PAEDIGREE CONSORTIUM

<sup>1</sup>Department of Mechanical Engineering, University of Sheffield, Sheffield, UK; <sup>2</sup>INSIGNEO Institute for In Silico Medicine, University of Sheffield, Sheffield, UK; <sup>3</sup>Department of Civil and Environmental Engineering, Imperial College London, London, UK; <sup>4</sup>Department of Mechanical and Aerospace Engineering, “Sapienza” University of Rome, Rome, Italy; <sup>5</sup>Pediatric Rheumatology Unit, IRCCS “Bambino Gesù” Children’s Hospital, Passoscuro, Rome, Italy; <sup>6</sup>Pediatria II - Reumatologia, Istituto Giannina Gaslini, Genoa, Italy; <sup>7</sup>Movement Analysis and Robotics Laboratory (MARLab), Neurorehabilitation Units, IRCCS “Bambino Gesù” Children’s Hospital, Passoscuro, Rome, Italy; <sup>8</sup>UOC Medicina Fisica e Riabilitazione, IRCCS Istituto Giannina Gaslini, Genoa, Italy; <sup>9</sup>Department of Imaging, IRCCS “Bambino Gesù” Children’s Hospital, Passoscuro, Rome, Italy; <sup>10</sup>Paediatric Immunology, University Medical Centre Utrecht Wilhelmina Children’s Hospital, Utrecht, The Netherlands; <sup>11</sup>Visual Healthcare Technologies, Fraunhofer IGD, Darmstadt, Germany; <sup>12</sup>Department of Industrial Engineering, Alma Mater Studiorum - University of Bologna, Bologna, Italy; and <sup>13</sup>Laboratorio di Tecnologia Medica, IRCCS Istituto Ortopedico Rizzoli, Bologna, Italy

(Received 22 February 2019; accepted 8 May 2019)

Associate Editor Jane Grande-Allen oversaw the review of this article.

**Abstract**—Juvenile Idiopathic Arthritis (JIA) is a paediatric musculoskeletal disease of unknown aetiology, leading to walking alterations when the lower-limb joints are involved. Diagnosis of JIA is mostly clinical. Imaging can quantify impairments associated to inflammation and joint damage. However, treatment planning could be better supported using dynamic information, such as joint contact forces (JCFs). To this purpose, we used a musculoskeletal model to predict JCFs and investigate how JCFs varied as a result of joint impairment in eighteen children with JIA. Gait analysis data and magnetic resonance images (MRI) were used to develop patient-specific lower-limb musculoskeletal models, which were evaluated for operator-dependent variability ( $< 3.6^\circ$ ,  $0.05 \text{ N kg}^{-1}$  and  $0.5 \text{ BW}$  for joint angles, moments, and JCFs, respectively). Gait alterations and JCF patterns showed high between-subjects variability reflecting the pathology heterogeneity in the cohort. Higher joint impairment, assessed with MRI-based evaluation, was weakly associated to overall joint overloading. A stronger correlation was observed between impairment of one limb and overload of the contralateral limb, suggesting risky compensatory strategies being adopted, especially at the knee level. This suggests that knee overloading during gait might be a good predictor of disease progression and gait biomechanics should be used to inform treatment planning.

**Keywords**—Biomechanics, Musculoskeletal, Gait analysis, MRI, Musculoskeletal modelling, Lower-limb, Juvenile arthritis, Opensim.

## INTRODUCTION

Juvenile Idiopathic Arthritis (JIA) is a group of paediatric chronic diseases of unknown aetiology, particularly affecting the knee and ankle joints,<sup>28</sup> which can lead to cartilage damage due to inflammation, articular malposition and altered mobility.<sup>19,28</sup> Current practice to quantify disease activity in JIA is based on composite tools such as the Juvenile Arthritis Disease Activity Score (JADAS<sup>7</sup>). The JADAS consists of the following items: the total number of joints with active arthritis, the physician and the patient’s/parent’s global assessment of the disease and the erythrocyte sedimentation rate as an inflammatory marker. The physician and patient’s/parent’s global assessment constitute a subjective element of evaluation of joints status and mobility, and as such can present strong disagreement.<sup>24,29</sup>

Medical imaging has been proposed as an alternative in improving the assessment of JIA with respect to traditional clinical examination with ultrasound tech-

Address correspondence to Erica Montefiori, INSIGNEO Institute for In Silico Medicine, University of Sheffield, Sheffield, UK. Electronic mail: e.montefiori@sheffield.ac.uk

niques being used to quantify the tendon and joint synovial inflammation, or cartilage and bone integrity.<sup>6</sup> More recently, Magnetic Resonance Imaging (MRI) has been introduced to support early diagnosis of JIA thanks to more reliable quantification of synovitis, bone marrow oedema, and bone erosions.<sup>17,26</sup> Image-based techniques, however, can only provide information about local impairment, as usually assessed in unloaded static conditions, and as such are not necessarily informative in terms of consequent functional alterations that could explain different patterns of pathology progression. For this reason, gait analysis techniques have been suggested as a tool to functionally characterise alterations in the joint kinematics and kinetics of patients with JIA.<sup>3,13,15,22</sup> These studies reported hyper-flexion of the hip and knee joints and reduced plantarflexion of the ankle joint, with associated reduction in ankle moment and power as common gait pattern traits of in JIA. These alterations returned to normal after treatment in the less severe cases, suggesting a clear connection between JIA activity and functional impairment.<sup>3,13,15</sup> Unfortunately, no insight into the specific causes of the observed biomechanical alterations that could have explained the absence of a response to treatment in more severe cases was provided. Since internal joint loading is directly related to bone and cartilage loading, it can be hypothesised that its estimate can provide further insight on the link between joint inflammation and impaired walking function. Understanding this link would support more accurate diagnosis and specific treatment planning. Musculoskeletal (MSK) modelling of the lower limb can be used for this purpose.<sup>42</sup>

Several MSK modelling approaches have been proposed in the literature for representing individual patients, from the scaling of generic models to match the subject's anatomical features<sup>1</sup> to more detailed image-based techniques.<sup>2,16,40</sup> The latter has proved to be a feasible approach for the investigation of lower limb biomechanics in juvenile populations<sup>20,22</sup> and can provide tools to gain insight in disease mechanisms, especially when MSK dysfunction appears causing functional limitations and altered locomotion.<sup>8,27,31,32</sup>

The aim of this paper is to provide further insight into the relationship of disease activity and joint impairment to altered joint loading in children with JIA, and to highlight compensatory strategies that potentially lead to joint damage. To this purpose, we will first establish the repeatability and reproducibility of a patient specific MSK modelling approach previously proposed for the analysis of juvenile gait.<sup>20</sup> This approach will then be used to investigate the rela-

tionship between joint involvement (intended as presence of inflammation and/or cartilage damage in one or more of the lower limb joints) and the hip, knee and ankle joint contact forces (JCFs) in a group of children with JIA. We hypothesised that in the presence of an active disease, where inflamed joints need to be protected to prevent pain, a reduction of the internal loads should be observed. The adopted protection strategies, however, might also lead to a compensation causing overloading of other joints in the same or opposite limb.

## MATERIALS AND METHODS

### *Subjects and Data Acquisition*

Eighteen participants (5 males, 13 females, age:  $12 \pm 3$  years, mass:  $50.2 \pm 17.3$  kg, height:  $150 \pm 16$  cm, Table 1) diagnosed with JIA were recruited from two different children's hospitals ("Bambino Gesù" Children's Hospital, Rome, Italy, and Istituto Giannina Gaslini, Genoa, Italy). The inclusion criteria were ankle arthritis in new onset JIA or ankle involvement in long lasting JIA (as assessed by clinical observation) and age between five and sixteen years. The ethical committees of both hospitals approved the study and written informed consent was obtained by the patients' carers.

Gait analysis data were collected in the two different hospitals using movement analysis based on infrared optical stereophotogrammetry. An 8-camera system (MX, Vicon Motion System Ltd, UK, 200 Hz) with two force platforms (OR6-6, AMTI, USA, 1000 Hz) was used in Rome and a 6-camera system (Smart DX, BTS Bioengineering, Italy, 100 Hz) with two force platforms (Kistler, UK, 1000 Hz) was used in Genoa. The marker-set was a combination of the Vicon PlugIn gait (Vicon Motion System) and the modified Oxford Foot Model (mOFM) protocols,<sup>35</sup> with a total of forty-four markers (Fig. 1). A subset of twenty-eight markers was retained during a following MRI exam (see Modenese *et al.*<sup>20</sup> for detailed protocol) including a full lower limb 3D T1-weighted fat-suppression sequence (e-THRIVE) with 1 mm in-plane resolution and 1 mm slice thickness.

### *Musculoskeletal Modelling Procedure*

Eighteen lower limb patient-specific MSK models were built following the procedure described in Modenese *et al.*<sup>20</sup> Bone geometries were segmented from the MRI with a statistical shape modelling approach.<sup>37</sup> The anatomical models were built by one

TABLE 1. Patients' anthropometric and clinical details.

Patient	Gender (F/M)	Age (year)	Height (m)	Weight (Kg)	Sub-type	MRI <sub>Index</sub>	
						Right	Left
1	F	10	1.39	41	PsA	0	3
2	F	15.5	1.61	68	Ext oligo	3	3
3	M	14	1.74	76.5	Poly-	0	0
4	F	11	1.45	54	Oligo	0	1
5	F	18.5	1.59	68	Ext oligo	3	0
6	F	16.5	1.68	83	Ext oligo	2	5
7	F	14.5	1.65	54.5	PsA	3	5
8	F	11	1.31	26.6	Poly-	2	0
9	F	14	1.63	63.8	Poly-	0	0
10	F	9	1.29	32.5	Poly-	2	1
11	M	10	1.5	37	Oligo	1	2
12	F	7	1.28	23	UndA	2	1
13	M	7.5	1.17	35.7	Oligo	1	1
14	F	13	1.68	49	Oligo	0	2
15	M	12.5	1.55	45.6	Oligo	0	0
16	M	10	1.36	32	Oligo	1	3
17	F	13.5	1.56	54.5	Oligo	0	0
18	F	13.5	1.54	63.5	Poly-	0	0
Average	–	11.9	1.48	47.8	–	–	–
SD	–	3.2	0.17	18.6	–	–	–
Total	15F	–	–	–	–	–	–

*Oligo* persistent oligoarticular JIA, *Ext oligo* extended oligoarticular JIA, *PsA* psoriatic arthritis, *Poly-* rheumatoid-factor-negative polyarticular JIA, *UndA* undifferentiated arthritis.

expert operator using specialised software (NMSBuilder<sup>39</sup>). Nine body segments were included in the model, namely one pelvis and bilateral femur, tibia, talus and foot segments. The inertial properties of each segment were computed accounting for both bone and soft tissue densities.<sup>41</sup> Eight joints were modelled as ideal ball-and-socket (hip) joint, or ideal hinge (knee, ankle, subtalar). The articular surfaces were identified and isolated in Meshlab<sup>5</sup> and the joints' axes of rotation were defined with a morphological fitting approach using a least square difference minimisation in MATLAB (v9.1, R2016b, The MathWorks Inc., USAMathWorks, USA) and following the ISB conventions.<sup>43</sup> Muscle attachments and *via* points were calculated through a supervised atlas registration approach<sup>40</sup> based on a reference model<sup>11</sup> and manually adjusted against the MRI if needed.

Musculotendon parameters were modelled as Hill-type muscle elements.<sup>38</sup> Optimal fibre length ( $l_{opt}$ ), tendon slack length ( $l_{tendon}$ ) were scaled to maintain the  $l_{opt}/l_{tendon}$  ratio as in the "gait2392" generic model<sup>11</sup> available with the OpenSim distribution. Pennation angle was set according to the value in the "gait2392",<sup>11</sup> and maximal contraction velocity was set to 10 fibres per second.<sup>38</sup> Maximal isometric force ( $F_{max}$ ) was linearly scaled based on the ratio between the lower-limb mass of the subject (derived from the MRI) and of the generic model.<sup>11</sup> The force-length-velocity (FLV) relationship was not considered

during the simulations, thus neglecting contraction dynamics.<sup>20</sup>

The experimental markers visible in the MRI were included into the model as virtual markers and then registered to those used for the gait analysis within OpenSim,<sup>10</sup> where gait was simulated using the Inverse Kinematics and Inverse Dynamics routines. Gait data were normalised over a gait cycle, identified from subsequent heel strikes of the same limb, which were determined either from the force platform or from the foot markers. Joint powers (JPs) were calculated as the product of joint moment and angular velocity. The Static Optimisation tool was used to estimate muscle activations and forces and the Joint Reaction Analysis tool<sup>36</sup> was then used to estimate the JCFs (intended as the norm of the reaction force vector).

The above modelling procedure entailed two operator-dependent steps: the identification of muscles origins, insertions and *via* points; and the selection of the joints' surface for morphological fitting (and consequent definition of joint frames, including their centre and axes orientation). Three operators were hence enrolled to assess both inter- and intra-operator variability of the procedure and their effects on the model output (Fig. 2). They produced three MSK models each using data from three randomly selected subjects (two females, one male,  $13.7 \pm 1.2$  years,  $1.63 \pm 0.10$  m,  $68.5 \pm 5.3$  kg). One of the operators was also asked to repeat the modelling three times for

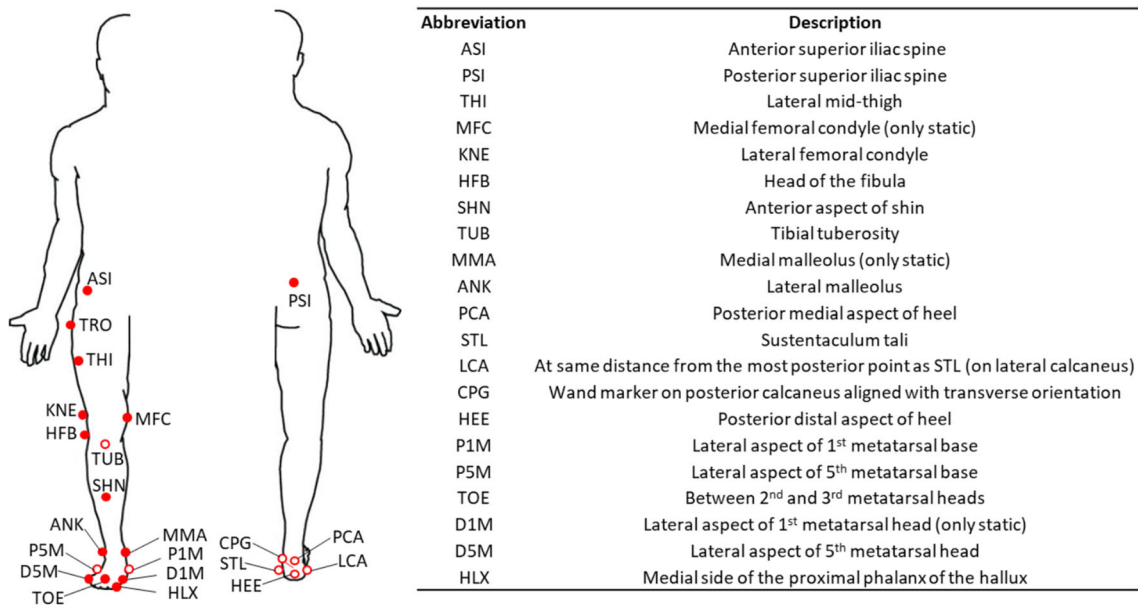


**FIGURE 1.** Experimental markers used in the stereophotogrammetric protocol (filled and empty dots) and retained during the imaging (filled dots) and relevant description.

each subject. Intra- and inter-operator variability of joint angles, joint moments and JCFs were quantified by standard deviation (SD) and range between repetitions over the entire gait cycle.

#### Imaging Evaluation Assessment

An MRI-based assessment of joint involvement was performed for the hip, knee, ankle, and mid-foot joints. For each joint the MRI inflammation score was assigned on the short tau inversion recovery (STIR) sequence using a 0–3 scale based on the amount of joint effusion (0 = no inflammation; 1 = mild/moderate inflammation; 2 = severe inflammation). After training and calibration sessions, the MRIs were read by a paediatric radiologist and a paediatric rheumatologist with more than 10 years expertise in musculoskeletal MRI. The readers were blind to the clinical status of the patient. Any disagreement was resolved by consensus.<sup>9</sup> This evaluation highlighted an active disease in 21 out of the 36 investigated limbs (Table 1). A total MRI score ( $MRI_{Index}$ ) was then calculated by adding the values of both lower limb joints and was used to divide the patients into two groups: impaired ( $IM$ ,  $n = 13$ ) and non-impaired ( $NI$ ,  $n = 5$ ). The  $NI$  group was then used as a control group.

#### Statistical Analysis

A 1D non-parametric  $t$  test was used to compare joint angles, moments (normalised to body mass times

height<sup>21</sup>), powers and contact forces (normalised to body weight,  $BW$ ), estimated with the MSK simulations in the  $IM$  and  $NI$  by means Statistical Parametric Mapping (SPM) in MATLAB, using the SPM1D package.<sup>25</sup>

Each patient's walking biomechanics was characterised using peaks of the hip ( $F_{H1}$ ,  $F_{H2}$ ), knee ( $F_{K1}$ ,  $F_{K2}$ ) and ankle ( $F_A$ ) JCFs; area under the hip ( $A_{FH}$ ), knee ( $A_{FK}$ ) and ankle ( $A_{FA}$ ) JCF curves; peak of ankle power ( $P_A$ ) and area under the hip ( $A_{PH}$ ), knee ( $A_{PK}$ ) and ankle ( $A_{PA}$ ) JP curves. For the  $IM$  group, the link between joint impairment and the biomechanical alterations was investigated analysing the correlation between the  $MRI_{Index}$  and the JCFs using the cumulative parameter including both limbs' joints:  $JCF_{Index} = F_{H1} + F_{H2} + F_{K1} + F_{K2} + F_A$ . Observed correlations were classified as weak ( $0.3 < \rho \leq 0.5$ ), moderate ( $0.5 < \rho \leq 0.7$ ) or strong ( $\rho > 0.7$ ), based on the Spearman's Rho non-parametric test.

The  $IM$  group was sub-divided into patients with mono-lateral impairment ( $MI$ ,  $n = 5$ ), and patients with bilateral impairment ( $BI$ ,  $n = 8$ ) to investigate differences between relevant gait patterns. Dunn's non-parametric multiple  $t$  test (critical  $Q$  value at 2.388) was used to highlight differences in the biomechanical parameters among  $MI$ ,  $BI$  and  $NI$  using multiple, stepdown comparisons.<sup>4</sup> Robust  $z$  score, based on outlier-insensitive median and median absolute deviation,<sup>30</sup> was used to normalise the parameters and quantify the deviation of the  $MI$  and  $BI$  groups from the  $NI$  group, intended as a control.

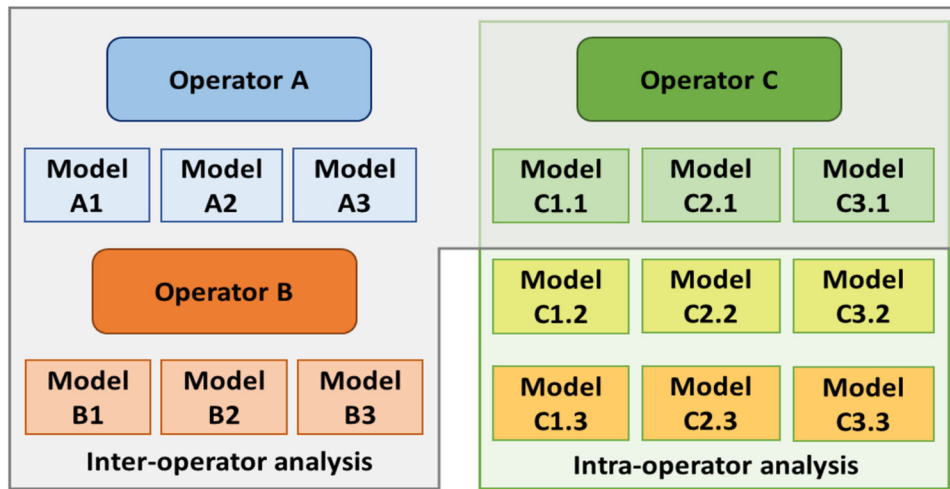


FIGURE 2. Outline of the repeatability study.

Finally, the presence of contralateral compensatory strategies was quantified testing the correlation (Spearman's Rho non-parametric test) between the  $MRI_{\text{Index}}$  of one limb and biomechanical parameters measured for the same limb and for the opposite limb. Significance was set to  $\alpha = 0.05$  for all the statistical tests.

## RESULTS

The three operators detected the muscle origins and insertions with an intra- and inter-operator variability of  $1.2 \pm 0.6$  mm and  $2.2 \pm 1.0$  mm, respectively. Intra- and inter-operator SD in the identification of the joint centres and axes orientation from morphological fitting was below 3 mm and  $3^\circ$ , respectively (Table 2), except for one model where intra- and inter-operator SD of the ankle axes orientation reached  $5.2^\circ$  and  $8.3^\circ$ . The propagation of these uncertainties to the models' output, led to a maximum SD of joint angles and moments which was always below  $3.0^\circ$  and  $0.03 \text{ N kg}^{-1}$ , respectively, for the intra-operator analysis and below  $3.6^\circ$  and  $0.05 \text{ N kg}^{-1}$ , respectively, for the inter-operator analysis. The average percentage of SD with respect to the range of motion (ROM) was always below 10% except for the inter-operator SD of two models' subtalar angles (Table 3). Intra- (Fig. 3a) and inter- (Fig. 3c) operator variations of the JCFs and their variations between-repetition (Figs. 3b and 3d) were all below 0.3 BW and 0.5 BW (equivalent to less than 10% of peak value).

The 1D  $t$  test between the *IM* and *NI* groups (Fig. 4) showed a significant difference only in the early stance phase of the hip moment, where the *IM* average joint flexion moment was up to  $0.4 \text{ N m kg}^{-1}$

smaller than *NI*, and in the second peak of the knee contact force, where the *IM* average JCF was up to 0.8 BW higher than the *NI*. All the remaining time-dependent comparisons were not significant.

Table 4 shows the values obtained for the biomechanical parameters in the three groups. A meaningful statistical analysis was hindered by the low sample size, but the values did not seem to suggest a clear trend in the differences between the two limbs within the groups. Relevant values were then grouped to calculate the normalised  $z$  score used to build the radar plots in Fig. 5, which summarises the deviation of *BI* and *MI* groups from the biomechanical pattern shown by the *NI* groups. Visual analysis of the graphs suggests an overall tendency of *BI* to excessively load the knee when compared to the other two groups. The largest differences were observed for the  $P_A$  ( $z = -3.0$  and  $z = -1.6$  for *BI* and *MI*, respectively),  $F_{K1}$  ( $z = -1.9$  for *MI*),  $F_{K2}$  ( $z = 1.7$  for *BI*),  $A_{PK}$  ( $z = -1.1$  for *MI*),  $F_A$  ( $z = 1.1$  for *BI*). Peculiarly,  $F_{K1}$  and  $A_{PK}$  showed a discordant deviation, with positive  $z$  score for the *BI* and negative  $z$  score for the *MI*. Dunn's test ( $Q_{\text{critic}} = 2.388$ ) highlighted a significantly higher  $F_{K1}$  ( $Q = 2.8468$ ) in the *BI* group compared to the *MI* (with 0.6 BW average difference) and  $F_{K2}$  ( $Q = 4.0224$ ), in the *BI* group compared to the *NI* (with 1 BW average difference).

A moderate correlation ( $\rho = 0.597$ ,  $p = 0.031$ ) was observed between the  $MRI_{\text{Index}}$  and  $JCF_{\text{Index}}$  (Fig. 6). When observing the link between  $MRI_{\text{Index}}$  of a single limb and the biomechanical parameters, a significant weak correlation was observed only for the  $F_{H1}$  ( $\rho = 0.490$ ,  $p = 0.011$ ),  $A_{PK}$  ( $\rho = 0.472$ ,  $p = 0.015$ ) and  $A_{PA}$  ( $\rho = 0.390$ ,  $p = 0.049$ ). When analysing the compensatory mechanisms involving the contralateral limb, significant weak to strong correlations were

found for  $F_{HI}$  ( $\rho = 0.501$ ,  $p = 0.009$ ),  $A_{FH}$  ( $\rho = 0.712$ ,  $p < 0.001$ ),  $P_A$  ( $\rho = 0.544$ ,  $p = 0.004$ ),  $F_{K1}$  ( $\rho = 0.427$ ,  $p = 0.029$ ),  $F_{K2}$  ( $\rho = 0.521$ ,  $p = 0.006$ ), and  $A_{FK}$  ( $\rho = 0.405$ ,  $p = 0.040$ ).

**DISCUSSION**

In this study, we proposed an MRI-based MSK model of the lower limb to investigate the relationship between joint impairment and joint loading during gait in a cohort of children with JIA, which was characterised by a variety of disease manifestations and consequent gait alterations. The reported results discouraged any hypothesis of a unique predictable cause-effect relationship, which suggests that adding a dynamic functional gait assessment to the image-based patient evaluation might help to better

identify joints at risk of critical compensatory overloading and hence better inform personalised treatment. Furthermore, it clearly emerged that patient-specific models do have an ability to combine multiple data into coherent, physics-based predictions that appear to be strongly discriminative even in a dramatically heterogeneous population like the one investigated here. Thus, these methods should be pursued to clinically investigate the complex compensatory strategies that JIA flares produce and the effect that such strategies may have on the response to first line treatments.

The model adopted in this study presented some limitations. Firstly, the joints were schematised as ideal joints. This simplification is commonly accepted for the hip, being well described by the ball-and-socket coupling but represents a limitation in the understanding of knee and ankle motion.<sup>34,44</sup> A second limitation was the estimation of musculotendon parameters. They were linearly scaled to lower-limb mass from a generic model available in the literature<sup>11</sup> where these parameters were specified for only a single nominal subject. Experimental data suggest that musculotendon parameters are highly variable between subjects, especially when anthropometrical differences are considerable (i.e., children vs. adults), therefore linear scaling of these quantities might not be appropriate for a juvenile population. On the other hand, a direct and non-invasive measure of these parameters is not possible *in vivo*. Future study will aim at improving this aspect, implementing methods to extract more

**TABLE 2. Repeatability of operator dependent input.**

	Joint centre (mm)		Axes orientation (°)	
	Intra	Inter	Intra	Inter
Hip	0.2 ± 0.1	0.2 ± 0.1	1.6 ± 0.9	0.9 ± 0.2
Knee	1.3 ± 1.6	2.0 ± 0.8	1.7 ± 1.1	1.6 ± 0.5
Ankle	0.5 ± 0.1	1.0 ± 0.6	4.0 ± 1.8	3.9 ± 3.8
Subtalar	0.8 ± 0.2	1.5 ± 0.7	1.0 ± 0.2	1.0 ± 0.3

Mean ± SD (across the three models) of the intra- and inter-operator SD of joint centre and axes orientation (defined as the average SD over the three joint axes) for the lower limb joints.

**TABLE 3. Repeatability of model output.**

	Hip flex/ext	Hip ab/ad	Hip int/ext	Knee flex/ext	Ankle PF/DF	Subtalar inv/ev
Joint angles (% ROM)						
M1						
Intra	0.6 ± 0.3	1.5 ± 0.4	3.8 ± 0.7	0.6 ± 0.4	7 ± 2.3	9.5 ± 3.2
Inter	0.4 ± 0.3	2.7 ± 1.5	5.8 ± 2.1	0.5 ± 0.2	7.8 ± 1.3	12.2 ± 2
M2						
Intra	1.2 ± 1.2	3.6 ± 1.8	5.2 ± 4.6	1.0 ± 0.6	9.6 ± 6.3	5.6 ± 4.9
Inter	2.4 ± 0.3	7.6 ± 1.4	6.1 ± 2.5	2.6 ± 0.5	4.4 ± 0.9	16.8 ± 5.3
M3						
Intra	0.4 ± 0.1	2.0 ± 1.0	2.9 ± 0.2	0.4 ± 0.1	1.7 ± 0.7	4.0 ± 0.0
Inter	3.7 ± 3.7	2.7 ± 1.5	9.4 ± 3.6	1.7 ± 0.7	5.6 ± 3.2	4.2 ± 1.6
Joint moments (% PP)						
M1						
Intra	0.8 ± 0.1	0.5 ± 0.0	1.0 ± 0.6	0.7 ± 0.6	0.3 ± 0.1	1.6 ± 0.4
Inter	0.8 ± 0.1	0.5 ± 0.2	1.5 ± 0.1	0.7 ± 0.4	0.3 ± 0.0	2.9 ± 1.0
M2						
Intra	1.0 ± 0.5	0.9 ± 0.5	1.5 ± 0.5	1.3 ± 0.3	0.3 ± 0.0	3.0 ± 0.7
Inter	2.1 ± 0.8	1.0 ± 0.2	3.3 ± 0.2	2.9 ± 0.6	0.8 ± 0.0	7.5 ± 2.6
M3						
Intra	0.4 ± 0.0	0.6 ± 0.1	0.8 ± 0.3	0.9 ± 0.4	0.2 ± 0.0	1.5 ± 0.3
Inter	0.9 ± 0.6	0.8 ± 0.0	8.4 ± 8.5	1.9 ± 0.9	0.5 ± 0.5	3.6 ± 2.8

Mean ± SD percentage of joint range of motion (ROM) and peak-to-peak moment (PP) for the intra- and inter-operator SD over the gait cycle for the three models (M1–3).

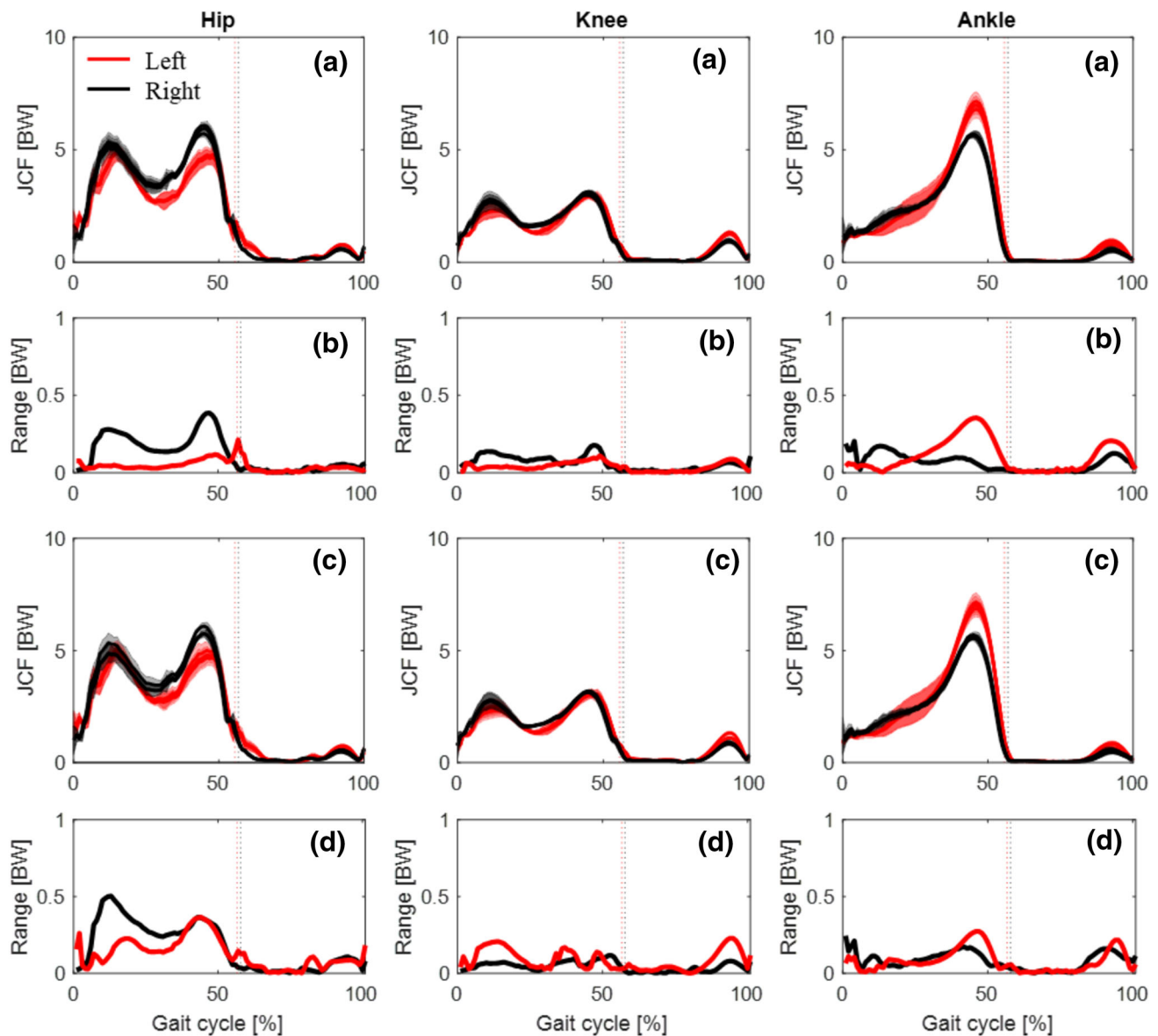


**FIGURE 3.** Repeatability of the model output: example of mean and SD (shadow) over three walking trials of hip, knee and ankle JCFs for one model (left and right side in red and black, respectively) built by the same operator three times (a) and three different operators (c). Ranges of variation of JCFs for (b) intra-operator and (d) inter-operator analysis

information from MRI (such as moment arm, individual muscle volume and cross-sectional area). Modenese *et al.*<sup>20</sup> showed that the choice of the scaling method does not influence the resulting JCFs if the FLV relationship is taken into account. Here, on the contrary, contraction dynamics was neglected, potentially causing the overestimate of the second knee contact force peak.<sup>20</sup> However, the consistency of this choice throughout all the simulations did not affect the comparison between impaired and non-impaired subjects' JCFs. Finally, we applied the Static Optimisation technique to estimate muscle forces assuming an

optimal force distribution strategy. This might not be the case in a pathological population, where suboptimal mechanisms can be adopted aiming at reducing joint loading.<sup>12</sup>

Despite the above limitations, the proposed approach led to satisfactory intra- and inter-operator repeatability of the estimated output in the context of the investigated application. The variability observed in the input did not substantially affect the output of the simulations, with limited variations observed for all joint kinematics and kinetics and for the joint contact forces. The combined effect of mis-locating joint centre

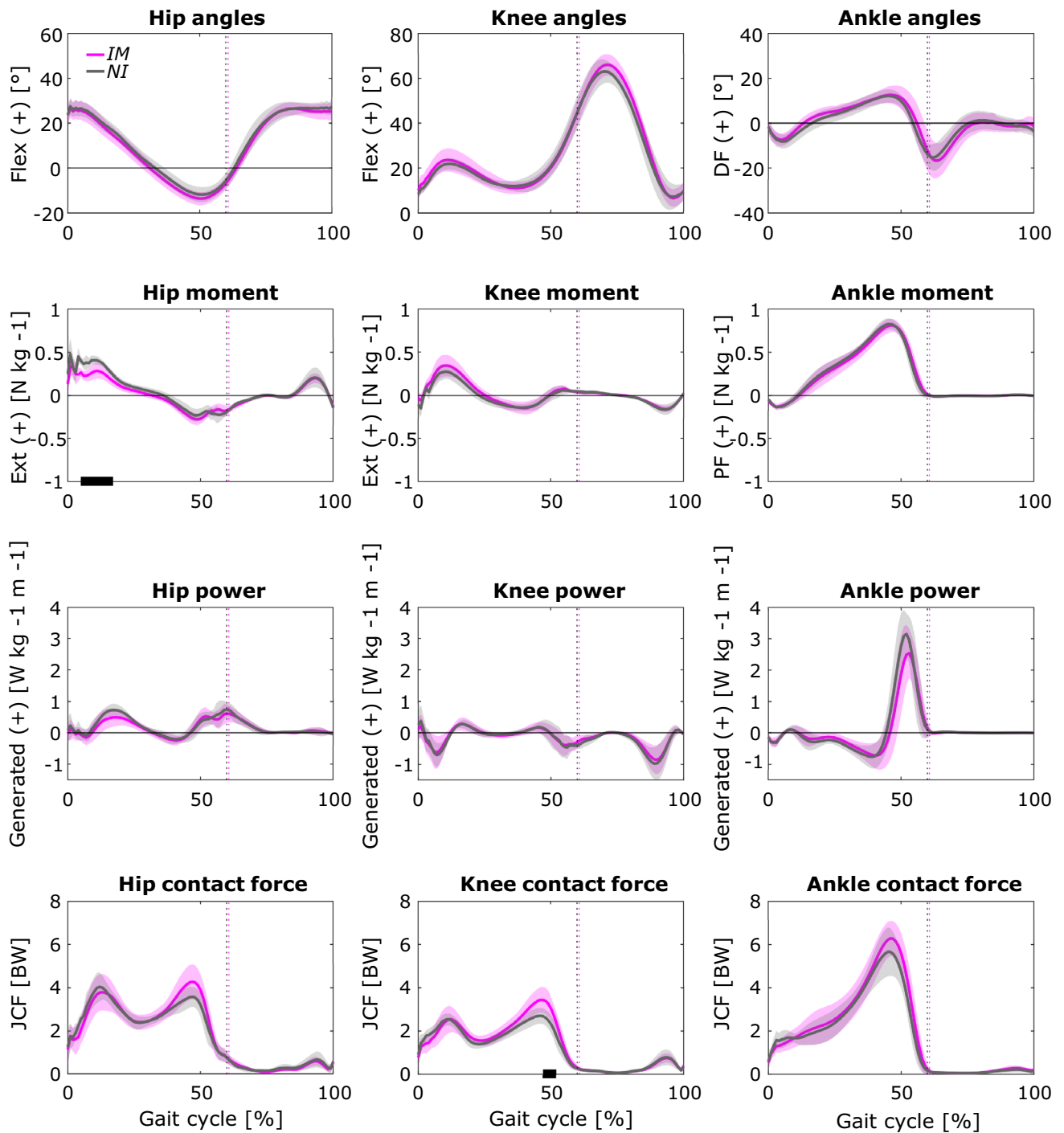


**FIGURE 4.** Comparison (non-parametric 1D  $t$  test in SPM) between joint angles, moments, powers (Abs = absorbed, Gen = generated) and contact forces of the *IM* (fuchsia) and *NI* (grey) groups over the gait cycle. Vertical dotted lines represent the instant in which toe off occurs and black bars identify the regions of the gait cycle where statistical significance was met ( $p < 0.05$ ).

and axes and misidentifying muscle points led to an overall uncertainty of 0.5 BW, which is lower than 10% of the estimated peak values. The operator-related uncertainty found in the repeatability study was considered reasonable to safely apply the modelling

protocol in a clinical scenario to estimate joint angles, moments, powers and contact forces, and to investigate the link between joint impairment and alteration of the relevant biomechanical parameters in JIA. Lower repeatability was observed for the movements

TABLE 4. Inter-group analysis.

		BI (n = 16)		MI (n = 10)		NI (n = 10)
		Most affected limb	Less affected limb	Affected limb	Non-affected limb	
		$\bar{X}$ (range)	$\bar{X}$ (range)	$\bar{X}$ (range)	$\bar{X}$ (range)	$\bar{X}$ (range)
Hip	$F_{H1}$ (BW)	3.9 (2.6/5.8)	4.2 (3.4/5.5)	3.7 (3.2/4.2)	3.3 (2.9/4.1)	3.9 (3.1/5.2)
	$F_{H2}$ (BW)	4.1 (3.8/6)	4.7 (3.6/6.1)	3.8 (3.4/3.9)	4 (3.7/5.6)	3.8 (2.7/4.3)
	$A_{FH}$ (BW s)	1.4 (1.6/2.3)	1.9 (1.7/2.4)	1.7 (1.5/1.7)	1.9 (1.6/2.1)	1.8 (1.6/2.1)
Knee	$A_{PH}$ (W s kg <sup>-1</sup> )	0.3 (0.1/0.4)	0.3 (0.2/0.4)	0.2 (0.1/1.0)	0.2 (0.1/0.3)	0.3 (0.2/0.4)
	$F_{K1}$ (BW)	2.6 (2.1/4.5)	2.7 (2.2/3.6)	2.0 (1.9/3.5)	2.1 (1.7/3)	2.5 (2.2/3.1)
	$F_{K2}$ (BW)	3.7 (2.9/4.4)	4 (3/5.1)	2.8 (2.6/3.2)	3.4 (2.9/3.9)	2.7 (2.3/3.5)
	$A_{FK}$ (BW s)	1.3 (1.1/1.5)	1.4 (1.2/1.6)	1.3 (1.1/1.6)	1.3 (1.1/1.7)	1.2 (1.1/1.5)
	$A_{PK}$ (W s kg <sup>-1</sup> )	0.3 (0.1/0.5)	0.3 (0.1/0.4)	0.2 (0.1/0.4)	0.2 (0.2/0.3)	0.3 (0.2/0.5)
Ankle	$F_A$ (BW)	6.6 (5.4/8.1)	6.4 (5.3/7.7)	6.0 (5.2/7.2)	6.3 (5.5/7.4)	5.7 (4.3/7.7)
	$A_{FA}$ (BW s)	1.9 (1.5/2.2)	1.8 (1.6/2.2)	1.9 (1.7/2.6)	2.0 (1.7/2.1)	1.8 (1.4/2.1)
	$P_A$ (W kg <sup>-1</sup> )	2.7 (2.4/4.8)	2.9 (2.2/4.3)	2.4 (1.9/3.3)	2.9 (2/3.4)	3.9 (2.2/4.7)
	$A_{PA}$ (W s kg <sup>-1</sup> )	0.4 (0.3/0.5)	0.4 (0.3/0.5)	0.3 (0.3/0.9)	0.4 (0.3/0.5)	0.4 (0.2/0.5)

Medians ( $\bar{X}$ ) and ranges of the JCF and JP parameters for the three groups with n representing the number of limbs in each group.

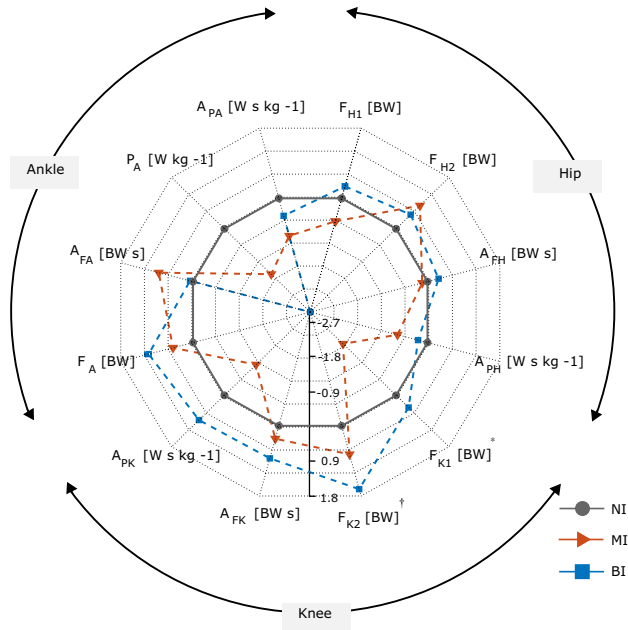


FIGURE 5. Radar plot visualisation of the JCF and JP parameters normalised using robust z score. \* = BI group significantly different from MI; † = BI group significantly different from NI.

out of the sagittal plane, for this reason, only flexion/extension movements were investigated in this study. This choice is certainly a limitation, but it is in line with previous gait analysis studies on JIA children.<sup>3,15,19,22</sup>

The uncertainty in the identification of the joint centre and axes was similar to what has been reported in the literature<sup>18</sup> for the knee and ankle joints of healthy adults (up to 6.4 mm and 4.5° and up to 4.6 mm and 4°, respectively), leading to JCF variations of up to 9% of peak values. Previous studies demonstrated that the repeatability of JCF estimates is highly

dependent on the definition of muscle geometries. Navacchia *et al.*<sup>23</sup> showed that muscle path uncertainty can have an average 10% effect on the predicted JCFs. In a previous study investigating a juvenile ankle model,<sup>14</sup> our group reported up to 20% of peak ankle JCF variability due to intra- and inter-operator uncertainties in muscle point identification equal to  $1.7 \pm 1.9$  and  $3.0 \pm 2.5$  mm, respectively, with maximum values up to 14.3 mm for single points. The intra- and inter-operator variability of muscle points in the present study was reduced to  $1.2 \pm 0.6$  and  $2.2 \pm 1.0$  mm, respectively, with maximum values of 5 mm. This progress was the result of an improved identification of the set of bony landmarks used for the supervised registration of muscle points.<sup>20</sup> Nonetheless, since muscle paths are a well-known critical factor in the estimate of moment arms, muscle forces, and JCFs,<sup>33</sup> future investigations should focus on further automating and improving this step.

The modest propagation of the input uncertainty on the models' predictions made these patient-specific models highly discriminative; we were able to highlight significant differences between individual patients, and between limbs in the same patients. However, the cohort of children enrolled in this study was characterised by a high clinical heterogeneity with different JIA subtypes and severity. Five children, despite a history of JIA, did not present active disease at the time of the visit, and were therefore classified as not impaired. Eight patients presented bilateral impairment and five mono-lateral impairment, mostly affecting the knee and ankle joints. This heterogeneity clearly affected the results of the group analysis of disease-related gait pattern, due to a large variability in the average joint angle, moment, and power curves. Consequently, no specific pathology-related pattern

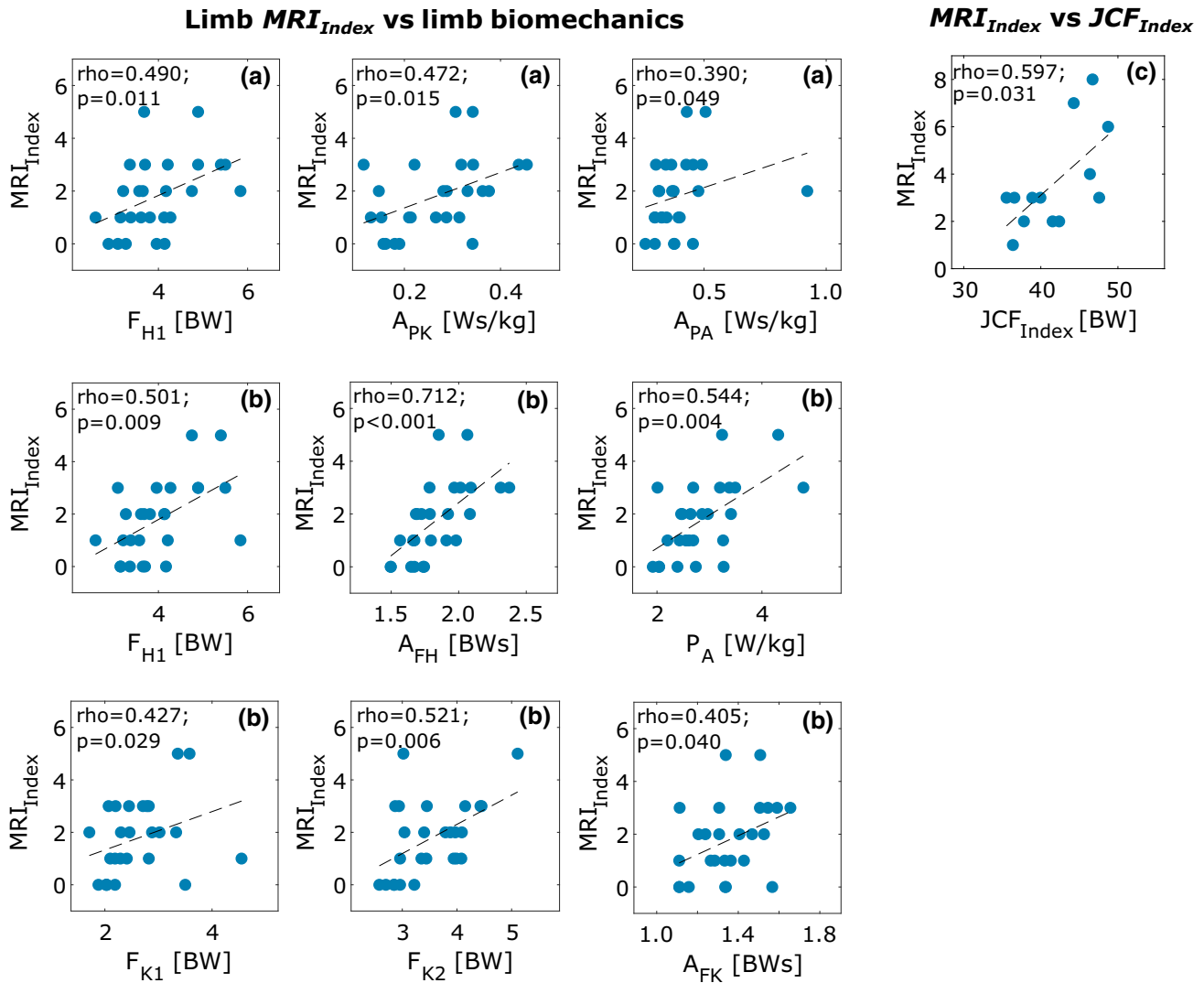


**FIGURE 6.** Spearman's  $\rho$  non-parametric correlation between: (a) the  $MRI_{Index}$  of a single limb and the biomechanical parameters of the same limb, (b) the  $MRI_{Index}$  of a single limb and the biomechanical parameters of the contralateral limb, (c) the total  $MRI_{Index}$  and the sum of JCF peaks ( $JCF_{Index}$ ) of the two limbs. Dashed black lines represent linear regression fitting;  $\rho$  and  $p$  are the correlation coefficient and statistical significance, respectively.

was detected in the *IM* group kinematics, contrary to what was reported in a previous study,<sup>15</sup> where hyperflexion of the hip and knee joints and reduced plantarflexion in the ankle were found to be a common trait in 36 patients with symmetrical polyarticular joint involvement. A possible explanation for this discrepancy can be found in the reduced numerosity ( $n = 5$ ) of our non-impaired group, and in the fact that JIA-related joint inflammation had been reported for these children within the previous 12 months. As such, rather than fully representative of a healthy population, their gait biomechanics was that of a group of individuals capable of responding to the disease activity by

leveraging on loading and walking strategies that enabled them to reduce joint inflammation and pain.

The limited number of participants and the variability of their clinical status drove the choice of using a cumulative impairment scoring index (accounting for all the lower limb joints), which prevented the investigation of individual contributions of each joint and the impact of different involvement levels to the overall functional alteration. Larger and more homogeneous datasets would be necessary to overcome this limitation. Nonetheless, the cumulative  $JCF_{Index}$  was found to be moderately correlated to disease activity level in the lower limbs, and when analysing the joints sepa-

rately, a significantly higher (up to 15%) knee peak contact force was observed during push off in the *IM* group. This result was partially confirmed when investigating distinctive features of mono-lateral and bilateral impaired groups. In fact, a positive  $z$  score was observed for all the JCF parameters of the *BI*, resulting in the overloading of the joints, with particular significance for the knee ( $F_{K1}$  and  $F_{K2}$ ).

When the behaviour of the two limbs was investigated separately, the presence of compensatory loading strategies became evident, with an increased loading of the contralateral hip (higher  $A_{FH}$ ) in the most impaired patients. Additionally, overloading of the hip arose for both limbs in the first phase of the stance (higher  $F_{H1}$ ). An overall higher loading of the knee ( $A_{FK}$ ) was observed, especially during push-off phase ( $F_{K2}$ ), in the less affected limb as a possible strategy for protecting the painful joints. This excessive loading might be one of the causes for further development of the pathology. From this perspective, the knee joint loading might be the best variable to monitor in order to predict disease progression and guide treatment.

In conclusion, this paper presented for the first time the application of a juvenile subject-specific MSK modelling approach to the investigation of the link between joint impairment and joint loading during walking in children with JIA. The model ensures repeatable estimates of lower-limb biomechanical parameters and the results of its application encourage further development of this approach as a support of the current clinical practice for understanding and preventing functional alterations associated to excessive joint loadings. In this sense, only knee JCF resulted as a good candidate for predicting JIA activity and potential indicator of compensatory mechanism associated to mono-lateral involvement, but future longitudinal studies are needed to test this hypothesis.

#### ACKNOWLEDGMENTS

The authors would like to acknowledge Dr Norman Powell for the writing assistance, and Mr Giorgos Marinou and Mr Michael Woodward for their contribution to data processing. This research was supported by the European Commission (MD-PAEDIGREE project, FP7-ICT Programme, Project ID: 600932), the UK EPSRC (Multisim project, Grant Number: EP/K03877X/1) and the NIHR Sheffield Biomedical Research Centre (BRC). The views expressed are those of the author(s) and not necessarily those of the NHS, the NIHR or the Department of Health and Social Care (DHSC). Data used to build

the models will be made publicly available as on-line material on Figshare (<https://doi.org/10.15131/shef.data.6237146>).

#### CONFLICT OF INTEREST

The authors declare that they do not have any financial or personal relationship with other people or organisations that could have inappropriately influenced this study.

#### OPEN ACCESS

This article is distributed under the terms of the Creative Commons Attribution 4.0 International License (<http://creativecommons.org/licenses/by/4.0/>), which permits unrestricted use, distribution, and reproduction in any medium, provided you give appropriate credit to the original author(s) and the source, provide a link to the Creative Commons license, and indicate if changes were made.

#### REFERENCES

- <sup>1</sup>Arnold, A. S., S. S. Blemker, and S. L. Delp. Evaluation of a deformable musculoskeletal model for estimating muscle-tendon lengths during crouch gait. *Ann. Biomed. Eng.* 29(3):263–274, 2001.
- <sup>2</sup>Arnold, A. S., S. Salinas, D. J. Hakawa, and S. L. Delp. Accuracy of muscle moment arms estimated from MRI-based musculoskeletal models of the lower extremity. *Comput. Aided Surg.* 5(2):108–119, 2000.
- <sup>3</sup>Broström, E., S. Hagelberg, and Y. Haglund-Åkerlind. Effect of joint injections in children with Juvenile Idiopathic Arthritis: evaluation by 3D-gait analysis. *Acta Paediatr.* 93(7):906–910, 2004.
- <sup>4</sup>Cardillo, G. Dunn's test: a procedure for multiple, not parametric, comparisons. Natick: MATLAB Central, MathWorks, 2006.
- <sup>5</sup>Cignoni, P., M. Callieri, M. Corsini, M. Dellepiane, F. Ganovelli, and G. Ranzuglia. Meshlab: an open-source mesh processing tool. *Eurographics Ital. Chap. Conf.* 2008:129–136, 2008.
- <sup>6</sup>Colebatch-Bourn, A. N., C. J. Edwards, P. Collado, M. A. D'Agostino, R. Hemke, S. Jousse-Joulin, M. Maas, A. Martini, E. Nared, M. Østergaard, M. Rooney, N. Tzaribachev, M. A. van Rossum, J. Vojinovic, P. G. Conaghan, and C. Malattia. EULAR-PreS points to consider for the use of imaging in the diagnosis and management of Juvenile Idiopathic Arthritis in clinical practice. *Ann. Rheum. Dis.* 74(11):1946–1957, 2015.
- <sup>7</sup>Consolaro, A., N. Ruperto, A. Bazso, A. Pistorio, S. Magni-Manzoni, G. Filocamo, C. Malattia, S. Viola, A. Martini, and A. Ravelli. Development and validation of a composite disease activity score for Juvenile Idiopathic Arthritis. *Arthritis Rheum.* 61(5):658–666, 2009.
- <sup>8</sup>Correa, T. A., and M. G. Pandy. A mass-length scaling law for modelling muscle strength in the lower limb. *J. Biomech.* 44(16):2782–2789, 2011.

- <sup>9</sup>Damasio, M. B., C. Malattia, L. T. de Horatio, C. Mattiuz, A. Pistorio, C. Bracaglia, D. Barbuti, P. Boavida, K. L. Juhan, L. S. Ordning, K. Rosendahl, A. Martini, G. Magnano, and P. Tomà. MRI of the wrist in Juvenile Idiopathic Arthritis: proposal of a paediatric synovitis score by a consensus of an international working group. Results of a multicentre reliability study. *Pediatr. Radiol.* 42(9):1047–1055, 2014.
- <sup>10</sup>Delp, S. L., F. C. Anderson, A. S. Arnold, P. Loan, A. Habib, C. T. John, E. Guendelman, and D. G. Thelen. OpenSim: open-source software to create and analyze dynamic simulations of movement. *IEEE Trans. Biomed. Eng.* 54:1940–1950, 2007.
- <sup>11</sup>Delp, S. L., J. P. Loan, M. G. Hoy, F. E. Zajac, E. L. Topp, and J. M. Rosen. An interactive graphics-based model of the lower extremity to study orthopaedic surgical procedures. *IEEE Trans. Biomed. Eng.* 37(8):757–767, 1990.
- <sup>12</sup>DeMers, M. S., S. Pal, and S. L. Delp. Changes in tibiofemoral forces due to variations in muscle activity during walking. *J. Orthop. Res.* 32:769–776, 2014.
- <sup>13</sup>Esbjörnsson, A. C., M. D. Iversen, M. André, S. Hagelberg, M. H. Schwartz, and E. W. Broström. Effect of intraarticular corticosteroid foot injections on walking function in children with Juvenile Idiopathic Arthritis. *Arthritis Care Res.* 67(12):1693–1701, 2015.
- <sup>14</sup>Hannah, I., E. Montefiori, L. Modenese, J. Prinold, M. Viceconti, and C. Mazzà. Sensitivity of a juvenile subject-specific musculoskeletal model of the ankle joint to the variability of operator-dependent input. *Proc. Inst. Mech. Eng. H* 231:415–422, 2017.
- <sup>15</sup>Hartmann, M., F. Kreuzpointner, R. Haefner, H. Michels, A. Schwirtz, and J. P. Haas. Effects of Juvenile Idiopathic Arthritis on kinematics and kinetics of the lower extremities call for consequences in physical activities recommendations. *Int. J. Pediatr.* 2010:835984, 2010.
- <sup>16</sup>Lenaerts, G., F. De Groote, B. Demeulenaere, M. Mulier, G. Van der Perre, A. Spaepen, and I. Jonkers. Subject-specific hip geometry affects predicted hip joint contact forces during gait. *J. Biomech.* 41(6):1243–1252, 2008.
- <sup>17</sup>Magni-Manzoni, S., C. Malattia, M. B. Damasio, A. Pistorio, M. Ioseliani, I. Vilca, M. Valle, N. Ruperto, S. Viola, A. Buoncompagni, G. M. Magnano, A. Ravelli, P. Tomà, and A. Martini. Development and preliminary validation of a paediatric-targeted MRI scoring system for the assessment of disease activity and damage in Juvenile Idiopathic Arthritis. *Ann. Rheum. Dis.* 70:440–446, 2011.
- <sup>18</sup>Martelli, S., G. Valente, M. Viceconti, and F. Taddei. Sensitivity of a subject-specific musculoskeletal model to the uncertainties on the joint axes location. *Comput. Methods Biomech. Biomed. Eng.* 18(14):1555–1563, 2015.
- <sup>19</sup>Merker, J., M. Hartmann, F. Kreuzpointner, A. Schwirtz, and J. P. Haas. Pathophysiology of Juvenile Idiopathic Arthritis induced pes planovalgus in static and walking condition: a functional view using 3D gait analysis. *Pediatr. Rheumatol. Online J.* 13(1):21, 2015.
- <sup>20</sup>Modenese, L., E. Montefiori, A. Wang, S. Wesarg, M. Viceconti, and C. Mazzà. Investigation of the dependence of joint contact forces on musculotendon parameters using a codified workflow for image-based modelling. *J. Biomech.* 73:108–118, 2018.
- <sup>21</sup>Moisio, K. C., D. R. Sumner, S. Shott, and D. E. Hurwitz. Normalization of joint moments during gait: a comparison of two techniques. *J. Biomech.* 36(4):599–603, 2003.
- <sup>22</sup>Montefiori, E., L. Modenese, R. Di Marco, S. Magni-Manzoni, C. Malattia, M. Petrarca, A. Ronchetti, L. T. de Horatio, E. H. P. van Dijkhuizen, A. Wang, S. Wesarg, M. Viceconti, and C. Mazzà. An image-based kinematic model of the tibiotalar and subtalar joints and its application to gait analysis in children with Juvenile Idiopathic. *J. Biomech.* 85:27–36, 2019.
- <sup>23</sup>Navacchia, A., C. A. Myers, P. J. Rullkoetter, and K. B. Shelburne. Prediction of in vivo knee joint loads using a global probabilistic analysis. *J. Biomech. Eng.* 138(3):031002, 2016.
- <sup>24</sup>Palmisani, E., N. Solari, A. Pistorio, N. Ruperto, C. Malattia, S. Viola, A. Buoncompagni, A. Loy, A. Martini, and A. Ravelli. Agreement between physicians and parents in rating functional ability of children with Juvenile Idiopathic Arthritis. *Pediatr. Rheumatol. Online J.* 5:23, 2007.
- <sup>25</sup>Pataky, T. C. One-dimensional statistical parametric mapping in Python. *Comput. Methods Biomech. Biomed. Eng.* 15(3):295–301, 2012.
- <sup>26</sup>Pradsgaard, D. Ø., B. Fiirgaard, A. H. Spannow, C. Heuck, and T. Herlin. Cartilage thickness of the knee joint in Juvenile Idiopathic Arthritis: comparative assessment by ultrasonography and magnetic resonance imaging. *J. Rheumatol.* 42:534–540, 2015.
- <sup>27</sup>Prinold, J. I., C. Mazzà, R. Di Marco, I. Hannah, C. Malattia, S. Magni-Manzoni, M. Petrarca, A. Ronchetti, L. T. de Horatio, E. H. P. van Dijkhuizen, S. Wesarg, and M. Viceconti. A patient-specific foot model for the estimate of ankle joint forces in patients with Juvenile Idiopathic Arthritis. *Ann. Biomed. Eng.* 44:247–257, 2016.
- <sup>28</sup>Ravelli, A., and A. Martini. Juvenile Idiopathic Arthritis. *Lancet* 369(9563):767–778, 2007.
- <sup>29</sup>Ravelli, A., S. Viola, A. Ruperto, B. Corsi, G. Ballardini, and A. Martini. Correlation between conventional disease activity measures in Juvenile Chronic Arthritis. *Ann. Rheum. Dis.* 56(3):197–200, 1997.
- <sup>30</sup>Rousseeuw, P. J., and M. Hubert. Anomaly detection by robust statistics. *Wiley Interdiscip. Rev.* 8(2):e1236, 2018.
- <sup>31</sup>Scheys, L., K. Desloovere, P. Suetens, and I. Jonkers. Level of subject-specific detail in musculoskeletal models affects hip moment arm length calculation during gait in pediatric subjects with increased femoral anteversion. *J. Biomech.* 44(7):1346–1353, 2011.
- <sup>32</sup>Scheys, L., D. Loeckx, A. Spaepen, P. Suetens, and I. Jonkers. Atlas-based non-rigid image registration to automatically define line-of-action muscle models: a validation study. *J. Biomech.* 42:565–572, 2009.
- <sup>33</sup>Scheys, L., A. Spaepen, P. Suetens, and I. Jonkers. Calculated moment-arm and muscle-tendon lengths during gait differ substantially using MR based versus rescaled generic lower-limb musculoskeletal models. *Gait Posture* 28:640–648, 2008.
- <sup>34</sup>Siegler, S., J. Chen, and C. D. Schneck. The three-dimensional kinematics and flexibility characteristics of the human ankle and subtalar joints—part I: kinematics. *J. Biomech. Eng.* 110(4):364–373, 1988.
- <sup>35</sup>Stebbins, J., M. Harrington, N. Thompson, A. Zavatsky, and T. Theologis. Repeatability of a model for measuring multi-segment foot kinematics in children. *Gait Posture* 23:401–410, 2006.
- <sup>36</sup>Steele, K. M., M. S. DeMers, M. H. Schwartz, and S. L. Delp. Compressive tibiofemoral force during crouch gait. *Gait Posture* 35(4):556–560, 2012.

- <sup>37</sup>Steger, S., M. Kirschner, and S. Wesarg. Articulated atlas for segmentation of the skeleton from head & neck CT datasets. *Med. Image Comput. Assist. Interv.* 15(2):66–73, 2012.
- <sup>38</sup>Thelen, D. G. Adjustment of muscle mechanics model parameters to simulate dynamic contractions in older adults. *J Biomech Eng.* 125(1):70–77, 2003.
- <sup>39</sup>Valente, G., G. Crimi, N. Vanella, E. Schileo, and F. Taddei. nmsBuilder: freeware to create subject-specific musculoskeletal models for OpenSim. *Comput. Methods Programs Biomed.* 152:85–92, 2017.
- <sup>40</sup>Valente, G., L. Pitto, D. Testi, A. Seth, S. L. Delp, R. Stagni, M. Viceconti, and F. Taddei. Are subject-specific musculoskeletal models robust to the uncertainties in parameter identification? *PLoS ONE* 9(11):e112625, 2014.
- <sup>41</sup>White, D. R., H. Q. Woodard, and S. M. Hammond. Average soft-tissue, and bone models for use in radiation dosimetry. *Br J Radiol.* 60:907–913, 1987.
- <sup>42</sup>White, S. C., H. J. Yack, and D. A. Winter. A three-dimensional musculoskeletal model for gait analysis. Anatomical variability estimates. *J. Biomech.* 22(8):885–893, 1989.
- <sup>43</sup>Wu, G., S. Siegler, P. Allard, C. Kirtley, A. Leardini, D. Rosenbaum, M. Whittle, D. D. D’Lima, L. Cristofolini, and H. Witte. ISB recommendation on definitions of joint coordinate system of various joints for the reporting of human joint motion—part I: ankle, hip, and spine. *J. Biomech.* 35:543–548, 2002.
- <sup>44</sup>Yamaguchi, G. T., and F. E. Zajac. A planar model of the knee joint to characterize the knee extensor mechanism. *J. Biomech.* 22(1):1–10, 1989.

**Publisher’s Note** Springer Nature remains neutral with regard to jurisdictional claims in published maps and institutional affiliations.

**7. The effect of muscle personalisation in  
the estimate of muscle forces and joint  
contact forces in post-menopausal women**

### *Acknowledgement of co-authorship*

This chapter includes the paper “The effect of muscle personalisation in the estimate of muscle forces and joint contact forces in post-menopausal women” planned for submission to IEEE Transactions on Biomedical Engineering in October 2019. The work is the result of the research carried out in collaboration with the co-authors listed in the paper.

My personal contribution was in the design of the study, implementation of the modelling procedure, quantification of the intra- and inter-subject anatomical and biomechanical variability, design of statistical analysis, interpretation of the results, and discussion with respect to the current knowledge available in the literature. Additionally, I was responsible for writing the paper and producing figures and tables.

Student:

Erica Montefiori  Date 25/07/2019

The main co-authors:

Claudia Mazza'  Date 25/07/2019

Barbara Maria Kalkman  Date 25/07/2019

Erica Montefiori<sup>1</sup>, Barbara Kalkman<sup>1</sup>, Bart van Veen<sup>1</sup>, Margaret Paggiosi<sup>1,3</sup>, Alison Clarke<sup>1,2</sup>,  
Eugene V. McCloskey<sup>1,3</sup>, Claudia Mazzà<sup>1</sup>

<sup>1</sup>Department of Mechanical Engineering and INSIGNEO Institute for *in silico* Medicine,  
University of Sheffield, Sheffield, UK.

<sup>2</sup>Gait and Movement Analysis Laboratory, Sheffield Teaching Hospitals NHS Foundation  
Trust, Sheffield, UK

<sup>3</sup>Mellanby Centre for Bone Research, Department of Oncology and Metabolism, University  
of Sheffield, Sheffield, UK

CORRESPONDING AUTHOR:

Erica Montefiori

Department of Mechanical Engineering  
INSIGNEO Institute for *in silico* Medicine  
University of Sheffield

Pam Liversidge Building - Room F14

Mappin Street, Sheffield, S1 3JD, UK

e-mail: e.montefiori@sheffield.ac.uk

Phone: +44 (0)114 2226073

TO BE SUBMITTED TO IEEE Transactions on Biomedical Engineering

## 7.1. Abstract

**Goal:** This study investigated the importance of muscle anatomical personalisation when estimating joint contact forces (JCFs) using musculoskeletal models (MSKMs) in a cohort of post-menopausal women. **Methods:** Motion capture and Magnetic Resonance Imaging data were used to produce three lower-limb MSKMs for eleven women: 1) a generic-scaled model (Gen); 2) a hybrid model (Hyb) with personalised joints and scaled muscle parameters; 3) a subject-specific model (SSp) with personalised joints and maximal isometric force ( $F_{\max}$ ) estimated from muscle volume ( $V_M$ ) and musculotendon length ( $l_{MT}$ ). Within- and between-subject comparison of  $V_M$  and  $l_{MT}$  was assessed to quantify asymmetry and anatomical variability across the cohort. Linearly scaled and personalised  $F_{\max}$  were compared and the effect of model personalisation on the estimated JCFs (OpenSim) was also assessed. **Results:**  $V_M$  and  $l_{MT}$  differed by up to 45% and 25%, respectively, both within and between subjects.  $F_{\max}$  varied by up to 230% when scaled or personalised leading to different muscle activation patterns affecting the muscle force estimates. JCFs were highly patient-specific and inter-model differences ranged between  $-1.2 \div 2.6$  BW,  $-1.4 \div 1.5$  BW, and  $-1.0 \div 1.8$  BW at the hip, knee, and ankle, respectively. **Conclusion:** The observed anatomical variability suggested that personalisation of  $F_{\max}$  should be pursued especially in certain clinical contexts, i.e. prediction of osteoporotic fracture, joint replacement or cerebral palsy. **Significance:** The proposed SSp model accounts for the first time for anatomical variability and asymmetry including personalised  $F_{\max}$ . A unique image-based dataset of bone and muscle anatomy of older women is now available to foster research in this field.

## 7.2. Introduction

Musculoskeletal (MSK) modelling is increasingly being adopted to estimate joint contact and muscle forces during dynamic tasks (Delp et al., 2007, Delp et al., 1990, Giarmatzis et al., 2015, Jonkers et al., 2008, Liu et al., 2008, Steele et al., 2010). Information about joint loading and muscle forces can be of particular interest in older individuals where both joint integrity and muscle strength are reduced, such as in the presence of sarcopenia, osteopenia, or osteoporosis.

MSK modelling techniques are often based on generic MSK models to be scaled to the subject anthropometric measures (Delp et al., 1990, Giarmatzis et al., 2015, Jonkers et al., 2008, Liu et al., 2008). However, these approaches tend to rely on many geometrical and anatomical assumptions, neglecting the individual variability and therefore, knowingly affecting the accuracy of the model outcomes (Bahl et al., 2019, Gerus et al., 2013, Martelli et al., 2015, Prinold et al., 2016, Scheys et al., 2006, Scheys et al., 2008a, Scheys et al., 2008b, Valente et al., 2014, Wesseling et al., 2016). Recently Ding et al. (2019) quantified how anthropometry (namely body mass, limb length and limb length to pelvis width ratio), together with gender, are particularly relevant when scaling a model. Bahl et al. (2019) observed errors of 37 mm in the identification of hip joint centre when using scaled models in populations with hip osteoarthritis and high body mass index. This error translated in erroneous estimates of hip muscles moment arm, especially affecting the flexor muscles. Additionally, scaled models do not account for loss of muscle strength typically associated to ageing (Brooks and Faulkner, 1994), which can be both subject- and muscle-specific (Maden-Wilkinson et al., 2013). These factors can influence the estimated muscle force distribution and thereby joint contact force (JCF) estimation (Ackland et al., 2012, De Groote et al., 2010). Therefore, a few studies have questioned whether the use of generic-scaled models with unscaled or linearly scaled muscle properties (derived from data of adult specimens) should be considered appropriate when investigating muscle function in pathological or juvenile populations (Kainz et al., 2018, Modenese et al., 2018). An attempt to overcome this limitation has come from clinical measurements of muscle strength (i.e. hand-held dynamometers), which however are not muscle-specific but rather assess muscle functional groups (Kainz et al., 2018).

Other authors investigated the effect of personalising geometrical and architectural muscle-tendon parameters, finding a moderate, but muscle-specific, sensitivity of models' output to maximal isometric force (Ackland et al., 2012, Valente et al., 2014). However, these studies were either based on the perturbation of the muscle parameters within small ranges (Ackland et al., 2012) or proportionally for all the muscles (Valente et al., 2014), therefore neglecting muscle or subject specificity in the variability of parameters such as maximal muscle stress (Buchanan et al., 2004).

Wesseling et al. (2016) presented an overview of the effect of different levels of model personalisation limited to the estimate of the hip JCF showing how highly personalised models can provide estimates of the first hip JCF peak more similar to those measured *in-vivo* with an instrumented prosthesis (Bergmann et al., 2001). They especially stressed the role of personalised muscle geometry, achieved introducing wrapping surfaces. Carbone et al. (2016) investigated the sensitivity of models to variations in the both MSK geometry and musculotendon (MT) parameters, highlighting its muscle-specificity. Arnold et al. (2010) used the average MT values from a large cadaveric dataset (n=21) (Ward et al., 2009) to personalise their model, reaching the conclusion that tuning individual muscle parameters might provide results that compare better to experimental measurements (Arnold et al., 2010). This conclusion supported the formulation of our hypothesis that intra- and inter-subject anatomical variability should be accounted in MSK models. In particular, we hypothesised that muscle volumes and, as a consequence, muscle paths and MT lengths might be especially variable across elderly due to preferential atrophy and muscle loss happening after a certain age (Handsfield et al., 2014). From here the choice of investigating anatomical variability in a cohort of older women. Additionally, to the best of our knowledge, a comprehensive analysis of the effect of an anatomical personalisation that includes both skeletal and MT parameters on the estimates of JCFs for the three main joints of the lower limb is still lacking in this population.

Therefore, the aim of this study was to investigate the effects of different levels of model personalisation on the estimation of the JCFs and muscle forces in postmenopausal women. To assess this, we created a linear scaled generic model as well as two subject-specific models, one with personalised skeletal and joint geometries and one with additional personalisation

of muscle paths and maximal isometric force ( $F_{\max}$ ). These models were applied to estimate joint contact forces (JCFs) in the main lower-limb joints of our cohort.

One of the barriers to image-based personalisation of MSK models is in the fact that this is highly time consuming and operator dependent. A few recent studies (Modenese et al., 2018, Montefiori et al., 2019, Scheys et al., 2006) have tried to promote standardised methodologies where an automated procedure can reduce modelling time. In this perspective, the availability of a database including muscles and bone geometries as obtained from Magnetic Resonance Imaging (MRI) segmentations would be essential to foster data and methods sharing and to promote the development of approaches based on statistical shape modelling or similar as an alternative to scaling from generic cadaver data. Ding et al. (2019) has proposed such a database for healthy young adults, however, the adoption of such data in studies involving older participants might not be appropriate.

The secondary aim of this study was hence that of providing the scientific community with an image-based dataset of bone and muscle anatomy of older individuals to foster the development of automatic image processing and modelling tools.

## **7.3. Methods**

### **7.3.1. Participants and data acquisition**

Eleven postmenopausal women ( $69\pm 7$  y,  $66.9\pm 7.7$  kg,  $159\pm 3$  cm) with osteopenia or osteoporosis presented to the Metabolic Bone Centre, Northern General Hospital in Sheffield, UK were recruited for this study. Inclusion criteria were having a DXA bone mineral density T-score at the lumbar spine or total hip (whichever is the lower value) below or equal to 1. Exclusion criteria included: BMI  $<18$  or  $>35$ , history of or current conditions known to affect bone metabolism and bone mass density, history of or current neurological disorders, prescription of oral corticosteroids for more than 3 months within the last year, history of any long term immobilisation ( $>3$  months), conditions that prevent the acquisition of musculoskeletal images, use of medications or treatment known to affect bone metabolism other than calcium/vitamin D supplementation and alcohol intake greater than 21 units per week. The study was approved by the UK NHS research ethics committee. The study was approved by the Health Research Authority East of England – Cambridgeshire and

Hertfordshire Research Ethics Committee and was conducted in accordance with the Declaration of Helsinki. Written informed consent was obtained from all participants.

Participants attended the hospital on one occasion. During this visit, participants underwent a 3D gait analysis and a lower limb MRI scan.

### *Gait analysis*

For the gait analysis, participants were asked to walk along a 10 m walkway barefoot at a self-selected walking speed. Marker trajectories from five valid walking trials were recorded at 100 Hz using a 12-camera motion capture system (Vicon, Oxford, UK). A modified Vicon plug-in-gait marker set was used (Figure 7-1). Ground reaction forces were simultaneously acquired at 1000 Hz using two force platforms (Kistler, Winterthur, Switzerland). Vicon Nexus was used to label marker trajectories and fill gaps <5 frames. Prior to the MRI scans, the position of several motion capture markers was drawn on the skin to allow exact replacement with MRI-visible markers during the scan.

Surface electromyography (EMG) data (Cometa srl, Milan, Italy) were recorded from five muscles: Vastus medialis, Biceps femoris long head, Gastrocnemius medial and lateral, Tibialis anterior.

### *Magnetic Resonance Imaging*

Full lower limb MRI was collected using a Magnetom Avanto 1.5 T scanner (Siemens, Erlangen Germany). A T1-weighted scanning sequence was used with an echo time of 2.59 ms, a repetition time of 7.64 ms, flip angle of 10 degrees and voxel sizes of 1.1x1.1x5.0 mm for the long bones and 1.1x1.1x3.0 mm for the joints. Within the MRI scans, all lower limb bones were segmented using Mimics 20.0 (Materialise, Leuven, Belgium). In each limb, 23 muscles were segmented, initially using the automated muscle segmentation toolbox (Mimics Research 20.0, Materialise, Belgium), after which the necessary manual adjustments were performed. To assess the inter-operator repeatability of the muscle segmentation procedure, muscle volume ( $V_M$ ) of three participants were determined independently by three different operators.

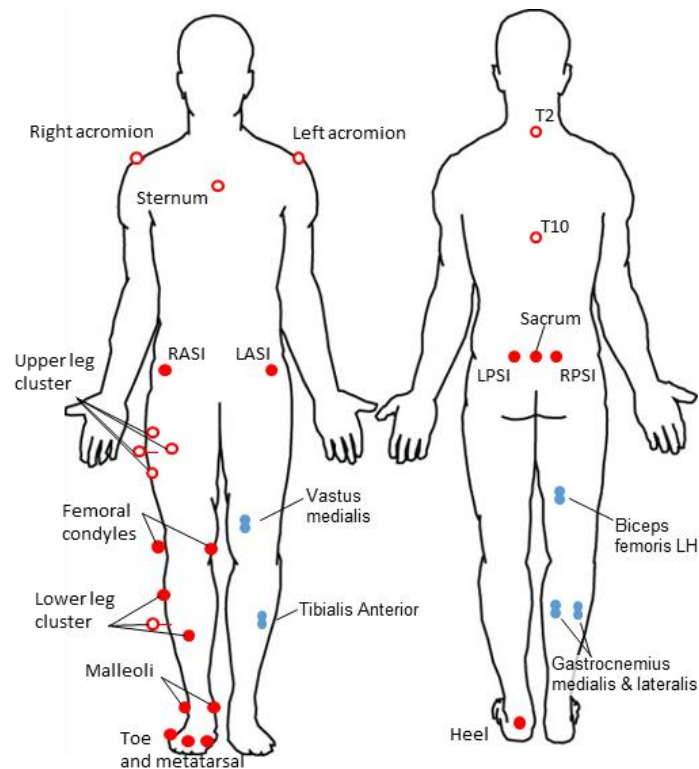


**Figure 7-1 - Marker placement as used during gait analysis and MRI scanning. Sixteen markers were placed during both gait analysis and MRI (filled red circles), nine extra markers were only used during gait analysis (open red circles). EMG of five muscles (blue closed circles) was collected during gait analysis.**

### 7.3.2. Musculoskeletal models

Three MSK models (Figure 7-2) were created for each individual with a different level of personalisation to estimate JCFs at the hip, knee, and ankle: (1) a generic-scaled MSK model (Gen); (2) a hybrid MSK model based on subject-specific bone geometries (Hyb); (3) a MSK model with subject-specific bone geometries as well as a personalised muscle parameters (SSp). Hyb and SSp models were complemented with virtual markers (visible in the MRI) used for the registration with gait analysis data.

#### *Generic-scaled model (Gen)*

The OpenSim gait2392 (Delp et al., 1990) model was adapted to include the experimental marker set used during the gait analysis and six additional markers corresponding to the joint's centres. The torso, with relevant joints and muscles, was removed and subtalar and metatarsophalangeal joints were locked. Best practice recommendations (Hicks et al., 2015) were followed to scale the model using the OpenSim Scaling Tool, with a maximum marker

error and RMS error below 2 cm and 1 cm, respectively. Joint centres were calculated from gait markers through the Harrington method (Harrington et al., 2007) (hip), or computed as the mid-point between condyle or malleoli experimental markers (knee and ankle, respectively). Body segments were scaled based on the ratio between pairs of corresponding experimental (from a static standing trial, including joint centre markers) and model markers placed on the generic model. The segment inertia was scaled based on the total body mass.

MT units were modelled using a three element Hill-type muscle model (Thelen, 2003), requiring the definition of the following five MT parameters: optimal fibre length ( $l_{opt}$ ), tendon slack length ( $l_{TS}$ ), pennation angle, maximal contraction velocity and  $F_{max}$ . The  $l_{opt}$  and  $l_{TS}$  were scaled to maintain the  $l_{opt}/l_{MT}$  and  $l_{TS}/l_{MT}$  ratios of the generic gait2392 model ( $l_{MT}$  = musculotendon length). The pennation angle was set according the gait2392 model and maximal contraction velocity was set to 10 fibres per second (Thelen, 2003). Values for  $F_{max}$  were linearly scaled to the whole-body mass from the gait2392 model according to the following equation:

$$F_{max} = \frac{m}{m_{Gen}} * F_{maxGen}$$

where  $m$  is the mass of the subject,  $m_{Gen}$  is the mass of the gait2392 model and  $F_{maxGen}$  is the default  $F_{max}$  of the muscles in the gait 2392 model.

### *Hybrid model (Hyb)*

The hybrid model was created segmenting bone geometries from the MRI and adapting a previously published modelling technique (Modenese et al., 2018, Montefiori et al., 2019), with the muscle origin and insertions directly identified on the MRI images. The kinematic model included seven body segments (pelvis, two femurs, two tibias, two feet) articulated by six joints. The hip joint was modelled as a ball-and-socket, and the knee and ankle as ideal hinges.

MT units were parametrised as previously described for the Gen model but updating  $l_{opt}$  and  $l_{tendon}$  with the values calculated from the origins and insertions identified on the MRI images.  $F_{max}$  was scaled to the lower-limb mass according to:

$$F_{max} = \frac{m_{LL}}{m_{LLGen}} * F_{maxGen}$$

where  $m_{LL}$  is the mass of the lower limb of the subject, calculated as a product of the volume of the lower limb (estimated from the MRI) and the density of the tissue (White et al., 1987)) and  $m_{LLGen}$  is the mass of the lower limb of the gait2392 model.

### *Subject-specific model (SSp)*

The SSp model was built adapting the Hyb model and differed from it for the definition of muscle points and  $F_{max}$ . Where possible, muscle paths from the Hyb model were adjusted checking against the MRI and moving via points to better match the centreline of the 3D segmentation. In particular, this was done for: origin points of the Gluteus medius and minimus, and Soleus; via points of the Iliacus, Psoas, Rectus femoris, Tensor fasciae latae, Semimembranosus, Gastrocnemius medial and lateral, and Sartorius; insertion points of the Gastrocnemius medial and lateral, and Soleus. The  $F_{max}$  was calculated on the basis of the well-known relationship with physiological cross-sectional area (PCSA) (Fick, 2012) using segmented muscle volumes according to:

$$F_{max} = k * \frac{V_M}{l_{opt}}$$

where  $k$  is the specific tension (61 N/cm<sup>2</sup>, (Arnold et al., 2010)),  $V_M$  is the volume of the segmented muscle, and  $V_M/l_{opt}$  corresponds to the muscle PCSA

To further evaluate the differences between the SSp and the Hyb models, two intermediate models were built: Hyb<sub>SSpPath</sub>, where the Hyb model was complemented with personalised muscle path from the MRI segmentations; Hyb<sub>SSpFmax</sub>, where the Hyb model had  $F_{max}$  calculated from the MRI  $V_M$ .

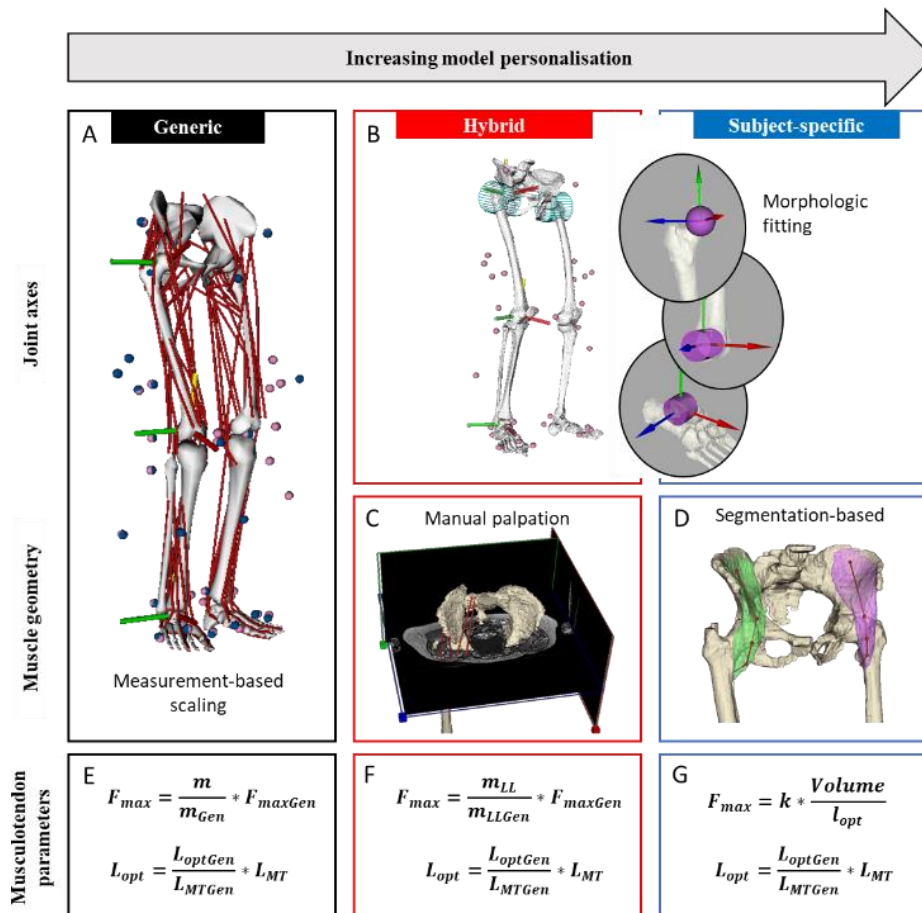


**Figure 7-2 – A) Gen model, with scaled joint axes and muscle geometry (OpenSim Scaling Tool); B) joint axes identification through morphologic fitting in Hyb and SSp; C) identification of the muscle attachments and via points from manual palpation of the MRI in the Hyb model; D) identification of the muscle attachments and via points from the centre line of the segmentations in the SSp model; E), F), G) calculation of the muscle parameters for Gen, Hyb and SSp, respectively.**

### *Dynamic simulations*

Joint angles and moments were computed with the Inverse Kinematics (marker weights set to 1 for all the markers) and Inverse Dynamics (coordinates filtered at 6 Hz) tools in OpenSim 3.3 using the MATLAB API (v9.1, R2017b, Mathworks, USA) and following the OpenSim recommendations (Hicks et al., 2015). Static Optimisation was then run minimizing the sum of muscle activations squared (Anderson and Pandy, 2001) and neglecting the force-length-velocity (FLV) relationship of the muscles to compute their force and activation. This choice was motivated by the fact that including FLV relationship led to saturation of most of the muscle activations. This was likely due to the use of personalised muscle parameters, instead of the default parameters, for whom the FLV relationship was meant to be implemented. This choice was pursued for all the models and simulations. Ideal moment generators (reserve

actuators), providing joint torque when muscle forces could not balance the external moments, were included for each degree of freedom, but made unfavourable to recruit by assigning them a unitary maximum force. Finally, Joint Reaction Analysis (Steele et al., 2012) was run to calculate joint contact forces (JCFs).

All analyses were repeated for the three modelling approaches and for all trials. A qualitative validation was performed comparing the estimated muscle activations to measured EMG data (when available) and by ensuring the contribution of reserve actuators to joint dynamics never exceeded 5% (van der Krogt et al., 2012). Joint angles, moments and resultant JCFs (scaled to body weight, BW) were estimated for the hip, knee and ankle and averaged among the available trials for each subject and each modelling approach.

### **7.3.3. Data analysis**

Intra- and inter-operator repeatability of the muscle segmentation and consequent  $V_M$  calculation was assessed for the 22 muscles fully visible in the MRI by calculating the maximum standard deviation (SD) and coefficient of variation (CoV) over three repetitions. All muscle segmentations used for the following analyses were generated by the same expert operator.

To discard the hypothesis of anatomical symmetry, the differences between the  $V_M$  of the muscles belonging to the left and right limbs were assessed with a paired *t-test* (significance level,  $\alpha=0.05$ ) and the CoV between subjects was quantified. The same analysis was used to investigate the symmetry of the  $I_{MT}$ , as calculated after extracting the paths of the 30 analysed muscles (22 muscles including 4 with three bundles) from the centre lines of the segmentations.

The effect of personalising  $V_M$  and  $I_{MT}$  on the calculated  $I_{TS}$ ,  $I_{opt}$ , and  $F_{max}$  was quantified by comparing the values in the Hyb and SSp and reported as a percentage difference for the right and left limb separately. This choice was dictated by the interest in understanding the propagation of possible asymmetries observed in the  $V_M$  and  $I_{MT}$  to the  $I_{TS}$ ,  $I_{opt}$ , and  $F_{max}$ . A paired *t-test* was used to investigate statistical significance of the observed differences in the 30 muscles personalised in the models.

A repeated measure ANOVA ( $\alpha=0.05$ ) was used to compare the JCFs estimated with the three different MSK approaches by means of 1D statistics based on Statistical Parametric Mapping (SPM) in MATLAB, using the SPM1D package (SPM1D, [www.spm1d.org](http://www.spm1d.org), v M.0.4.5, (Pataky, 2012)). If statistical significance was reached, post hoc independent paired *t*-tests were performed to determine between which groups significant differences occurred. Bonferroni corrections were used to calculate the critical p-value used for post hoc analysis being set to  $p=0.017$ . A further repeated measure ANOVA ( $\alpha=0.05$ ) assessed differences between peak JCFs using the Hyb and SSp and the intermediate models Hyb<sub>SSpPath</sub> and Hyb<sub>SSpFmax</sub>. Post hoc independent paired *t*-tests were run when relevant (Bonferroni correction,  $p=0.0125$ ).

## 7.4. Results

Inter-operator repeatability resulted in a maximum SD between 2.8 cm<sup>3</sup> (Gastrocnemius lateral) and 31.5 cm<sup>3</sup> (Vastus lateralis) corresponding to a CoV of 4.6% and 9.8%, respectively. The values of individual  $V_M$  for the left and right leg have been included as supplementary material in Appendix II.

### 7.4.1. Anatomical variability

#### *Volumes*

The group mean and SD values for muscle volumes are reported in Figure 7-3 as a fraction of the total limb muscle volume as this allows comparison of the results to previous *in-vivo* literature (Handsfield et al., 2014). The calculated  $V_M$  of the hip, knee, and ankle main muscles are also listed in Figure 7-4 to highlight the evident intra- and inter-subject variability of these quantities. The Sartorius, Gluteus maximus, Adductor magnus, and Vastus lateralis, were on average all significantly lower in the left than in the right limb. In some subjects, the asymmetry between the two limbs was over 45% for single  $V_M$ . The inter-subject CoV ranged between 13% (Tibialis anterior) and 35% (Gracilis).

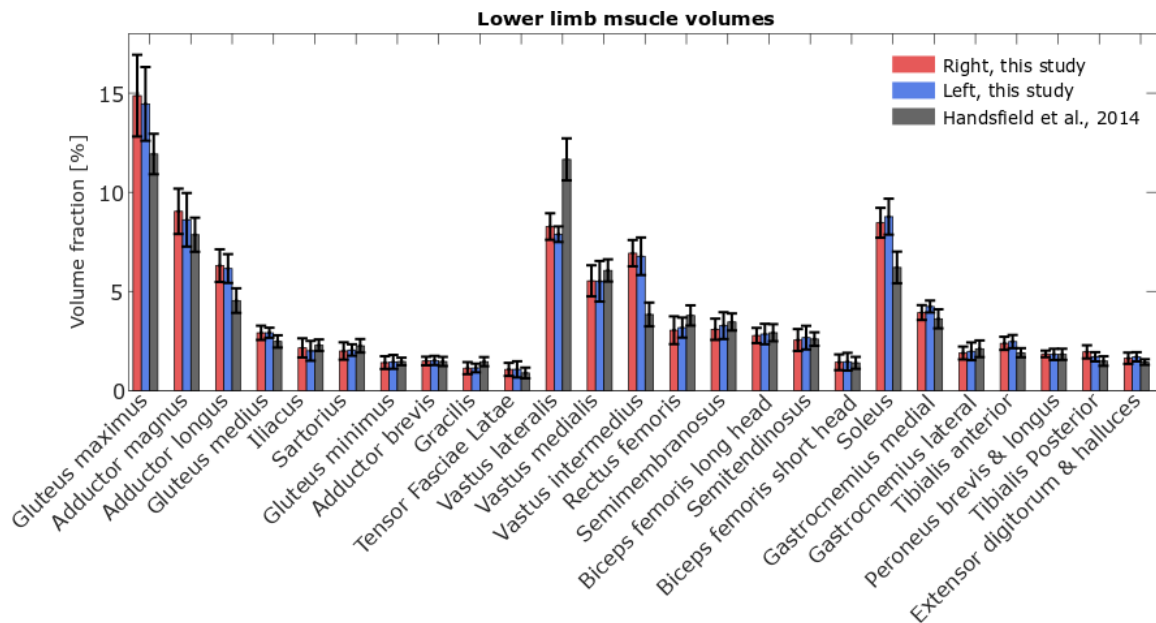


**Figure 7-3 – Mean±SD muscle volume calculated as a fraction of total limb muscle volume for the right and left limb of the eleven subjects in the present study and for the cohort of young adults enrolled by Handsfield et al. (2014).**

### *Musculotendon lengths*

The personalised  $l_{MT}$  measured in the SSp model are reported in Figure 7-5. Differences between limbs reached 25% of the value and were particularly high for the Glutei. A significant difference between the two limbs was observed on average for the Gluteus maximus (II bundle), Gluteus medius (II and III bundles), Gluteus minimus (I bundle), Iliacus, Adductor magnus (III bundle), Rectus femoris, and Vastus intermedius and lateralis. Once again, high inter-subject variability was observed: inter-subjects CoV ranged between 2% (Tensor fasciae latae) and 14% (Gluteus medius II bundle). Longer MT units were measured in the right limb for certain muscles of a given individual and in the left limb for others, without any obviously recognisable pattern.

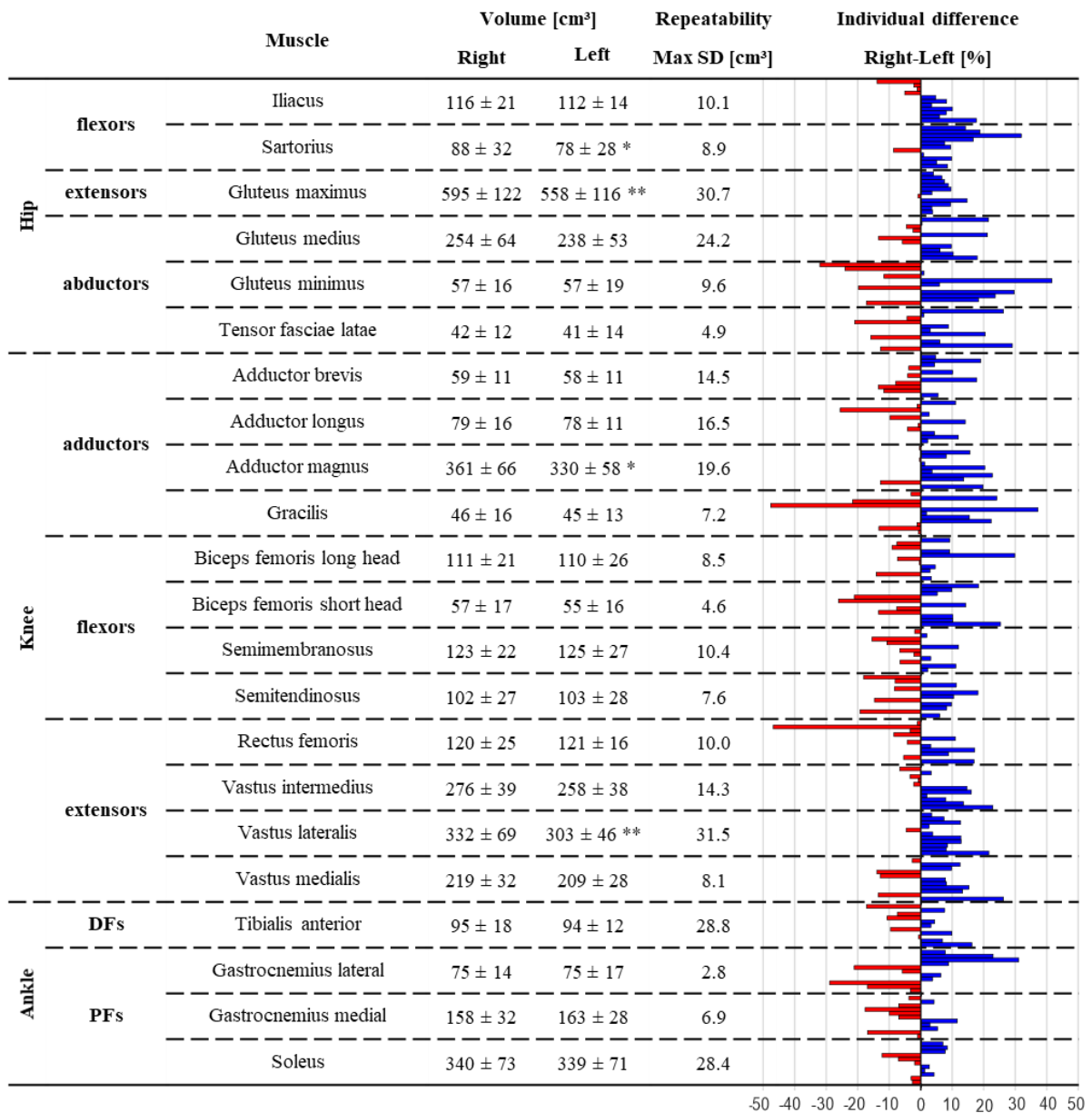


**Figure 7-4 - Mean±SD of muscle volumes (significant difference between left and right: \* p<0.05, \*\*p<0.01) and maximum SD from the repeatability analysis. Individual percentage difference between the legs is reported as a bar plot where each bar represents a participant: blue positive (red negative) values show that the right leg is bigger (smaller). DFs and PFs stand for dorsi and plantar flexors, respectively.**

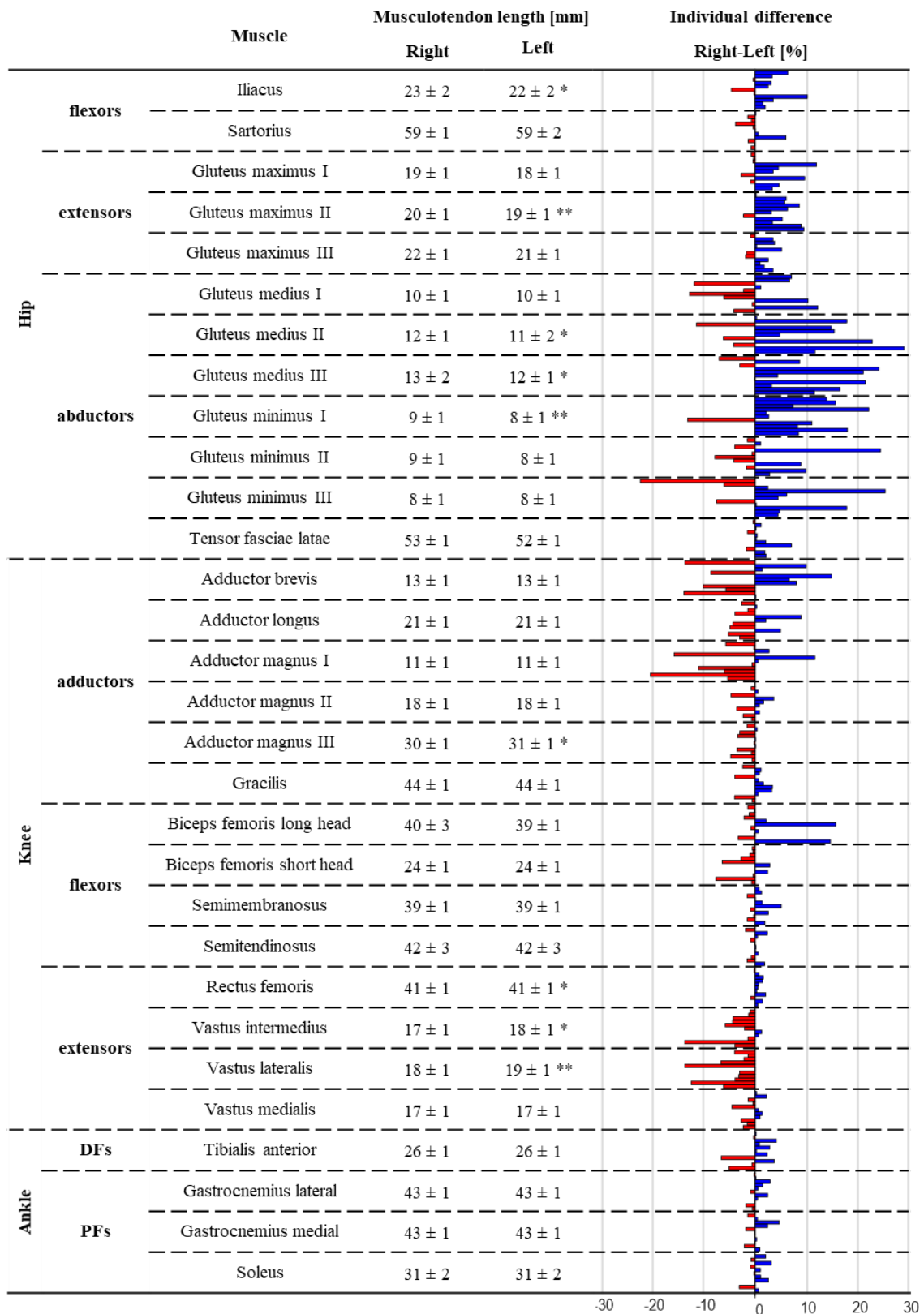


Figure 7-5 - Mean±SD of musculotendon length (significant difference between left and right: \* p<0.05, \*\*p<0.01). Individual percentage difference between the legs is reported as a bar plot where each bar represents a participant: blue positive (red negative) values show that the right leg is bigger (smaller). DFs and PFs stand for dorsi and plantar flexors, respectively.

## 7.4.2. Musculotendon parameters

### *Tendon slack length and optimal fibre length*

The comparison between the  $l_{ST}$  and  $l_{opt}$  estimated in the Hyb and SSp models highlighted differences above 80% (for  $l_{ST}$ ) and 50% (for  $l_{opt}$ ) in some isolated cases (i.e Vastus lateralis and medialis). The CoV of the difference between Hyb and SSp across all the muscles and subjects was 150% for both parameters. A specific pattern could not be identified, since none of the subjects presented values consistently higher (or smaller) in any of the two models. The values differed from subject to subject and from muscle to muscle and significant difference between Hyb and SSp values was found only for the  $l_{ST}$  and  $l_{opt}$  of the Soleus ( $p < 0.01$ ) and for the  $l_{opt}$  of the Sartorius, Gluteus medius (III bundle), Tensor fasciae latae and Gastrocnemius lateralis ( $p < 0.05$ ). The inter-model differences were consistent for the two body sides (see Appendix II for additional material).

### *Maximal isometric force*

The  $F_{max}$  was calculated from the PCSA, obtained dividing the MRI-measured  $V_M$  by the  $l_{opt}$ . The PCSA values are reported in Figure 7-6, where they are also compared to literature data from an *ex-vivo* study (Ward et al., 2009).

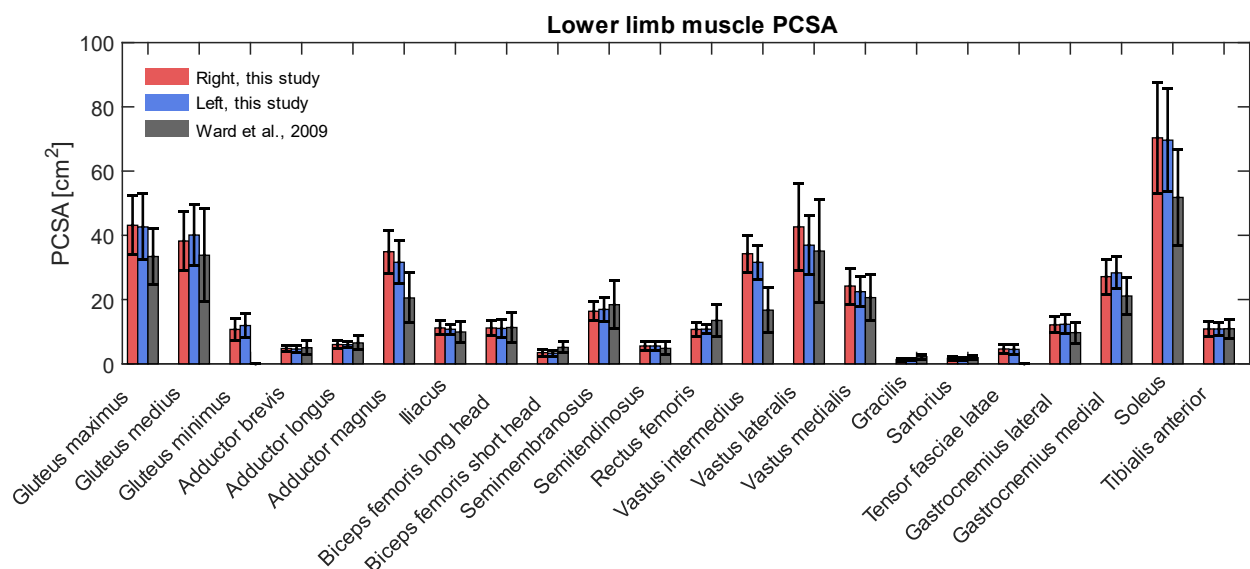


**Figure 7-6 – Mean±SD physiological cross-sectional area (PCSA) of the main muscles of the right and left lower limb estimated from muscle volumes of the eleven subjects in the present study and compared to those measured from cadavers by Ward et al. (2009).**

The  $F_{max}$  calculated from the individual  $V_M$  (SSp) differed from that of the Hyb for up to 230% of the value for single cases. CoV of the difference between Hyb and SSp was above 80% across all the muscles and subjects (Figure 7-7). For this parameter, a trend could be observed in some muscles with the Gluteus maximus, Gluteus medius (I bundle), Adductor magnus, and Vastus intermedius, presenting consistently and significantly bigger  $F_{max}$  in the SSp. Similarly, the Iliacus, Gracilis, Biceps femoris short head, and Rectus femoris presented a significantly smaller  $F_{max}$  in the SSp for all subjects and in both limbs.

### **7.4.3. Muscle activations**

Muscle activations were compared for 86 muscle (the 92 included in the gait2393 minus those removed as attaching to the torso) at each point of the gait cycle quantifying the differences between SSp and Hyb, SSp and Gen, and Hyb and Gen (Figure 7-8). The SSp model showed constantly lower activation of the hip abductors during stance and lower activation of the knee flexors and ankle plantar flexors during mid- and late stance, with respect to both SSp and Hyb. This was associated to higher activation of the knee adductors during late stance and of the knee extensors during mid- and late stance. The Gen model presented higher activation of the hip rotators and flexors, especially during mid- and late stance, associated to lower knee extensors activation.

Unfortunately, EMG data was not recorded on regular basis due to technical difficulties. Nonetheless, in those subjects/trials where the EMG signals were available, these showed consistency with the muscle activations estimated by the three models (Figure 7-9).

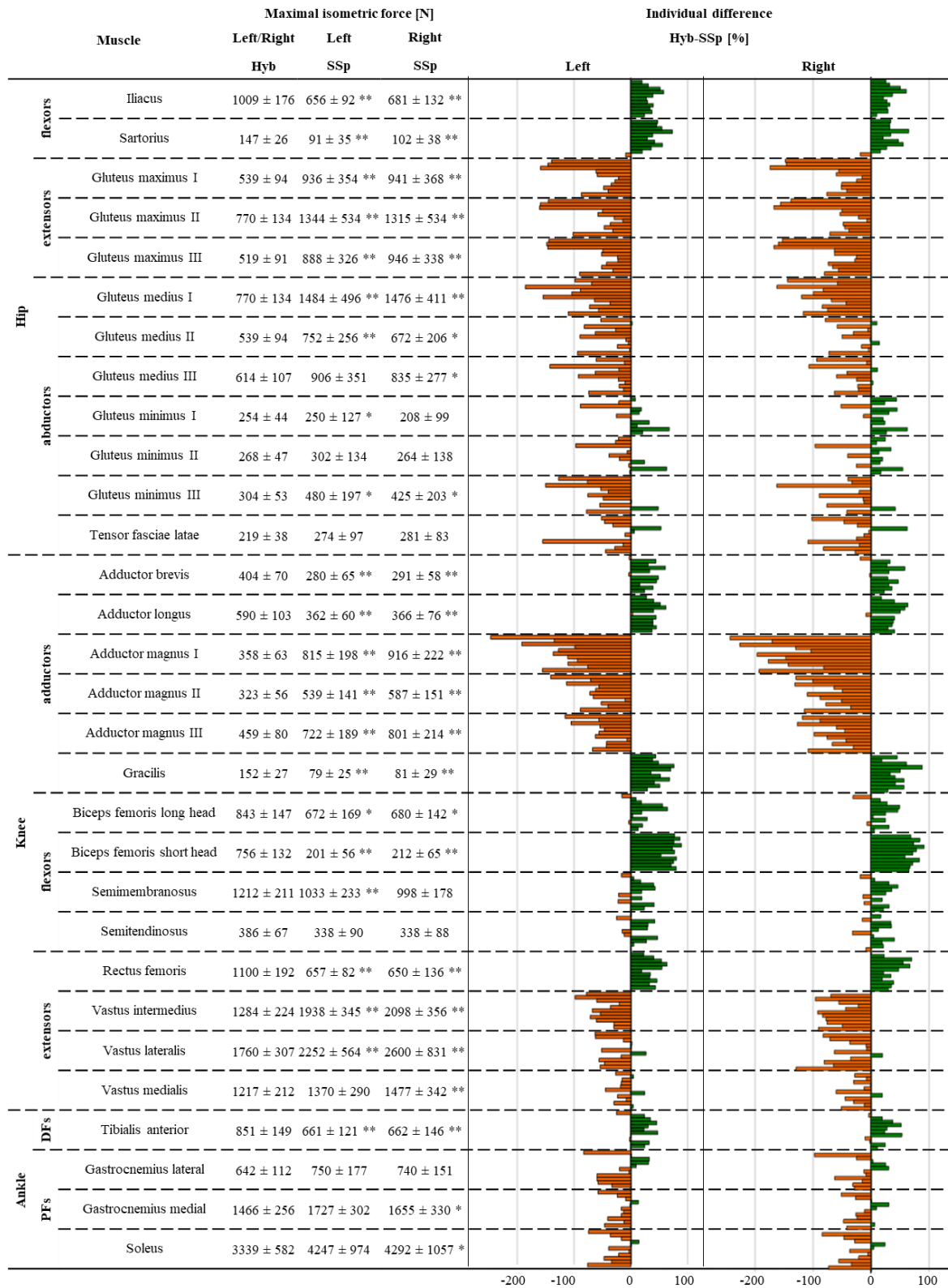


Figure 7-7 Mean±SD of the maximal isometric force for the right and left muscles personalised in the SSp model and percentage difference between Hyb and SSp (\* p<0.05, \*\*p<0.01). Individual percentage difference is reported as a bar plot where each bar represents a participant: green positive (orange negative) values show that the optimal fibre length in the Hyb model is bigger (smaller). DFs and PFs stand for dorsi and plantar flexors, respectively.

#### 7.4.4. Joint contact forces

JCFs were found to vary both between individuals and between models, with the repeated measure ANOVA highlighting some significant differences; the post hoc paired *t*-test (Figure 7-10) revealed higher average estimates of hip contact force during push off phase for the SSp model, whereas the Hyb model estimated higher hip contact forces during initial contact. On average, the Gen model always provided the lowest hip peak JCF values among the three models. At the knee, the SSp model showed the smallest contact force during initial contact, whereas the Hyb presented the highest estimates for the second knee peak and push off phase. At the ankle, a significant difference was observed only between Hyb and Gen, with the former estimating higher peak JCFs.

Average peak differences of JCFs were generally small, between 0.4 BW (between Hyb and Gen at the ankle peak) and 0.7 BW (between SSp and Gen at the second hip peak). However, inter-model absolute differences for individual subjects reached up to 2.5 BW, 1.2 BW, and 1.8 BW, at the hip, knee, and ankle late stance peaks, respectively (Figure 7-10). Moreover, as a consequence of inter-subject differences in the MT parameters, some subjects presented consistently higher estimates with one model throughout the gait cycle, whereas others showed higher values with one model during early stance and lower during late stance and vice versa. Similarly, inter-model differences varied notably throughout the gait cycle, with maximum values not necessarily found in correspondence of JCF peaks.

Despite being of negligible amplitudes and as such of little relevance, JCFs were found to vary significantly between models during most of the swing phase at the hip and knee and during terminal swing phase at the ankle.

The peak values for the hip, knee, and ankle JCFs obtained at intermediate stages of model personalisation are shown in Figure 7-11. A clear pattern was observed for the first hip and the two knee peaks, with Hyb giving the highest estimates, followed by Hyb<sub>SSpPath</sub>, Hyb<sub>SSpFmax</sub>, and SSp, respectively. The opposite trend was observed for the second hip peak. In detail, negligible differences were observed on average between Hyb and Hyb<sub>SSpPath</sub> (all below 0.3 BW) and between SSp and Hyb<sub>SSpFmax</sub> (below 0.2 BW). The largest difference was 0.6 BW between Hyb and SSp at the second knee peak. The repeated measure ANOVA with post hoc paired *t*-test ( $p=0.0125$ ) showed significant difference between the peaks ( $p<0.001$ ) for most

comparisons at the first knee and hip peaks and at the second hip and knee peaks. Less consistent patterns were observed at the ankle.

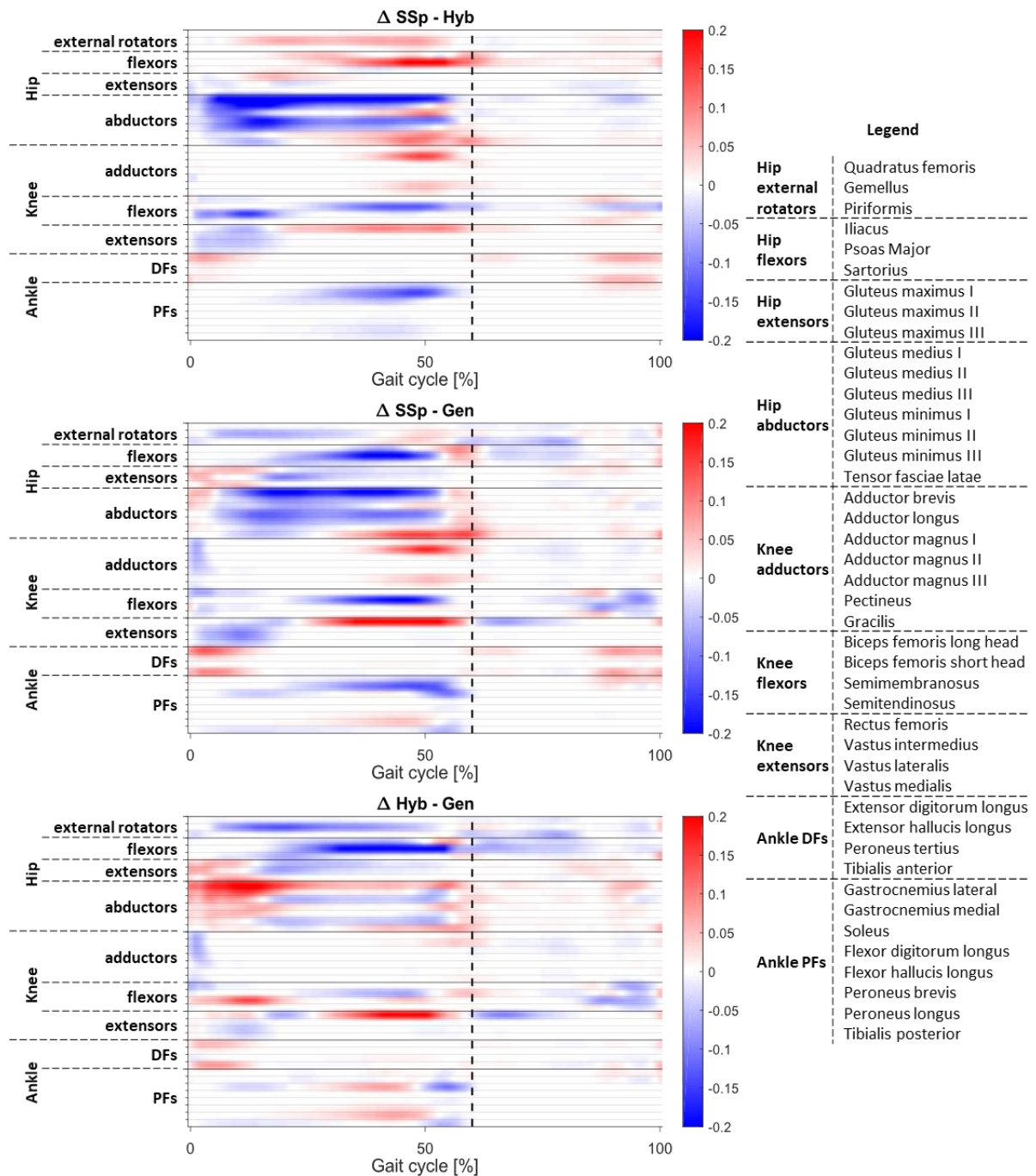


**Figure 7-8 - Comparison of muscle activation patterns between the different models. Average difference over all subjects for SSp vs Gen model (top), SSp vs Hyb model (middle) and Hyb vs Gen model (bottom). Each row corresponds to an individual muscle according to the list specified in the table. Vertical dashed line indicates the time instant when toe off occurred. DFs and PFs stand for dorsi and plantar flexors, respectively.**

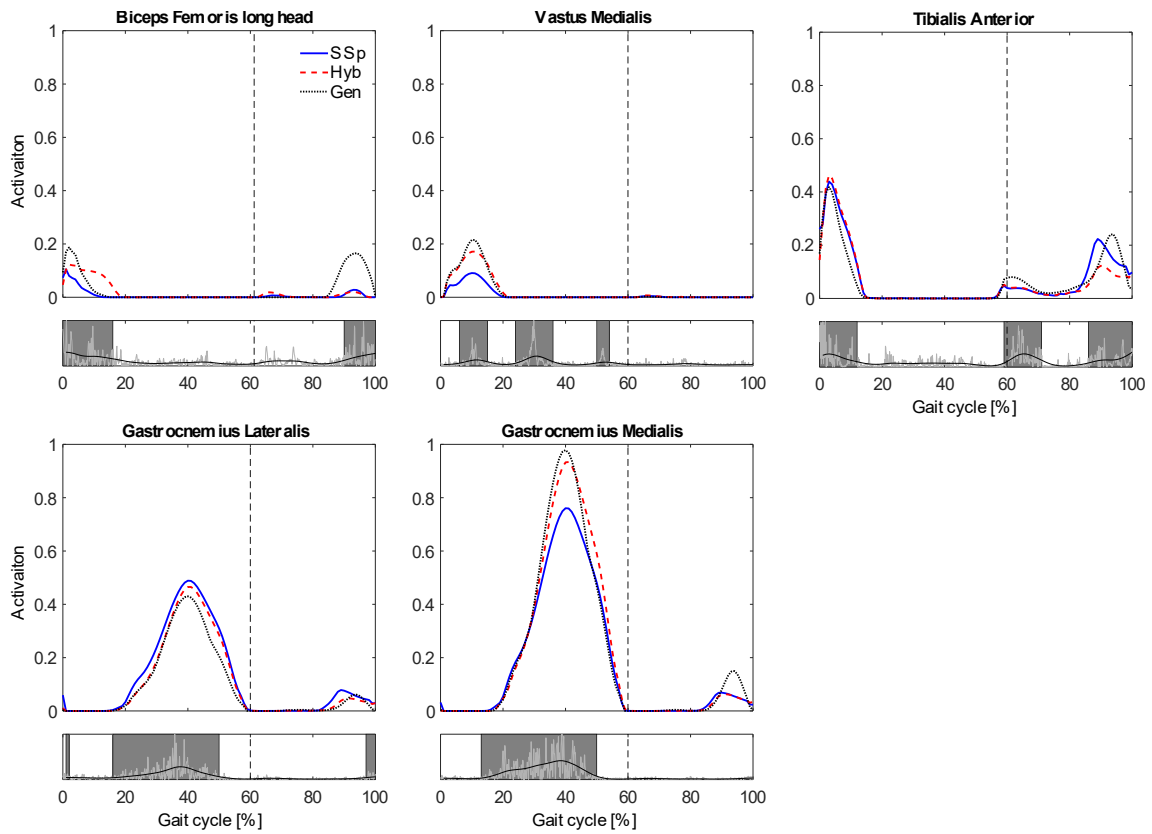


**Figure 7-9 - Example of EMG signal (bottom box) and muscle activation (top box) estimated with SSp, Hyb and Gen for five muscles of one subject.**

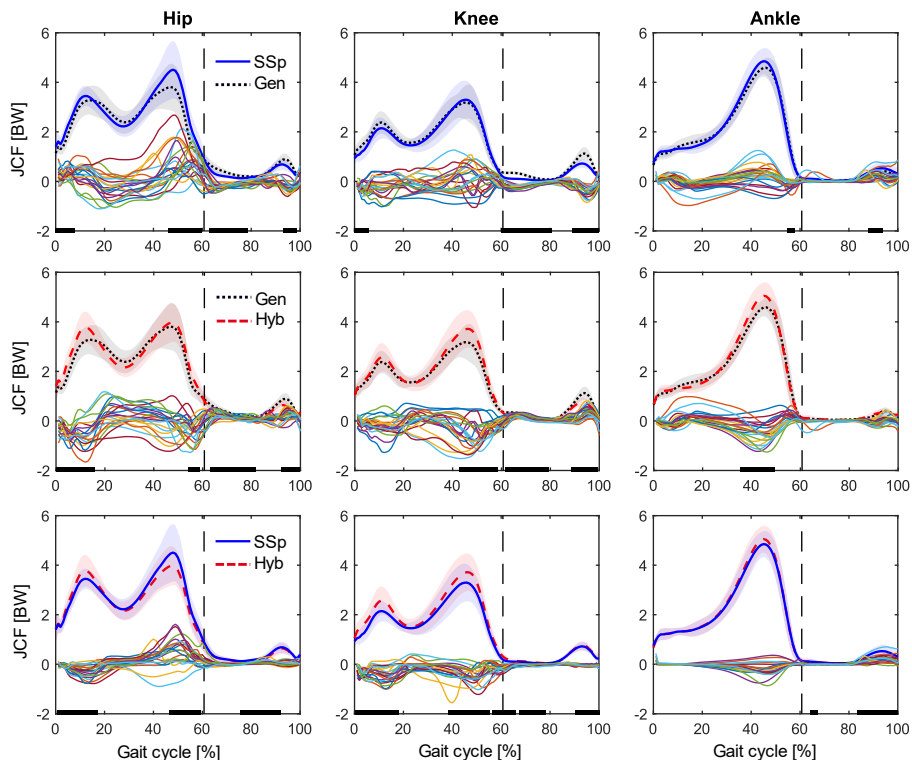


**Figure 7-10 - Mean  $\pm$  1SD JCFs (bold lines) for the SSp and Gen (top), Gen and Hyb (middle), and SSp and Hyb (bottom) and SSp-Gen (top), Gen-Hyb (middle), and SSp-Hyb (bottom) differences for individual limbs (thin lines). Black bars indicate significant differences (post hoc test,  $p=0.017$ ).**

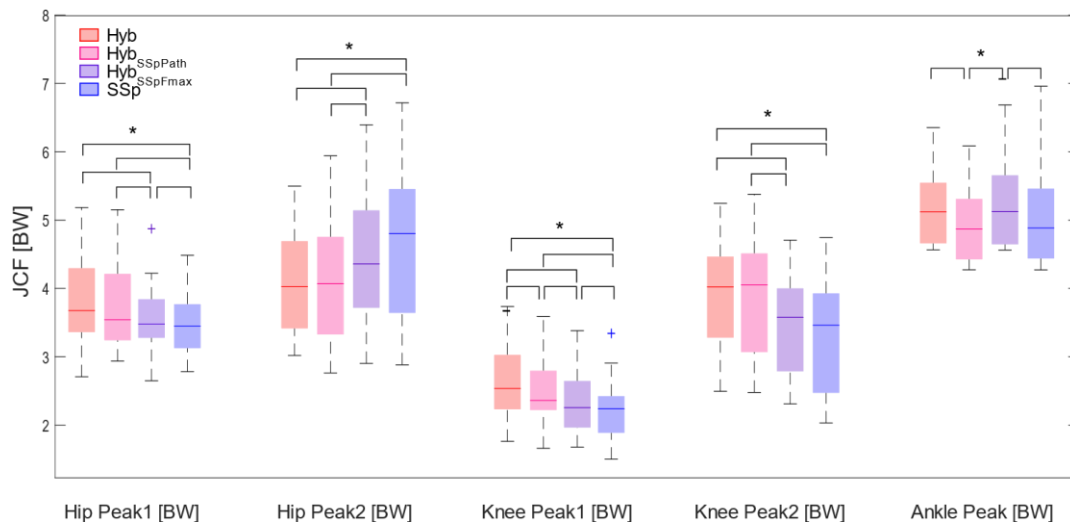


**Figure 7-11 - Statistical distribution of the peak JCF for hip, knee, and ankle with the Hyb, by Hyb<sub>SSpPath</sub>, Hyb<sub>SSpFmax</sub>, and SSp models. \* = significant difference ( $p < 0.001$ ).**

## 7.5. Discussion

This study aimed at quantifying to what extent model specificity can affect the results of MSK simulations, in light of a newly quantified variability of muscle anatomy in older women. To this purpose, 3D bone and muscle geometries extracted from MRI data collected from eleven post-menopausal women were combined with motion capture data to generate MSK models at various level of personalisation.

This is, to our knowledge, the first study providing a quantification of muscle volumes and musculotendon lengths in older women. Despite the average height and weight of our cohort being smaller we found slightly larger  $V_M$  than those previously reported for an *ex-vivo* cohort (Ward et al., 2009), This could be explained by the loss in muscle mass in cadavers, which in that study was used to calculate the volumes (Ward and Lieber, 2005). On the contrary, our  $V_M$  were slightly smaller than those estimated *in-vivo* from MRI in both young ( $25.5 \pm 11.1$  years) (Handsfield et al., 2014) and older adults ( $61.5 \pm 6$  years) (Almurudhi et al., 2016), which might be justified by those studies involving also male participants. This likely also explains the smaller inter-subject variability found in our study. When quantified as a fraction of total limb muscle volume, the  $V_M$  values of our cohort were indeed similar to those reported for young adults (Handsfield et al., 2014).

This study also presented, for the first time, a thorough assessment of the effects of skeletal and muscle anatomical variability between body sides and across individuals. When looking

into variability between limbs of the same subject, we observed up to 45% of  $V_M$  and up to 25% of  $l_{MT}$  differences. This suggests that, conversely from most common approaches, care should be taken in assuming symmetry when assigning MT parameters, even in healthy populations. The inter-subject variability was between 13% and 35% for the  $V_M$  and between 2% and 14% for the  $l_{MT}$ , in line with previous literature (Ward et al., 2009). The largest values were observed for the Gluteus medius and minimus, Biceps femoris short head, Semitendinosus, Gracilis, Sartorius, Tensor fasciae latae (for the  $V_M$ ) and for the Gluteus medius and minimus, Vastus medialis and lateralis, Soleus, Tibialis anterior (for the  $l_{MT}$ ). Subject-specific models can better resemble anatomical variability compared to generic-scaled models (Ding et al., 2019) and skeletal personalisation alone does not significantly modify the model estimates of the hip JCF (Wesseling et al., 2016). Furthermore, the force/torque-generation capacity of a given muscle can be more or less sensitive than that of others to changes either in the moment arm and length of the musculotendon units or in the MT parameters (Carbone et al., 2016). In light of these considerations and of the here observed intra-and inter- subject variability, it seems evident that personalisation should be pursued for muscle volumes and lengths.

In the present study, we investigated the effects of both skeletal personalisation and different degrees of muscle personalisation. The interpretation of these results needs to be handled with care, due to the intrinsic limitation associated to using ideal hinge joints to represent the knee and the ankle, which might not account for their real movement (Siegler et al., 1988, Yamaguchi and Zajac, 1989). While this simplification is widely accepted in MSK modelling (Modenese et al., 2018), a more realistic representation, possibly including the patellofemoral joint and tendons, might change the sensitivity of the output to the model personalisation investigated here.

Identifying the MT path from the centre line of the segmented muscle ( $Hyb_{SSpPath}$ ) did not significantly alter the estimates of JCFs with respect to a manual identification of the muscle points on the MRI (Hyb), except for lower peak values of the ankle JCF. The first procedure, however, allows the automation of the MT path identification, which would significantly reduce the operator time and favour repeatability. An intrinsic limitation of this approach, however, is associated to the fact that the MRI data were acquired in supine position, which

certainly affected the muscle centre line and moment arm estimation. Alternative technologies, allowing for standing imaging, might help to overcome this issue.

The maximal force that a muscle can produce is highly affected by its PCSA (Fick, 2012). In our study, we calculated the PCSA dividing the MRI-measured  $V_M$  by the  $l_{opt}$ , with the latter being scaled from a generic model (gait2392 (Delp et al., 1990)) while maintaining the  $l_{opt}/l_{MT}$  ratio. The specific tension ( $k$ ) of a muscle also contribute to the estimate of  $F_{max}$ . Previous studies suggested that muscle weakening associated to aging may exceed the muscle mass loss, causing a decrease in the muscle specific tension (Davies et al., 1986), but contrasting findings disproved this hypothesis (Häkkinen and Häkkinen, 1991). The lack of consensus on this matter justified the choice of setting  $k$  to 61 N/cm<sup>2</sup> for all the muscles, for consistency with previous literature (Arnold et al., 2010). Sensitivity of models to this parameter was previously tested by Valente et al. (2014) finding a moderate effect on the model output. In the effort of maximally personalising the muscle parameters, individual values for the specific tension should be obtained for different subjects and different muscles, however such a measure is not currently available *in-vivo*. The use of dynamometer could provide further insight in the specific tension of muscle groups and overcome this limitation.

Our approach led to PCSA values in agreement with literature cadaveric data (Ward et al., 2009). Further efforts in automated extraction of  $V_M$  from the MRI would be needed for a broader implementation of this method, since muscle segmentation is indeed extremely time-consuming (10 hours per subject on average for this study). The dataset shared with this paper will likely foster advances in this field.

The estimated  $F_{max}$  were overall bigger when based on  $V_M$  than when linearly scaled to lower-limb mass, especially for the hip extensors (Gluteus maximus) and abductors (Gluteus medius and Tensor fasciae latae) and for the knee extensors (Vastii) and adductors (Adductor magnus). As a consequence of muscle strength and volumes loss associated with ageing (Brooks and Faulkner, 1994), a reduction of 20% of  $F_{max}$  could be expected at an age of about seventy years (Thelen, 2003). This would have suggested smaller  $F_{max}$  values for most muscles when using a SSp approach as opposed to scaling. Surprisingly, this was only true for the Iliopsoas, Hamstrings, Rectus femoris, Gracilis, Sartorius and Tibialis anterior. Nonetheless, this result somehow confirms previous literature suggesting that the linearly scaled approaches, such as the one implemented in Hyb, might only be appropriate for certain

muscles (De Groote et al., 2010). Further research would be needed to confirm this hypothesis.

When looking at the JCFs, it was observed that  $\text{Hyb}_{\text{SSpF}_{\text{max}}}$  provided significantly lower early stance hip peak, and early and late stance knee peaks, but significantly higher late stance hip peak than Hyb, where  $F_{\text{max}}$  was linearly scaled from literature values. No differences were observed at the ankle. This partially contrasts with findings from a sensitivity study from Ackland et al. (2012), whose model output was not affected by either  $F_{\text{max}}$  or muscle moment arm variations. However, in their study, a variation limited to +10% and -10% of the nominal value was imposed, whereas our data showed that  $F_{\text{max}}$  might vary by up to 230%. Model personalisation (SSp and Hyb) led on average to higher estimates of the JCFs than when using a generic (Gen) approach, particularly in correspondence of the peaks. Differences between the three models ranged between 0.0 BW and 2.5 BW and were not consistent for the two limbs of the same subjects. Additionally, maximum differences between the models tended to occur in different phases of the gait cycle. This result is easily explained by the anatomical variability observed in the cohort, which is only accounted for in the SSp model. In fact, it is well known that  $F_{\text{max}}$ ,  $l_{\text{opt}}$ , and especially  $l_{\text{ST}}$  heavily impact the estimate of MSK models (Carbone et al., 2016, De Groote et al., 2010), and that a reduction in an individual muscle ability to produce force can be compensated by the action of other muscles (Carbone et al., 2016). Nonetheless, a comprehensive understanding of these compensatory mechanisms would require a different modelling approach, accounting for muscle synergies (Lloyd and Besier, 2003).

In all models, muscles were treated as ideal force generators (i.e. no force-length-velocity relationship was implemented). It has been shown that during normal gait, muscles operate close to their optimal length (Lichtwark et al., 2007, Rubenson et al., 2012) and in a generic model the effect of this assumption on JCFs can be considered as negligible (Anderson and Pandy, 2001). Moreover, since this modelling choice was consistent throughout all the simulations, we do not expect this limitation to have influenced our results. As expected, different values of  $F_{\text{max}}$  calculated for the three models led to different muscle activation patterns, which in turn affected the muscle forces estimates. This was particularly evident when comparing SSp and Hyb, differing only for muscle geometry and MT parameters. Most evident compensatory activations emerged for the Tibialis anterior when contributing to the

dorsiflexion moment estimated during swing phase and the Rectus femoris and Iliopsoas when providing the required hip flexion moment during stance phase. The reduction in Gluteus medius and minimus activity in the SSp corresponded to higher  $F_{max}$  in the abductor muscles. This suggests that the SSp model could be more suitable when dealing with large hip abduction moments, such those typical of stance phase. This was also observed for the Vasti in relation to the knee extension moment. Further analyses, however, would be needed to better investigate these aspects, which were not possible in this study due to the limited validation data.

Overall the reported findings suggest that personalised estimates of muscle volumes and geometry and consequently of the maximal isometric force can be critical to the quantification of hip and knee peak contact forces. This could be of substantial relevance when these forces are used in clinical contexts, such as prediction of osteoporotic risk of fracture (Gallagher et al., 1994) and even more when asymmetries between limbs could be significant, such as in joint replacement (Jonkers et al., 2008) or cerebral palsy (Kainz et al., 2018).

## **7.6. Conflict of interest**

The authors declare that they do not have any financial or personal relationships with other people or organizations that could have inappropriately influenced this study.

## **7.7. Acknowledgments**

The authors would like to acknowledge Dr Amy Scarfe and Dr Jill Van der Meulen for the support with the data collection, and Mr Thomas Milton and Mr Michael Woodward for the relevant contribution in generating the models. This research was supported by the UK EPSRC (Multisim project, Grant number: EP/K03877X/1) and the NIHR Sheffield Biomedical Research Centre (BRC). The views expressed are those of the author(s) and not necessarily those of the NHS, the NIHR or the Department of Health and Social Care (DHSC).

## 7.8. References

- Ackland, D. C., Lin, Y.-C. & Pandy, M. G. 2012. Sensitivity of model predictions of muscle function to changes in moment arms and muscle–tendon properties: a Monte-Carlo analysis. *Journal of Biomechanics*, 45, 1463-1471.
- Almurthi, M. M., Reeves, N. D., Bowling, F. L., Boulton, A. J., Jeziorska, M. & Malik, R. A. 2016. Reduced lower-limb muscle strength and volume in patients with type 2 diabetes in relation to neuropathy, intramuscular fat, and vitamin D levels. *Diabetes Care*, 39, 441-447.
- Anderson, F. C. & Pandy, M. G. 2001. Static and dynamic optimization solutions for gait are practically equivalent. *Journal of Biomechanics*, 34, 153-161.
- Arnold, E. M., Ward, S. R., Lieber, R. L. & Delp, S. L. 2010. A model of the lower limb for analysis of human movement. *Annals of biomedical engineering*, 38, 269-279.
- Bahl, J. S., Zhang, J., Killen, B. A., Taylor, M., Solomon, L. B., Arnold, J. B., Lloyd, D. G., Besier, T. F. & Thewlis, D. 2019. Statistical shape modelling versus linear scaling: effects on predictions of hip joint centre location and muscle moment arms in people with hip osteoarthritis. *Journal of Biomechanics*.
- Bergmann, G., Deuretzbacher, G., Heller, M., Graichen, F., Rohlmann, A., Strauss, J. & Duda, G. 2001. Hip contact forces and gait patterns from routine activities. *Journal of Biomechanics*, 34, 859-871.
- Brooks, S. V. & Faulkner, J. A. 1994. Skeletal muscle weakness in old age: underlying mechanisms. *Medicine and science in sports and exercise*, 26, 432-439.
- Buchanan, T. S., Lloyd, D. G., Manal, K. & Besier, T. F. 2004. Neuromusculoskeletal modeling: estimation of muscle forces and joint moments and movements from measurements of neural command. *Journal of applied biomechanics*, 20, 367-395.
- Carbone, V., Van Der Krogt, M., Koopman, H. F. & Verdonschot, N. 2016. Sensitivity of subject-specific models to Hill muscle–tendon model parameters in simulations of gait. *Journal of Biomechanics*, 49, 1953-1960.
- Davies, C., Thomas, D. & White, M. 1986. Mechanical properties of young and elderly human muscle. *Acta Medica Scandinavica*, 220, 219-226.
- De Groote, F., Van Campen, A., Jonkers, I. & De Schutter, J. 2010. Sensitivity of dynamic simulations of gait and dynamometer experiments to hill muscle model parameters of knee flexors and extensors. *Journal of Biomechanics*, 43, 1876-1883.
- Delp, S. L., Anderson, F. C., Arnold, A. S., Loan, P., Habib, A., John, C. T., Guendelman, E. & Thelen, D. G. 2007. OpenSim: open-source software to create and analyze dynamic simulations of movement. *IEEE transactions on biomedical engineering*, 54, 1940-1950.
- Delp, S. L., Loan, J. P., Hoy, M. G., Zajac, F. E., Topp, E. L. & Rosen, J. M. 1990. An interactive graphics-based model of the lower extremity to study orthopaedic surgical procedures. *IEEE Transactions on Biomedical engineering*, 37, 757-767.

- Ding, Z., Tsang, C. K., Nolte, D., Kedgley, A. E. & Bull, A. M. 2019. Improving musculoskeletal model scaling using an anatomical atlas: the importance of gender and anthropometric similarity to quantify joint reaction forces. *IEEE Transactions on Biomedical Engineering*.
- Fick, R. 2012. *Handbuch der anatomie und mechanik der gelenke*, Рипол Классик.
- Gallagher, J., Riggs, B. & Eisman, J. 1994. Diagnosis, prophylaxis, and treatment of osteoporosis. *The American Journal of Medicine*, 90, 646-650.
- Gerus, P., Sartori, M., Besier, T. F., Fregly, B. J., Delp, S. L., Banks, S. A., Pandy, M. G., D'lima, D. D. & Lloyd, D. G. 2013. Subject-specific knee joint geometry improves predictions of medial tibiofemoral contact forces. *Journal of Biomechanics*, 46, 2778-2786.
- Giarmatzis, G., Jonkers, I., Wesseling, M., Van Rossom, S. & Verschueren, S. 2015. Loading of hip measured by hip contact forces at different speeds of walking and running. *Journal of Bone Mineral Research*, 30, 1431-1440.
- Häkkinen, K. & Häkkinen, A. 1991. Muscle cross-sectional area, force production and relaxation characteristics in women at different ages. *European journal of applied physiology and occupational physiology*, 62, 410-414.
- Handsfield, G. G., Meyer, C. H., Hart, J. M., Abel, M. F. & Blemker, S. S. 2014. Relationships of 35 lower limb muscles to height and body mass quantified using MRI. *Journal of biomechanical engineering*, 47, 631-638.
- Harrington, M., Zavatsky, A., Lawson, S., Yuan, Z. & Theologis, T. 2007. Prediction of the hip joint centre in adults, children, and patients with cerebral palsy based on magnetic resonance imaging. *Journal of Biomechanics*, 40, 595-602.
- Hicks, J. L., Uchida, T. K., Seth, A., Rajagopal, A. & Delp, S. L. 2015. Is my model good enough? Best practices for verification and validation of musculoskeletal models and simulations of movement. *Journal of biomechanical engineering*, 137, 020905.
- Jonkers, I., Sauwen, N., Lenaerts, G., Mulier, M., Van Der Perre, G. & Jaecques, S. 2008. Relation between subject-specific hip joint loading, stress distribution in the proximal femur and bone mineral density changes after total hip replacement. *Journal of Biomechanics*, 41, 3405-3413.
- Kainz, H., Goudriaan, M., Falisse, A., Huenaerts, C., Desloovere, K., De Groote, F. & Jonkers, I. 2018. The influence of maximum isometric muscle force scaling on estimated muscle forces from musculoskeletal models of children with cerebral palsy. *Gait & posture*, 65, 213-220.
- Lichtwark, G., Bougoulias, K. & Wilson, A. 2007. Muscle fascicle and series elastic element length changes along the length of the human gastrocnemius during walking and running. *Journal of Biomechanics*, 40, 157-164.
- Liu, M. Q., Anderson, F. C., Schwartz, M. H. & Delp, S. L. 2008. Muscle contributions to support and progression over a range of walking speeds. *Journal of Biomechanics*, 41, 3243-3252.
- Lloyd, D. G. & Besier, T. F. 2003. An EMG-driven musculoskeletal model to estimate muscle forces and knee joint moments in vivo. *Journal of Biomechanics*, 36, 765-776.

- Maden-Wilkinson, T., Degens, H., Jones, D. & Mcphee, J. 2013. Comparison of MRI and DXA to measure muscle size and age-related atrophy in thigh muscles. *Journal of musculoskeletal neuronal interactions*, 13, 320-8.
- Martelli, S., Valente, G., Viceconti, M. & Taddei, F. 2015. Sensitivity of a subject-specific musculoskeletal model to the uncertainties on the joint axes location. *Computer methods in biomechanics biomedical engineering*, 18, 1555-1563.
- Modenese, L., Montefiori, E., Wang, A., Wesarg, S., Viceconti, M. & Mazzà, C. 2018. Investigation of the dependence of joint contact forces on musculotendon parameters using a codified workflow for image-based modelling. *Journal of Biomechanics*, 73, 108-118.
- Montefiori, E., Modenese, L., Di Marco, R., Magni-Manzoni, S., Malattia, C., Petrarca, M., Ronchetti, A., De Horatio, L. T., Van Dijkhuizen, P. & Wang, A. J. J. O. B. 2019. An image-based kinematic model of the tibiotalar and subtalar joints and its application to gait analysis in children with Juvenile Idiopathic Arthritis.
- Pataky, T. C. 2012. One-dimensional statistical parametric mapping in Python. *Comput Methods Biomech Biomed Engin*, 15, 295-301.
- Prinold, J. A., Mazzà, C., Di Marco, R., Hannah, I., Malattia, C., Magni-Manzoni, S., Petrarca, M., Ronchetti, A. B., De Horatio, L. T. & Van Dijkhuizen, E. P. 2016. A patient-specific foot model for the estimate of ankle joint forces in patients with juvenile idiopathic arthritis. *Annals of biomedical engineering*, 44, 247-257.
- Rubenson, J., Pires, N. J., Loi, H. O., Pinniger, G. J. & Shannon, D. G. 2012. On the ascent: the soleus operating length is conserved to the ascending limb of the force-length curve across gait mechanics in humans. *Journal of Experimental Biology*, 215, 3539-3551.
- Scheys, L., Jonkers, I., Loeckx, D., Maes, F., Spaepen, A. & Suetens, P. Image Based Musculoskeletal Modeling Allows Personalized Biomechanical Analysis of Gait. 2006 Berlin, Heidelberg. Springer Berlin Heidelberg, 58-66.
- Scheys, L., Spaepen, A., Suetens, P. & Jonkers, I. 2008a. Calculated moment-arm and muscle-tendon lengths during gait differ substantially using MR based versus rescaled generic lower-limb musculoskeletal models. *Gait & posture*, 28, 640-648.
- Scheys, L., Van Campenhout, A., Spaepen, A., Suetens, P. & Jonkers, I. 2008b. Personalized MR-based musculoskeletal models compared to rescaled generic models in the presence of increased femoral anteversion: effect on hip moment arm lengths. *Gait & posture*, 28, 358-365.
- Siegler, S., Block, J. & Schneck, C. D. 1988. The mechanical characteristics of the collateral ligaments of the human ankle joint. *Foot & ankle*, 8, 234-242.
- Steele, K. M., Demers, M. S., Schwartz, M. H. & Delp, S. L. 2012. Compressive tibiofemoral force during crouch gait. *Gait & posture*, 35, 556-560.
- Steele, K. M., Seth, A., Hicks, J. L., Schwartz, M. S. & Delp, S. L. 2010. Muscle contributions to support and progression during single-limb stance in crouch gait. *Journal of Biomechanics*, 43, 2099-2105.
- Thelen, D. G. 2003. Adjustment of muscle mechanics model parameters to simulate dynamic contractions in older adults. *Journal of biomechanical engineering*, 125, 70-77.

- Valente, G., Pitto, L., Testi, D., Seth, A., Delp, S. L., Stagni, R., Viceconti, M. & Taddei, F. 2014. Are subject-specific musculoskeletal models robust to the uncertainties in parameter identification? *PLoS One*, 9, e112625.
- Van Der Krogt, M. M., Delp, S. L. & Schwartz, M. H. 2012. How robust is human gait to muscle weakness? *Gait & posture*, 36, 113-119.
- Ward, S. R., Eng, C. M., Smallwood, L. H. & Lieber, R. L. 2009. Are current measurements of lower extremity muscle architecture accurate? *Clinical orthopaedics related research*, 467, 1074-1082.
- Ward, S. R. & Lieber, R. L. 2005. Density and hydration of fresh and fixed human skeletal muscle. *Journal of Biomechanics*, 38, 2317-2320.
- Wesseling, M., De Groote, F., Bosmans, L., Bartels, W., Meyer, C., Desloovere, K. & Jonkers, I. 2016. Subject-specific geometrical detail rather than cost function formulation affects hip loading calculation. *Computer methods in biomechanics biomedical engineering*, 19, 1475-1488.
- White, D., Woodard, H. & Hammond, S. 1987. Average soft-tissue and bone models for use in radiation dosimetry. *The British journal of radiology*, 60, 907-913.
- Yamaguchi, G. T. & Zajac, F. E. 1989. A planar model of the knee joint to characterize the knee extensor mechanism. *Journal of Biomechanics*, 22, 1-10.

## 8. General discussion and conclusions

The research collected in this PhD thesis supported the achievement of the objectives listed in chapter 1 as a coherent body of work, which stemmed from the lack of a standard and reliable approach to musculoskeletal modelling and led to the development of a fully-personalised, highly automated, robust procedure which can be easily implemented by other researchers.

In details, chapter 3 presented an innovative methodology to improve the identification of tibiotalar and subtalar joint axes in order to reduce the dependence on the location of the experimental markers (Montefiori et al., 2019a). Previous works highlighted how *in-vivo* tracking of the ankle joint kinematics can be complicated by the marker placement on such a small area with no visible superficial landmarks (Di Marco et al., 2016, Scott and Winter, 1991). The location of joint axes based on these markers, although commonly adopted (Wu et al., 2002), is unavoidably affected by the same limitations (Prinold et al., 2016). As an alternative, a morphological fitting-based approach was used to automatically define the tibiotalar and subtalar joint centre and axis from the articular surface of the segmented bone. The anatomical consistency of the obtained axes was verified against *ex-vivo* measurements available in the literature (Isman et al., 1969).

Chapter 4 allowed to identify the modelling steps generating the biggest intra- and inter-operator errors when personalising MRI-based musculoskeletal models (MSKMs) of the foot and ankle complex. The most critical element was found to be the definition of muscle points, contributing to errors in the estimate of muscle and joint contact forces by up to 24% and 64% of the peak values, respectively (Hannah et al., 2017). This finding promoted the development of alternative methods for the identification of muscles path, based on supervised atlas registration (Modenese et al., 2018, Montefiori et al., 2019b) and iterative closest point mapping, briefly described in chapter 5.

The developed methodologies were further extended to the modelling of the whole lower-limb and fully documented (Appendix I) in order to promote its adoption within the biomechanics community. Recommendations for the acquisition of the appropriate experimental data were also formulated in chapter 5.

The resulting MSKM was successfully applied to both juveniles (chapters 4 and 6) and elderly subjects (chapter 7) for the investigation of kinematics and kinetics, including muscle and joint contact forces. The application to Juvenile Idiopathic Arthritis (JIA) demonstrated the capability of MSKMs to track individual kinematics changes over time consistently with traditional gait analysis (Montefiori et al., 2019a) with the further potential of predicting disease progression and inform treatment planning thanks to the monitoring of JCFs (Montefiori et al., 2019b). Within the context of osteopenia in post-menopausal women, the MSKM was further personalised in order to account for individual muscle properties. The anatomical variability of muscles observed across individuals was significant. Comparing the estimates of JCFs to those from generic-scaled models proved that muscle variability should not be neglected, especially in elderly populations where monitoring joint loading is crucial to the conservation of both bone and cartilage tissue.

## **8.1. Limitations**

The limitation of the work carried out in the thesis have been detailed in the various chapters and will be now globally discussed.

Inevitable errors associated to the experimental data collections directly translate into inaccuracies in the model estimates. Although recommendations for the minimisation of these errors were formulated, experimental variability, including human mistakes, is inherent in the adopted techniques, especially within clinical context. However, a quantification of these errors and of their impact has been carried on when possible, both for the gait analysis and the imaging data.

Assessment of the model accuracy was hindered by practical and ethical limitations. For instance, fluoroscopy data were not collected due to the poisoning effect of X-ray radiations. MRI acquisition time, and hence image quality, was reduced to limit the burden to the patients. Aiming at minimising the ethical impact of the research, a control group was not enrolled in the paediatric study, not to expose healthy children to the potential distress of the clinical examination and experimental data collection.

From a modelling perspective, one of the limitations of the work was that of neglecting the abduction/adduction movement of the knee. This was a reasonable simplification, especially

in the context of investigating the kinematics of the JIA population as previous gait analysis works only highlighted alterations in the sagittal plane. The same reasoning applied to the abduction/adduction joint moments. Conversely, when looking at the contact forces, the analysis of the medial and lateral knee forces acting on the medial and lateral condyle, respectively, could have provided a further insight on the disease and its progression mechanism. For example, the observation of compartmental loading proved to be particularly informative in understanding the onset of osteoarthritis (Andriacchi et al., 2004, Meireles et al., 2017), therefore the two knee force components should be considered when investigating the loading in elderly (i.e. post-menopausal women). Future work should aim at introducing more accurate and complex knee mechanisms in the lower-limb MSKM. Another important limitation is that the adopted model does not account for muscle physiology and activation-contraction dynamics, which of course limits the range of possible clinical applications.

Finally, a comprehensive validation of the muscle and joint contact forces estimated by the models is not currently feasible *in-vivo*. Measurements from subjects with instrumented implants can be used to validate the estimates of JCF in the hip, knee, and less frequently in the ankle. These measurements can be used as a reference to evaluate the models' predictions in healthy populations. However, differences in the estimates should be expected due to geometrical and anatomical differences between the natural joint and the instrumented joint, with the latter most likely to record lower contact forces (Ding et al., 2019).

## **8.2. Critical appraisal of published work**

The anatomical models described in chapters 3, 4, 6, and 7 included the 3D geometry of the fibula; however, this bone was rigidly fixed to the tibia, neglecting its contribution to the stabilisation of the ankle. This simplification is common to most of the MSKMs available in the literature (Arnold et al., 2010, Carbone et al., 2015, Delp et al., 1990, Horsman et al., 2007, Malaquias et al., 2017, Modenese et al., 2018, Prinold et al., 2016, Saraswat et al., 2010, Valente et al., 2014), and therefore it is widely accepted.

In all papers, when joint contact forces were presented, their value was scaled to body weight (BW) as common practice across the musculoskeletal community (Wannop et al., 2012). This

choice was dictated by the need for comparing curves across individuals, and against literature data, removing their dependence on body mass. On the other hand, when estimating the articular damage caused by the joint loading, one should consider the local pressure on the articular surface, therefore accounting for the absolute (non-normalised) force acting on the contacting area of the joint. Alternatively, more complex normalisation algorithm should be implemented, also accounting for how joint size scales with body size across individuals.

In chapter 3, the representation of the tibiotalar and subtalar joints as purely plantar/dorsiflexion and inversion/eversion joints, respectively, had an impact on the understanding of the real movement of the ankle complex. However, this simplification is widely accepted in the musculoskeletal modelling community, especially for the investigation of *in-vivo* kinematics during walking tasks. More complicated representations are proposed within the context of *ex-vivo* studies under controlled movements, but these implementations go beyond the scope of this thesis.

In chapter 4, a two-segment foot model was adopted. The ground reaction force collected by the force platforms was applied to either hindfoot or forefoot, depending on the location of the centre of pressure. This model provides an overestimate of the loading of the forefoot during the push-off phase when suddenly all the external force is applied to this segment, whereas in the reality the load gradually passes from hindfoot to forefoot during the forefoot rocker and the two segments share the force. Pressure measurements using pressure mats would allow more accurate distribution of the ground reaction force; however, in the context of studying the repeatability of the modelling procedure and assessing the sensitivity of the model to operator-dependent steps, this assumption had a negligible impact on the analysis. In the Discussion section of the same chapter it is also concluded that having access to medical images improves the repeatability of muscle points location. In this respect, the authors wanted to highlight that the availability of images and segmentations of bones only, despite proved to be valuable data for the location of muscle attachments (Ascani et al., 2015, Pal et al., 2007), guarantees less repeatability in the identification of muscle paths compared to when muscle images are available as well. The high sensitivity of the muscle forces to operator-dependent error reported in this work was mostly associated to the variability in the identification of joint reference systems and muscle paths, having an effect on the

resultant muscle moment arm. Interestingly, this had a limited impact on the estimated contact forces. In fact, altered moment arms affected the muscle recruitment strategies employed by the static optimisation tool. Despite this, the total muscle force acting on the ankle was similar, limiting the sensitivity of the joint contact forces to operator variability.

In chapter 6, within the Statistical Analysis section, a non-parametric  $t$  test was used. By definition, a  $t$  test can be applied when the analysed sample follows a normal distribution. Alternatively, a Wilcoxon signed-rank test is used when the normality condition is not met. In this work, we referred to non-parametric “ $t$  test” to describe the test chosen to conduct the statistical analysis consistently with the name assigned to the relevant algorithm implemented in the MATLAB package SPM1D, based on the work by Nichols and Holmes (2002). Furthermore, the Discussion section of this chapter presents the observed compensation mechanisms as a possible indicator of disease progression. This hypothesis is not meant to discourage or prevent compensation, acknowledged here as an effective strategy to deal with disease and impairment. Conversely, we suggest that compensation should be quantified in order to recognise those individuals at risk of further developing alterations in the joints, potentially compromising the biomechanics of the healthy limb.

### **8.3. Impact**

This PhD work contributed to the publication of five journal papers (two as a first author and three as a second author), one user guide and several repositories (available on Figshare) containing code and material for the implementation of MRI-based MSKMs and simulations of gait. Two further co-authored papers are currently under revision and one paper is currently being reviewed by other co-authors aiming at submission in October 2019.

The modelling procedure and the newly developed tools and methods have now been shared with the research community together with a detailed documentation (explicitly written to limit operator errors) and associated models and datasets. Despite developed within the framework of OpenSim and MATLAB, the shared procedure can be easily adapted to different software and is suitable for wider modelling context, such as forward dynamics or EMG-driven modelling.

The application of the models to the investigation of the biomechanical characteristics of JIA allowed to complement and integrate the current knowledge of the disease, based on gait analysis. In fact, the model could estimate internal joint loading in the lower limb highlighting specific features of JIA, such as overloading of the knee during push off and existing compensatory mechanisms causing the overloading of the unimpaired limb in monolateral cases. The investigation of internal loads enabled for the first time to bridge the information about the local joint damage, gained from imaging techniques such as MRI and US, and the functional impairment observed through gait analysis. In fact, it is known that local cartilage or bone damage in the articular region is most likely to be caused and magnified by excessive or concentrated loading. The results reported in this thesis enhanced the potential benefits of applying MSK modelling to unsolved clinical questions where experimental measurements cannot provide enough information, whereas simulations can be valuable tools for evaluating and predicting disease progression and intervention outcomes.

Furthermore, output parameters from MSKMs such as muscle forces and JCFs have the potential to inform finite element (FE) analysis providing the individual forces acting on single bone geometries in time during a certain locomotor task (Geier et al., 2019). To this purpose MRI data, useful for the generation of the MSKM, need to be integrated with higher resolution data, i.e. CT images, in order to gain accurate information on the bone geometry and a description of its mechanical properties. Image registration techniques can be used to register data from the two imaging modalities and find the optimal transformation to translate the muscle forces and JCFs estimated with MRI-based MSKMs into input data for the CT-based FE models. The main advantage of this approach is that of enabling fully subject-specific analyses and predictions as opposed to more hybrid approaches where gait analysis data are combined with generic MSKMs available in the literature and generic estimates are used to feed FE models. This approach is currently being used within the multiscale framework of the MultiSim project for coupling body and organ simulations and predicting risk of fracture in elderly.

Two projects have already been funded to further exploit the work done within this thesis, where I am a named investigator: "MultiSim2 - Frontier Engineering Progression Grant", funded by the UK EPSRC to develop new approaches for better imaging, characterisation and modelling of the muscles and of their interaction with the skeletal system; and "Clinical

consequences of adult presenting hypophosphatasia with special focus on gait, bone microarchitecture and cognition: The PORTRAIT Study”, funded by Alexion Pharmaceuticals Inc. aiming at examining the risks associated to joint overloading in hypophosphatasia, an inherited condition which causes a defect in bone calcification, leading to weak bones.

## 8.4. Future work

Future work will focus on:

- The validation of the proposed tibiotalar model through a collaboration with Dr Michele Conconi at the University of Bologna comparing the ankle kinematics estimated by the model to that resulting from a validated congruence-based approach developed by Conconi and Castelli (2014). The ultimate goal is to understand the anatomical consistency of different kinematic models commonly adopted within the OpenSim community. Preliminary results will be presented at the international conferences of the International Society of Biomechanics (ISB) in Calgary (CA) and at the International Symposium on Computer Methods in Biomechanics and Biomedical Engineering (CMBBE) in New York, NY. A more comprehensive analysis is planned to be completed within the next year to ultimately lead to a journal publication.
- The exploitation of alternative techniques (i.e. Ultrasounds, US) for the acquisition of meaningful musculoskeletal information. Data have been collected and are currently being processed with the purpose of proving the feasibility of replacing MRI with US (Greatrex et al., 2017) synchronised to a motion capture system to estimate joint axes and muscle parameters. This will enable the development of US-based MSKMs with the advantage of reducing errors associated to data registration and enabling standing imaging acquisition. The use of US would also reduce imaging costs and time, making personalised modelling more sustainable within clinical contexts.

- The development of more advanced and automated techniques for image processing and segmentation. In this framework, preliminary work has been conducted using lower-limb MRI available within the Juvenile Idiopathic Arthritis study. The image registration toolkit SHIRT, developed in Sheffield, has been tested in order to assess the feasibility of using elastic registration to automate image segmentation. Further work will aim at producing a large database of segmented medical images to be used in the training of the automatic algorithm and ultimately develop a robust segmentation tool.

## 8.5. References

- Andriacchi, T. P., Mündermann, A., Smith, R. L., Alexander, E. J., Dyrby, C. O. & Koo, S. 2004. A framework for the in vivo pathomechanics of osteoarthritis at the knee. *Annals of biomedical engineering*, 32, 447-457.
- Arnold, E. M., Ward, S. R., Lieber, R. L. & Delp, S. L. 2010. A model of the lower limb for analysis of human movement. *Annals of biomedical engineering*, 38, 269-279.
- Ascani, D., Mazzà, C., De Lollis, A., Bernardoni, M. & Viceconti, M. 2015. A procedure to estimate the origins and the insertions of the knee ligaments from computed tomography images. *Journal of biomechanics*, 48, 233-237.
- Carbone, V., Fluit, R., Pellikaan, P., Van Der Krogt, M., Janssen, D., Damsgaard, M., Vigneron, L., Feilkas, T., Koopman, H. F. & Verdonshot, N. 2015. TLEM 2.0—A comprehensive musculoskeletal geometry dataset for subject-specific modeling of lower extremity. *Journal of Biomechanics*, 48, 734-741.
- Conconi, M. & Castelli, V. P. 2014. A sound and efficient measure of joint congruence. *Proceedings of the Institution of Mechanical Engineers, Part H: Journal of Engineering in Medicine*, 228, 935-941.
- Delp, S. L., Loan, J. P., Hoy, M. G., Zajac, F. E., Topp, E. L. & Rosen, J. M. 1990. An interactive graphics-based model of the lower extremity to study orthopaedic surgical procedures. *IEEE Transactions on Biomedical engineering*, 37, 757-767.
- Di Marco, R., Rossi, S., Racic, V., Cappa, P. & Mazzà, C. 2016. Concurrent repeatability and reproducibility analyses of four marker placement protocols for the foot-ankle complex. *Journal of Biomechanics*, 49, 3168-3176.
- Ding, Z., Tsang, C. K., Nolte, D., Kedgley, A. E. & Bull, A. M. 2019. Improving musculoskeletal model scaling using an anatomical atlas: the importance of gender and anthropometric similarity to quantify joint reaction forces. *IEEE Transactions on Biomedical Engineering*.
- Geier, A., Keibach, M., Soodmand, E., Woernle, C., Kluess, D. & Bader, R. 2019. Neuro-musculoskeletal flexible multibody simulation yields a framework for efficient bone failure risk assessment. *Scientific reports*, 9.
- Hannah, I., Montefiori, E., Modenese, L., Prinold, J., Viceconti, M. & Mazza, C. 2017. Sensitivity of a juvenile subject-specific musculoskeletal model of the ankle joint to the variability of operator-dependent input. *Proceedings of the Institution of Mechanical Engineers, Part H: Journal of Engineering in Medicine*, 231, 415-422.
- Horsman, M. K., Koopman, H., Veeger, H. & Van Der Helm, F. 2007. The Twente Lower Extremity Model: a comparison of muscle moment arms with the literature. *The Twente Lower Extremity Model*, 45.
- Isman, R. E., Inman, V. T. & Poor, P. 1969. Anthropometric studies of the human foot and ankle. *Bull Prosthet Res*, 11, 129.

- Malaquias, T. M., Silveira, C., Aerts, W., De Groote, F., Dereymaeker, G., Vander Sloten, J. & Jonkers, I. 2017. Extended foot-ankle musculoskeletal models for application in movement analysis. *Computer methods in biomechanics and biomedical engineering*, 20, 153-159.
- Meireles, S., Wesseling, M., Smith, C. R., Thelen, D. G., Verschueren, S. & Jonkers, I. 2017. Medial knee loading is altered in subjects with early osteoarthritis during gait but not during step-up-and-over task. *PLoS one*, 12, e0187583.
- Modenese, L., Montefiori, E., Wang, A., Wesarg, S., Viceconti, M. & Mazzà, C. 2018. Investigation of the dependence of joint contact forces on musculotendon parameters using a codified workflow for image-based modelling. *Journal of Biomechanics*, 73, 108-118.
- Montefiori, E., Modenese, L., Di Marco, R., Magni-Manzoni, S., Malattia, C., Petrarca, M., Ronchetti, A., De Horatio, L. T., Van Dijkhuizen, P., Wang, A., Wesarg, S., Viceconti, M. & Mazzà, C. 2019a. An image-based kinematic model of the tibiotalar and subtalar joints and its application to gait analysis in children with Juvenile Idiopathic Arthritis. *Journal of Biomechanics*, 85, 27-36.
- Montefiori, E., Modenese, L., Di Marco, R., Magni-Manzoni, S., Malattia, C., Petrarca, M., Ronchetti, A., De Horatio, L. T., Van Dijkhuizen, P., Wang, A., Wesarg, S., Viceconti, M. & Mazzà, C. 2019b. Linking Joint Impairment and Gait Biomechanics in Patients with Juvenile Idiopathic Arthritis. *Annals of biomedical engineering*, 1-13.
- Nichols, T. E. & Holmes, A. P. 2002. Nonparametric permutation tests for functional neuroimaging: a primer with examples. *Human brain mapping*, 15, 1-25.
- Pal, S., Langenderfer, J. E., Stowe, J. Q., Laz, P. J., Petrella, A. J. & Rullkoetter, P. J. 2007. Probabilistic modeling of knee muscle moment arms: effects of methods, origin–insertion, and kinematic variability. *Annals of biomedical engineering*, 35, 1632-1642.
- Prinold, J. A., Mazzà, C., Di Marco, R., Hannah, I., Malattia, C., Magni-Manzoni, S., Petrarca, M., Ronchetti, A. B., De Horatio, L. T. & Van Dijkhuizen, E. P. 2016. A patient-specific foot model for the estimate of ankle joint forces in patients with juvenile idiopathic arthritis. *Annals of biomedical engineering*, 44, 247-257.
- Saraswat, P., Andersen, M. S. & Macwilliams, B. A. 2010. A musculoskeletal foot model for clinical gait analysis. *Journal of biomechanics*, 43, 1645-1652.
- Scott, S. H. & Winter, D. A. 1991. Talocrural and talocalcaneal joint kinematics and kinetics during the stance phase of walking. *Journal of Biomechanics*, 24, 743-752.
- Valente, G., Pitto, L., Testi, D., Seth, A., Delp, S. L., Stagni, R., Viceconti, M. & Taddei, F. 2014. Are subject-specific musculoskeletal models robust to the uncertainties in parameter identification? *PLoS One*, 9, e112625.
- Wannop, J. W., Worobets, J. T. & Stefanyshyn, D. J. 2012. Normalization of ground reaction forces, joint moments, and free moments in human locomotion. *Journal of applied biomechanics*, 28, 665-676.
- Wu, G., Siegler, S., Allard, P., Kirtley, C., Leardini, A., Rosenbaum, D., Whittle, M., D D'lima, D., Cristofolini, L. & Witte, H. 2002. ISB recommendation on definitions of joint coordinate system of various joints for the reporting of human joint motion—part I: ankle, hip, and spine. *Journal of Biomechanics*, 35, 543-548.

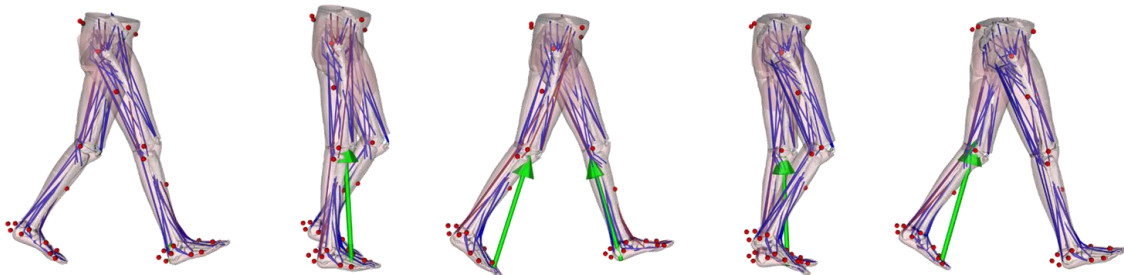


# Appendix I

# Pipeline for building a subject-specific MSK model from MRI and motion capture data

**Authors:** Montefiori, E., Modenese, L., Marinou, G., Woodward, M., Prinold, J., Hannah, I.,  
Viceconti, M., Mazzà, C.

Department of Mechanical Engineering and INSIGNEO Institute for *in silico* Medicine,  
University of Sheffield, Sheffield, UK.



The Pam Liversidge Building, The Sir Frederick Mappin Building, Mappin Street, Sheffield S1 3JD, UK

email: [info@insigneo.org](mailto:info@insigneo.org)

phone: +44 1142 220162

website: [www.insigneo.org](http://www.insigneo.org)

## LICENSE

This work is licensed under the Creative Commons Attribution-NonCommercial-ShareAlike 4.0 International License. To view a copy of this license, visit <http://creativecommons.org/licenses/by-nc-sa/4.0/> or send a letter to Creative Commons, PO Box 1866, Mountain View, CA 94042, USA.

## PERMISSION

Use of the document is permitted provided that the following condition is met: use of the presented document and related scripts must be acknowledged in all publications, presentations, or documents using the document and accompanying scripts is used by citing the following work: Modenese, L., Montefiori, E., Wang, A., Wesarg, S., Viceconti, M., Mazzà, C., 2018. Investigation of the dependence of joint contact forces on musculotendon parameters using a codified workflow for image-based modelling. *Journal of Biomechanics* 73, 108-118.

## DISCLAIMER

This document is provided by the copyright holders and contributors "as is"; and any express or implied warranties, including, but not limited to, the implied warranties of merchantability and fitness for a particular purpose are disclaimed. In no event shall the copyright owner or contributors be liable for any direct, indirect, incidental, special, exemplary, or consequential damages (including, but not limited to, procurement of substitute goods or services; loss of use, data, or profits; or business interruption) however caused and on any theory of liability, whether in contract, strict liability, or tort (including negligence or otherwise) arising in any way out of the use of this software, even if advised of the possibility of such damage.

## CONDITIONS

The use of this document is not for clinical purpose.

If you use this pipeline for your published research, please cite:

Modenese, L., Montefiori, E., Wang, A., Wesarg, S., Viceconti, M., Mazzà, C., 2018. Investigation of the dependence of joint contact forces on musculotendon parameters using a codified workflow for image-based modelling. *Journal of Biomechanics* 73, 108-118.

## Contents

Contents .....	3
1 Required software .....	5
2 Preprocessing.....	5
2.1 Dataset.....	5
2.2 Definition of model segments .....	5
2.3 Definition of Joint Parameter .....	6
2.3.1 Hip Joint Surface .....	6
2.3.2 Knee Joint Surface.....	6
2.3.3 Ankle Joints Surfaces.....	7
2.3.4 Surface Fitting.....	8
3 Anatomical model in NMSBuilder .....	9
3.1 Importing Data in NMSBuilder .....	9
3.2 Joint parameters .....	10
3.3 Virtual Palpation.....	10
3.4 Joint Axes Definition .....	11
3.4.1 Pelvis Joint Axes.....	11
3.4.2 Hip Joint Axes.....	12
3.4.3 Knee Joint Axes .....	12
3.4.4 Foot Sole Axes.....	13
3.4.5 Ankle Joint Axes .....	13
3.4.6 Subtalar Joint Axes.....	14
3.4.7 Metatarso-phalangeal Joint Axis .....	14
4 Surface Markers Palpation .....	15
5 Muscles Definition.....	16
5.1 Registering Landmark Clouds .....	16
5.2 MATLAB Muscle Snapping.....	16
5.3 Toes muscles.....	17
5.4 Muscle Adjustments.....	17
5.4.1 Pelvis.....	17
5.4.2 Femur.....	18
5.4.3 Tibia .....	18
5.4.4 Calcaneus.....	20
6 Creating an OpenSim Model .....	21
6.1 Bodies .....	21
6.1.1 Inertial properties.....	21

6.2	Joints .....	21
6.3	Surface Markers .....	22
6.4	Muscles .....	22
6.5	Exporting the OpenSim Model .....	22
6.6	Update of joint coordinates name and rotations order.....	23
7	Definition of conditional via points in OpenSim .....	23
8	Quality check .....	23
8.1	Experimental data .....	23
8.2	Post processing .....	24
8.3	Model building .....	24
8.4	Dynamic simulations .....	24
9	Feedback – help us improving .....	24
	Acknowledgements.....	25
	References.....	25

# 1 Required software

For implementing the procedure described in this pipeline the following software packages are required:

- Meshlab, (<http://www.meshlab.net>) [1]
- NMSBuilder, (<http://www.nmsbuilder.org>) [2]
- OpenSim, (<https://simtk.org/projects/opensim>) [3]
- Netfabb, Autodesk Inc. (<https://www.autodesk.com>)
- MATLAB™, The Mathworks Inc., USA (<https://www.mathworks.com/products/matlab.html>)

## 2 Preprocessing

### 2.1 Dataset

The procedure assumes that the following data is available:

- 1) Full lower limb MRI/CT scans
- 2) Skin segmentation (.stl files)
- 3) Bone segmentation (.stl files):
  - a. Iliacus and Sacrum
  - b. Femur
  - c. Tibia and Fibula
  - d. Talus
  - e. Cuboid, Navicular, Calcaneus and Cuneiformis
  - f. Metatarsals
  - g. Phalanges
- 4) Gait Data (Marker Trajectories)
- 5) Force Plate Data (Ground Reaction Forces)

**NB: in the following, when referred to 'xxx\_side', it means that '\_side' must be replaced with either '\_l' or '\_r' if left or right side of the body.**

### 2.2 Definition of model segments

Meshlab is used for preparing the required limb and foot segments from the individual meshes by following these steps:

- 1) Load all .stl files in Meshlab. [File > Import Mesh]
- 2) Pelvis: Select as visible only the pelvis and save it as 'pelvis.stl'. [File > Export Mesh As...]. Hide the mesh by selecting the eye icon.
- 3) Femur: Select the femur as the only visible mesh and save the mesh as 'femur\_side'. Repeat the process for the other side. Hide the mesh by selecting the eye icon.
- 4) Tibia, Fibula & Patella: Select as visible meshes only the tibia, fibula and patella from one side. Select Filters > Mesh Layer > Flatten Visible Layers. Save the resulting mesh as 'tibia\_side.stl'. Repeat for the other side. Hide the resulting mesh by reselecting the eye icon.

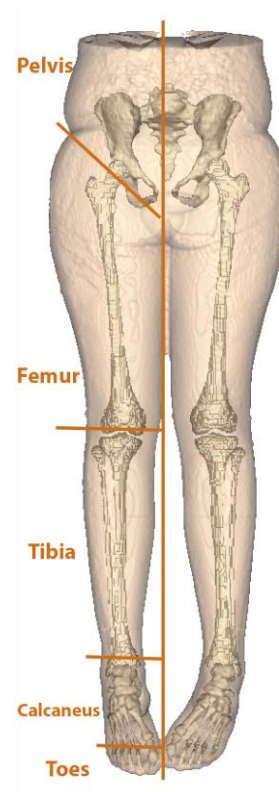


**Figure 1 – Soft tissue model segments and mesh cut lines (in orange).**

- 5) Talus: Select as the visible mesh only the talus and save the mesh as 'talus\_side.stl'. Repeat for the other side. Hide the mesh by reselecting the eye icon.
- 6) Phalanges: Select as visible meshes only the phalanges. Select Filters > Mesh Layer > Flatten Visible Layers. Save the resulting mesh as 'toes\_side.stl'. Repeat for the other side. Hide the resulting mesh by reselecting the eye icon.
- 7) Calcaneus: Select as visible all the remaining meshes from one side. Select Filters > Mesh Layer > Flatten Visible Layers. Save the resulting mesh as 'calcn\_side.stl'.
- 8) Repeat the operation for the soft tissue after cutting the different body segments following the lines according to Figure 1.
- 9) Rename each body segment with the relevant name plus the suffix 'ST' (i.e. 'segment\_sideST'). 'ST' stays for 'soft tissue'.

Bone .stl files are saved in folder **1\_Meshlab\_processing** included in the "Folder Structure" template.

Soft tissue .stl files produced here are saved in the **3\_NetFabb\_cuts** folder included in the "Folder Structure" template

## 2.3 Definition of Joint Parameter

Articular surfaces can be approximated using geometrical shapes that provide parameters for defining mechanical joints in NMSBuilder. The surfaces are selected in Meshlab and relevant MATLAB (available in "Matlab Functions/Fitting\_functions"), scripts are provided for fitting the surfaces with analytical shapes (sphere and cylinder) using a 'least-square' algorithm-based approach. For Meshlab tutorials see:

[https://www.youtube.com/channel/UC70CKZQPj\\_ZAJ0OsrM6TyTg?nohtml5=False](https://www.youtube.com/channel/UC70CKZQPj_ZAJ0OsrM6TyTg?nohtml5=False).

### 2.3.1 Hip Joint Surface

- 1) Open Meshlab and load '*femur\_side.stl*'
- 2) To select a surface, click on the 'Select Faces in a rectangular region' button (.
- 3) Select the part of the femur head that could represent a sphere as shown in Figure 2.
- 4) Select Filters > Selection > Invert Selection to select all the other faces (untick "invert vertices") and delete them by clicking on the 'Delete the current set of selected faces' button (.
- 5) Select Filters again, Selection > Select None. Inspect the surface and make sure that all the other faces have been successfully deleted.
- 6) Export the geometry as '*femur\_head\_side.stl*' in **2\_Meshlab\_joint\_surface\_selection/Hip** and repeat for the other side.

### 2.3.2 Knee Joint Surface

- 1) Load '*femur\_side.stl*' in Meshlab again.

- 2) Flip the geometry so that the knee side (the distal end) is directed upwards. Another way to select a surface is by using the 'brush' tool located on the toolbar. Click on the brush button (  ) and then  which is for selecting (Figure 2). This is an easier method for selecting the 'cylindrical' knee surfaces as shown below.
- 3) Repeat the process as above and save the geometry as '*epicondyle\_side.stl*' in **2\_Meshlab\_joint\_surface\_selection/Knee** and repeat for the other body side.

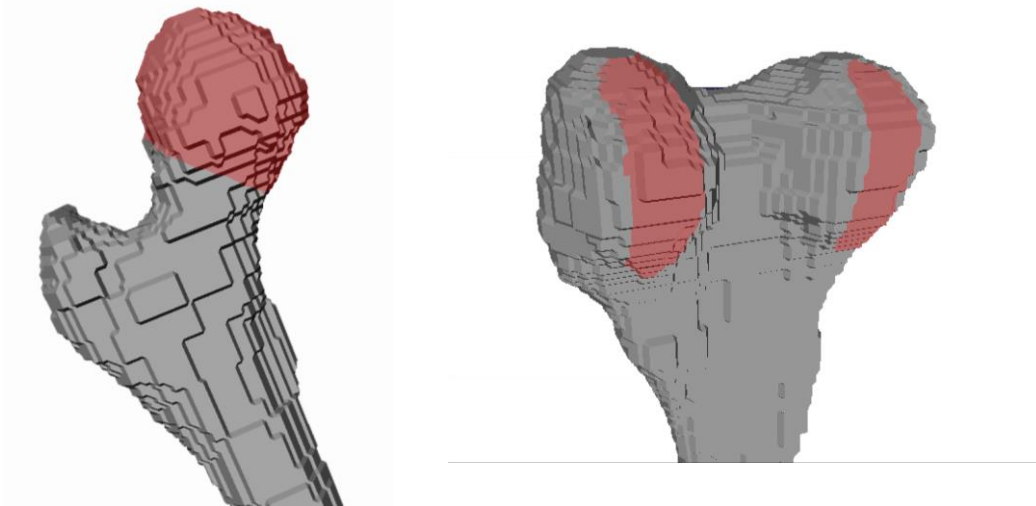


Figure 2 – Selection of articular surfaces on femur

### 2.3.3 Ankle Joints Surfaces

- 1) Load 'talus\_side.stl' in Meshlab.
- 2) Select the 'cylindrical' articular top surface of the talus as shown in Figure 3. Cut and save it as 'talartrochlea' in **2\_Meshlab\_joint\_surface\_selection/Ankle/Side**. Repeat for the other side.
- 3) Load 'talus\_side' again and flip it vertically as to make the bottom side visible.
- 4) Select the surface that closest represents a sphere on the calcaneal joint.
- 5) Cut and save as 'talocalcaneal'. Repeat for the other side.
- 6) Load 'calcaneus\_side' and zoom to better see the navicular bone.
- 7) Select the surface that closest represents a sphere.
- 8) Cut and save as 'talonavicular'. Repeat for the other side.
- 9) Separate all files into different folders for left and right.

All the .stl files generated are saved in **2\_Meshlab\_joint\_surface\_selection** (included in the "Folder Structure" template) under the specific folder (hip, knee, or ankle).

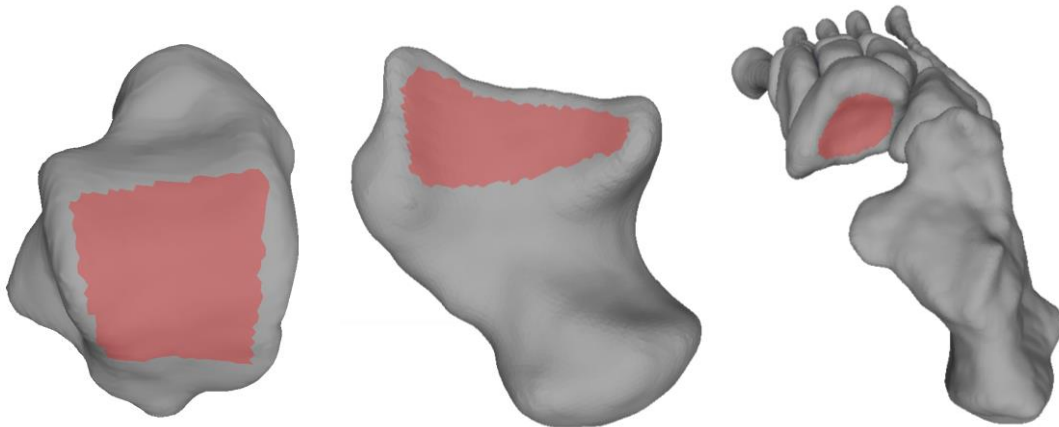


Figure 3 – Selection of articular surfaces on talus and navicular bone

### 2.3.4 Surface Fitting

The provided MATLAB scripts are used for the generation of a corresponding geometry from the selected articular surfaces. For the hip joint use the script 'DefineHipJointCentre.m', 'DefineKneeJointAxis.m' for the knee joint and 'DefineAnkleJointAxis.m' (available in the "Matlab Functions" folder) for the ankle joints axes.

**NB: the Least Squares Geometric Elements library MATLAB package (LSGE) needs to be downloaded at:**

[http://www.eurometros.org/gen\\_report.php?category=distributions&pkey=14&subform=yes](http://www.eurometros.org/gen_report.php?category=distributions&pkey=14&subform=yes)

**and corresponding functions need to be added to the MATLAB path.**

By running the scripts and selecting the containing folders of the corresponding geometries (STL files), the script will fit, using least square algorithms (Figure 4):

- 1) A sphere to the femoral head, talocalcaneal and talonavicular joints
- 2) A cylinder to the epicondyles and talar trochlea:
  - These geometries are saved alongside log files of the joint parameters and figures in **2\_Meshlab\_joint\_surface\_selection** under the specific folder (hip, knee, or ankle).

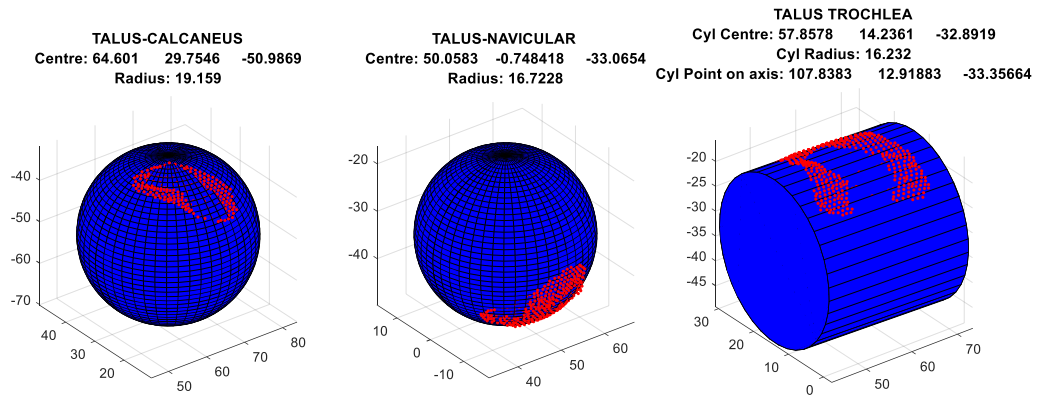


Figure 4 – Example of output of fitting procedure in Matlab.

### 3 Anatomical model in NMSBuilder

#### 3.1 Importing Data in NMSBuilder

The musculoskeletal model is built using NMSBuilder. To import the required data for model preparation, follow these steps:

- 1) Load the data tree template NMSBuilder\_model\_structure\_template.msf into the software. [File > Import > MSF]
- 2) Import each of the STL mesh segments (from folder **1\_Meshlab\_processing**), under the appropriate group on the template tree (by clicking the folder before importing) and selecting [File > Import > Surfaces > STL]. To display segments (Figure 5), click View > Surface, then check the square box next to each segment.
- 3) Follow the procedure to import the soft tissue and negative soft tissue segments under their appropriate bodies in NMSBuilder.
- 4) Import subject MRI images. [File > Import > Images > DICOM]. To display images, click on View > Ortho Slice.

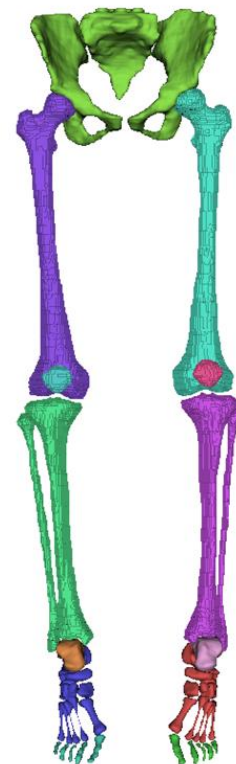


Figure 5 – Example of visualisation of the anatomical model in NMSBuilder

**\*NOTE:** To ensure bone geometries are aligned with MRI images, click to display the segments as well.

## 3.2 Joint parameters

The next step is introducing the calculated joint parameters from MATLAB in NMSBuilder. The provided data tree already includes entries for the required geometries of each joint (defined as parametric surfaces in NMSBuilder). Assigning the radius of each parametric surface is a manual process and it is easily done:

- 1) Select the required geometry from the data tree (taskbar on the right) in NMSBuilder, for example 'HJC\_side' for the femoral head.
- 2) On the bottom part of the control panel select the 'VME' tab.
- 3) Navigate to the appropriate shape (Sphere or Cylinder) and change the radius of the specific geometry according to the results from MATLAB.

To assign the parametric surface's coordinates:

- 1) Select the bone geometry from the data tree that the surface is to be fitted on, for example for fitting the hip sphere, select 'femur\_side'.
- 2) Select File > Import > Landmark. Navigate to the folder where the MATLAB log is located and select to import 'Fitted\_geometries' or 'Fitted\_geometries\_side' from **2\_Meshlab\_joint\_surface\_selection** folder. On the next window press ok.
- 3) In order to translate the centre of the geometry to the appropriate coordinates, select the parametric surface ( ) under the geometry in the data tree.
- 4) Press **Ctrl + T** in order to enter the Transform Operations window.
- 5) On the drop down menu under 'Choose Reference System' select 'Relative' and from the data tree that pops up select the fitted geometry you have just imported.
- 6) The 'Translations' boxes indicate the distance of the object centre from the position defined by the fitted geometry. Zero the translation boxes and you will observe the sphere moving to the appropriate joint - the femoral head for example. Click 'Ok' to save the changes.

Repeat the process above for all 10 joints and save the model.

## 3.3 Virtual Palpation

Virtual palpation of landmarks is needed to describe bone geometries in order to register a landmark cloud of muscle points (from cadaveric studies) and define joint reference systems. By selecting an STL bone geometry in NMSBuilder and pressing Ctrl + A, a side window appears enabling virtual palpation of markers (Figure 6). By clicking on any location on the bone segment a marker is attached on to it. To help aid the process, a dictionary file ("Atlas\_virtual\_palpation.dic", available in NMSBuilder\_dictionaries) with the landmark names is provided and can be loaded by selecting 'Load Dictionary' on the bottom of the side window. A representation of the muscle attachments available in the atlas can be visualised in NMSBuilder importing the .txt files in "NMSBuilder\_gait2392\_muscle\_attachments (mm)" as landmarks cloud. These attachments come from the OpenSim model gait2392, therefore, importing the .vtp files of the bone geometries from that model a complete visualisation can help understanding the location of each muscle attachment on the specific body segment. A detailed description of the anatomical markers location can be found in "Description\_virtual\_palpation.xlsx" (available in NMSBuilder\_dictionaries). Using the drop-

down menu on the top of the side window the dictionary can be filtered as to show the landmarks concerning the specific segment. Additional information can be find in the book ‘Color Atlas of Skeletal Landmark Definitions’ by Serge van Sint Jan (2007) [4].

A further cloud of virtually palpated markers is required for the definition of the ankle joint reference system (which will be described in the following section of the document). These markers are loaded as a dictionary file (“Ankle\_joint\_technical\_markers.dic”, available in NMSBuilder\_dictionaries) and palpated on the calcaneus segment.

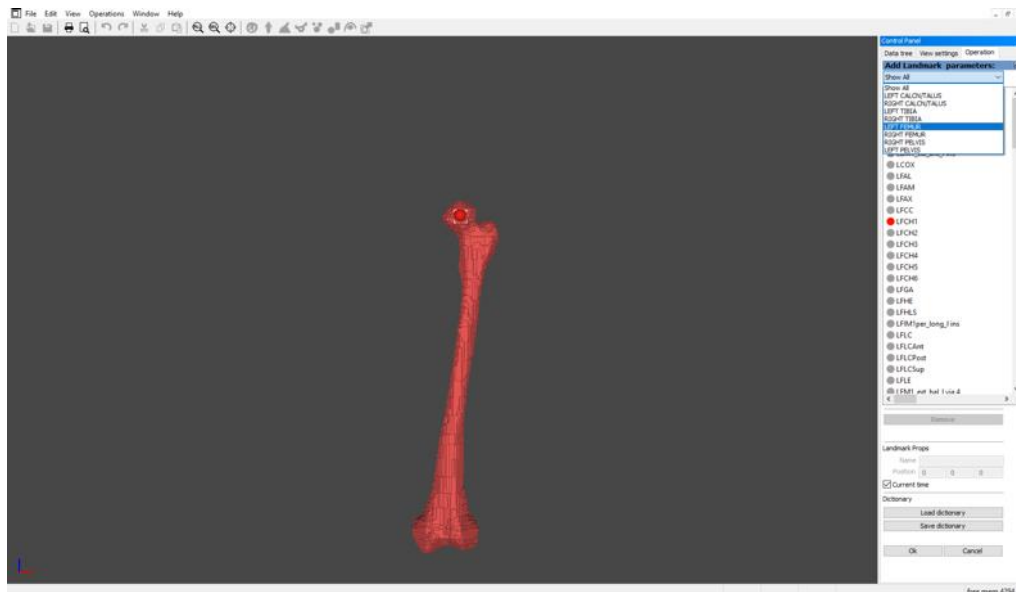


Figure 6 – NMS Builder interface. Virtual palpation of anatomical landmarks

### 3.4 Joint Axes Definition

An orthogonal anatomical reference system (according to ISB [5, 6] recommendations) has to be assigned to every joint to define rotations and translations and link the segments. These reference systems are assigned by using the already fitted geometries and the virtually palpated landmarks. The appropriate reference systems exist in the provided data tree and they need to be defined to the specific model as such:

#### 3.4.1 Pelvis Joint Axes

- 1) Select the landmark cloud of the virtually palpated points on pelvis and copy and paste ‘RIAS’ and ‘LIAS’ (using **Ctrl + Shft + C** and **Ctrl + Shft + V**) respectively.
- 2) Create a new landmark cloud by selecting ‘pelvis’ bone geometry and pressing **Ctrl + A**. Click ‘Ok’ on the palpation window without palpating any markers.
- 3) Reparent the copied landmarks from the original cloud to the newly created one by right-clicking on the landmarks, selecting ‘Reparent to...’ and then indicating the second cloud from the data tree on the pop-up menu.
- 4) Select the new cloud and go to Operations > Create > Average Landmark. This will create a new landmark mid-distanced from the two.

- 5) Select the 'ground\_pelvis\_child' reference system under the pelvis folder in the data tree. Select the VME tab at the bottom of the Control Panel and change the Scale to 100 so that the axes are visible. On the three options below select on 'Select Plane' and assign the following:
  - **Origin:** The average landmark you have just created
  - **Point 1:** RIAS from the virtually palpated landmarks (pelvis)
  - **Point 2:** RIPS from the virtually palpated landmarks (pelvis)
- 6) Make sure to select 'Normal' again before proceeding to the next step.
- 7) Click back on the 'ground\_pelvis\_child' reference system and press Ctrl + T to transform the axes according to ISB recommendations. Under 'Reference System' choose 'VME Reference System'.
- 8) By adjusting the rotations (in steps of  $\pm 90/180^\circ$ ), fix the axes so that the X-axis pointing forward, Y-axis pointing upwards and Z-axis resulting from the cross product. (For identifying the axes: **RGB** corresponds to **XYZ**). Click 'Ok' to save the changes.

### 3.4.2 Hip Joint Axes

- 1) Copy and paste **twice** the newly defined 'ground\_pelvis\_child' under 'pelvis'. Reparent one of these copied reference systems under 'femur\_side > hip\_side' for both sides.
- 2) Rename the reference system as 'hip\_side\_parent' under the VME tab.
- 3) Select 'hip\_side\_parent' and press **Ctrl + T**. On the operations window, under 'Reference Systems' select 'Relative' from the drop down menu and select the imported geometry from MATLAB 'Femur\_Head\_Sphere\_C'. Again, zero the translations to move the centre of the axes to the hip joint centre. Repeat for both sides.
- 4) Select 'hip\_side\_child' under 'hip\_side'. In the VME tab change the scale to 100, select 'Select plane' and assign the following:
  - **Origin:** 'Femur\_Head\_Sphere\_C'
  - **Point 1:** 'O\_cylinder\_side' (fitted geometry under 'tibia\_side') → from **femur** surface fitting
  - **Point 2:** 'P\_cylinder\_side' (fitted geometry under 'tibia\_side') → from **femur** surface fitting
- 5) Make sure to select 'Normal' again before proceeding to the next step.
- 6) Select 'hip\_side\_child' and press **Ctrl + T** to enter operations. Select 'VME Reference System' under 'Reference Systems' and fix the rotations as to follow the ISB recommendations. Click 'Ok' to save. Repeat for both sides.

### 3.4.3 Knee Joint Axes

- 1) Select 'knee\_side\_parent' under 'tibia\_side > knee\_side'.
- 2) Select the VME tab at the bottom of the Control Panel and change the Scale to 100 so that the axes are visible. On the three options below select 'Select Plane' and assign the following:
  - **Origin:** 'O\_cylinder\_side'
  - **Point 1:** 'P\_cylinder\_side'
  - **Point 2:** 'Femur\_Head\_Sphere\_C' → from **femur** surface fitting

Make sure to select 'Normal' again before proceeding to the next step.

- 3) Select 'knee\_side\_child' under 'tibia\_side > knee\_side'.
- 4) Select the VME tab at the bottom of the Control Panel and change the Scale to 100 so that the axes are visible. On the three options below select on 'Select Plane' and assign the following:
  - **Origin:** 'O\_cylinder\_side'
  - **Point 1:** 'P\_cylinder\_side'
  - **Point 2:** 'O\_cylinder\_side' → from **talus** surface fitting

Make sure to select 'Normal' again before proceeding to the next step.

- 5) Transform both reference systems to ISB recommendations.

### 3.4.4 Foot Sole Axes

- 1) Select the technical palpated landmarks under 'calcn\_side'. Create an average landmark named 'Average' for 'IDHLX\_side' and 'IDM5\_side'.
- 2) Select 'foot\_sole\_ref\_sys' under 'calcn\_side > foot\_sole\_ref\_syst'.
- 3) Select the VME tab at the bottom of the Control Panel and change the Scale to 100 so that the axes are visible. On the three options below select on 'Select Plane' and assign the following:
  - **Origin:** 'calcn\_floor\_side'
  - **Point 1:** 'Average'
  - **Point 2:** 'IDHLX\_side'

Make sure to select 'Normal' again before proceeding to the next step.

- 4) Transform the reference system to ISB recommendation and translate it relative to the talar cylinder's centre 'O\_cylinder'.
- 5) From the fitted geometries under the talus, select point 'X\_cylinder' and press **Ctrl + T** to transform it. Translate it relative to 'foot\_sole\_ref\_sys' on each side with the following translations: [**x**=100, **y**=0, **z**=0] – so that it is visible. This step is taken as to be able to assign the third line of action for the ankle child reference system later on.

### 3.4.5 Ankle Joint Axes

- 1) Select 'ankle\_side\_parent' under 'talus\_side > ankle\_side'.
- 2) Select the VME tab at the bottom of the Control Panel and change the Scale to 100 so that the axes are visible. On the three options below select on 'Select Plane' and assign the following:
  - **Origin:** 'O\_cylinder\_side'
  - **Point 1:** 'P\_cylinder\_side'

- **Point 2:** 'O\_cylinder\_side' → from **femur** surface fitting

Make sure to select 'Normal' again before proceeding to the next step.

- 3) Select 'ankle\_side\_child' under 'talus\_side > ankle\_side'.
- 4) Select the VME tab on the bottom of the Control Panel and change the Scale to 100 so that the axes are visible. On the three options below select on 'Select Plane' and assign the following:
  - **Origin:** 'O\_cylinder'
  - **Point 1:** 'P\_cylinder'
  - **Point 2:** 'X\_cylinder'

Make sure to select 'Normal' again before proceeding to the next step.

- 5) Transform both reference systems to ISB recommendations.

### 3.4.6 Subtalar Joint Axes

- 1) Select 'subtalar\_side' under 'calcn\_side > subtalar\_side'.
- 2) Select the VME tab on the bottom of the Control Panel and change the Scale to 100 so that the axes are visible. On the three options below select on 'Select Plane' and assign the following:
  - **Origin:** 'Calc\_Sphere\_Centre' → from talus surface fitting
  - **Point 1:** 'Navic\_Sphere\_Centre' → from talus surface fitting
  - **Point 2:** 'O\_cylinder\_side' → from tibia surface fitting
- 3) Make sure to select 'Normal' again before proceeding to the next step.
- 4) Transform both reference systems via rotations of  $\pm 90/180^\circ$  so that the ISB recommended orientation is rotated through by  $90^\circ$  about the y-axis (X-axis pointing forward, Y-axis pointing upwards and Z-axis resulting from the cross product).

### 3.4.7 Metatarso-phalangeal Joint Axis

- 1) Select 'mtp\_side\_ref\_sys' under 'toes\_side > mtp\_side'.
- 2) Select the VME tab at the bottom of the Control Panel and change the Scale to 100 so that the axes are visible. On the three options below select on 'Select Plane' and assign the following:
  - **Origin:** 'JHLX\_side'
  - **Point 1:** 'JMD5\_side'
  - **Point 2:** 'calcn\_floor\_side'
- 3) Make sure to select 'Normal' again before proceeding to the next step.
- 4) Transform both reference systems to ISB recommendations.

## 4 Surface Markers Palpation

For successfully registering gait analysis data, i.e. marker trajectories, onto the computational model, correspondent markers are identified in the MRI images and virtually palpated so that gait simulation can be produced. This process takes place again in NMSBuilder.

- 1) To import the MRI images, select the MRI folder from the data tree and click on File > Import > Images > DICOM. Locate and import the MRI folder.
- 2) To view the MRI images, select View > Ortho Slice and check the circle next to the MRI folder. For better manipulating and viewing the images, right-click on the first quadrant and select 'Maximize SubView'.
- 3) Markers are identified by small white 'circular spots' on the periphery of the body (on the skin) and their location is illustrated below (Figure 7) along with a descriptive table (Table I). The list of markers to be palpated can be loaded in NMSBuilder as a dictionary ("MRI\_visible\_markers.dic", available in NMSBuilder\_dictionaries).
- 4) Once palpated in the MRI VME, the markers need to be reparented to their specific group, under the 'Surface Markers' landmark loud by right clicking on each landmark point.

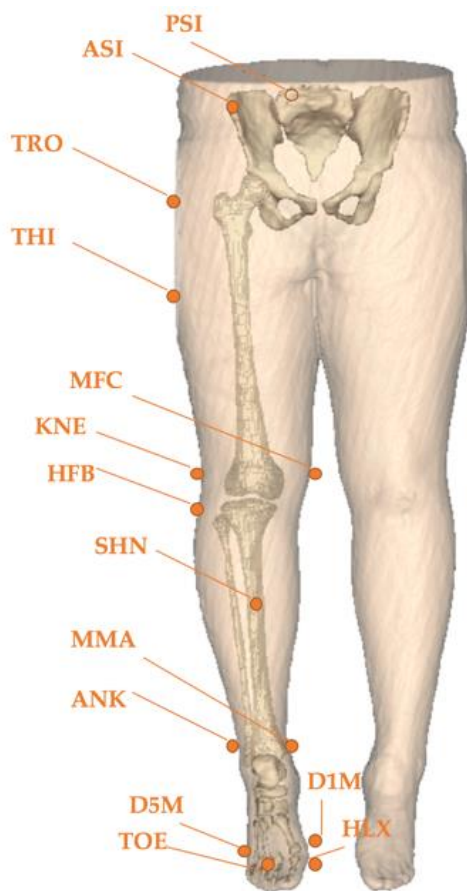


Table I – List of surface markers and their description

<i>Pelvis</i>	PSI	Posterior superior iliac spine
	ASI	Anterior superior iliac spine
<i>Femur</i>	TRO	Greater trochanter
	THI	Thigh (femur bone)
	MFC	Medial femur condyle
<i>Tibia</i>	KNE	Lateral femur condyle
	HFB	Lateral tibia condyle
	SHN	Shin (tibia bone)
	MMA	Medial malleolus
<i>Calcaneus</i>	ANK	Ankle (lateral malleolus)
	D1M	First distal metatarsal
	D5M	Fifth distal metatarsal
<i>Toes</i>	TOE	Third distal metatarsal
	HLX	First proximal phalanx

Figure 7 – MRI visible surface markers

NOTE: Some markers might be difficult to identify (such as PSI because the subject might be laying on them) therefore different MRI sequences might be needed. Even though it is preferred to use the same sequence used for segmentation, if other sequences are available it is preferable to use those rather than 'guessing' markers' positions.

## 5 Muscles Definition

### 5.1 Registering Landmark Clouds

At the bottom of the NMSBuilder data tree is a collection of registration clouds that must firstly be registered to the manually palpated anatomical landmarks (see Section 3.3). These registered clouds are then exported to MATLAB:

- 1) Firstly, navigate to the 'registration\_clouds' folder in the template data tree and select one of the clouds corresponding to specific geometries.
- 2) From the top menus select 'Operations' > 'Modify' > 'Register Landmark Cloud'.
- 3) Select 'target' and navigate the pop-up menu to the cloud of manually palpated landmarks corresponding to the same segment as the registration cloud.
- 4) In the 'reg. type' drop-down menu select 'affine'.
- 5) Check that the 'apply' box is ticked and then click 'ok'.
- 6) Repeat this step for all registration clouds.

### 5.2 MATLAB Muscle Snapping

The registered clouds that appear at the bottom of the data tree can now be exported to MATLAB:

- 1) Select a registered muscle cloud and then 'File' > 'Export' > 'Landmark' to export the cloud as a .txt file and name the files by geometry, e.g. 'femur\_r.txt'.
- 2) Once all clouds have been exported, open MATLAB and run the '*snapLandmarks.m*' script available in Matlab Functions folder.
- 3) Select the mesh (the .stl file corresponding to the cloud being fitted) from the MeshLab Processing folder.
- 4) Select the exported cloud that is to be snapped.
- 5) Repeat these steps for all the registered clouds.

The output from the MATLAB script is a series of .txt files describing the positions of muscle landmarks which can now be imported back into NMSBuilder:

Import each snapped muscle cloud under the corresponding bone geometry. Both the registered and unregistered muscle clouds at the bottom of the data tree can now be deleted, leaving just the snapped muscle clouds under their individual geometries.

## 5.3 Toes muscles

The flexors and extensors muscles inserting at the phalanges and hallux are easily identifiable at the level of the toes. In fact their paths are constrained by the shape of the bones they have to stick to. For this reason, a direct palpation of the distal via points and insertion points is recommended at this stage. The points to be defined are shown in Figure 8 and can be palpated by selecting the toe bone geometry in NMSBuilder and following the instruction as in section 3.3. To help aid the process, a dictionary file (“Toes\_muscles\_side.dic”, available in NMSBuilder\_dictionaries) with the landmark names is provided.

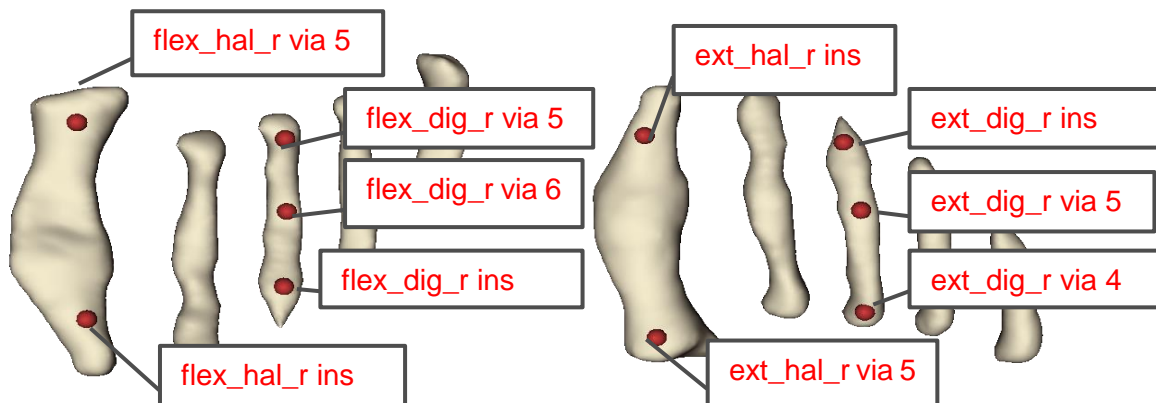


Figure 8 – Virtual palpation of the muscle attachments belonging to the toes segment, bottom view (Right) and top view (Left)

## 5.4 Muscle Adjustments

The muscle origin, via and insertion points calculated by MATLAB are approximations derived from a generic model after being transformed to match the manually palpated geometries of the subject-specific model. Because of this, the muscle locations in the model are often slightly different from the location in the subject’s MRI and so manual adjustment of the muscle points is needed to acquire a more accurate model.

Adjustment is carried out by checking the calculated points in each body alongside the participant MRI data in NMSBuilder. By positioning the transverse slice of the MRI so it is level with the point being checked, the points can be adjusted to match the actual anatomy; often this involves moving the point to sit more in the centre of large muscles such as the Gluteus Maximus.

Included in each of the following sections are the codes used in NMSBuilder and the muscles they correspond to, allowing them to be looked up in an Atlas of Cross-sectional Anatomy.

### 5.4.1 Pelvis

The pelvis does not often require much adjustment. One common discrepancy that can occur in the muscle snapping is that origin points (often points related to the gluteus) can be snapped

to the wrong side of the ilium (this is especially common if the segmentation of the iliac wall is particularly thin).

The only point which should be on the medial surface of the ilium should be the iliacus origin (Figure 9). To move mislocated points onto the correct surface and keep the relative position, the opacity of the geometry can be changed by selecting the geometry from the data tree and then the 'Visual props' tab. Select the material icon and then adjust the opacity slider down to around 85-90%. When editing the muscle point it is then easier to move the point straight through to the correct side.

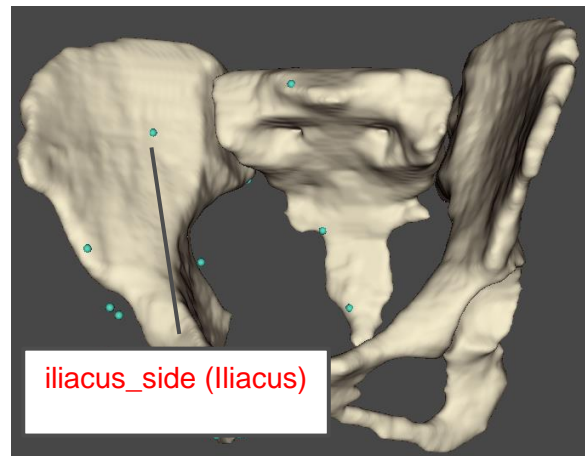


Figure 9 - Pelvis muscle origin locations

### 5.4.2 Femur

Points to be checked in the femur often include the quadriceps muscle group (comprised of the rectus femoris and the three vastus muscles: the vastus medialis, vastus intermedius and vastus lateralis). These points often require adjustment to the centre of their muscle cross-section (Figure 10).

Points to be checked in Femur:

- vas\_med\_side via 1 → Vastus Medialis
- vas\_int\_side via 1 → Vastus Intermedius
- vas\_lat\_side via 1 → Vastus Lateralis
- sar\_side via 1 → Sartorius
- tfl\_side via 1 → Tensor Fasciae Latae
- glut\_max\_side(1,2&3) via 2 → Gluteus Maximus
- med\_gas\_side via 1 → Gastrocnemius (Medial Head)
- lat\_gas\_side via 1 → Gastrocnemius (Lateral Head)

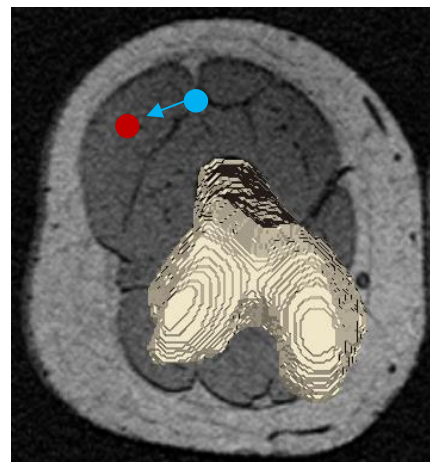


Figure 10 – Vastus lateralis via point shifted from wrong location (blue) according to the MRI to match centre of the muscle cross section (red)

### 5.4.3 Tibia

Points to be checked in tibia:

- semimem\_side via 1 → Semimembranosus
- semiten\_side (via 1, 2 & 3) → Semitendinosus

- bifemlh\_side via 1 → Biceps Femoris (Long Head)
- bifemsh\_side via 1 → Biceps Femoris (Short Head)
- sar\_side (via 2 & 3) → Sartorius
- grac\_side (via 1 & 2) → Gracilis
- tib\_post\_side via 1 → Tibialis Posterior
- flex\_dig\_side via 1 → Flexor Digitorum
- flex\_hal\_side via 1 → Flexor Hallucis

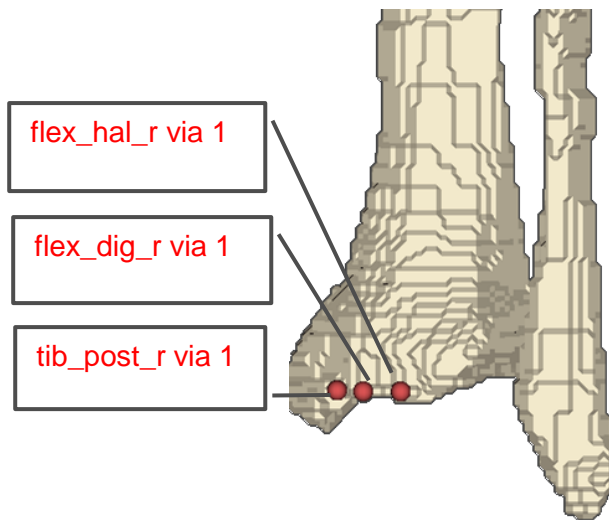


Figure 11 - Right tibia, posterior view

The via points for the muscle paths of the tibialis posterior, flexor digitorum and flexor hallucis must be located on the posterior surface of the tibia (Figure 11) in a specific order. The tibialis posterior should be the most medial and the flexor hallucis the most lateral, with flexor digitorum between them.

- tib\_ant\_side via 1 → Tibialis Anterior
- ext\_hal\_side via 1 → Extensor Hallucis
- ext\_dig\_side via 1 → Extensor Digitorum

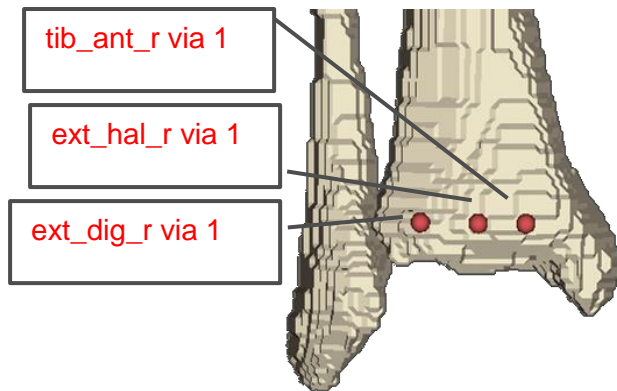


Figure 12 - Right tibia, anterior view

As with the posterior via points, the anterior points must also be ordered. Facing in the anterior view, the tibialis anterior should be the most medial and the extensor digitorum should be the most lateral with the extensor hallucis between them (Figure 12).

- per\_brev\_side (via 1 & 2) → Peroneus Brevis
- per\_long\_side (via 1 & 2) → Peroneus Longus

The Peroneus Brevis (red) and Peroneus Longus (green) need to be arranged correctly on the fibula. In real anatomy, the two tendons run down the distal apex of the fibula and then cross each other (Figure 13).

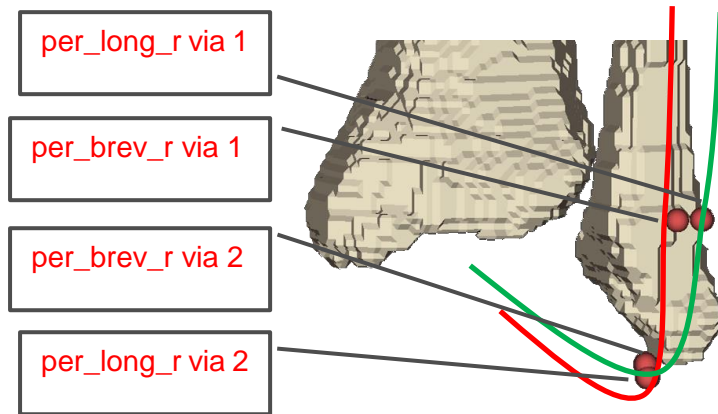


Figure 13 - Right tibia/fibula, posterior view

- rect\_fem\_r → Rectus Femoris
- vas\_int\_r ins → Vastus Intermedius
- vas\_lat\_r ins → Vastus Lateralis
- vas\_med\_r ins → Vastus Medialis

The Vastus muscles, which model the quadriceps group minus the Rectus Femoralis, insert onto the Patella and then transfer their force via the Patella tendon. As the patella is fixed with respect to the Tibia in this model, the Patella tendon is not modeled and the three muscles simply insert upon the Patella in the order shown in the Figure 14.

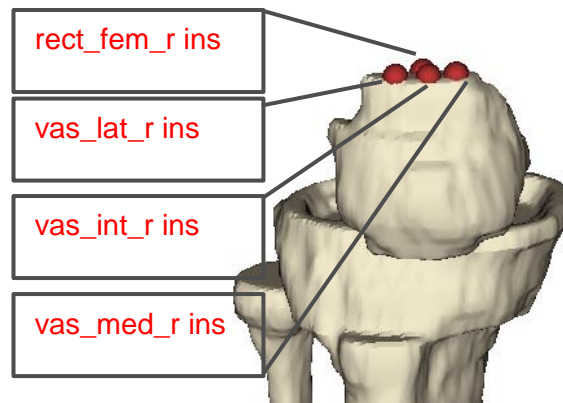


Figure 14– Right patella, anterior view

#### 5.4.4 Calcaneus

Points to be checked in calcaneus:

- med\_gas\_side ins → Medial Gastrocnemius
- lat\_gas\_side ins → Lateral Gastrocnemius
- soleus\_side ins → Soleus

The insertion points for the *triceps surae* are distributed on the cross section of the Achilles' tendon as shown in Figure 15.

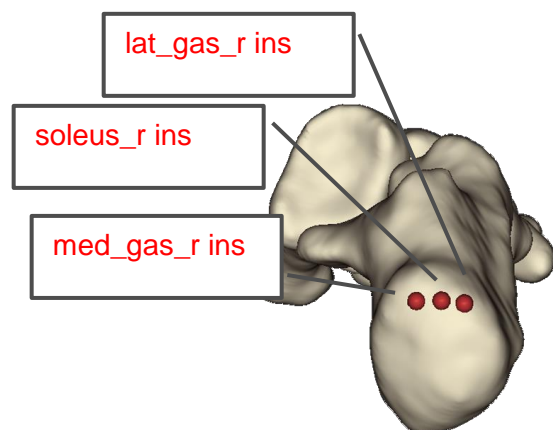


Figure 15 - Right Calcaneus, posterior view

- tib\_post\_side via 2 → Tibialis Posterior
- flex\_dig\_side (via 2 & 3) → Flexor Digitorum

- flex\_hal\_side (via 2 & 3) → Flexor Hallucis
- per\_brev\_side via 3 → Peroneus Brevis
- per\_long\_side (via 3, 4 & 5) → Peroneus Longus
- ext\_dig\_side via 2 → Extensor Digitorum
- ext\_hal\_side via 2 → Extensor Hallucis

## 6 Creating an OpenSim Model

### 6.1 Bodies

- 1) To create an OpenSim model, select the following icon from the top toolbar in NMSBuilder:  .
- 2) A new blank branch will now be created at the base of the data tree. To add bodies to the model select the 'OpenSim Model' branch and then the 'Create Body' (  ) icon from the toolbar and select the folder for the desired body section from the pop-up menu.

#### 6.1.1 Inertial properties

For building the dynamic model, it is important that inertial properties are computed. This is done by incorporating two different 'densities' in the model, one for soft tissue (muscles, tendons, fat, skin etc...) and one for bones. By selecting each body of the 'OpenSim Model' tree, the 'VME' tab in the control panel can be used to edit each segment density according to the values in Table II.

Table II – Values of the tissue density as reported in White et al., 1989 [7]

TISSUE	Density	
	MALE	FEMALE
<b>Bone</b>	1.42E-06	1.42E-06
<b>Soft tissue</b>	1.03E-06	1.02E-06
<b>Negative soft tissue</b>	-1.03E-06	-1.02E-06

### 6.2 Joints

- 1) Select the 'pelvis Body' section from the OpenSim data tree and then the 'Create Joint' (  ) icon from the OpenSim toolbar.
- 2) Select 'Type' > 'Custom Joint' from the top drop-down menu.
- 3) Tick the 'Use ground as parent' option.
- 4) Select 'Child Body' option and then 'pelvis Body' body from the OpenSim tree in the pop-up menu.

- 5) Set the 'Ref. Sys. In Child' option to 'ground\_pelvis\_child' under the 'ground\_pelvis' reference system file in the main data tree.
- 6) Select 'Ok'

Repeat this process for each OpenSim body on both sides with the options in Table III for each joint.

**Table III – Definition of lower limb joints in the OpenSim model**

	<b>hip</b>	<b>knee</b>	<b>ankle</b>	<b>subtalar</b>	<b>mtp</b>
<b>Type</b>	Ball Joint	Pin Joint	Pin Joint	Pin Joint	Pin Joint
<b>Parent Body</b>	pelvis	femur_side	tibia_side	talus_side	calc_n_side
<b>Ref. Sys. In Child</b>	hip_side_parent	knee_side_parent	ankle_side_parent	subtalar_side	mtp_side
<b>Child Body</b>	femur_side	tibia_side	talus_side	calc_n_side	toes_side
<b>Ref. Sys. In Child</b>	hip_side_child	knee_side_child	ankle_side_child	subtalar_side	mtp_side

### 6.3 Surface Markers

- 1) Select 'pelvis Body' from the OpenSim data tree and then 'Create MarkerSet' (  ) icon from the toolbar.
- 2) Select 'Landmark Cloud' and navigate to the Surface Markers landmark cloud for the pelvis geometry.
- 3) Make sure the 'Marker Set Body' is set to the correct body (e.g. 'pelvis').
- 4) Select 'Ok'.

Repeat this process for each OpenSim Body **except the 'Talus Body'** (as there is no specific surface marker set for this body), selecting the surface marker landmark cloud that corresponds to that body.

### 6.4 Muscles

- 1) Navigate through 'Operations' > 'Create' > 'OpenSim' > 'Auto Create Muscles'.
- 2) Wait for the OpenSim muscles to automatically be created and then visually inspect the results before exporting the OpenSim model.

### 6.5 Exporting the OpenSim Model

The OpenSim model can now be exported from NMSBuilder by selecting the 'OpenSim Model' root in the data tree and then selecting the 'Export OpenSim Model' (  ) icon from the toolbar.

Save the model with an appropriate name in the '5\_OpenSim' folder.

## 6.6 Update of joint coordinates name and rotations order

The model exported from NMSBuilder, depending on the version of the software, may include automatically generated names for joints and joint coordinates. Moreover, the default rotation order will be XYZ, which for our modelling conventions would be ab/adduction, internal/external rotation, flexion/extension. It is common practice in biomechanics to use a ZXY rotation order (flexion/extension, ab/adduction, internal/external rotation) to describe three-dimensional joint rotations. The MATLAB script “upd\_model\_coords.m” (located in “Matlab Functions” folder) allows to modify the names of the joint coordinates, their range of motion and the order of the rotations so that they match the coordinate nomenclature of the OpenSim model gait2392 and the kinematic recommendations of the International Society of Biomechanics.

## 7 Definition of conditional via points in OpenSim

Depending on the bone geometries and bone definitions, sometimes it will be necessary to define, in the muscle actuators included in the OpenSim model, conditional via points. Conditional via points are like normal via points used in musculoskeletal models, but they are active only within ranges of values of a specified generalized coordinate. They are useful to avoid penetration between muscle paths and bone geometries but often they need to be manually defined.

In the lower limb models, we often included via points in the definition of the following muscles:

- 1) Gastrocnemius lateralis and gastrocnemius medialis: to avoid compenetration with the proximal tibia and the calcaneus
- 2) Vastii: to avoid compenetration with the patellar groove
- 3) Hamstrings: to implement a muscle path similar to gait2392 for increasing knee flexion.
- 4) Iliacus and psoas: to avoid underestimation of muscle moment arms at high hip flexion angles.

## 8 Quality check

### 8.1 Experimental data

- 1) Medical images: all the bones, soft tissue and muscles tissue must be visible and in the field of view to allow correct segmentation and definition of muscles paths; gait markers must be visible in the images to allow the correct registration of the images with gait data
- 2) Gait analysis data must be evaluated based on objective criteria, e.g. number of visible markers in the frames of interest and trajectories noise level, by an experienced operator;

If quality tests are not passed, the model cannot be built, however an incomplete dataset can be adapted if the minimum requirements are met.

## 8.2 Post processing

Geometries fitting:

- 1) After the fitting algorithm has been run, residuals are calculated to evaluate the goodness of the fit.
- 2) The fitted analytical shapes are imported into NMSBuilder and a visual checks ensure good agreement with the fitted bones geometries.

## 8.3 Model building

Muscles paths:

- 1) A visual check is performed to assess the quality of the supervised atlas registration superimposing the muscles paths (defined as active lines in NMSBuilder) onto the medical images. If good match is not achieved, then muscles attachments and via points are updated to follow the subject's individual muscle shape.
- 2) A further comparison with anatomical atlases and the generic model gait2392, enables muscle paths being not visible in the MRI imaging to be identified.

## 8.4 Dynamic simulations

Inverse kinematics:

- 1) Tracking errors computed from the OpenSim IK tool are evaluated against error limits recommended in simulation best practices by Hicks et al., 2015 [8]

Static optimization:

- 1) Predicted muscle forces are checked for unrealistic tetanic activations.
- 2) Coordinate actuator contributions are quantified and verified to stay within the limits indicated in simulation best practices by Hicks et al., 2015 [8]

NB: Additional checks on the simulation quality, e.g. pelvis residual analysis to test the model dynamic consistency, are not applicable to the mono-lateral models employed in this study.

## 9 Feedback – help us improving

Please report any inaccuracy or imprecision in this document to:

- Erica Montefiori: e.montefiori@sheffield.ac.uk

## Acknowledgements

This study was supported by the European Commission, (7th FP, ICT large integrated project MD-Paedigree, Contract Number 600932) and by the UK EPSRC (Frontier Engineering Awards, EP/K03877X/1).



## References

- [1] Valente, G., Crimi, G., Vanella, N., Schileo, E. and Taddei, F., 2017. nmsBuilder: Freeware to create subject-specific musculoskeletal models for OpenSim. *Computer Methods and Programs in Biomedicine* 152, 85-92.
- [2] Delp, S. L., Anderson, F. C., Arnold, A. S., Loan, P., Habib, A., John, C. T., Guendelman, E. and Thelen, D. G., 2007. OpenSim: open-source software to create and analyze dynamic simulations of movement. *IEEE Transactions on Biomedical Engineering* 54, 1940-1950.
- [3] Cignoni, P., Callieri, M., Corsini, M., Dellepiane, M., Ganovelli, F. and Ranzuglia, G., 2008. Meshlab: an open-source mesh processing tool. *Eurographics Italian Chapter Conference*.
- [4] van Sint Jan, S., 2007. *Color Atlas of Skeletal Landmark Definitions*. Churchill Livingstone
- [5] Baker, R., 2003. Letter to the editor: ISB recommendation on definition of joint coordinate systems for the reporting of human joint motion—part I: ankle, hip and spine. *Journal of Biomechanics* 36(2), 300-302
- [6] Wu, G., Siegler, S., Allard, P., Kirtley, C., Leardini, A., Rosenbaum, D., Whittle, M., D'Lima, D. D., Cristofolini, L., Witte, H., Schmid, O. and Stokes, I., 2002. ISB recommendation on definitions of joint coordinate system of various joints for the reporting of human joint motion - part I: ankle, hip, and spine. *Journal of Biomechanics* 35, 543-548.
- [7] White, D., Woodard, H., Hammond, S., 1987. Average soft-tissue and bone models for use in radiation dosimetry. *British journal of radiology* 60, 907-913.
- [8] Hicks, J., Uchida, T., Seth, A., Rajagopal, A. and Delp, S. L., 2015. Is my model good enough? Best practices for verification and validation of musculoskeletal models and simulations of human movement. *Journal of Biomechanical Engineering* 137(2):020905.

# Appendix II

**Table AII- 1 - Inter-operator repeatability of muscle segmentation for three subjects enrolled in the study. Individual muscle values have been reported for each subject and each operator with corresponding mean, standard deviation (SD) and coefficient of variation (CoV). Root mean square error across the three subjects was calculated as well.**

Muscles	Subj1 volumes [cm <sup>2</sup> ]						Subj2 volumes [cm <sup>2</sup> ]						Subj3 volumes [cm <sup>2</sup> ]						
	OP1	OP2	OP3	Mean	SD	CoV	OP1	OP2	OP3	Mean	SD	CoV	OP1	OP2	OP3	Mean	SD	CoV	RMSE
Adductor brevis	65.5	48.3	55.4	56.4	8.6	15.3	48.2	59.6	56.0	54.6	5.8	10.6	61.4	79.1	50.3	63.6	14.5	22.8	9.6
Adductor longus	75.9	95.6	108.7	93.4	16.5	17.7	66.8	78.7	71.7	72.4	6.0	8.3	81.1	91.6	77.6	83.4	7.3	8.8	9.9
Adductor magnus	291.2	316.1	294.7	300.7	13.5	4.5	313.3	329.4	352.3	331.7	19.6	5.9	322.2	352.2	346.8	340.4	16.0	4.7	16.3
Biceps femoris caput breve	51.5	42.2	46.9	46.9	4.6	9.9	87.2	82.7	84.9	84.9	2.2	2.6	61.9	60.5	61.2	61.2	0.7	1.2	2.5
Biceps femoris caput longum	131.7	143.7	143.2	139.5	6.8	4.8	119.6	135.0	124.8	126.5	7.8	6.2	110.7	120.8	104.0	111.9	8.5	7.6	7.7
Gluteus maximus	561.4	617.1	592.2	590.2	27.9	4.7	409.1	447.4	469.9	442.1	30.7	6.9	574.1	559.7	577.3	570.4	9.4	1.6	22.7
Gluteus medius	236.8	257.8	271.7	255.4	17.6	6.9	208.7	220.1	255.1	228.0	24.2	10.6	256.7	293.9	262.7	271.1	20.0	7.4	20.6
Gluteus minimus	62.1	75.3	67.1	68.2	6.7	9.8	56.9	64.5	75.9	65.7	9.6	14.6	33.6	42.9	37.3	37.9	4.7	12.3	7.0
Gracilis	48.1	52.7	57.3	52.7	4.6	8.7	40.6	40.4	39.3	40.1	0.7	1.7	43.3	52.5	38.2	44.7	7.2	16.1	4.2
Iliacus	109.0	119.5	123.7	117.4	7.6	6.4	123.4	119.2	138.4	127.0	10.1	8.0	117.1	112.1	125.6	118.3	6.8	5.8	8.2
Psoas	97.1	108.6	99.4	101.7	6.1	6.0	70.1	78.7	76.1	75.0	4.4	5.9	51.6	57.6	49.7	53.0	4.1	7.7	4.9
Rectus femoris	103.7	101.1	110.1	105.0	4.6	4.4	123.6	135.7	138.8	132.7	8.1	6.1	132.3	152.2	144.4	143.0	10.0	7.0	7.6
Sartorius	77.7	90.2	95.1	87.7	8.9	10.2	69.0	77.2	71.7	72.6	4.2	5.7	96.9	98.5	88.9	94.8	5.1	5.4	6.1
Semimembranosus	165.2	163.8	167.0	165.3	1.6	1.0	157.0	167.4	163.1	162.5	5.2	3.2	88.2	108.5	94.5	97.1	10.4	10.7	5.7
Semitendinosus	81.8	92.5	87.9	87.4	5.4	6.1	118.5	130.6	120.0	123.0	6.6	5.4	109.4	119.5	104.5	111.2	7.6	6.9	6.5
Tensor fasciae latae	33.9	43.2	41.4	39.5	4.9	12.4	28.9	32.5	33.3	31.5	2.3	7.4	41.3	48.5	45.1	45.0	3.6	7.9	3.6
Vastus intermedius	251.6	266.3	272.4	263.4	10.7	4.1	233.9	250.2	233.9	239.3	9.4	3.9	199.6	223.5	225.1	216.0	14.3	6.6	11.5
Vastus lateralis	321.1	326.0	326.4	324.5	2.9	0.9	286.4	348.2	328.3	321.0	31.5	9.8	303.0	335.4	339.2	325.8	19.9	6.1	18.1
Vastus medialis	182.0	195.9	196.2	191.3	8.1	4.2	208.1	206.8	206.5	207.1	0.8	0.4	205.6	207.0	201.2	204.6	3.0	1.5	4.0
Extensor digitorum longus	32.9	44.6	50.5	42.7	8.9	21.0	33.3	41.5	24.9	33.2	8.3	25.0	36.4	53.1	34.1	41.2	10.4	25.3	9.2
Extensor hallucis longus	25.9	36.8	29.2	30.6	5.6	18.4	46.1	19.3	15.3	26.9	16.8	62.4	33.0	24.5	34.2	30.6	5.3	17.3	9.2
Flexor digitorum longus	24.9	26.2	16.6	22.6	5.2	23.0	23.7	17.2	11.0	17.3	6.4	36.7	21.7	28.0	20.6	23.4	4.0	17.0	5.2
Flexor hallucis longus	54.9	64.0	63.1	60.7	5.0	8.2	61.6	40.9	40.8	47.7	12.0	25.2	59.6	51.2	61.3	57.4	5.4	9.4	7.5
Gastrocnemius lateralis	96.5	99.5	95.8	97.2	2.0	2.0	59.9	60.3	65.0	61.7	2.8	4.6	97.8	102.8	99.4	100.0	2.5	2.5	2.4
Gastrocnemius medialis	179.0	187.7	184.5	183.7	4.4	2.4	139.2	146.5	149.2	145.0	5.1	3.5	147.5	158.0	160.6	155.4	6.9	4.5	5.5
Peroneus brevis	18.6	20.8	43.3	27.6	13.6	49.4	32.7	29.9	31.8	31.5	1.4	4.4	33.6	42.8	55.4	43.9	11.0	25.0	8.7
Peroneus longus	37.6	42.9	14.3	31.6	15.2	48.2	25.4	24.0	21.5	23.6	2.0	8.3	39.4	36.4	23.2	33.0	8.6	26.1	8.6
Soleus	346.3	373.0	369.0	362.8	14.4	4.0	297.3	345.1	347.9	330.1	28.4	8.6	338.1	341.0	347.1	342.1	4.6	1.3	15.8
Tibialis anterior	110.6	100.6	116.6	109.3	8.1	7.4	82.2	120.9	138.5	113.9	28.8	25.3	83.1	119.1	88.6	96.9	19.4	20.0	18.8
Tibialis posterior	76.2	70.9	81.4	76.2	5.2	6.9	60.9	72.4	77.4	70.2	8.5	12.1	65.8	81.1	68.4	71.7	8.2	11.4	7.3

**Table AII- 2 – Individual muscle volumes for right limb of the eleven subjects enrolled in the study**

	Right volumes [cm <sup>2</sup> ]										
	Subj1	Subj2	Subj3	Subj4	Subj5	Subj6	Subj7	Subj8	Subj9	Subj10	Subj11
<b>Gluteus maximus</b>	606.1	786.2	653.7	474.1	646.3	469.2	405.6	514.9	617.7	593.2	777.0
<b>Gluteus medius</b>	250.8	257.1	284.0	195.9	237.2	232.6	196.8	183.0	251.3	285.1	419.0
<b>Gluteus minimus</b>	36.3	52.3	80.1	42.4	48.0	66.1	45.8	55.3	80.9	40.9	75.0
<b>Adductor brevis</b>	61.2	61.8	77.8	46.7	58.5	69.4	58.4	38.6	56.8	54.2	70.7
<b>Adductor longus</b>	69.6	83.4	59.7	72.1	69.0	117.2	66.2	69.9	79.0	91.7	89.7
<b>Adductor magnus</b>	447.7	396.2	378.6	317.2	323.6	370.4	324.0	294.2	335.6	281.5	498.4
<b>Iliacus</b>	81.8	127.0	107.4	101.1	110.0	110.8	127.4	104.8	118.2	124.1	164.6
<b>Biceps femoris caput longum</b>	127.7	123.0	121.7	92.9	78.2	96.5	119.1	89.8	135.3	95.3	140.5
<b>Biceps femoris caput breve</b>	52.2	40.9	73.2	31.5	50.7	60.4	80.7	34.6	57.1	68.6	77.1
<b>Semimembranosus</b>	122.0	151.2	126.2	103.8	97.7	107.8	153.7	107.1	154.5	98.9	125.1
<b>Semitendinosus</b>	71.6	142.1	92.6	94.7	102.2	140.4	101.3	63.1	88.8	88.5	136.6
<b>Rectus femoris</b>	114.7	68.7	111.7	94.0	113.3	151.0	127.2	141.3	113.3	125.3	156.8
<b>Vastus intermedius</b>	221.6	352.6	295.4	255.8	257.9	283.5	277.2	255.8	272.3	229.8	329.0
<b>Vastus lateralis</b>	303.5	392.6	351.8	293.1	245.1	306.6	326.8	259.9	349.6	328.3	499.2
<b>Vastus medialis</b>	167.4	207.9	267.9	223.9	202.9	241.2	225.7	220.2	208.9	178.2	266.8
<b>Gracilis</b>	36.2	76.1	43.2	16.9	44.7	53.6	47.8	34.2	47.6	37.6	67.5
<b>Sartorius</b>	60.0	93.2	105.3	64.0	84.7	90.7	63.1	50.9	85.8	101.7	165.7
<b>Tensor fasciae latae</b>	46.3	52.9	49.5	17.4	34.4	33.2	36.1	57.8	36.0	57.9	45.6
<b>Gastrocnemius lateralis</b>	87.2	85.3	80.3	67.3	47.9	63.7	63.7	86.3	68.9	81.4	96.9
<b>Gastrocnemius medialis</b>	141.1	185.0	175.8	131.8	131.2	134.4	156.9	143.4	188.4	122.9	225.7
<b>Soleus</b>	306.0	401.0	405.9	323.4	257.7	285.7	304.7	266.9	360.4	328.1	502.6
<b>Tibialis anterior</b>	82.7	103.7	94.2	78.8	89.0	78.2	74.4	110.6	109.9	88.9	135.5
<b>Extensor digitorum longus</b>	21.5	33.9	54.6	44.2	20.8	14.9	30.1	36.9	42.8	31.4	40.6
<b>Extensor hallucis longus</b>	26.1	34.5	37.3	13.0	18.8	30.0	49.1	32.6	32.9	29.8	41.3
<b>Flexor digitorum longus</b>	18.4	25.6	24.9	20.1	14.3	22.9	17.9	28.9	19.7	15.2	26.3
<b>Flexor hallucis longus</b>	29.4	45.6	51.7	64.0	43.3	82.3	53.2	48.6	65.3	39.3	51.9
<b>Peroneus brevis</b>	40.1	41.2	41.6	33.7	29.4	33.0	38.8	33.6	24.6	40.9	38.6
<b>Peroneus longus</b>	34.3	39.7	59.0	34.0	36.4	29.8	25.7	29.5	39.2	35.1	53.4
<b>Tibialis posterior</b>	65.8	87.2	90.6	89.0	57.7	73.2	56.3	86.5	68.4	72.7	109.1

**Table AII- 3 – Individual muscle volumes for the left limb of the eleven subjects enrolled in the study**

	Left volumes [cm <sup>2</sup> ]										
	Subj1	Subj2	Subj3	Subj4	Subj5	Subj6	Subj7	Subj8	Subj9	Subj10	Subj11
<b>Gluteus maximus</b>	583.4	736.2	606.5	434.5	586.5	454.0	409.1	441.1	561.4	574.1	749.8
<b>Gluteus medius</b>	198.0	256.6	297.4	200.6	188.2	268.0	208.7	165.9	236.8	256.7	345.8
<b>Gluteus minimus</b>	53.2	68.6	79.5	47.9	28.3	62.3	56.9	39.2	62.1	33.6	90.4
<b>Adductor brevis</b>	58.5	50.4	74.6	48.5	52.8	72.3	48.2	41.9	65.5	61.4	67.0
<b>Adductor longus</b>	62.2	84.4	79.9	70.3	76.3	101.1	66.8	72.9	75.9	81.1	88.0
<b>Adductor magnus</b>	449.2	336.1	349.3	318.2	320.6	296.8	313.3	228.8	291.2	322.2	402.1
<b>Iliacus</b>	94.9	129.8	108.6	106.4	105.1	102.1	123.4	94.7	109.0	117.1	136.3
<b>Biceps femoris caput longum</b>	116.4	132.9	133.7	84.7	55.3	104.0	119.6	85.9	131.7	110.7	136.2
<b>Biceps femoris caput breve</b>	42.8	37.0	69.6	39.8	68.4	52.0	87.2	39.9	51.5	61.9	58.0
<b>Semimembranosus</b>	124.4	148.8	149.1	116.1	86.3	115.4	157.0	104.0	165.2	88.2	122.7
<b>Semitendinosus</b>	87.2	154.5	82.5	103.2	84.1	126.3	118.5	57.2	81.8	109.4	128.8
<b>Rectus femoris</b>	115.9	128.0	115.5	102.6	101.3	157.6	123.6	117.7	103.7	132.3	131.0
<b>Vastus intermedius</b>	237.2	342.1	305.5	257.8	263.6	242.9	233.9	251.5	251.6	199.6	255.3
<b>Vastus lateralis</b>	293.8	365.0	308.7	286.2	256.8	295.8	286.4	227.6	321.1	303.0	393.6
<b>Vastus medialis</b>	171.9	182.7	242.6	259.6	232.4	223.1	208.1	187.4	182.0	205.6	198.2
<b>Gracilis</b>	37.3	58.1	55.0	31.9	28.3	52.7	40.6	26.7	48.1	43.3	68.0
<b>Sartorius</b>	51.7	76.1	72.3	53.6	78.6	82.4	69.0	50.5	77.7	96.9	152.2
<b>Tensor fasciae latae</b>	34.4	52.5	51.7	21.9	31.5	32.3	28.9	68.6	33.9	41.3	52.2
<b>Gastrocnemius lateralis</b>	80.7	66.1	55.8	61.6	60.6	67.6	59.9	83.2	96.5	97.8	100.1
<b>Gastrocnemius medialis</b>	146.4	177.8	188.8	159.7	145.5	144.2	139.2	139.7	179.0	147.5	227.9
<b>Soleus</b>	285.5	368.6	375.9	367.9	277.0	291.2	297.3	264.3	346.3	338.1	516.0
<b>Tibialis anterior</b>	99.7	96.1	101.6	88.1	85.3	75.9	82.2	100.1	110.6	83.1	114.1
<b>Extensor digitorum longus</b>	34.5	25.9	50.0	46.3	28.5	21.6	33.3	25.9	32.9	36.4	59.4
<b>Extensor hallucis longus</b>	21.6	37.4	32.1	11.4	19.3	27.0	46.1	31.0	25.9	33.0	44.6
<b>Flexor digitorum longus</b>	20.4	28.9	23.1	20.9	21.6	20.8	23.7	31.7	24.9	21.7	32.1
<b>Flexor hallucis longus</b>	36.0	44.8	45.0	40.2	48.6	82.0	61.6	40.8	54.9	59.6	63.1
<b>Peroneus brevis</b>	29.7	35.7	36.5	56.9	27.5	41.8	32.7	23.9	18.6	33.6	34.3
<b>Peroneus longus</b>	24.5	37.7	47.7	34.3	48.0	24.2	25.4	24.4	37.6	39.4	56.4
<b>Tibialis posterior</b>	72.2	80.8	84.2	84.3	57.3	75.8	60.9	77.7	76.2	65.8	111.1

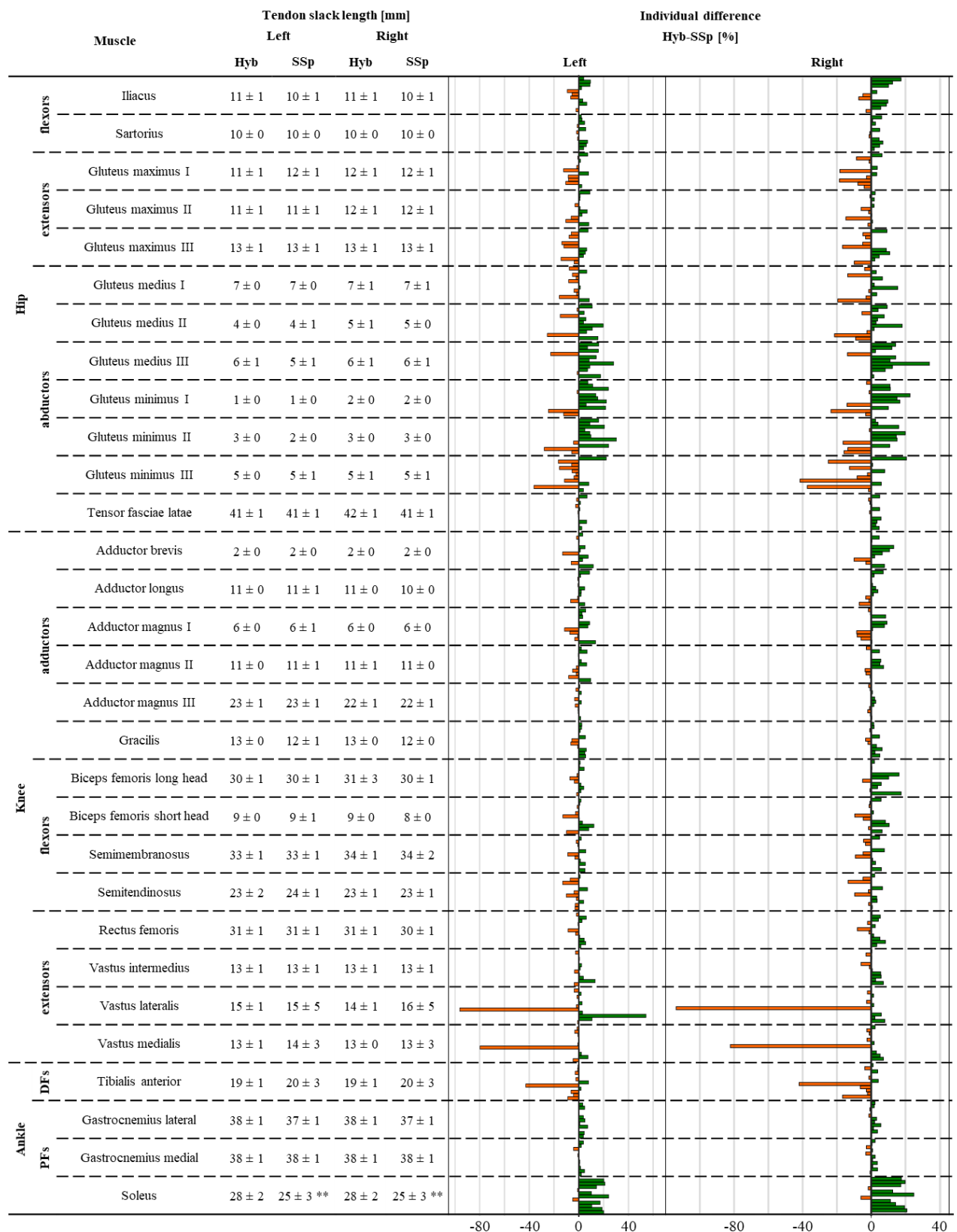


**Figure AII- 1 - Mean±SD of the tendon slack length for the left and right muscles personalised in the SSp model and percentage difference between Hyb and SSp (\* p<0.05, \*\*p<0.01). Individual percentage difference is reported as a bar plot where each bar represents a participant: green positive (orange negative) values show that the tendon slack length in the Hyb model is bigger (smaller). DFs and PFs stand for dorsi and plantar flexors, respectively.**

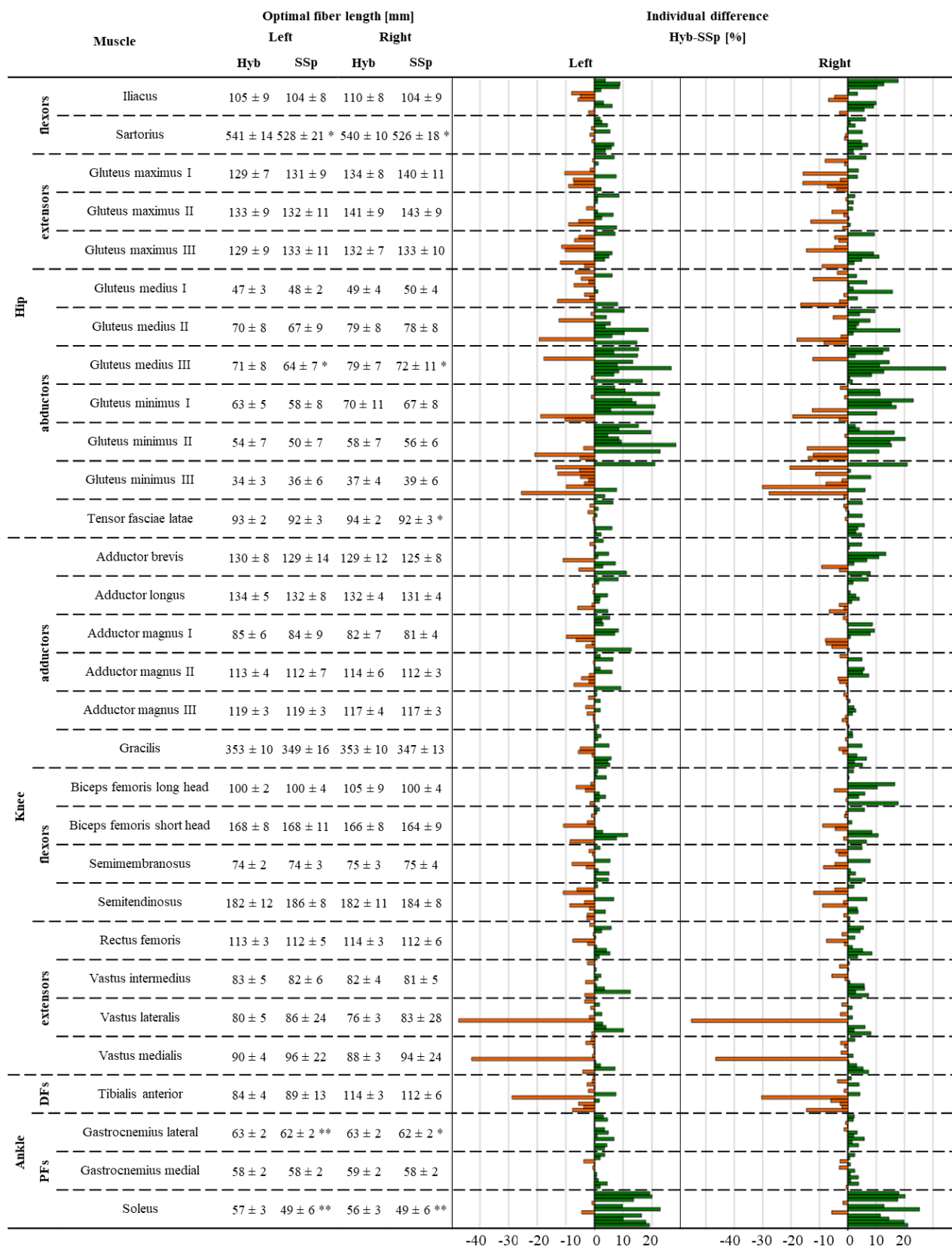


**Figure AII- 2 - Mean±SD of the optimal fibre length for the left and right muscles personalised in the SSp model and percentage difference between Hyb and SSp (\* p<0.05, \*\*p<0.01). Individual percentage difference is reported as a bar plot where each bar represents a participant: green positive (orange negative) values show that the optimal fibre length in the Hyb model is bigger (smaller). DFs and PFs stand for dorsi and plantar flexors, respectively.**